

The finite cell method for the computation of cellular materials

Vom Promotionsausschuss der
Technischen Universität Hamburg
zur Erlangung des akademischen Grades
Doktor-Ingenieur (Dr.-Ing.)

genehmigte Dissertation

von
Stephan Gnegel, Dipl.-Ing.

aus
Eckernförde

2019

Vorsitzender des Prüfungsausschusses

Prof. Dr.-Ing. Norbert Huber

Gutachter

1. Gutachter: Prof. Dr.-Ing. habil. Alexander Düster
2. Gutachter: Prof. Dr.-Ing. Stefan Diebels

Tag der mündlichen Prüfung: 25.03.2019

Vorwort

Die vorliegende Arbeit entstand während meiner Tätigkeit als wissenschaftlicher Mitarbeiter am Institut für Konstruktion und Festigkeit von Schiffen (M-10) der TU Hamburg (Dezember 2012 bis September 2018) im Rahmen des DFG Verbundprojektes *Modellierung der mechanischen Eigenschaften verstärkter Metallschäume auf unterschiedlichen Skalen*, welches zusammen mit den Lehrstühlen Technische Mechanik und Physikalische Chemie der Universität des Saarlandes bearbeitet wurde.

Mein erster Dank gilt meinem Doktorvater, Herrn Prof. Dr.-Ing. habil. Alexander Düster, für die Betreuung und Begleitung dieser Arbeit. Während meiner Doktorarbeit ließ er mir die Freiheit mich mit vielen interessanten Themen innerhalb der numerischen Mechanik zu befassen. Durch die Betreuung von Lehrveranstaltungen konnte ich zudem die zugrunde liegenden Grundlagen besser begreifen und es war mir eine Freude diese weiteren Studenten zu vermitteln.

Desweiteren möchte ich mich bei Herrn Prof. Dr.-Ing. Stefan Diebels für die Übernahme der Zweitkorrektur und die Zusammenarbeit im Forschungsprojekt bedanken. Herrn Prof. Norbert Huber gilt mein Dank für die Übernahme des Prüfungsvorsitzes.

Bei meinen ehemaligen Projektpartnern, insbesondere PD Dr.-Ing. Dr. rer. nat. Anne Jung, möchte ich mich zudem bedanken für den interessanten Einblick in die experimentelle Mechanik und die damit verbundenen Untersuchungen an Metallschäumen.

Einen großen Anteil an dieser Arbeit haben zudem meine Arbeitskollegen. Bei Marcel König und Christian Woitzik möchte ich mich bedanken für die Unterstützung beim Programmieren und die Einblicke in die Linuxwelt. Bei Lars Radtke und Simeon Hubrich möchte ich mich für die vielen hilfreichen Diskussionen bezüglich der Kontinuumsmechanik und numerischer Methoden bedanken. Ein weiterer Dank gilt Meysam Joulaian, für die großartige Zusammenarbeit zu Beginn meiner Tätigkeit und für inhaltliche Korrekturen diese Arbeit betreffend. Bei meinem ehemaligen Bürokollegen Aliakbar Taghipour möchte ich mich für die schöne Zeit und gemeinsame konstruktive Arbeit während seines Aufenthaltes in Deutschland bedanken.

Meinen Eltern gilt meinen Dank für ihre kontinuierliche Unterstützung während meiner gesamten Ausbildung. Meiner Schwester danke ich insbesondere für die Zeit, die Sie der Korrektur dieser Arbeit gewidmet hat.

Meiner Frau Maja danke ich für die fortwährende Motivation, den Glauben an mich und dem Beseitigen vieler zweifelnder Fragen. Ohne dich hätte ich diese Arbeit sicher nicht zuende gebracht.

Flensburg, den 08.11.2019

Stephan Heinze

Abstract

Open cell aluminum foams present an attractive class of materials that are applied in many engineering disciplines ranging from automotive, naval and aerospace industry to biomedical applications. In order to design engineering structures composed of foams, a detailed experimental and numerical investigation of their mechanical properties is necessary. The structure of metal foams consists of a complicated stochastic distribution of pores which requires an immense labor effort to generate a suitable finite element discretization. The finite cell method is a combination of the fictitious domain approach and high order finite elements. Due to the fictitious domain approach the finite cell method has shown to drastically simplify the mesh generation process. Motivated by this promising property we employ the finite cell method and enhance it in order to investigate the mechanical behavior of aluminum foams.

The following topics are addressed in this thesis:

The starting point for any numerical investigation is the discretization of the geometry. A realistic geometric model of metal foams can be provided using voxel models stemming from computed tomography scans. Such models are of course not free from artifacts. In order to achieve automatic **mesh generation for voxel-based models**, algorithms known from computer graphics will be applied to remove these artifacts. In addition voxel models will be modified numerically for example by the application of a thin coating to the metal foams. The effect of the coating on the homogenized elastic properties will be examined using the **window method**. In order to accelerate the homogenization procedure *Aitken's Δ^2 -method* will be applied in this context.

To study the buckling and the **finite elastoplastic deformations** of cell walls the finite cell method will be extended by a *hyperelastic based von Mises plasticity model* which makes use of the multiplicative split of the deformation gradient into its elastic and plastic contributions. By employing this model different structural levels of the aluminum metal foams will be analyzed under large deformations. A focus here is on the **investigation of single pores** that serve to find the microscopic material properties of the aluminum by combining experiments and simulations on pores. Finally computations of larger foam samples will be carried out aiming to find a representative volume element and to verify the material parameters obtained by single pore experiments and inverse computations.

Two different contact formulations based on the penalty method – one for sticking and one for frictionless contact conditions – will be introduced and investigated by comparing their results to the analytical solution derived by Hertz. The **self-contact of metal foams** will be modeled using sticking contact formulation and finally applied to a single pore to show the influence of self-contact on the load displacement curve.

Zusammenfassung

Offenporige Aluminiumschäume repräsentieren eine interessante Art von Materialien, die in vielen Bereichen wie dem Automobilsektor, der Luftfahrtindustrie und der Medizin Anwendung finden. Um Bauteile, die aus Schäumen bestehen, zu entwickeln, sind detaillierte Untersuchungen ihrer mechanischen Eigenschaften notwendig. Die Struktur von Metallschäumen besteht aus einer komplexen stochastischen Verteilung von Poren, und es erfordert einen hohen Arbeitsaufwand eine geeignete Finite Element Diskretisierung zu erstellen. Die Finite Cell Methode ist eine Kombination der Fictitious Domain Methode mit Finiten Elementen hoher Ordnung. Aufgrund des Fictitious Domain Ansatzes kann die Finite Cell Methode den Vernetzungsaufwand drastisch vereinfachen. Motiviert durch diese vielversprechenden Eigenschaften wurde die Finite Cell Methode angewendet und erweitert, um das mechanische Verhalten von Aluminiumschäumen untersuchen zu können.

Folgende Themengebiete werden in dieser Arbeit behandelt:

Der Anfang einer jeden numerischen Untersuchung stellt die Diskretisierung der Geometrie dar. Ein realitätsgetreues Voxelmanifest von Metallschäumen kann mit Hilfe eines Computertomographen erhalten werden. Solche Modelle sind nicht frei von Artefakten. Um eine automatische **Vernetzung von Voxel-basierten Modellen** zu erreichen, werden Algorithmen, die aus der Computergrafik bekannt sind, angewandt. Zudem werden die Voxelmanifeste numerisch modifiziert, zum Beispiel durch das Aufbringen einer dünnen Beschichtung. Der Effekt der Beschichtung auf die homogenisierten elastischen Eigenschaften wird mittels der **Window Methode** untersucht. In diesem Zusammenhang wird die *Aitken's Δ^2 -Methode* angewandt, um die Homogenisierungsprozedur zu beschleunigen. Um das Ausknicken und die **finiten elastoplastischen Deformationen** der Zellstege zu untersuchen, wird die Finite Cell Methode mit einem *hyperelastisch basierten von Mises Plastizitätsmodell* erweitert, welches auf der multiplikativen Unterteilung des Deformationsgradienten in einen elastischen und einen plastischen Anteil beruht. Durch Anwendung dieses Modells wird der Metallschaum auf unterschiedlichen strukturellen Ebenen unter großen Deformationen untersucht. Ein Hauptaugenmerk hier ist die Untersuchung einzelner Poren, die dazu dienen die mikroskopischen Materialeigenschaften des Aluminiums mittels Vergleich von Experiment und Simulation zu bestimmen. Schließlich werden die Rechnungen auf größere Mikrostrukturen ausgedehnt, um Repräsentative Volumen Elemente zu ermitteln und die bereits an den einzelnen Poren ermittelten Eigenschaften zu verifizieren.

Zwei unterschiedliche Ansätze zur Berechnung von Kontaktproblemen basierend auf der „Penalty“ Methode werden eingeführt. Der erste Ansatz beschreibt ein Zusammenkleben der Kontaktflächen („sticking“), wohingegen der zweite Ansatz den reibungsfreien Kontakt zwischen den Körpern beschreibt. Beide Formulierungen werden untersucht, indem die erzielten Ergebnisse mit der analytischen Lösung nach Hertz verglichen werden. Der **Selbstkontakt des Metallschaums** wird mittels der „sticking“ Kontaktformulierung modelliert und schlussendlich auf eine einzelne Pore angewandt, um den Einfluss des Selbstkontaktes auf die Last-Verschiebungskurve zu untersuchen.

Contents

Glossary	3
Notation	4
1 Introduction	5
1.1 Motivation	5
1.2 Scope and outline of this work	8
2 Basic relations of continuum mechanics	10
2.1 Kinematics	10
2.1.1 Strain measures	12
2.1.2 Time derivative	13
2.2 Strong form of the balance of linear and angular momentum	14
2.3 Constitutive models	15
2.3.1 Hyperelastic material models	15
2.3.1.1 The Saint Venant-Kirchhoff material model	16
2.3.1.2 The Hencky material model	17
2.3.2 J_2 small strain plasticity	17
2.3.2.1 General model	17
2.3.2.2 Associative von Mises plasticity	18
2.3.2.3 Integration of the elastoplastic constitutive equations	19
2.3.2.4 The consistent elastoplastic tangent	21
2.3.3 J_2 finite strain plasticity	24
2.3.3.1 General model	24
2.3.3.2 The exponential integrator	24
2.3.3.3 The consistent elastoplastic tangent	27
2.4 Weak form of the equilibrium conditions	28
2.4.1 Weak form of the balance equation in the current configuration	28
2.4.2 Weak form of the balance equation in the reference configuration	29
2.5 Linearization of the weak form	29
2.5.1 The linearized virtual work equation in the reference configuration	29
2.5.2 The linearized virtual work equation in the current configuration	30
3 Finite cell method	32
3.1 Spatial discretization	33
3.2 Mesh generation for voxel-based models	37

3.2.1	Seed-fill algorithm	38
3.3	Adaptive Gaussian quadrature schemes	41
3.3.1	Quadtree space partitioning	41
3.3.2	K-d tree space partitioning	43
3.3.3	Numerical examples	43
3.4	Numerical stabilization methods for the FCM	48
3.4.1	The indicator function	49
4	Numerical homogenization	53
4.1	Basic equations	54
4.1.1	Average stress/ strain theorem	54
4.1.2	Hill-Mandel condition	56
4.1.3	Voigt-Reuss bounds	56
4.2	The window method	56
4.2.1	Acceleration of the window method	60
4.3	Hybrid metal foams	61
4.3.1	Preliminary study	61
4.3.1.1	Accuracy of the spatial discretization	61
4.3.1.2	Acceleration of the window method	63
4.3.2	Influence of the coating thickness	64
5	Computational contact mechanics	68
5.1	Contact kinematics	68
5.1.1	Linearization and variation of the gap function	70
5.2	Weak form and enforcement of contact conditions	71
5.2.1	Linearization	72
5.3	Discretization of contact interface	73
5.3.1	The contact stiffness matrix and right-hand side	76
5.4	The mapping procedure	78
5.4.1	Global contact search	81
5.5	Hertzian contact	81
5.6	Numerical examples	83
5.6.1	Patch test	83
5.6.2	Sticking contact between a cylinder and a rigid plate	86
5.6.2.1	Contact mesh refinement	89
5.6.2.2	h - and p -refinement	91
5.6.2.3	Influence of the penalty factor	93
5.6.2.4	Influence of indentation depth	94
5.6.2.5	Influence of the fictitious domain	96
5.6.2.6	Influence of the numerical quadrature scheme	96
5.6.2.7	Investigation of contact conditions	97
5.6.3	Frictionless contact	98
5.6.3.1	Cylinder and a rigid plate	98
5.6.3.2	Cylinder and a rigid plate with sliding	100
5.6.3.3	Two deformable cylinders	102
5.6.4	Self-contact of a metal foam	104

6	Aluminum foams	107
6.1	The foam struts	108
6.2	Single pore experiments	109
6.2.1	Mesh size	111
6.2.2	Comparison of finite element and finite cell computations	113
6.2.3	Comparison of small and large strain simulations with experiments	113
6.2.4	Comparison of a pore with averaged properties to experiments	115
6.3	20 ppi aluminium foam	116
6.3.1	The geometrical representative volume element	116
6.3.2	The mechanical representative volume element	118
6.3.2.1	Comparison of sample size	119
6.3.2.2	Investigation of different voxel samples	119
6.3.3	Comparison of simulations and experiments	121
7	Summary and Outlook	124
A	Gauss-Legendre quadrature for triangles	126
B	Flow chart of finite J_2 plasticity implementation	129
	Bibliography	131

Glossary

- b** Left Cauchy-Green deformation tensor.
- C** Right Cauchy-Green deformation tensor.
- ϵ Engineering strain tensor.
- F** Deformation gradient.
- E** Green-Lagrange strain tensor.
- H** Displacement gradient.
- ϵ Eulerian logarithmic strain tensor.
- l** Spatial velocity gradient.
- R** Orthogonal rotation tensor.
- U** Right stretch tensor.
- V** Left stretch tensor.
- \mathbf{D}^e Fourth-order elasticity tensor.
- G Shear modulus.
- K Bulk modulus.
- $\mathbf{1}$ Second-order identity tensor.
- \mathbf{I} Fourth-order identity tensor $I_{ijkl} = \delta_{ik}\delta_{jl}$.
- \mathbf{I}_d Fourth-order deviatoric projection tensor $\mathbf{I}_d = \mathbf{I}_S - \frac{1}{3}\mathbf{1} \otimes \mathbf{1}$.
- \mathbf{I}_S Fourth-order symmetric identity tensor $I_{Sijkl} = \frac{1}{2}(\delta_{ik}\delta_{jl} + \delta_{il}\delta_{jk})$.
- σ Cauchy stress tensor.
- s Deviatoric stress tensor.
- τ Kirchhoff stress tensor.
- P** First Piola-Kirchhoff stress tensor.
- S** Second Piola-Kirchhoff stress tensor.

Notation

Tensors

Throughout this thesis different tensors of different orders are used. Besides the fact that tensors are written with bold letters no further indication is made concerning the order of the quantity. In most cases their order should be clear from the context.

Multiplications and contractions

Multiplications (contractions) of tensors are denoted by the dot operators (\cdot) and ($:$). The former is used for a single contraction, the latter denotes a double contraction of the related tensors. The single contraction symbol for the multiplication of two tensors and a tensor and a vector is omitted.

The dyadic product is represented by \otimes .

Indicial notation

In the indicial notation *Einstein's* convention is applied, meaning that whenever an index appears twice in the same product, summation over the repeated index is implied.

Matrices

In a computer-based implementation tensors are transformed to vectors and matrices. Based on the method for transforming matrices to vectors the computer-based implementation reads different. In addition, the notation is not unique and it depends on the type of quantity under consideration.

For the stress and the strain tensor it is common to apply *Voigt* notation. In the literature different definitions of the *Voigt* notation can be found. Belytschko et al. [9], for example, use a different notation than Wriggers [73] or Neto et al. [66]. Whenever the *Voigt* notation is referenced in this work we follow the notation given in Wriggers [73] or Neto et al. [66]. For symmetric tensors, for example, the stress tensor, the notation reads:

$$\boldsymbol{\sigma} \iff \left[\begin{array}{cccccc} \sigma_{xx} & \sigma_{yy} & \sigma_{zz} & \sigma_{xy} & \sigma_{yz} & \sigma_{xz} \end{array} \right]^T. \quad (1)$$

For all other non-symmetric second-order tensors that are transformed into column vectors we apply the following scheme:

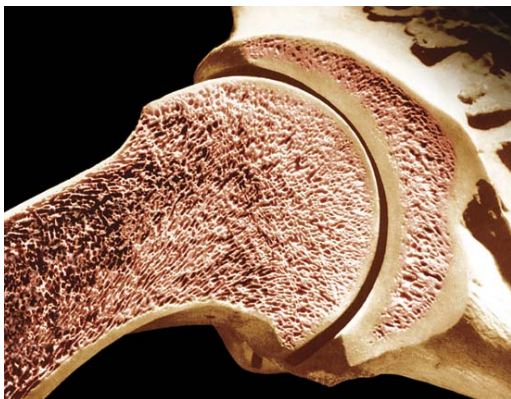
$$\left[\begin{array}{ccc} 11 & 12 & 13 \\ 21 & 22 & 23 \\ 31 & 32 & 33 \end{array} \right] \iff \left[\begin{array}{ccccccccc} 11 & 12 & 13 & 21 & 22 & 23 & 31 & 32 & 33 \end{array} \right]^T. \quad (2)$$

Chapter 1

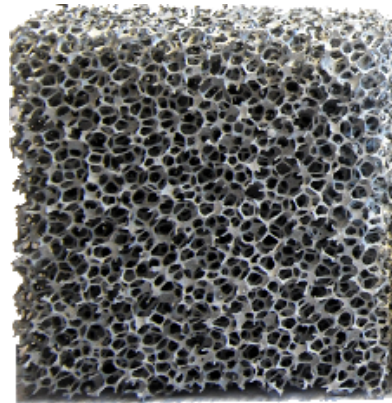
Introduction

1.1 Motivation

Many organic materials are formed by cellular structures. Bones, for example, consist of a hard outer layer, called the cortical bone, and the cancellous bone on its inside which is a porous open cell network; see Fig. 1.1a). Cork, which can be harvested from trees, is another example for a cellular structure. Honeycomb structures, known from the nest of honeybees, also form a cellular structure of hexagonal wax cells. The manifold properties of cellular materials such



a)



b)

Figure 1.1: a) Longitudinal section of the humerus (upper arm bone) [1] and b) metal foam.

as these served as the blueprint for the development of metal foams.

A metal foam is a solid structure made of metals like aluminum, steel or copper; containing a large volume of pores that can be either sealed (closed-cell foam) or interconnected (open-cell foam); see Fig. 1.1b).

By imitating cellular materials and using their metallic counterparts one can improve the characteristics of many engineering structures. For instance, porous tantalum is used in orthopedics for knee arthroplasty (Fig. 1.2a), artificial hip replacement (Fig. 1.2b), hip osteonecrosis surgery or spine surgery. Prosthesis made of open-cell metal foams can be implanted into the host bone. They allow the bone to grow into the metal which enhances the osseointegration of implants. In addition, due to their low modulus of elasticity – close to that of subchondral

and cancellous bone – they lead to better transfer of loads from the implant into the host bone and minimize the stress shielding phenomenon [47, 49, 53].

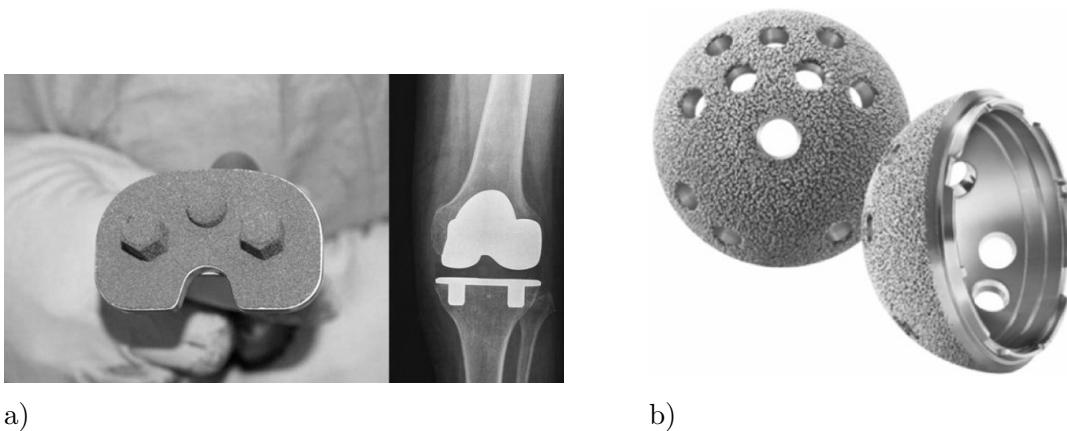


Figure 1.2: Different applications of metal foams in orthopedics: a) Tantalum trabecular metal tibial baseplate for uncemented total knee replacement and x-ray of implants osteointegration [47] and b) Trident tritanium acetabular shell used in artificial hip replacement [49].

Another application area of metal foams is in the design of construction elements. An aluminum foam sandwich (AFS) is a sandwich plate made of two metallic face sheets and a metal foam core made of an aluminum alloy. While the aluminum foam holds the face sheets in place and is responsible for the low weight of the structure, the face sheets carry the load so that in combination they offer a structure with a high specific stiffness. The use of such sandwich panels, for example, as the shell of high-speed trains as depicted in Fig. 1.3a), renders a supporting rip structure unnecessary [40]. Consequently, the cabin size can be increased and more passengers can be transported. Moreover, it reduces the production time and cost as well as the weight of the structure. Metal foams can undergo large deformations at moderate stress

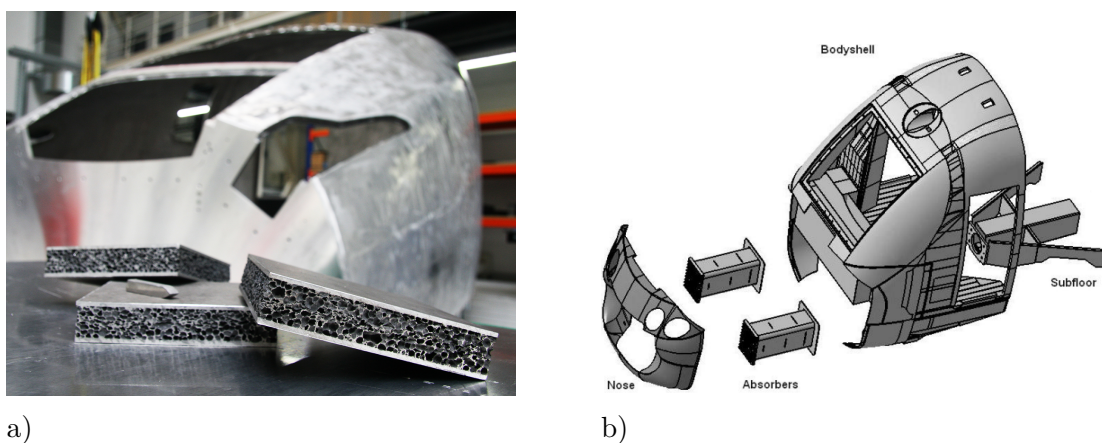


Figure 1.3: Applications of metal foams in transportation systems: a) Lightweight cabin of high speed train made of AFS [30] and b) Front end of a train with foamed crash absorber elements [56].

due to the large volume of their pores that collapse at the same stress level. This behavior

makes them useful as crash elements in all types of vehicles; see Fig.1.4 for the application in the automotive industry or Fig.1.3b) for the use in trains. In an experimental study [28, 29],

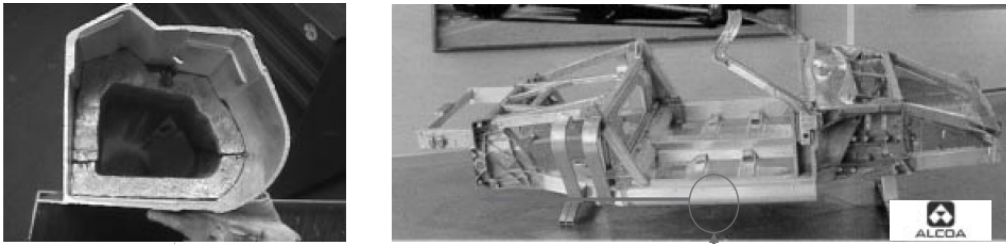


Figure 1.4: Stiffener and crash absorber in the Ferrari 360 and 430 Spider [8].

metal sandwich plates were used in the shipbuilding industry to build the baseplate of a gear box, see Fig. 1.5a). The resulting structure not only had a lower weight, but also reduced the transmission of sound significantly compared to the conventional method of construction. In the same project the rudder depicted in Fig. 1.5b) was also built from metal foam sandwich plates which led to a reduction in weight, a simplified building procedure and to fewer parts needed to assemble the whole rudder [28].

As all these different application areas illustrate it is of great importance to understand the

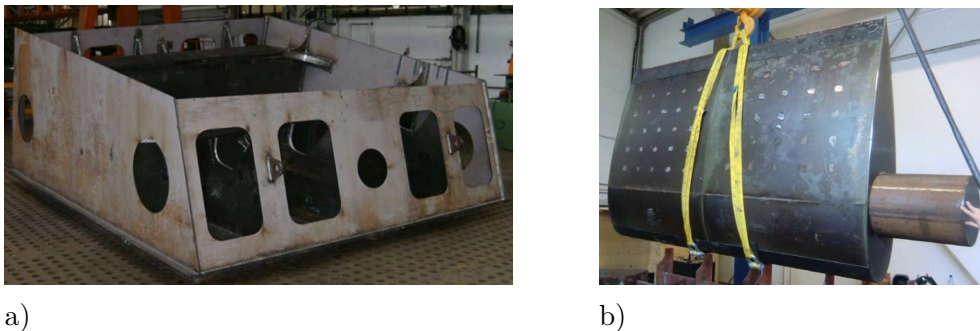


Figure 1.5: Metal foams in the naval industry: a) Base plate of gear box [28, 29] and b) Rudder [28].

mechanical behavior of metal foams and to develop appropriate material models. The macroscopic behavior of foams strongly depends on local phenomena to be observed on the length scale of the microstructure. This includes buckling of the cell walls and finite elastoplastic deformations as well as self-contact of single struts under large deformations. One method to understand and investigate these phenomena is by means of numerical simulations based on a realistic geometrical model. Such models can be obtained, for example, by using computed tomography scans (CT-scans). However, one of the main obstacles for such simulations is the complicated and irregular geometry of the models and, consequently, the immense labor effort to generate a suitable discretization. In order to avoid this problem we employ the finite cell method (FCM) [54, 17] which is a combination of the fictitious domain approach and high order finite elements. The fictitious domain approach drastically simplifies the mesh generation and allows to automatically obtain a simple Cartesian grid using the voxel model which comes out of a CT-scan. Due to the high order shape functions each element – or cell as referred to in terms of the finite cell method – can represent a set of voxels. As a

consequence the number of degrees of freedom can be reduced significantly as compared to a voxel finite element simulation [26] and high convergence rates can be obtained if the voxel model is sufficiently smooth. Motivated by the promising properties of the finite cell method – particularly its simple mesh generation capabilities – we extend the finite cell method and apply it to the investigation of cellular materials.

1.2 Scope and outline of this work

Within the scope of this thesis we extend the finite cell method with the goal to perform realistic numerical simulations on CT-image based geometric models of open cell aluminum foams. To this end, we augment the FCM by a constitutive material model that takes into account the large elastoplastic deformations and buckling of the cell walls that occur when a metal foam is compressed. In addition, a sticking contact approach is implemented to simulate the self-contact which occurs during the densification process of the metal foam at the final stage of a compression test. After some intensive numerical studies of these methods, they are applied within the investigation of metal foams, focusing on single pores.

The detailed outline of the thesis is as follows:

- In Chapter 2 an introduction into the basics of continuum mechanics is given. Here all necessary strain and stress measures, the equilibrium conditions, its weak form, as well as the constitutive equations for different types of materials are explained. Specifically, we introduce a material model for the description of large elastoplastic deformations based on *Hencky's* hyperelastic model and a multiplicative split of the deformation gradient.
- In Chapter 3 the spatial discretization of the governing equations by the finite cell method is introduced. The influence of the fictitious domain on the condition number is discussed by means of a one-dimensional example. The numerical integration of the weak form by an adaptive quadrature scheme is explained by a two-dimensional example and the efficiency of the quadtree and k-d tree based quadrature scheme is compared. In order to derive a finite cell discretization based on image-based CT-data, we present an approach to remove artifacts from the raw voxel model such that a proper discretization can be obtained.
- In Chapter 4 we introduce an iterative self-consistent numerical homogenization approach based on the window method and the finite cell method. In addition, we present the *Aitken* acceleration scheme and show how it can be leveraged to reduce the number of iterations within the window method. Finally, we apply the window method to compute effective properties of nickel-coated aluminum foams and investigate the influence of a coating thickness on the mechanical properties.
- In Chapter 5 we extend the finite cell method by two different contact formulations. The contact approaches are systematically studied by means of simple examples and compared to their analytical solutions. After demonstrating the capabilities of the newly developed approaches, their application is shown by computing the self-contact of different struts in a metal foam.

- In Chapter 6 we employ the finite cell method to compute the effective microscopic material properties of aluminum metal foams which significantly differ from their bulk values due to the manufacturing process. To this end, we simulate experiments done on single pores – using the corresponding digital model of the pores that were obtained by a photogrammetric method – and adjust the parameters of the material model such that we meet the experimental force-displacement curve.

Finally in Chapter 7 we draw a conclusion and discuss the results of this thesis. In addition, we give an outlook for further research possibilities within the finite cell method.

Chapter 2

Basic relations of continuum mechanics

This chapter is intended to give an introduction into the basics of continuum mechanics and the related equations that are used throughout this thesis. For a more complete overview the books of Wriggers [73], Belytschko et al. [9], Simo and Hughes [64] and Neto et al. [66] are recommended. The notation used here is closely related to the notation chosen by Wriggers and Neto et al.

2.1 Kinematics

In order to describe the motion of an object we consider a body B that is subjected to a deformation as depicted in Fig. 2.1. The undeformed state of the body is usually called

Reference configuration

Current configuration

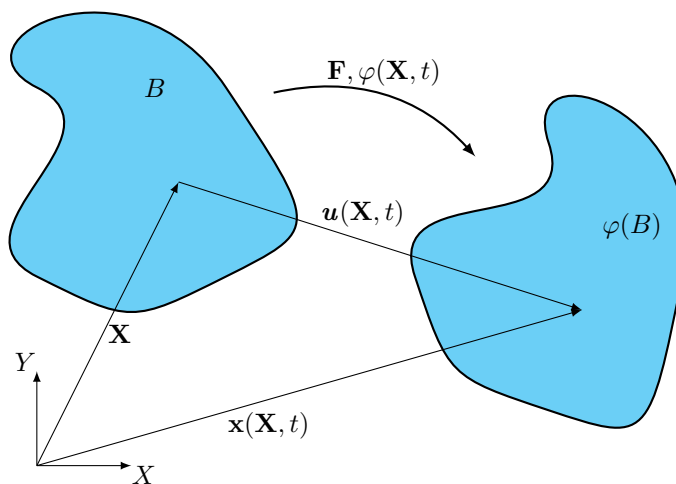


Figure 2.1: Description of motion.

the *reference configuration*. In the literature the terms *reference*, *undeformed* and *material*

configuration are equivalently used to describe this state. Every point of this configuration is described by its position vector \mathbf{X} . After deformation every point is moved by $\mathbf{u}(\mathbf{X}, t)$ to its new position $\mathbf{x}(\mathbf{X}, t)$ which is known as the *spatial* position of this point. The corresponding configuration is equivalently termed *current*, *deformed* or *spatial configuration*. The use of capital letters for quantities or operators associated with the reference configuration and small letters for the current configuration is common and will be explained in more detail later in this chapter.

A mapping between the reference and the current configuration is given by the mapping function:

$$\varphi(\mathbf{X}, t) = \mathbf{x}(\mathbf{X}, t). \quad (2.1)$$

In order to describe the deformation locally we introduce the *deformation gradient* \mathbf{F} which is the gradient of the mapping function. The derivatives are computed with respect to the initial coordinates. This is indicated by the use of a capital letter for the gradient operator Grad or the capital index of the *nabla* operator $\nabla_{\mathbf{X}}$:

$$\mathbf{F} = \text{Grad } \varphi(\mathbf{X}, t) = \nabla_{\mathbf{X}} \varphi(\mathbf{X}, t). \quad (2.2)$$

The deformation gradient relates an infinitesimal line element $d\mathbf{X}$ in the undeformed configuration to its counterpart $d\mathbf{x}$ in the deformed configuration:

$$d\mathbf{x} = \mathbf{F} d\mathbf{X}. \quad (2.3)$$

The deformation gradient is related to the *displacement field* $\mathbf{u}(\mathbf{X}, t)$ by the following relation:

$$\mathbf{F} = \text{Grad} (\mathbf{X} + \mathbf{u}(\mathbf{X}, t)) = \mathbf{1} + \text{Grad } \mathbf{u}(\mathbf{X}, t) = \mathbf{1} + \mathbf{H}, \quad (2.4)$$

where \mathbf{H} is the *displacement gradient* and $\mathbf{1}$ the *second-order identity tensor*. In case the displacement field is described based on the spatial coordinates $\mathbf{u}(\mathbf{x}, t)$, the deformation gradient can be computed by the following formula:

$$\mathbf{F} = (\mathbf{1} - \text{grad } \mathbf{u})^{-1} = (\mathbf{1} - \nabla_{\mathbf{x}} \mathbf{u})^{-1}. \quad (2.5)$$

The deformation gradient is used to transform several geometric quantities from the *undeformed* to the *deformed* configuration. Applying *Nanson's* formula an infinitesimal surface element $d\mathbf{A}$ can be transformed from the *undeformed* to the *deformed* configuration via:

$$d\mathbf{a} = J\mathbf{F}^{-T} d\mathbf{A} = \text{cof } \mathbf{F} d\mathbf{A}. \quad (2.6)$$

In this equation J is the *Jacobian* which is the determinant of the deformation gradient. It has to be greater than zero in order to exclude self-intersection during deformations

$$J = \det \mathbf{F} \geq 0. \quad (2.7)$$

2.1.1 Strain measures

In order to quantify the amount of deformation in a deformable body we introduce different strain measures that are used together with different constitutive models that are described in later sections of this chapter.

The *small strain tensor* or *engineering strain tensor* $\boldsymbol{\varepsilon}$ is known from linear elasticity theory:

$$\boldsymbol{\varepsilon} = \frac{1}{2} (\mathbf{H} + \mathbf{H}^T) . \quad (2.8)$$

It describes the strain accurately when only small displacements and small deformations are involved. For problems in which large rigid body rotations occur this measure is no longer suited.

In elastoplastic computations of metals the additive split of the small strain tensor into a volumetric and a deviatoric contribution is often needed:

$$\boldsymbol{\varepsilon} = \boldsymbol{\varepsilon}_d + \boldsymbol{\varepsilon}_v . \quad (2.9)$$

The *volumetric strain tensor* $\boldsymbol{\varepsilon}_v$ can be computed by:

$$\boldsymbol{\varepsilon}_v = \frac{1}{3} \text{tr}(\boldsymbol{\varepsilon}) \mathbf{1} , \quad (2.10)$$

where $\text{tr}(\cdot)$ denotes the trace of the tensor. The isochoric component of the deformation is given by the *deviatoric strain tensor* $\boldsymbol{\varepsilon}_d$:

$$\boldsymbol{\varepsilon}_d = \boldsymbol{\varepsilon} - \boldsymbol{\varepsilon}_v . \quad (2.11)$$

For problems involving large deformations the *Green-Lagrange strain tensor* \mathbf{E} is used which vanishes for (large) rigid body motions:

$$\mathbf{E} = \frac{1}{2} (\mathbf{F}^T \mathbf{F} - \mathbf{1}) . \quad (2.12)$$

Beside these two strain measures we introduce the *Eulerian logarithmic strain tensor* $\boldsymbol{\epsilon}$ that is used in the finite strain elastoplastic model in Section 2.3.3. The Eulerian logarithmic strain tensor is defined by:

$$\boldsymbol{\epsilon} = \ln(\mathbf{V}) = \frac{1}{2} \ln(\mathbf{b}) = \frac{1}{2} \ln(\mathbf{F} \mathbf{F}^T) , \quad (2.13)$$

where \mathbf{V} denotes the *left stretch tensor* and \mathbf{b} indicates the *left Cauchy-Green deformation tensor*. The left stretch tensor can be obtained from the polar decomposition $\mathbf{F} = \mathbf{V} \mathbf{R}$ of the deformation gradient using the orthogonal rotation tensor \mathbf{R} . The *tensor logarithm* $\ln(\cdot)$ used in Eq. (2.13) is computed by the following formula:

$$\ln(\mathbf{V}) = \sum_{n=1}^{\infty} \frac{(-1)^{n-1}}{n!} (\mathbf{V} - \mathbf{1})^n . \quad (2.14)$$

In the application of this formula the series needs to be truncated when a prescribed convergence criteria is met. In case of small deformations, where the deformation gradient \mathbf{F} is close

to identity, the series converges after a small number of terms and Eq. (2.14) can be efficiently applied, see [52]. In case of large deformations it is better to apply a spectral decomposition and to compute the Eulerian logarithmic strain tensor by:

$$\boldsymbol{\epsilon} = \ln(\lambda_i) \mathbf{n}_i \otimes \mathbf{n}_i \quad (2.15)$$

where λ_i are the eigenvalues of \mathbf{V} and \mathbf{n}_i the related eigenvectors. For further computations related to the tensor logarithm, especially the computation of its derivative that is needed, for example, during linearization of the constitutive equations, we refer to [66].

Similar to the engineering strains we can define the volumetric/deviatoric split by:

$$\boldsymbol{\epsilon} = \boldsymbol{\epsilon}_d + \boldsymbol{\epsilon}_v, \quad \boldsymbol{\epsilon}_v = \frac{1}{3} \text{tr}(\boldsymbol{\epsilon}) \mathbf{1} \quad (2.16)$$

2.1.2 Time derivative

The material time derivative plays an important role in continuum mechanics. In the material configuration derivatives with respect to time directly describe the rate of change of a material particle. In the spatial configuration the derivative with respect to time describes the rate of change at a fixed spatial position, so the change in the measured quantity is caused by different particles that passed this point in an infinitesimal time interval. To account for this change the time derivative is complemented by the convective rate. For example the velocity of a particle can be computed as:

$$\mathbf{v}(\mathbf{X}, t) = \frac{\partial \mathbf{x}}{\partial t} = \lim_{\Delta t \rightarrow 0} \frac{\varphi(\mathbf{X}, t + \Delta t) - \varphi(\mathbf{X}, t)}{\Delta t}. \quad (2.17)$$

The velocity field can be equivalently expressed in terms of spatial coordinates using the relation $\mathbf{x} = \varphi(\mathbf{X}, t)$.

$$\hat{\mathbf{v}}(\mathbf{x}, t) = \hat{\mathbf{v}}(\varphi(\mathbf{X}, t), t) = \mathbf{v}(\mathbf{X}, t) \quad (2.18)$$

When computing the *material time derivative* of the spatial velocity field one has to consider the time dependence of the position of the particle $\mathbf{x}(\mathbf{X}, t)$ which requires applying the chain rule:

$$\frac{\partial \hat{\mathbf{v}}(\mathbf{x}(\mathbf{X}, t), t)}{\partial t} = \frac{\partial \hat{\mathbf{v}}(\mathbf{x}, t)}{\partial t} + \frac{\partial \hat{\mathbf{v}}(\mathbf{x}, t)}{\partial \mathbf{x}} \frac{\partial \mathbf{x}}{\partial t} = \hat{\mathbf{a}} + \text{grad } \hat{\mathbf{v}}(\mathbf{x}, t) \hat{\mathbf{v}}. \quad (2.19)$$

The concept of the material time derivative helps to formulate the time derivative of the deformation gradient in the material and the spatial configuration. Its rate can be computed from the velocity field which can either be given in material coordinates $\mathbf{v}(\mathbf{X}, t)$ or in spatial coordinates $\hat{\mathbf{v}}(\mathbf{x}, t)$:

$$\dot{\mathbf{F}} = \text{Grad } \mathbf{v} = \text{grad } \hat{\mathbf{v}} \mathbf{F} = \mathbf{1} \mathbf{F}, \quad (2.20)$$

where $\mathbf{1}$ is called the *spatial velocity gradient*.

2.2 Strong form of the balance of linear and angular momentum

In order to derive the governing equations of continuum mechanics that describe the balance of linear and angular momentum, we consider an infinitesimal volume element of a body $\varphi(B)$ in its deformed configuration that is subjected to a loading as depicted in Fig. 2.2. For simplicity we refer to the two-dimensional case, but the three-dimensional counterpart can be derived in an analogous way. The infinitesimal element is in equilibrium when the forces acting on its

Current configuration

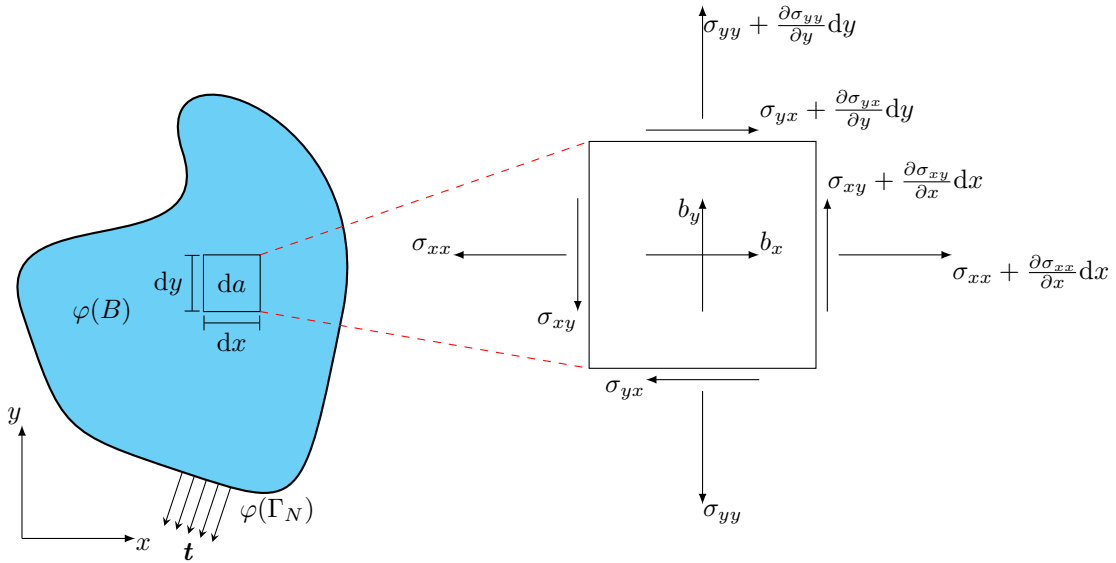


Figure 2.2: Equilibrium on the infinitesimal surface element.

surface and the volumetric forces like gravity forces $\rho \mathbf{b}$ and inertia terms $\rho \dot{\mathbf{v}}$ are in balance. So formulating the balance of linear and angular momentum for each direction leads to the following system of partial differential equations:

$$\begin{aligned} \frac{\partial \sigma_{xx}}{\partial x} + \frac{\partial \sigma_{yx}}{\partial y} + \rho b_x &= \rho \dot{v}_x, \\ \frac{\partial \sigma_{yy}}{\partial y} + \frac{\partial \sigma_{xy}}{\partial x} + \rho b_y &= \rho \dot{v}_y. \end{aligned} \quad (2.21)$$

These equations can be written in compact form in the three-dimensional space using the *divergence operator* div and are also known as the strong form of the balance of linear momentum:

$$\text{div } \boldsymbol{\sigma} + \rho \mathbf{b} = \rho \dot{\mathbf{v}}. \quad (2.22)$$

Please note that the use of small letters for the divergence operator indicates that it has to be evaluated with respect to the spatial coordinates. The consideration of the balance of angular momentum implies that the stress tensor is symmetric

$$\boldsymbol{\sigma} = \boldsymbol{\sigma}^T. \quad (2.23)$$

Often it is useful to formulate the balance equations with respect to the initial configuration, i.e. the undeformed body. To this end, we define the *first Piola-Kirchhoff stress tensor* \mathbf{P} , which can be computed from the *Cauchy stress tensor* $\boldsymbol{\sigma}$ by applying *Nanson's formula*, given in Eq. (2.6):

$$\mathbf{P} = J\boldsymbol{\sigma}\mathbf{F}^{-T}. \quad (2.24)$$

Substituting Eq. (2.24) into Eq. (2.23) shows that the first Piola-Kirchhoff stress tensor is an unsymmetric tensor and $\mathbf{P}\mathbf{F}^T = \mathbf{F}\mathbf{P}^T$ holds. Using the first Piola-Kirchhoff stress tensor the balance of linear momentum can be rewritten as follows:

$$\text{Div } \mathbf{P} + \rho_0 \mathbf{b} = \rho_0 \dot{\mathbf{v}}. \quad (2.25)$$

Another important measure is the *second Piola-Kirchhoff stress tensor* \mathbf{S} :

$$\mathbf{S} = \mathbf{F}^{-1}\mathbf{P} = J\mathbf{F}^{-1}\boldsymbol{\sigma}\mathbf{F}^{-T}. \quad (2.26)$$

The operation $\mathbf{F}^{-1}(\cdot)\mathbf{F}^{-T}$ needed to transform certain quantities from the current configuration to the reference configuration is called a *pull backward* operation and the inverse operation $\mathbf{F}(\cdot)\mathbf{F}^T$ is called a *push forward*.

2.3 Constitutive models

Constitutive relations are needed in the mechanical analysis of a body to link a strain measure to a certain stress tensor. In the first part of this section elastic material models are addressed. Materials are called elastic when the deformation is totally reversible. The stress state in elastic materials only depends on the actual deformation and not on the loading path. In contrast, the behavior of a material is plastic, when the deformation is not reversible and the stress state depends on the loading path.

Two elastoplastic material models, one for small deformations and one for large deformations, are presented in the second part of this section. The elastoplastic material model for small strains will be presented first together with the general computation steps that are performed during plastic computations. The elastoplastic material model for large strains is based on logarithmic strains. Its algorithmic treatment is equivalent to the small strain model, only the strain measure needs to be replaced. Therefore, only some transformations will be explained and otherwise the reader is referred to the small strain elastoplastic model. For a deeper insight into the concepts of constitutive equations we refer to the textbooks [9, 73].

2.3.1 Hyperelastic material models

Hyperelastic material models are well suited for the description of elastic materials since they can describe a total path independent and reversible behavior. The mathematical formulation of such models is based on the definition of a strain energy potential ψ . The constitutive equation for the second Piola-Kirchhoff stress tensor can be obtained by taking the derivative of ψ with respect to a kinematic measure of the deformation. In the following some equivalent relations are given that are used in the following chapters:

$$\mathbf{P} = \rho_0 \frac{\partial \psi}{\partial \mathbf{F}} = 2\rho_0 \mathbf{F} \frac{\partial \tilde{\psi}}{\partial \mathbf{C}} = \rho_0 \mathbf{F} \frac{\partial \tilde{\psi}}{\partial \mathbf{E}}. \quad (2.27)$$

For the second Piola-Kirchhoff stress tensor the same constitutive equation is given by:

$$\mathbf{S} = \rho_0 \mathbf{F}^{-1} \frac{\partial \psi}{\partial \mathbf{F}} = 2\rho_0 \frac{\partial \tilde{\psi}}{\partial \mathbf{C}} = \rho_0 \frac{\partial \tilde{\psi}}{\partial \mathbf{E}}, \quad (2.28)$$

or in terms of Cauchy stress by:

$$\boldsymbol{\sigma} = \frac{\rho_0}{J} \frac{\partial \psi}{\partial \mathbf{F}} \mathbf{F}^T = 2 \frac{\rho_0}{J} \mathbf{F} \frac{\partial \tilde{\psi}}{\partial \mathbf{C}} \mathbf{F}^T = \frac{\rho_0}{J} \mathbf{F} \frac{\partial \tilde{\psi}}{\partial \mathbf{E}} \mathbf{F}^T. \quad (2.29)$$

If the material is isotropic \mathbf{b} and $\frac{\partial \psi}{\partial \mathbf{b}}$ are commutable and the Cauchy stress tensor can be expressed in terms of the left Cauchy-Green deformation tensor as follows:

$$\boldsymbol{\sigma} = 2 \frac{\rho_0}{J} \mathbf{b} \frac{\partial \tilde{\psi}}{\partial \mathbf{b}} = 2 \frac{\rho_0}{J} \frac{\partial \tilde{\psi}}{\partial \mathbf{b}} \mathbf{b}. \quad (2.30)$$

2.3.1.1 The Saint Venant-Kirchhoff material model

A frequently used hyperelastic model is the *Saint-Venant Kirchhoff* material. The strain energy function of this model reads:

$$\rho_0 \psi(\mathbf{E}) = \frac{\lambda}{2} (\text{tr}(\mathbf{E}))^2 + \mu \text{tr}(\mathbf{E}^2). \quad (2.31)$$

By taking the derivative with respect to the Green-Lagrange strain tensor, we obtain the following relation for the second Piola-Kirchhoff stress tensor:

$$\mathbf{S} = \lambda \text{tr}(\mathbf{E}) \mathbf{1} + 2\mu \mathbf{E}. \quad (2.32)$$

Often this equation is expressed via:

$$\mathbf{S} = \mathbf{D}^e : \mathbf{E}, \quad (2.33)$$

where \mathbf{D}^e is the *fourth-order elasticity tensor*. Using the *fourth-order symmetric identity tensor* \mathbf{I}_S and the second order identity tensor $\mathbf{1}$ it can be written as follows:

$$\mathbf{D}^e = 2\mu \mathbf{I}_S + \lambda \mathbf{1} \otimes \mathbf{1}, \quad D_{ijkl}^e = \mu (\delta_{ik} \delta_{jl} + \delta_{il} \delta_{jk}) + \lambda \delta_{ij} \delta_{kl}. \quad (2.34)$$

The material parameters in this equation are the *Lamé constants* λ, μ . The Saint-Venant Kirchhoff material is independent from rigid body rotations so this model can also be used for problems that involve large rotation. For large compressive strains the stresses tend to zero instead of to infinity. This is an unphysical behavior so this model is not suited for the computations of large compressive strains.

Hooke's Law

Hooke's law is used in linear theory where only are considered. It connects the engineering strain tensor $\boldsymbol{\varepsilon}$ to the Cauchy stress tensor $\boldsymbol{\sigma}$ and can be obtained from Eq. (2.32) by linearizing the Green-Lagrange strain tensor:

$$\boldsymbol{\sigma} = \lambda \text{tr}(\boldsymbol{\varepsilon}) \mathbf{1} + 2\mu \boldsymbol{\varepsilon}. \quad (2.35)$$

2.3.1.2 The Hencky material model

The strain energy function of the *Hencky's hyperelastic material model* is given by:

$$\rho\psi(\boldsymbol{\epsilon}) = \frac{\lambda}{2} (\text{tr}(\boldsymbol{\epsilon}))^2 + \mu \text{tr}(\boldsymbol{\epsilon}^2), \quad (2.36)$$

see [66]. The Hencky model is an isotropic finite strain elasticity model assuming a linear relationship between the *Kirchhoff stress tensor* $\boldsymbol{\tau}$ and the Eulerian logarithmic strain tensor:

$$\boldsymbol{\tau} = 2\rho_0 \frac{\partial\psi}{\partial\mathbf{b}} \mathbf{b} = 2\rho_0 \left[\frac{1}{2} \frac{\partial\psi}{\partial\boldsymbol{\epsilon}} \frac{\partial\boldsymbol{\epsilon}}{\partial\mathbf{b}} \right] \mathbf{b} = \rho_0 \frac{\partial\psi}{\partial\boldsymbol{\epsilon}} = \mathbf{D}^e : \boldsymbol{\epsilon}. \quad (2.37)$$

The model can be seen as the finite logarithmic strain based extension of the standard linear elastic material, see [75, 19]. The constitutive tensor \mathbf{D}^e obeys the same material constants as the small strain elasticity tensor which can be obtained from Eq. (2.35). Please note that this equation can also be expressed by another set of material constants. For the consideration of plasticity it is useful to express the elasticity tensor by the *bulk modulus* K and the *shear modulus* G :

$$\mathbf{D}^e = 2G\mathbf{I}_d + K\mathbf{1} \otimes \mathbf{1}. \quad (2.38)$$

In this equation \mathbf{I}_d is the *fourth-order deviatoric projection tensor* that projects the strain tensor into its deviatoric representation.

2.3.2 J_2 small strain plasticity

In this section we summarize an elastoplastic material model for small deformations. Starting with a short review of the general mathematical description of plasticity, we will then focus on the associative von Mises plasticity model with isotropic hardening. In the following the discretization of the constitutive equations and their solution by an elastic predictor/plastic corrector scheme will be demonstrated. Finally, we will show how to compute the consistent tangent modulus.

2.3.2.1 General model

Many materials like metals, rocks and soils undergo a permanent (plastic) deformation when they are loaded beyond a certain limit point, the so-called yield strength. In the small strain regime the mathematical formulation of this phenomenon is based on an additive split of the small strain tensor $\boldsymbol{\epsilon}$ into an elastic $\boldsymbol{\epsilon}^e$ and a plastic part $\boldsymbol{\epsilon}^p$:

$$\boldsymbol{\epsilon} = \boldsymbol{\epsilon}^e + \boldsymbol{\epsilon}^p. \quad (2.39)$$

The constitutive relation for the stress is given by the derivative of the strain energy function with respect to the elastic strains $\boldsymbol{\epsilon}^e$:

$$\boldsymbol{\sigma} = \rho \frac{\partial\psi}{\partial\boldsymbol{\epsilon}^e}. \quad (2.40)$$

The elastic domain is bounded by the *yield function* $\Phi(f(\boldsymbol{\sigma}), \bar{\varepsilon}^p) < 0$. The isosurface of the yield function

$$\Phi(f(\boldsymbol{\sigma}), \sigma_y(\bar{\varepsilon}^p)) = 0 \quad (2.41)$$

restricts the space of the elastic stress states and defines the beginning of yielding. The yield function generally depends on a function of the actual stress state $f(\boldsymbol{\sigma})$ and on the accumulated hardening variable $\bar{\varepsilon}^p$, that describes the evolution of the yield surface $\sigma_y(\bar{\varepsilon}^p)$. The evolution of the plastic strains $\dot{\boldsymbol{\varepsilon}}^p$ is defined by a flow rule:

$$\dot{\boldsymbol{\varepsilon}}^p = \dot{\gamma} \frac{\partial \Psi}{\partial \boldsymbol{\sigma}}. \quad (2.42)$$

It is based on the derivative of a flow potential Ψ and the *plastic multiplier* $\dot{\gamma}$.

The equations given above need to be solved under the constraints of the loading/unloading or *Kuhn-Tucker* conditions:

$$\dot{\gamma} \geq 0 \quad , \quad \Phi \leq 0 \quad , \quad \dot{\gamma} \Phi = 0. \quad (2.43)$$

In this equation $\dot{\gamma} \Phi$ is known as the *complementary condition*. In Eq. (2.43) the plastic multiplier can take any non-negative value during plastic flow. Therefore the following *additional complementary condition* is introduced:

$$\dot{\Phi} \dot{\gamma} = 0 \quad (2.44)$$

which implies the *consistency condition* [66]:

$$\dot{\Phi} = 0. \quad (2.45)$$

2.3.2.2 Associative von Mises plasticity

The *von Mises* plasticity model or *J₂ flow theory* uses the von Mises equivalent stress $f(\boldsymbol{\sigma}) = \sigma_{vM}$ to define the yielding behavior:

$$f(\boldsymbol{\sigma}) = \sigma_{vM} = \sqrt{3J_2(\boldsymbol{s})} = \sqrt{\frac{3}{2} \boldsymbol{s} : \boldsymbol{s}}, \quad (2.46)$$

where \boldsymbol{s} is the *deviatoric stress tensor*:

$$\boldsymbol{s} = \boldsymbol{\sigma} - \frac{1}{3} \text{tr}(\boldsymbol{\sigma}) \mathbf{1}, \quad (2.47)$$

and J_2 its second invariant. The yield function only depends on the deviatoric stress tensor, so hydrostatic stress states do not cause yielding. This condition reflects experimental observations made for metals. In the principal stress space the yield function describes an infinitely long cylinder along the hydrostatic axis.

Associativity implies that the plastic flow potential and the yield function $\Psi = \Phi$ are identical. In case the von Mises equivalent stress given in Eq. (2.46) is used to define the plastic flow, the flow rule is known as *Prandtl-Reuss* flow rule. The *flow vector* \boldsymbol{n} points normal to the

yield surface and can be computed by differentiating the yield function with respect to the stress tensor:

$$\mathbf{n} = \frac{\partial \Phi}{\partial \boldsymbol{\sigma}} = \frac{\partial}{\partial \boldsymbol{\sigma}} \sqrt{\frac{3}{2} \mathbf{s} : \mathbf{s}} = \sqrt{\frac{3}{2}} \frac{\mathbf{s}}{\|\mathbf{s}\|}. \quad (2.48)$$

The evolution of the hardening variable $\bar{\varepsilon}^p$ is obtained from the time integration of the von Mises accumulated plastic strain rate:

$$\bar{\varepsilon}^p = \int_0^t \dot{\bar{\varepsilon}}^p dt, \quad \text{with} \quad \dot{\bar{\varepsilon}}^p = \sqrt{\frac{2}{3} \dot{\boldsymbol{\varepsilon}}^p : \dot{\boldsymbol{\varepsilon}}^p} = \sqrt{\frac{2}{3}} \|\dot{\boldsymbol{\varepsilon}}^p\|. \quad (2.49)$$

This procedure directly relates the plastic multiplier $\dot{\gamma}$ to the rate of the *accumulated plastic strain* $\dot{\bar{\varepsilon}}^p$:

$$\dot{\gamma} = \dot{\bar{\varepsilon}}^p. \quad (2.50)$$

2.3.2.3 Integration of the elastoplastic constitutive equations

In order to solve the constitutive equations given for path-dependent (plastic) material models a numerical algorithm is required to integrate the corresponding rate equations.

The discrete form of the plastic flow equations, obtained by a backward Euler time integration scheme, reads:

$$\begin{aligned} \boldsymbol{\varepsilon}_{n+1}^e &= \boldsymbol{\varepsilon}_n^e + \Delta \boldsymbol{\varepsilon} - \Delta \gamma \sqrt{\frac{3}{2}} \frac{\mathbf{s}_{n+1}}{\|\mathbf{s}_{n+1}\|} \\ \bar{\varepsilon}_{n+1}^p &= \bar{\varepsilon}_n^p + \Delta \gamma, \end{aligned} \quad (2.51)$$

which needs to be solved under the constraints:

$$\Delta \gamma \geq 0, \quad \Phi(\boldsymbol{\sigma}_{n+1}, \bar{\varepsilon}_{n+1}^p) \leq 0, \quad \Delta \gamma \Phi(\boldsymbol{\sigma}_{n+1}, \bar{\varepsilon}_{n+1}^p) = 0. \quad (2.52)$$

It should be remarked here that the *backward Euler* or *fully implicit* time integration scheme is not the only possibility to be applied, but it has several advantages over other schemes like its stability, its finite step accuracy and the suitability for a derivation of a consistent elastoplastic tangent. Different discretization schemes lead to a different algorithmic treatment and can be found for example in [66].

Due to the presence of the complementary condition an elastic predictor/plastic corrector scheme needs to be applied. The elastic predictor/plastic corrector scheme is a two step algorithm consisting of an elastic predictor and a plastic corrector. The exact procedure is described in the following.

2.3.2.3.1 The elastic predictor

In the *trial step* $(\cdot)^{tr}$ we assume that all deformations are elastic, so $\Delta \gamma = 0$. Eq. (2.51) then reads:

$$\boldsymbol{\varepsilon}_{n+1}^{e,tr} = \boldsymbol{\varepsilon}_n^e + \Delta \boldsymbol{\varepsilon} \quad (2.53)$$

$$\bar{\varepsilon}_{n+1}^{p,tr} = \bar{\varepsilon}_n^p. \quad (2.54)$$

The trial stress can be computed by the hyperelastic material law:

$$\boldsymbol{\sigma}_{n+1}^{tr} = \mathbf{D}^e : \boldsymbol{\varepsilon}_{n+1}^{e,tr} \quad (2.55)$$

and subsequently the yield function needs to be evaluated:

$$\Phi(\boldsymbol{\sigma}_{n+1}^{tr}, \bar{\boldsymbol{\varepsilon}}_n^{p,tr}) = \sqrt{3J_2(\mathbf{s}_{n+1}^{tr})} - \sigma_y(\bar{\boldsymbol{\varepsilon}}_n^{p,tr}) \leq 0. \quad (2.56)$$

In case the trial step results in a stress state fulfilling the yield criterion $\Phi(\boldsymbol{\sigma}_{n+1}^{tr}, \bar{\boldsymbol{\varepsilon}}_n^{p,tr}) \leq 0$, a solution has been found and all variables are updated by their trial values. Otherwise if the trial state does not fulfill Eq. (2.56), we use the plastic corrector step to compute the solution.

2.3.2.3.2 The plastic corrector step

If Eq. (2.56) is not fulfilled, we have to solve the return mapping equations in the corrector step:

$$\boldsymbol{\varepsilon}_{n+1}^e = \boldsymbol{\varepsilon}_{n+1}^{e,tr} - \Delta\gamma \sqrt{\frac{3}{2}} \frac{\mathbf{s}_{n+1}}{\|\mathbf{s}_{n+1}\|} \quad (2.57)$$

$$\bar{\boldsymbol{\varepsilon}}_{n+1}^p = \bar{\boldsymbol{\varepsilon}}_n^p + \Delta\gamma \quad (2.58)$$

$$\Phi(\boldsymbol{\sigma}_{n+1}, \bar{\boldsymbol{\varepsilon}}_n^p) = 0 = \sqrt{3J_2(\mathbf{s}_{n+1})} - \sigma_y(\bar{\boldsymbol{\varepsilon}}_n^p). \quad (2.59)$$

In case of the von Mises associative plasticity model with isotropic hardening this set of equations can be reduced to one single nonlinear equation, where the incremental plastic multiplier $\Delta\gamma$ is the only unknown. This makes the von Mises model computationally efficient which is of great importance especially when applied within the finite cell method where the constitutive equations have to be evaluated at many points. In the following we will briefly summarize the procedure:

The plastic strains are purely deviatoric, so we make use of the deviatoric/volumetric decomposition of the strain tensor and are able to update the volumetric strains directly:

$$\boldsymbol{\varepsilon}_{v,n+1}^e = \boldsymbol{\varepsilon}_{v,n+1}^{e,tr}. \quad (2.60)$$

The update of the deviatoric strains reads:

$$\boldsymbol{\varepsilon}_{d,n+1}^e = \boldsymbol{\varepsilon}_{d,n+1}^{e,tr} - \Delta\gamma \sqrt{\frac{3}{2}} \frac{\mathbf{s}_{n+1}}{\|\mathbf{s}_{n+1}\|} \quad (2.61)$$

and by taking into account the relationship between the deviatoric part of the stress and strains:

$$\mathbf{s} = 2G\boldsymbol{\varepsilon}_d^e \quad (2.62)$$

we can reformulate Eq. (2.57) in terms of the deviatoric stresses:

$$\mathbf{s}_{n+1} = \mathbf{s}_{n+1}^{tr} - \Delta\gamma 2G \sqrt{\frac{3}{2}} \frac{\mathbf{s}_{n+1}}{\|\mathbf{s}_{n+1}\|}. \quad (2.63)$$

Since the trial flow direction $(\cdot)_{n+1}^{tr}$ equals the one of the final result $(\cdot)_{n+1}$, the following equation holds:

$$\frac{\mathbf{s}_{n+1}}{\|\mathbf{s}_{n+1}\|} = \frac{\mathbf{s}_{n+1}^{tr}}{\|\mathbf{s}_{n+1}^{tr}\|}. \quad (2.64)$$

We can use this relation together with Eq. (2.63) to obtain an expression that gives the updated deviatoric stress \mathbf{s}_{n+1} as a function of the incremental plastic multiplier $\Delta\gamma$:

$$\mathbf{s}_{n+1} = \mathbf{s}_{n+1}^{tr} - \Delta\gamma 2G \sqrt{\frac{3}{2}} \frac{\mathbf{s}_{n+1}^{tr}}{\|\mathbf{s}_{n+1}^{tr}\|} = \mathbf{s}_{n+1}^{tr} \left(1 - \Delta\gamma 2G \sqrt{\frac{3}{2}} \frac{1}{\|\mathbf{s}_{n+1}^{tr}\|} \right). \quad (2.65)$$

By replacing \mathbf{s}_{n+1} in Eq. (2.59) by Eq. (2.65) we obtain:

$$\left(1 - \Delta\gamma \frac{3G}{\sqrt{3J_2(\mathbf{s}_{n+1}^{tr})}} \right) \sqrt{3J_2(\mathbf{s}_{n+1}^{tr})} - \sigma_y(\bar{\varepsilon}_n^p + \Delta\gamma) = 0 \quad (2.66)$$

and finally after performing some algebraic manipulations we end up with a single nonlinear equation that only depends on the incremental plastic multiplier:

$$\sqrt{3J_2(\mathbf{s}_{n+1}^{tr})} - 3G\Delta\gamma - \sigma_y(\bar{\varepsilon}_n^p + \Delta\gamma) = 0. \quad (2.67)$$

The solution of this equation by the Newton-Raphson method requires its linearization with respect to the unknown plastic multiplier and depends on the definition of the hardening curve $\sigma_y(\bar{\varepsilon}^p)$. In case of linear hardening we can extract $\Delta\gamma$ and a closed solution for Eq. (2.67) can be obtained.

After solving Eq. (2.67) the state variables can be updated:

$$\begin{aligned} \mathbf{s}_{n+1} &= \mathbf{s}_{n+1}^{tr} \left(1 - \Delta\gamma 2G \sqrt{\frac{3}{2}} \frac{1}{\|\mathbf{s}_{n+1}^{tr}\|} \right) \\ \boldsymbol{\sigma}_{n+1} &= \mathbf{s}_{n+1} + K \boldsymbol{\varepsilon}_{v,n+1}^{e,tr} \\ \boldsymbol{\varepsilon}_{n+1}^e &= \frac{1}{2G} \mathbf{s}_{n+1} + \frac{1}{3} \boldsymbol{\varepsilon}_{v,n+1}^{e,tr} \\ \bar{\varepsilon}_{n+1}^p &= \bar{\varepsilon}_n^p + \Delta\gamma. \end{aligned} \quad (2.68)$$

2.3.2.4 The consistent elastoplastic tangent

In order to preserve the quadratic convergence of the global Newton-Raphson scheme we need to compute the *elastoplastic material tangent* \mathbf{D}^{ep} that is consistent with the discretization of the plastic model Eq.(2.51). The material tangent modulus is therefore also termed consistent tangent modulus and usually differs from the continuum tangent modulus [65, 66]. In order to derive the consistent tangent modulus we first express the stress tensor in terms of the elastic trial strains. To this end we use the volumetric/deviatoric split of the strain tensor and express the elastic constitutive relation as follows:

$$\boldsymbol{\sigma}_{n+1} = K \boldsymbol{\varepsilon}_{v,n+1}^e + 2G \boldsymbol{\varepsilon}_{d,n+1}^e \quad (2.69)$$

The volumetric strains are not affected by the plastic corrector step. The deviatoric strains depend on the incremental plastic multiplier so that Eq. (2.69) can be expressed as follows:

$$\boldsymbol{\sigma}_{n+1} = K \boldsymbol{\varepsilon}_{v,n+1}^{e,tr} + 2G \left(\boldsymbol{\varepsilon}_{d,n+1}^{e,tr} - \Delta\gamma \sqrt{\frac{3}{2}} \frac{\mathbf{s}_{n+1}}{\|\mathbf{s}_{n+1}\|} \right). \quad (2.70)$$

Reordering the equations and introducing the small strain elasticity tensor yields:

$$\boldsymbol{\sigma}_{n+1} = \mathbf{D}^e : \boldsymbol{\varepsilon}_{n+1}^{e,tr} - 2G \Delta\gamma \sqrt{\frac{3}{2}} \frac{\mathbf{s}_{n+1}}{\|\mathbf{s}_{n+1}\|}. \quad (2.71)$$

Making use of the coaxial property of the deviatoric stress given in Eq. (2.64) yields:

$$\boldsymbol{\sigma}_{n+1} = \mathbf{D}^e : \boldsymbol{\varepsilon}_{n+1}^{e,tr} - 2G \Delta\gamma \sqrt{\frac{3}{2}} \frac{\mathbf{s}_{n+1}^{tr}}{\|\mathbf{s}_{n+1}^{tr}\|}. \quad (2.72)$$

Finally, after making use of the deviatoric projection tensor \mathbf{I}_d and using Eq. (2.62), we obtain:

$$\boldsymbol{\sigma}_{n+1} = \mathbf{D}^e : \boldsymbol{\varepsilon}_{n+1}^{e,tr} - 2G \Delta\gamma \sqrt{\frac{3}{2}} 2G \frac{\boldsymbol{\varepsilon}_{d,n+1}^{tr}}{\|\mathbf{s}_{n+1}^{tr}\|} = \left[\mathbf{D}^e - \frac{\Delta\gamma 6G^2}{q_{n+1}^{tr}} \mathbf{I}_d \right] \boldsymbol{\varepsilon}_{n+1}^{e,tr}, \quad (2.73)$$

where

$$q_{n+1}^{tr} = \sqrt{\frac{3}{2}} \|\mathbf{s}_{n+1}^{tr}\|. \quad (2.74)$$

In order to obtain the consistent tangent for the von Mises model, we start from Eq. (2.73) and differentiate the updated stress with respect to the trial strain. For the differentiation the product rule needs to be applied since $\Delta\gamma$ and q_{n+1}^{tr} depend on the trial strains:

$$\frac{\partial \boldsymbol{\sigma}_{n+1}}{\partial \boldsymbol{\varepsilon}_{n+1}^{e,tr}} = \mathbf{D}^e - \frac{\Delta\gamma 6G^2}{q_{n+1}^{tr}} \mathbf{I}_d - \frac{6G^2}{q_{n+1}^{tr}} \boldsymbol{\varepsilon}_{d,n+1}^{e,tr} \otimes \frac{\partial \Delta\gamma}{\partial \boldsymbol{\varepsilon}_{n+1}^{e,tr}} + \frac{\Delta\gamma 6G^2}{(q_{n+1}^{tr})^2} \boldsymbol{\varepsilon}_{d,n+1}^{e,tr} \otimes \frac{\partial q_{n+1}^{tr}}{\partial \boldsymbol{\varepsilon}_{n+1}^{e,tr}}. \quad (2.75)$$

The dependency of q_{n+1}^{tr} on the trial strains $\boldsymbol{\varepsilon}_{n+1}^{e,tr}$ can be seen by the following form:

$$\begin{aligned} q_{n+1}^{tr} &= \sqrt{\frac{3}{2}} \mathbf{s}_{n+1}^{tr} : \mathbf{s}_{n+1}^{tr} = \sqrt{3 J_2(\mathbf{s}_{n+1}^{tr})} = \sqrt{\frac{3}{2}} 2G \sqrt{\boldsymbol{\varepsilon}_{d,n+1}^{e,tr} : \boldsymbol{\varepsilon}_{d,n+1}^{e,tr}} \\ &= \sqrt{\frac{3}{2}} 2G \sqrt{\mathbf{I}_d : \boldsymbol{\varepsilon}_{n+1}^{e,tr} : \mathbf{I}_d : \boldsymbol{\varepsilon}_{n+1}^{e,tr}}. \end{aligned} \quad (2.76)$$

For the computation the chain rule and the product rule need to be applied. In addition the identity $\boldsymbol{\varepsilon}_{d,n+1}^{e,tr} : \mathbf{I}_d = \boldsymbol{\varepsilon}_{d,n+1}^{e,tr}$ holds.

$$\frac{\partial q_{n+1}^{tr}}{\partial \boldsymbol{\varepsilon}_{n+1}^{e,tr}} = \sqrt{\frac{3}{2}} 2G \frac{1}{2} \frac{1}{\|\boldsymbol{\varepsilon}_{d,n+1}^{e,tr}\|} (\mathbf{I}_d : \mathbf{I} : \mathbf{I}_d : \boldsymbol{\varepsilon}_{n+1}^{e,tr} + \mathbf{I}_d : \boldsymbol{\varepsilon}_{n+1}^{e,tr} : \mathbf{I}_d : \mathbf{I}) = \sqrt{\frac{3}{2}} 2G \frac{\boldsymbol{\varepsilon}_{d,n+1}^{e,tr}}{\|\boldsymbol{\varepsilon}_{d,n+1}^{e,tr}\|} \quad (2.77)$$

The derivative of $\Delta\gamma$ is obtained by taking Eq. (2.67) into account:

$$\Delta\gamma = \frac{1}{3G} \left(\sqrt{3J_2(\mathbf{s}_{n+1}^{tr})} - \sigma_y(\bar{\varepsilon}_n^p + \Delta\gamma) \right). \quad (2.78)$$

The first part of the derivative can be computed using Eq. (2.77) and (2.76):

$$\frac{\partial\Delta\gamma}{\partial\boldsymbol{\varepsilon}_{n+1}^{e,tr}} = \frac{1}{3G} \left(\sqrt{\frac{3}{2}} 2G \frac{\boldsymbol{\varepsilon}_{d,n+1}^{e,tr}}{\|\boldsymbol{\varepsilon}_{d,n+1}^{e,tr}\|} - \frac{\partial\sigma_y(\bar{\varepsilon}_n^p + \Delta\gamma)}{\partial\bar{\varepsilon}_n^p} \Big|_{(\bar{\varepsilon}_n^p + \Delta\gamma)} \frac{\partial\Delta\gamma}{\partial\boldsymbol{\varepsilon}_{n+1}^{e,tr}} \right). \quad (2.79)$$

Introducing the actual *hardening modulus* H that is the slope of the hardening curve at $\bar{\varepsilon}_n^p + \Delta\gamma$:

$$H = \frac{\partial\sigma_y(\bar{\varepsilon}_n^p + \Delta\gamma)}{\partial\bar{\varepsilon}_n^p} \Big|_{\bar{\varepsilon}_n^p + \Delta\gamma} \quad (2.80)$$

and reordering the equations, the unknown derivative can be found:

$$\frac{\partial\Delta\gamma}{\partial\boldsymbol{\varepsilon}_{n+1}^{e,tr}} = \frac{2G}{3G + H} \sqrt{\frac{3}{2}} \frac{\boldsymbol{\varepsilon}_{d,n+1}^{e,tr}}{\|\boldsymbol{\varepsilon}_{d,n+1}^{e,tr}\|}. \quad (2.81)$$

After replacing the derivatives in Eq. (2.75) by Eq. (2.77) and Eq. (2.81) the full elastoplastic tangent modulus reads:

$$\begin{aligned} \mathbf{D}^{ep} &= \mathbf{D}^e - \frac{\Delta\gamma 6G^2}{q_{n+1}^{tr}} \mathbf{I}_d - \frac{6G^2}{q_{n+1}^{tr}} \boldsymbol{\varepsilon}_{d,n+1}^{e,tr} \otimes \frac{2G}{3G + H} \sqrt{\frac{3}{2}} \frac{\boldsymbol{\varepsilon}_{d,n+1}^{e,tr}}{\|\boldsymbol{\varepsilon}_{d,n+1}^{e,tr}\|} \\ &+ \frac{\Delta\gamma 6G^2}{(q_{n+1}^{tr})^2} \boldsymbol{\varepsilon}_{d,n+1}^{e,tr} \otimes \sqrt{\frac{3}{2}} 2G \frac{\boldsymbol{\varepsilon}_{d,n+1}^{e,tr}}{\|\boldsymbol{\varepsilon}_{d,n+1}^{e,tr}\|} \\ &= \mathbf{D}^e - \frac{\Delta\gamma 6G^2}{q_{n+1}^{tr}} \mathbf{I}_d - \frac{6G^2}{q_{n+1}^{tr}} \frac{2G}{3G + H} \sqrt{\frac{3}{2}} \boldsymbol{\varepsilon}_{d,n+1}^{e,tr} \otimes \frac{\boldsymbol{\varepsilon}_{d,n+1}^{e,tr}}{\|\boldsymbol{\varepsilon}_{d,n+1}^{e,tr}\|} \\ &+ \frac{\Delta\gamma 6G^2}{(q_{n+1}^{tr})^2} \sqrt{\frac{3}{2}} 2G \boldsymbol{\varepsilon}_{d,n+1}^{e,tr} \otimes \frac{\boldsymbol{\varepsilon}_{d,n+1}^{e,tr}}{\|\boldsymbol{\varepsilon}_{d,n+1}^{e,tr}\|}. \end{aligned} \quad (2.82)$$

By introducing the following relation:

$$\frac{\boldsymbol{\varepsilon}_{d,n+1}^{e,tr}}{q_{n+1}^{tr}} = \sqrt{\frac{2}{3}} \frac{1}{2G} \frac{\boldsymbol{\varepsilon}_{d,n+1}^{e,tr}}{\|\boldsymbol{\varepsilon}_{d,n+1}^{e,tr}\|}, \quad (2.83)$$

we can simplify Eq. (2.82) and obtain:

$$\begin{aligned} \mathbf{D}^{ep} &= \mathbf{D}^e - \frac{\Delta\gamma 6G^2}{q_{n+1}^{tr}} \mathbf{I}_d - \frac{6G^2}{3G + H} \frac{\boldsymbol{\varepsilon}_{d,n+1}^{e,tr}}{\|\boldsymbol{\varepsilon}_{d,n+1}^{e,tr}\|} \otimes \frac{\boldsymbol{\varepsilon}_{d,n+1}^{e,tr}}{\|\boldsymbol{\varepsilon}_{d,n+1}^{e,tr}\|} + \frac{\Delta\gamma 6G^2}{q_{n+1}^{tr}} \frac{\boldsymbol{\varepsilon}_{d,n+1}^{e,tr}}{\|\boldsymbol{\varepsilon}_{d,n+1}^{e,tr}\|} \otimes \frac{\boldsymbol{\varepsilon}_{d,n+1}^{e,tr}}{\|\boldsymbol{\varepsilon}_{d,n+1}^{e,tr}\|} \\ &= \mathbf{D}^e - \frac{\Delta\gamma 6G^2}{q_{n+1}^{tr}} \mathbf{I}_d + 6G^2 \left(\frac{\Delta\gamma}{q_{n+1}^{tr}} - \frac{1}{3G + H} \right) \frac{\boldsymbol{\varepsilon}_{d,n+1}^{e,tr}}{\|\boldsymbol{\varepsilon}_{d,n+1}^{e,tr}\|} \otimes \frac{\boldsymbol{\varepsilon}_{d,n+1}^{e,tr}}{\|\boldsymbol{\varepsilon}_{d,n+1}^{e,tr}\|}. \end{aligned} \quad (2.84)$$

After substituting the small strain elasticity tensor given in Eq. (2.38) we end up with the following expression:

$$\mathbf{D}^{ep} = 2G \left(1 - \frac{\Delta\gamma 3G}{q_{n+1}^{tr}} \right) \mathbf{I}_d + K \mathbf{1} \otimes \mathbf{1} + 6G^2 \left(\frac{\Delta\gamma}{q_{n+1}^{tr}} - \frac{1}{3G + H} \right) \frac{\boldsymbol{\varepsilon}_{d,n+1}^{e,tr}}{\|\boldsymbol{\varepsilon}_{d,n+1}^{e,tr}\|} \otimes \frac{\boldsymbol{\varepsilon}_{d,n+1}^{e,tr}}{\|\boldsymbol{\varepsilon}_{d,n+1}^{e,tr}\|}. \quad (2.85)$$

2.3.3 J_2 finite strain plasticity

In this section we present a hyperelastic based formulation for elastoplasticity that combines the Hencky's material model with the associative von Mises plastic flow theory and isotropic hardening [66]. The model can be applied in the small strain as well as in the large strain regime.

After a brief introduction to the governing equations of this model we will present the discretization of the flow rule and show how to recover the small strain format in terms of logarithmic strains. Due to this procedure the solution scheme is similar to the small strain elastoplastic model presented in section 2.3.2 and only a summary of the equations that need to be solved in the elastic predictor and the plastic corrector step are given.

2.3.3.1 General model

Hyperelastic based elastoplastic models for large deformations utilize the multiplicative split of the deformation gradient

$$\mathbf{F} = \mathbf{F}^e \mathbf{F}^p \quad (2.86)$$

into an elastic \mathbf{F}^e and a plastic \mathbf{F}^p contribution. This is in contrast to the additive split of the *symmetric spatial velocity gradient*, that is used in so-called *hypo-elastic* approaches.

Furthermore, the elastic regime is described by a hyperelastic material formulation:

$$\boldsymbol{\tau} = \rho_0 \frac{\partial \tilde{\psi}}{\partial \boldsymbol{\epsilon}^e}. \quad (2.87)$$

In the finite strain regime the flow rule reads as follows:

$$\dot{\mathbf{F}}^p \mathbf{F}^{p-1} = \dot{\gamma} \mathbf{R}^{eT} \frac{\partial \Psi}{\partial \boldsymbol{\tau}} \mathbf{R}^e, \quad (2.88)$$

where \mathbf{R}^e is the elastic orthogonal rotation tensor obtained from the polar decomposition of the elastic deformation gradient. The evolution of the hardening variables is given by the following relation:

$$\dot{\bar{\epsilon}}_p = \dot{\gamma}. \quad (2.89)$$

The given equations need to be solved under the constraints of the Kuhn-Tucker conditions:

$$\dot{\gamma} \geq 0 \quad , \quad \Phi(\boldsymbol{\tau}, \bar{\epsilon}_p) \leq 0 \quad , \quad \dot{\gamma} \Phi(\boldsymbol{\tau}, \bar{\epsilon}_p) = 0. \quad (2.90)$$

2.3.3.2 The exponential integrator

The form of the plastic flow rule is ideal for the use of an exponential map integrator. The use of the exponential map backward discretization leads to a discrete version of the flow rule that resembles the small strain version explained above. Besides this the volume preserving property of the plastic flow is exactly preserved. In the following the main transformation steps will be explained. The discrete form of the flow rule is given by:

$$\mathbf{F}_{n+1}^p = \mathbf{R}_{n+1}^{eT} \left(\Delta \gamma \frac{\partial \Psi}{\partial \boldsymbol{\tau}} \Big|_{n+1} \right) \mathbf{R}_{n+1}^e \mathbf{F}_n^p, \quad (2.91)$$

where $\exp(\cdot)$ denotes the *tensor exponential*, see [42]. Using the multiplicative split of the deformation gradient $\mathbf{F}^p = \mathbf{F}^{e^{-1}}\mathbf{F}$ we can replace the plastic deformation gradient in Eq. (2.91).

$$\mathbf{F}_{n+1}^{e^{-1}}\mathbf{F}_{n+1} = \mathbf{R}_{n+1}^{e^T} \exp\left(\Delta\gamma \frac{\partial\Psi}{\partial\boldsymbol{\tau}}\Big|_{n+1}\right) \mathbf{R}_{n+1}^e \mathbf{F}_n^{e^{-1}} \mathbf{F}_n \quad (2.92)$$

By left multiplication with \mathbf{F}_{n+1}^e we obtain the following form:

$$\mathbf{F}_{n+1} = \mathbf{F}_{n+1}^e \mathbf{R}_{n+1}^{e^T} \exp\left(\Delta\gamma \frac{\partial\Psi}{\partial\boldsymbol{\tau}}\Big|_{n+1}\right) \mathbf{R}_{n+1}^e \mathbf{F}_n^{e^{-1}} \mathbf{F}_n, \quad (2.93)$$

and further rearranging the terms yields:

$$\mathbf{F}_{n+1} \mathbf{F}_n^{-1} \mathbf{F}_n^e \mathbf{R}_{n+1}^{e^T} \exp\left(-\Delta\gamma \frac{\partial\Psi}{\partial\boldsymbol{\tau}}\Big|_{n+1}\right) \mathbf{R}_{n+1}^e = \mathbf{F}_{n+1}^e. \quad (2.94)$$

Next, we introduce the *incremental deformation gradient* \mathbf{F}_Δ that is computed by the gradient ∇_{x_n} of the *incremental displacement field* $\Delta\mathbf{u}$ with respect to x_n and the second order identity tensor:

$$\mathbf{F}_\Delta = \mathbf{F}_{n+1} \mathbf{F}_n^{-1} = \mathbf{1} + \nabla_{x_n} \Delta\mathbf{u}. \quad (2.95)$$

Substituting the incremental deformation gradient in Eq. (2.94) gives:

$$\mathbf{F}_{n+1}^e = \mathbf{F}_\Delta \mathbf{F}_n^e \mathbf{R}_{n+1}^{e^T} \exp\left(-\Delta\gamma \frac{\partial\Psi}{\partial\boldsymbol{\tau}}\Big|_{n+1}\right) \mathbf{R}_{n+1}^e. \quad (2.96)$$

The update of the elastic deformation gradient yields the trial elastic deformation gradient:

$$\mathbf{F}_{n+1}^{e,tr} = \mathbf{F}_\Delta \mathbf{F}_n^e. \quad (2.97)$$

In a more compact form, we can rewrite Eq. (2.96):

$$\mathbf{F}_{n+1}^e = \mathbf{F}_{n+1}^{e,tr} \mathbf{R}_{n+1}^{e^T} \exp\left(-\Delta\gamma \frac{\partial\Psi}{\partial\boldsymbol{\tau}}\Big|_{n+1}\right) \mathbf{R}_{n+1}^e. \quad (2.98)$$

After making use of the polar decomposition $\mathbf{F}_{n+1}^e = \mathbf{V}_{n+1}^e \mathbf{R}_{n+1}^e$ of the elastic deformation gradient we multiply this equation from the right side with the elastic orthogonal rotation tensor $\mathbf{R}_{n+1}^{e^T}$:

$$\mathbf{V}_{n+1}^e = \mathbf{F}_{n+1}^{e,tr} \mathbf{R}_{n+1}^{e^T} \exp\left(-\Delta\gamma \frac{\partial\Psi}{\partial\boldsymbol{\tau}}\Big|_{n+1}\right) \quad (2.99)$$

and obtain a formulation for the elastic left stretch tensor \mathbf{V}_{n+1}^e :

$$\mathbf{V}_{n+1}^e \exp\left(\Delta\gamma \frac{\partial\Psi}{\partial\boldsymbol{\tau}}\Big|_{n+1}\right) = \mathbf{F}_{n+1}^{e,tr} \mathbf{R}_{n+1}^{e^T} \quad (2.100)$$

Multiplying each side by its transpose yields:

$$\mathbf{V}_{n+1}^e \exp \left(\Delta\gamma \frac{\partial \Psi}{\partial \boldsymbol{\tau}} \Big|_{n+1} \right) \left(\exp \left(\Delta\gamma \frac{\partial \Psi}{\partial \boldsymbol{\tau}} \Big|_{n+1} \right) \right)^T \mathbf{V}_{n+1}^{eT} = \mathbf{F}_{n+1}^{e,tr} \mathbf{R}_{n+1}^{eT} \mathbf{R}_{n+1}^e (\mathbf{F}_{n+1}^{e,tr})^T. \quad (2.101)$$

Using the properties $\mathbf{R}_{n+1}^{eT} \mathbf{R}_{n+1}^e = \mathbf{1}$ and $\mathbf{F}_{n+1}^{e,tr} (\mathbf{F}_{n+1}^{e,tr})^T = (\mathbf{V}_{n+1}^{e,tr})^2$ together with $(\exp(\cdot))^T = \exp((\cdot)^T)$ and the symmetry of the gradient of the flow rule $\frac{\partial \Psi}{\partial \boldsymbol{\tau}} = \left(\frac{\partial \Psi}{\partial \boldsymbol{\tau}} \right)^T$ we obtain:

$$\mathbf{V}_{n+1}^e \mathbf{e} \exp \left(2\Delta\gamma \frac{\partial \Psi}{\partial \boldsymbol{\tau}} \Big|_{n+1} \right) \mathbf{V}_{n+1}^{eT} = (\mathbf{V}_{n+1}^{e,tr})^2. \quad (2.102)$$

Due to the assumed elastic and plastic isotropy, see [66], $\exp \left(2\Delta\gamma \frac{\partial \Psi}{\partial \boldsymbol{\tau}} \Big|_{n+1} \right)$ and \mathbf{V}_{n+1}^{eT} commute and we can rearrange the terms:

$$\mathbf{V}_{n+1}^e \mathbf{V}_{n+1}^{eT} \exp \left(2\Delta\gamma \frac{\partial \Psi}{\partial \boldsymbol{\tau}} \Big|_{n+1} \right) = (\mathbf{V}_{n+1}^{e,tr})^2. \quad (2.103)$$

After making use of $\mathbf{V}_{n+1}^e \mathbf{V}_{n+1}^{eT} = (\mathbf{V}_{n+1}^e)^2$ and taking the roots we have:

$$\mathbf{V}_{n+1}^e = \mathbf{V}_{n+1}^{e,tr} \mathbf{e}^{-\Delta\gamma \frac{\partial \Psi}{\partial \boldsymbol{\tau}} \Big|_{n+1}}. \quad (2.104)$$

Finally, after using the tensor logarithm and Eq. (2.13), we obtain the flow rule that has the same format as the small strain equivalent in Eq. (2.57), this time formulated for Hencky strains:

$$\boldsymbol{\epsilon}_{n+1}^e = \boldsymbol{\epsilon}_{n+1}^{e,tr} - \Delta\gamma \frac{\partial \Psi}{\partial \boldsymbol{\tau}} \Big|_{n+1}. \quad (2.105)$$

Having presented all transformation steps, we can now present the algorithm for the state update in the finite strain regime.

2.3.3.2.1 The elastic predictor

Let us briefly summarize the governing equations of the elastic predictor in the finite strain regime. In the elastic predictor step we assume that all deformations are elastic. With $\Delta\gamma = 0$ Eq. (2.96) reads:

$$\mathbf{F}_{n+1}^{e,tr} = \mathbf{F}_\Delta \mathbf{F}_n^e \quad (2.106)$$

and the evolution equation for the hardening variable is given by:

$$\bar{\boldsymbol{\epsilon}}_{n+1}^{p,tr} = \bar{\boldsymbol{\epsilon}}_n^p. \quad (2.107)$$

The trial stress is computed by Hencky's hyperelastic material law:

$$\boldsymbol{\tau}_{n+1}^{tr} = \mathbf{D}^e : \boldsymbol{\epsilon}_{n+1}^{e,tr}. \quad (2.108)$$

The yield condition reads:

$$\Phi(\boldsymbol{\tau}_{n+1}^{tr}, \bar{\boldsymbol{\epsilon}}_n^{p,tr}) = \sqrt{3J_2(\boldsymbol{s}_{n+1}^{tr})} - \sigma_y(\bar{\boldsymbol{\epsilon}}_n^{p,tr}) \leq 0 \quad (2.109)$$

2.3.3.2 The plastic corrector

The plastic corrector step for the finite strain plastic model directly follows its small strain counterpart. The return mapping equations in terms of logarithmic strains read:

$$\boldsymbol{\epsilon}_{n+1}^e = \boldsymbol{\epsilon}_{n+1}^{e,tr} - \Delta\gamma \left. \frac{\partial \Psi}{\partial \boldsymbol{\tau}} \right|_{n+1} \quad (2.110)$$

$$\bar{\boldsymbol{\epsilon}}_{n+1}^p = \bar{\boldsymbol{\epsilon}}_n^p + \Delta\gamma \quad (2.111)$$

$$0 = \sqrt{3J_2(\boldsymbol{s}_{n+1})} - \sigma_y(\bar{\boldsymbol{\epsilon}}_{n+1}^p) \quad (2.112)$$

In terms of the von Mises model with an associative flow rule, the flow potential is the von Mises yield function Φ . As already demonstrated for the small strain case these equations reduce to one single nonlinear equation similar to Eq. (2.67).

2.3.3.3 The consistent elastoplastic tangent

The consistent spatial tangent modulus for the current configuration is given by:

$$a_{ijkl} = \frac{1}{J} \frac{\partial \tau_{ij}}{\partial F_{kq}^{tr}} F_{lq}^{tr} - \sigma_{il} \delta_{jk} . \quad (2.113)$$

The functional dependency of $\frac{\partial \tau_{ij}}{\partial F_{kq}^{tr}}$ in terms of the rate constitutive model can be obtained by applying the chain rule:

$$\frac{\partial \tau_{ij}}{\partial F_{kq,n+1}^{e,tr}} = \frac{\partial \tau_{ij}}{\partial \epsilon_{mn,n+1}^{e,tr}} \frac{\partial \epsilon_{mn,n+1}^{e,tr}}{\partial b_{op,n+1}^{e,tr}} \frac{\partial b_{op,n+1}^{e,tr}}{\partial F_{kq,n+1}^{e,tr}} . \quad (2.114)$$

Substituting Eq. (2.114) into Eq. (2.113) yields:

$$a_{ijkl} = \frac{1}{J} \frac{\partial \tau_{ij}}{\partial \epsilon_{mn,n+1}^{e,tr}} \frac{\partial \epsilon_{mn,n+1}^{e,tr}}{\partial b_{op,n+1}^{e,tr}} \frac{\partial b_{op,n+1}^{e,tr}}{\partial F_{kq,n+1}^{e,tr}} F_{lq}^{e,tr} - \sigma_{il} \delta_{jk} . \quad (2.115)$$

By computing the derivative of the left Cauchy-Green strain tensor we can simplify this equation.

$$\begin{aligned} B_{opkl} &= \frac{\partial b_{op,n+1}^{e,tr}}{\partial F_{kq,n+1}^{e,tr}} F_{lq}^{e,tr} = \left(\frac{\partial (F_{or,n+1}^{e,tr} F_{pr,n+1}^{e,tr})}{\partial F_{kq,n+1}^{e,tr}} \right) F_{lq}^{e,tr} \\ &= (\delta_{ok} \delta_{rq} F_{pr,n+1}^{e,tr} + F_{or,n+1}^{e,tr} \delta_{pk} \delta_{rq}) F_{lq}^{e,tr} \\ &= (\delta_{ok} F_{pq,n+1}^{e,tr} + F_{oq,n+1}^{e,tr} \delta_{pk}) F_{lq}^{e,tr} \\ &= \delta_{ok} b_{pl,n+1}^{e,tr} + b_{ol,n+1}^{e,tr} \delta_{pk} \end{aligned} \quad (2.116)$$

The elastoplastic tangent in Eq. (2.115) has the same format as the small strain elastoplastic consistent tangent operator and reads:

$$\begin{aligned} D_{ijmn}^{ep} &= \frac{\partial \tau_{ij}}{\partial \epsilon_{mn,n+1}^{e,tr}} = 2G \left(1 - \frac{\Delta\gamma 3G}{q_{n+1}^{tr}} \right) \left(\frac{1}{2} (\delta_{im} \delta_{jn} + \delta_{in} \delta_{mj}) - \frac{1}{3} \delta_{ij} \delta_{mn} \right) + K \delta_{ij} \delta_{mn} \\ &\quad + \frac{6G^2}{(\|\boldsymbol{\epsilon}_{d,n+1}^{e,tr}\|)^2} \left(\frac{\Delta\gamma}{q_{n+1}^{tr}} - \frac{1}{3G + H} \right) (\boldsymbol{\epsilon}_{d,n+1}^{e,tr})_{ij} (\boldsymbol{\epsilon}_{d,n+1}^{e,tr})_{mn} . \end{aligned} \quad (2.117)$$

The second multiplicand in Eq. (2.115)

$$L_{mnop} = \frac{\partial \epsilon_{mn,n+1}^{e,tr}}{\partial b_{op,n+1}^{e,tr}} = \frac{1}{2} \frac{\partial \ln(b_{mn,n+1}^{e,tr})}{\partial b_{op,n+1}^{e,tr}} \quad (2.118)$$

is the derivative of the tensor logarithm. Its computation is not straightforward and complex. Interested readers are referred to [66].

2.4 Weak form of the equilibrium conditions

Finding the analytical solution for the system of differential equations given by the balance equations 2.22 is only possible for simple geometries and boundary conditions. In the general case we have to find an approximate solution. The weak form, also known as the principle of virtual work, allows to compute the best approximation in the sense of a weighted residual within a given ansatz.

2.4.1 Weak form of the balance equation in the current configuration

In order to derive the weak form of the problem we consider the strong form of the quasi-static equilibrium conditions with $\hat{\mathbf{v}} = \mathbf{0}$:

$$\operatorname{div} \boldsymbol{\sigma} + \rho \mathbf{b} = \mathbf{0}. \quad (2.119)$$

To solve the problem in a weak sense we multiply it by a set of *test functions* and postulate that the residual vanishes in the mean over the whole domain.

$$\int_{\varphi(B)} \operatorname{div} \boldsymbol{\sigma} \cdot \boldsymbol{\eta} + \rho \mathbf{b} \cdot \boldsymbol{\eta} \, dv = 0 \quad (2.120)$$

Making use of partial integration and the divergence theorem we obtain the weak form of the equilibrium equations:

$$g(\varphi, \boldsymbol{\eta}) = \int_{\varphi(B)} \boldsymbol{\sigma} : \operatorname{grad} \boldsymbol{\eta} \, dv - \int_{\varphi(B)} \rho \mathbf{b} \cdot \boldsymbol{\eta} \, dv - \int_{\varphi(\Gamma^N)} \mathbf{t} \cdot \boldsymbol{\eta} \, da = 0, \quad (2.121)$$

where \mathbf{t} describes tractions acting on the Neumann boundary $\varphi(\Gamma^N)$ of the body. Due to the symmetry of the Cauchy stress tensor we can replace the spatial gradient by its symmetric part:

$$g(\varphi, \boldsymbol{\eta}) = \int_{\varphi(B)} \boldsymbol{\sigma} : \nabla_x^S \boldsymbol{\eta} \, dv - \int_{\varphi(B)} \rho \mathbf{b} \cdot \boldsymbol{\eta} \, dv - \int_{\varphi(\Gamma^N)} \mathbf{t} \cdot \boldsymbol{\eta} \, da = 0, \quad (2.122)$$

where

$$\nabla_x^S \boldsymbol{\eta} = \frac{1}{2} (\operatorname{grad} \boldsymbol{\eta} + \operatorname{grad}^T \boldsymbol{\eta}). \quad (2.123)$$

2.4.2 Weak form of the balance equation in the reference configuration

The weak form of the balance equation in the reference configuration can be equivalently derived from Eq. (2.25) by following the same steps as for the spatial configuration. The weak form for the quasi-static case with $\dot{\mathbf{v}} = \mathbf{0}$ reads:

$$G(\varphi, \boldsymbol{\eta}) = \int_B \mathbf{P} : \text{Grad } \boldsymbol{\eta} \, dV - \int_B \rho_0 \mathbf{b} \cdot \boldsymbol{\eta} \, dV - \int_{\Gamma^N} \mathbf{t} \cdot \boldsymbol{\eta} \, dA = 0. \quad (2.124)$$

An alternative form is obtained by replacing the first Piola-Kirchhoff stress tensor by the second Piola-Kirchhoff stress tensor:

$$G(\varphi, \boldsymbol{\eta}) = \int_B \mathbf{S} : \delta \mathbf{E} \, dV - \int_B \rho_0 \mathbf{b} \cdot \boldsymbol{\eta} \, dV - \int_{\Gamma^N} \mathbf{t} \cdot \boldsymbol{\eta} \, dA = 0, \quad (2.125)$$

where $\delta \mathbf{E}$ denotes the variation of the Green-Lagrange strain tensor.

2.5 Linearization of the weak form

The weak formulation either given for the current or for the reference configuration generally is a nonlinear functional. In order to solve this equation we introduce the load factor λ_i to apply the load increment-wise and employ the Newton-Raphson in every load-step. The Newton-Raphson algorithm is based on a first order *Taylor series* expansion of the problem at an already known solution $\bar{\varphi}$:

$$G(\varphi, \boldsymbol{\eta}) = G(\bar{\varphi}, \boldsymbol{\eta}) + \text{D} G(\bar{\varphi}, \boldsymbol{\eta}) [\Delta \mathbf{u}] + r(\bar{\varphi}, \boldsymbol{\eta}) \approx G(\bar{\varphi}, \boldsymbol{\eta}) + \text{D} G(\bar{\varphi}, \boldsymbol{\eta}) [\Delta \mathbf{u}] = 0. \quad (2.126)$$

In this equation $r(\bar{\varphi}, \boldsymbol{\eta})$ denotes the higher order terms that are neglected for the computation of the solution.

Applying the Newton-Raphson scheme leads to a that has to be solved in each load-step i several times until a solution within a predefined accuracy is found. The equations solved in each Newton-Raphson iteration k reads:

$$\text{D} G(\varphi(\mathbf{u}_i^k), \boldsymbol{\eta}) [\Delta \mathbf{u}] = -G(\varphi(\mathbf{u}_i^k), \boldsymbol{\eta}, \lambda_i). \quad (2.127)$$

The Newton-Raphson scheme requires to compute the linearization of Eq. (2.124) or Eq. (2.121). In this section we represent the linearization of the weak form in the reference and current configuration. To obtain the formulation for the current configuration we apply a *push forward* operation on the previously derived linearization of the reference configuration.

2.5.1 The linearized virtual work equation in the reference configuration

In order to simplify the notation we assume that external loads \mathbf{t} and body forces \mathbf{b} do not depend on the actual deformation, so the linearization of Eq. (2.124) is given by the following form:

$$\text{D} G(\bar{\varphi}, \boldsymbol{\eta}) [\Delta \mathbf{u}] = \int_B \mathbf{A} : \text{Grad } \Delta \mathbf{u} : \text{Grad } \boldsymbol{\eta} \, dV, \quad (2.128)$$

where \mathbf{A} :

$$\mathbf{A} \equiv \frac{\partial \mathbf{P}}{\partial \mathbf{F}} \quad (2.129)$$

is usually referred to as the *first elasticity tensor* or the *material tangent modulus* and depends on the choice of the constitutive model. Using this relation we can state the material description of the linearized virtual work equation:

$$\int_B \mathbf{A} : \text{Grad } \Delta \mathbf{u} : \text{Grad } \boldsymbol{\eta} \, dV = - \int_B (\mathbf{P} : \text{Grad } \boldsymbol{\eta} - \rho_0 \mathbf{b} \cdot \boldsymbol{\eta}) \, dV + \int_{\Gamma_N} \mathbf{t} \cdot \text{Grad } \boldsymbol{\eta} \, dA. \quad (2.130)$$

2.5.2 The linearized virtual work equation in the current configuration

Eq. (2.130) can be equivalently expressed in the spatial description. To this end we replace the material gradient with the spatial gradient:

$$\begin{aligned} D g(\bar{\boldsymbol{\varphi}}, \boldsymbol{\eta}) [\Delta \mathbf{u}] &= \int_{\varphi(B)} \frac{1}{J} \mathbf{A} : (\text{grad } \Delta \mathbf{u} \mathbf{F}) : (\text{grad } \boldsymbol{\eta} \mathbf{F}) \, dv \\ &= \int_{\varphi(B)} \frac{1}{J} \mathbf{a} : \text{grad } \Delta \mathbf{u} : \text{grad } \boldsymbol{\eta} \, dv \end{aligned} \quad (2.131)$$

and define the *spatial tangent modulus* \mathbf{a} that is related to its material counterpart via the following expression:

$$\begin{aligned} \frac{1}{J} A_{imkn} \Delta u_{k,n} \eta_{i,m} &= \frac{1}{J} A_{imkn} \Delta u_{k,j} F_{jn} \eta_{i,l} F_{lm} \\ &= \frac{1}{J} A_{imkn} F_{jn} F_{lm} \Delta u_{k,j} \eta_{i,l} \\ &= a_{ijkl} \Delta u_{k,j} \eta_{i,l} \quad \text{with} \\ a_{ijkl} &= \frac{1}{J} A_{imkn} F_{jn} F_{lm} \end{aligned} \quad (2.132)$$

The dependency of the Kirchhoff stress tensor on the material tangent modulus can be obtained by considering the following relation:

$$P_{im} = J \sigma_{ip} F_{mp}^{-1} = \tau_{ip} F_{mp}^{-1} \quad (2.133)$$

Using Eq. (2.133) in the definition of the first Piola-Kirchhoff stress tensor we obtain the following relation:

$$A_{imkn} = \frac{\partial P_{im}}{\partial F_{kn}} = \frac{\partial}{\partial F_{kn}} (\tau_{ip} F_{mp}^{-1}) = \frac{\partial \tau_{ip}}{\partial F_{kn}} F_{mp}^{-1} + \tau_{ip} \frac{\partial F_{mp}^{-1}}{\partial F_{kn}}. \quad (2.134)$$

The derivative of the inverse deformation gradient with respect to itself reads:

$$\frac{\partial F_{mp}^{-1}}{\partial F_{kn}} = -F_{mk}^{-1} F_{np}^{-1}, \quad (2.135)$$

so that we finally arrive at the following expression relating the Kirchhoff stress tensor to the material tangent modulus:

$$A_{imkn} = \frac{\partial \tau_{ip}}{\partial F_{kn}} F_{mp}^{-1} - \tau_{ip} F_{mk}^{-1} F_{np}^{-1}. \quad (2.136)$$

For the spatial tangent modulus, after making use of Eq. (2.132), we arrive at the following expression:

$$\begin{aligned} a_{ijkl} &= \frac{1}{J} A_{imkn} F_{jm} F_{ln} = \frac{1}{J} \frac{\partial \tau_{ip}}{\partial F_{kn}} F_{mp}^{-1} F_{jm} F_{ln} - \frac{1}{J} \tau_{ip} F_{mk}^{-1} F_{np}^{-1} F_{jm} F_{ln} \\ &= \frac{1}{J} \frac{\partial \tau_{ip}}{\partial F_{kn}} \delta_{jp} F_{ln} - \frac{1}{J} \tau_{ip} \delta_{jk} \delta_{lp} \\ &= \frac{1}{J} \frac{\partial \tau_{ip}}{\partial F_{kn}} \delta_{jp} F_{ln} - \frac{1}{J} \tau_{il} \delta_{jk} \\ &= \frac{1}{J} \frac{\partial \tau_{ij}}{\partial F_{kn}} F_{ln} - \sigma_{il} \delta_{jk}. \end{aligned} \quad (2.137)$$

Now we can state the linearized form of the spatial virtual work:

$$\int_{\varphi(B)} \mathbf{a} : \text{grad } \Delta \mathbf{u} : \text{grad } \boldsymbol{\eta} \, dv = - \int_{\varphi(B)} (\boldsymbol{\sigma} : \nabla_x^S \boldsymbol{\eta} - \rho \mathbf{b} \cdot \boldsymbol{\eta}) \, dv + \int_{\varphi(\Gamma_N)} \mathbf{t} \cdot \text{grad } \boldsymbol{\eta} \, da \quad (2.138)$$

Chapter 3

Finite cell method

The finite cell method [54, 17] is a combination of the fictitious domain method [58, 59] and the high order finite element method [67, 7]. The fictitious domain approach allows to substitute the original problem posed on a complex domain by a modified problem on a simple shaped domain (extended domain Ω_{ext}), see Fig. 3.1. The extended domain can be discretized by structured or Cartesian grids, reducing the pre-processing effort. This is advantageous especially for problems dealing with image-based CT data [77, 76, 78, 18] where the geometry is often very complex and a finite element discretization is hard to obtain, see Fig. 3.2. The

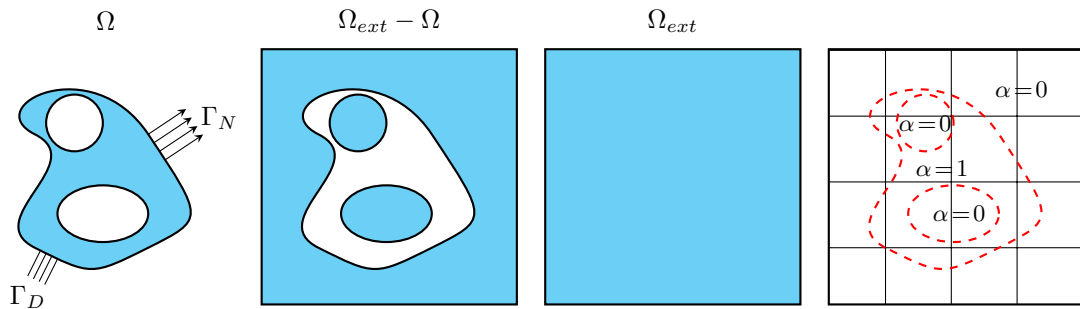


Figure 3.1: Generation of a finite cell discretization.

idea of high order finite element methods is to increase the accuracy of the finite element solution by increasing the polynomial order of the hierarchic ansatz functions (p -refinement) that are integrated Legendre polynomials.

Combining these two approaches the FCM obtains two beneficial properties. The fictitious domain approach, on the one hand, leads to a simple meshing procedure whereas the high order finite element method, on the other hand, gives rise to higher convergence rates for smooth problems.

In the last years the finite cell method was further extended to compute nonlinear problems of continuum mechanics. Elastoplastic deformations under small strains were considered in [3, 5, 4]. Geometrical nonlinear problems were first treated in [61, 62]. The extension of the FCM to solve finite strain elastoplastic problems is part of this thesis.

Due to the high order approach the FCM normally utilizes large elements with a high polynomial order. This feature is beneficial for smooth problems but not for problems involving an intra element discontinuity or a singularity. To resolve these problems enrichment strategies

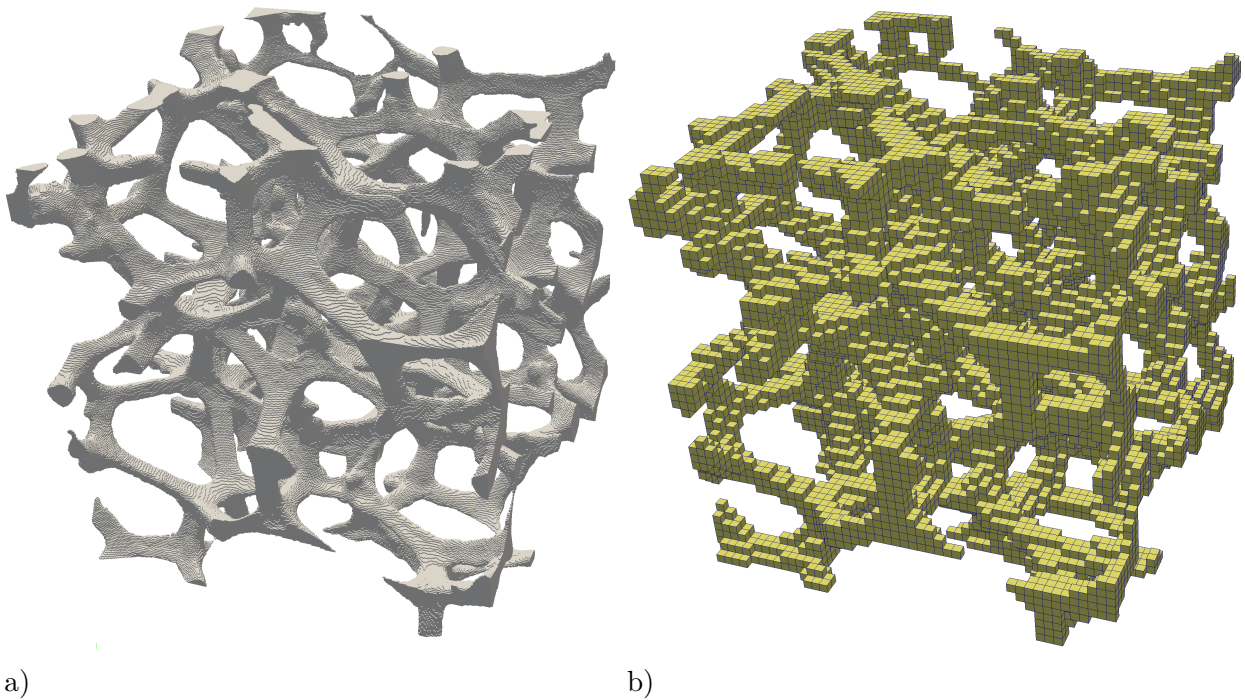


Figure 3.2: a) Voxel model obtained from CT Scan and b) automatically generated finite cell discretization [25].

based on the partition-of-unity method (PUM) [34], or on an *hp-d* overlay strategy [60] were proposed.

For problems involving contact two different formulations have been considered. Wriggers et al. [74] and Bog et al. [13] utilized the fictitious domain that, on the one hand, describes the fictitious domain itself and, on the other hand, a stiff contact material when the contact constraints need to be enforced. The second formulation is based on an additional discretization of the contact interface by contact elements and was first considered by Konyukhov et al. [41] for an unilateral contact problem. The extension of this method for contact between two elastic bodies is addressed in Section 5.

3.1 Spatial discretization

The governing equation for the development of a spatial discretization is the weak form of the equilibrium equations Eq. (2.121) and its linearization Eq. (2.138) given in the current configuration. In the context of the finite cell method these equations are reformulated such that they hold for the extended domain Ω_{ext} .

The weak form for the finite cell method reads:

$$g(\varphi, \boldsymbol{\eta}) = \int_{\varphi(\Omega_{ext})} \alpha \boldsymbol{\sigma} : \nabla_x^S \boldsymbol{\eta} \, dv - \int_{\varphi(\Omega_{ext})} \alpha \rho \mathbf{b} \cdot \boldsymbol{\eta} \, dv - \int_{\varphi(\Gamma_N)} \mathbf{t} \cdot \boldsymbol{\eta} \, da = 0, \quad (3.1)$$

respectively its linearization:

$$\int_{\varphi(\Omega_{ext})} \alpha \mathbf{a} : \text{grad } \Delta \mathbf{u} : \text{grad } \boldsymbol{\eta} \, dv = - \int_{\varphi(\Omega_{ext})} \alpha (\boldsymbol{\sigma} : \nabla_x^S \boldsymbol{\eta} - \rho \mathbf{b} \cdot \boldsymbol{\eta}) \, dv + \int_{\varphi(\Gamma_N)} \mathbf{t} \cdot \text{grad } \boldsymbol{\eta} \, da. \quad (3.2)$$

The equivalence with the original equation Eq. (2.138) is enforced by the discontinuous *indicator function* $\alpha = 10^{-q}$ that penalizes the fictitious domain $\Omega_f (\Omega_{ext} - \Omega)$.

$$\alpha(\mathbf{X}) = \begin{cases} 1 & \forall \mathbf{X} \in \Omega \\ \alpha_0 = 10^{-q} & \forall \mathbf{X} \in \Omega_{ext} - \Omega \end{cases} \quad (3.3)$$

Both formulations are equivalent for $q = \infty$ but in fact we choose $q \in [5, \dots, 12]$ to avoid ill conditioning of the problem.

The spatial discretization of the problem requires to subdivide the extended domain into a set of n_c cells Ω_c .

$$\Omega_{ext} = \bigcup_{c=1}^{n_c} \Omega_c \quad (3.4)$$

Shape functions

On each cell a set of local shape functions is defined that are used to approximate the displacements and test functions. The shape functions are connected at the cell boundaries to enforce C_0 continuity between the cells.

In the displacement based finite cell method the unknown displacements \mathbf{u} and test functions $\boldsymbol{\eta}$ are approximated by the following ansatz:

$$\mathbf{u} = \sum_{i=1}^n N_I(\xi, \eta, \zeta) \mathbf{u}^I, \quad \boldsymbol{\eta} = \sum_{i=1}^n N_I(\xi, \eta, \zeta) \mathbf{v}^I, \quad (3.5)$$

where $N_I(\xi, \eta, \zeta)$ are the so called *hierarchic shape functions*, $\mathbf{u}^I = [U_x^I, U_y^I, U_z^I]^T$ are the unknowns and $\mathbf{v}^I = [V_x^I, V_y^I, V_z^I]^T$ are the arbitrary virtual displacements, with $I \in [1, \dots, n]$. The number of unknowns n depends on the polynomial order selected for the finite cell. For a computer-based implementation this relation is often presented in matrix vector notation given by:

$$\mathbf{u} = \mathbf{N} \mathbf{u}^c = \begin{bmatrix} N_1(\boldsymbol{\xi}) & & \dots & N_n(\boldsymbol{\xi}) \\ & N_1(\boldsymbol{\xi}) & & & & \\ & & N_1(\boldsymbol{\xi}) & \dots & & \\ & & & \dots & N_n(\boldsymbol{\xi}) & \\ & & & & & N_n(\boldsymbol{\xi}) \end{bmatrix} \begin{bmatrix} U_x^1 \\ U_y^1 \\ U_z^1 \\ \vdots \\ U_x^n \\ U_y^n \\ U_z^n \end{bmatrix}. \quad (3.6)$$

The shape functions are formulated based on the *standard or parent element* with its local coordinates $\boldsymbol{\xi} = [\xi, \eta, \zeta]^T$. The relationship between the global and local coordinates of the

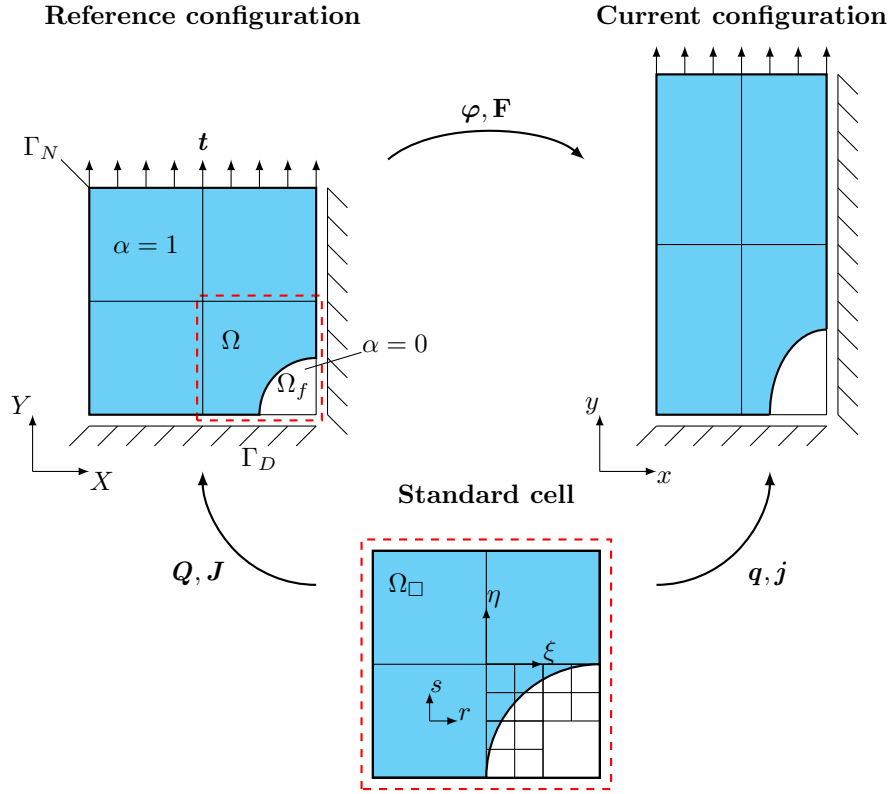


Figure 3.3: Spatial discretization in the context of the finite cell method.

shape functions is described by the mapping functions $\mathbf{Q}(\xi, \eta, \zeta)$ or $\mathbf{q}(\xi, \eta, \zeta)$ depending on what configuration is used to describe the problem, see Fig. 3.3.

Inserting the approximation Eq. (3.6) into Eq. (2.138) under consideration of the Newton-Raphson scheme given by Eq. (2.127) leads to a :

$$\mathbf{K}^{k-1} \Delta \mathbf{u}_i^k = \mathbf{F}_{\text{int}}^{k-1} (\mathbf{u}_i^{k-1}) - \bar{\lambda}_i \mathbf{F}_{\text{ext}}, \quad (3.7)$$

where \mathbf{K} is called the *global tangent stiffness matrix*, \mathbf{F}_{int} is called the *internal load vector* and \mathbf{F}_{ext} is called the *external load vector*. Due to the local support of the shape functions these quantities can be computed cell-wise. Subsequently, the contributions can be combined using the *assembly process* denoted by \mathbf{A} :

$$\mathbf{K} = \mathbf{A} \mathbf{k}_c \quad \mathbf{F}_{\text{int}} = \mathbf{A} \mathbf{f}_{\text{int},c} \quad \mathbf{F}_{\text{ext}} = \mathbf{A} \mathbf{f}_{\text{ext},c}. \quad (3.8)$$

For a three-dimensional problem the cell-wise expressions for \mathbf{k} , \mathbf{f}_{int} and \mathbf{f}_{ext} read:

$$\mathbf{K}^c = \int_{\Omega_{\square}} \alpha \mathbf{G}^T \mathbf{a} \mathbf{G} \det \mathbf{j} d\Omega_{\square}, \quad \mathbf{f}_{\text{int}} = \int_{\Omega_{\square}} \alpha \mathbf{B}^T \boldsymbol{\sigma} \det \mathbf{j} d\Omega_{\square}, \quad \mathbf{f}_{\text{ext}} = \int_{\Gamma_N} \mathbf{N}^T \mathbf{t} \|\mathbf{q}_{,\alpha} \times \mathbf{q}_{,\beta}\| d\alpha d\beta. \quad (3.9)$$

In analogy to Fig. 3.3 for a three-dimensional problem $d\Omega_{\square}$ denotes the volume of the standard cell. The computation of the external load vector requires to integrate the surface traction over a cell surface. The transformation between the global to local coordinates of the cell

surface $[\alpha, \beta]^T$, which correspond to a pair of $[\xi, \eta, \zeta]^T$ depending on what cell surface the traction is acting on, is described by $da = \|\mathbf{q}_{,\alpha} \times \mathbf{q}_{,\beta}\| d\alpha d\beta$. The spatial tangent modulus \mathbf{a} as already given by Eq. (2.137) stems from the constitutive relation and more information can be found in Section 2.5. In the following all other quantities appearing in this equation will be explained.

The computation of derivatives

The discretization of the weak form requires to compute the derivatives of the shape functions – that explicitly depend on the local cell coordinates $\boldsymbol{\xi}$ – with respect to the spatial coordinates \mathbf{x} . The relation between these two coordinate systems is given either by the mapping function $\mathbf{q}(\boldsymbol{\xi})$ or by $\mathbf{Q}(\boldsymbol{\xi})$ and the deformation gradient \mathbf{F} , see Fig. 3.3.

Applying the chain rule the derivatives of the shape functions with respect to the local coordinates are:

$$\begin{aligned} \frac{\partial N_i(\xi, \eta, \zeta)}{\partial \xi} &= \frac{\partial N_i(\xi, \eta, \zeta)}{\partial x_1} \frac{\partial x_1}{\partial \xi} + \frac{\partial N_i(\xi, \eta, \zeta)}{\partial x_2} \frac{\partial x_2}{\partial \xi} + \frac{\partial N_i(\xi, \eta, \zeta)}{\partial x_3} \frac{\partial x_3}{\partial \xi} \\ \frac{\partial N_i(\xi, \eta, \zeta)}{\partial \eta} &= \frac{\partial N_i(\xi, \eta, \zeta)}{\partial x_1} \frac{\partial x_1}{\partial \eta} + \frac{\partial N_i(\xi, \eta, \zeta)}{\partial x_2} \frac{\partial x_2}{\partial \eta} + \frac{\partial N_i(\xi, \eta, \zeta)}{\partial x_3} \frac{\partial x_3}{\partial \eta} \\ \frac{\partial N_i(\xi, \eta, \zeta)}{\partial \zeta} &= \frac{\partial N_i(\xi, \eta, \zeta)}{\partial x_1} \frac{\partial x_1}{\partial \zeta} + \frac{\partial N_i(\xi, \eta, \zeta)}{\partial x_2} \frac{\partial x_2}{\partial \zeta} + \frac{\partial N_i(\xi, \eta, \zeta)}{\partial x_3} \frac{\partial x_3}{\partial \zeta}. \end{aligned} \quad (3.10)$$

Writing Eq. (3.10) in matrix-vector notation gives:

$$\begin{bmatrix} \frac{\partial N_i(\xi, \eta, \zeta)}{\partial \xi} \\ \frac{\partial N_i(\xi, \eta, \zeta)}{\partial \eta} \\ \frac{\partial N_i(\xi, \eta, \zeta)}{\partial \zeta} \end{bmatrix} = \begin{bmatrix} x_{1,\xi} & x_{2,\xi} & x_{3,\xi} \\ x_{1,\eta} & x_{2,\eta} & x_{3,\eta} \\ x_{1,\zeta} & x_{2,\zeta} & x_{3,\zeta} \end{bmatrix} \begin{bmatrix} \frac{\partial N_i(\xi, \eta, \zeta)}{\partial x_1} \\ \frac{\partial N_i(\xi, \eta, \zeta)}{\partial x_2} \\ \frac{\partial N_i(\xi, \eta, \zeta)}{\partial x_3} \end{bmatrix}, \quad (3.11)$$

where the Jacobian matrix \mathbf{j} :

$$\mathbf{j} = \begin{bmatrix} x_{1,\xi} & x_{2,\xi} & x_{3,\xi} \\ x_{1,\eta} & x_{2,\eta} & x_{3,\eta} \\ x_{1,\zeta} & x_{2,\zeta} & x_{3,\zeta} \end{bmatrix} \quad (3.12)$$

is the transposed gradient of the spatial mapping function \mathbf{q} . Inverting this relation allows to compute the derivatives of the shape functions with respect to the global spatial coordinates. In a computer-based implementation often only the nodal coordinates of the undeformed configuration and the actual displacements are stored. In this case the spatial Jacobian matrix can be obtained by:

$$\mathbf{j} = \mathbf{J}\mathbf{F}^T, \quad (3.13)$$

where \mathbf{J} :

$$\mathbf{J} = \begin{bmatrix} X_{1,\xi} & X_{2,\xi} & X_{3,\xi} \\ X_{1,\eta} & X_{2,\eta} & X_{3,\eta} \\ X_{1,\zeta} & X_{2,\zeta} & X_{3,\zeta} \end{bmatrix} \quad (3.14)$$

is the Jacobian matrix corresponding to the initial configuration. For Cartesian grids as usually employed in the finite cell method \mathbf{J} is a constant, diagonal matrix.

The discrete spatial gradient operator

Using the derivatives with respect to the global coordinates $N_{(\cdot),i}$ in the current configuration we can state the *discrete spatial gradient operator*:

$$\mathbf{G} = \begin{bmatrix} N_{1,1} & 0 & 0 & \cdots & N_{n,1} & 0 & 0 \\ N_{1,2} & 0 & 0 & \cdots & N_{n,2} & 0 & 0 \\ N_{1,3} & 0 & 0 & \cdots & N_{n,3} & 0 & 0 \\ 0 & N_{1,1} & 0 & \cdots & 0 & N_{n,1} & 0 \\ 0 & N_{1,2} & 0 & \cdots & 0 & N_{n,2} & 0 \\ 0 & N_{1,3} & 0 & \cdots & 0 & N_{n,3} & 0 \\ 0 & 0 & N_{1,1} & \cdots & 0 & 0 & N_{n,1} \\ 0 & 0 & N_{1,2} & \cdots & 0 & 0 & N_{n,2} \\ 0 & 0 & N_{1,3} & \cdots & 0 & 0 & N_{n,3} \end{bmatrix} \quad (3.15)$$

and the *spatial discrete symmetric gradient operator*:

$$\mathbf{B} = \begin{bmatrix} N_{1,1} & 0 & 0 & \cdots & N_{n,1} & 0 & 0 \\ 0 & N_{1,2} & 0 & \cdots & 0 & N_{n,2} & 0 \\ 0 & 0 & N_{1,3} & \cdots & 0 & 0 & N_{n,3} \\ N_{1,2} & N_{1,1} & 0 & \cdots & N_{n,2} & N_{n,1} & 0 \\ 0 & N_{1,3} & N_{1,2} & \cdots & 0 & N_{n,3} & N_{n,2} \\ N_{1,3} & 0 & N_{1,1} & \cdots & N_{n,3} & 0 & N_{n,1} \end{bmatrix}. \quad (3.16)$$

3.2 Mesh generation for voxel-based models

One way to obtain a realistic geometric model of cellular materials is to use computed tomography that creates a voxel model of the scanned object, see Fig. 3.4. The voxel model is a



Figure 3.4: Voxel model generated from CT image.

structured grid with a spacing that equals the voxel size. Based on the interpretation of the data either the space between the nodes of the grid or the nodes itself can represent a voxel. In the following we will consider the space between the nodes as a voxel. Each node of the grid

stores a value for the attenuation of the X-rays that intersect the material during the scan. Different materials have different values for the attenuation, which is measured in terms of the Hounsfield unit. In a *segmentation* process these values can be classified and assigned to a certain material. By looking at the material at the nodes, the space in-between i.e. the voxel, can be considered to be full or empty. The representation of geometrical objects by voxels leads to their typical staircase shape. The voxel geometry can be stored in three-dimensional arrays. Alternatively, the geometry can be stored using a single vector and a mapping function that maps the spatial indices i, j – here we consider a two-dimensional example – to the index k indicating its location in the vector. In Fig. 3.5 this procedure is depicted. Generally voxel

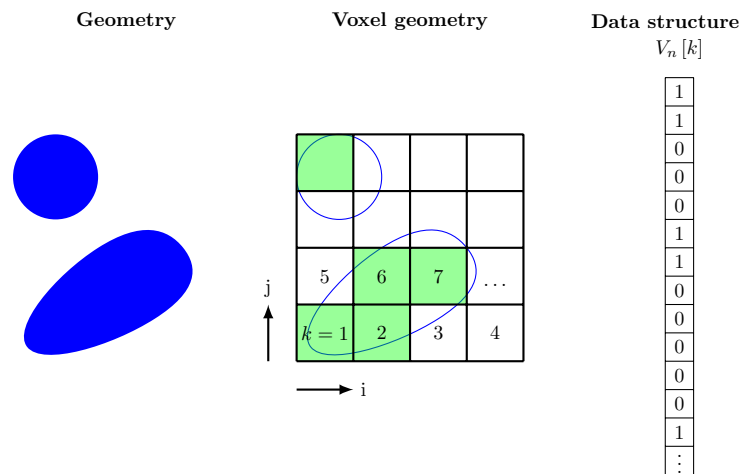


Figure 3.5: Simple geometry with voxelized domain for two-dimensional case.

models are not free from artifacts caused by shielding effects during the scanning process. Such artifacts are, for example, disconnected regions, as shown in Fig. 3.6. In the following some algorithms used to remove such artifacts are presented.

3.2.1 Seed-fill algorithm

The *seed-fill* or *flood fill algorithm* [6] is a fast and robust method to detect the connected parts of a structure by setting a seed point and continuously marking its neighbors as demonstrated in Fig. 3.7. The algorithm is widely used in the major of computer graphics. Its implementation can be either based on an queue- or stack-based data structure. The stack-based implementation relies on recursive function calls which can lead to a stack overflow for large problems. In the following we will explain the queue-based implementation of the algorithm which was used for the pre-processing of the voxel-based models presented in this thesis. In Fig. 3.8 the algorithm is explained by a simple two-dimensional example. The voxel representation of the geometry consists of two parts, the connected major part and a single isolated voxel that should be detected by the algorithm. In a first step a seed voxel within the major part of the geometry must be found. In order to find this seed point the seed-fill algorithm is used with an arbitrary seed point in a first step followed by the computation of the volume of the detected region. The volume can then be compared to a predefined value that defines the minimum size of the major region, respectively the maximum size of the isolated regions.

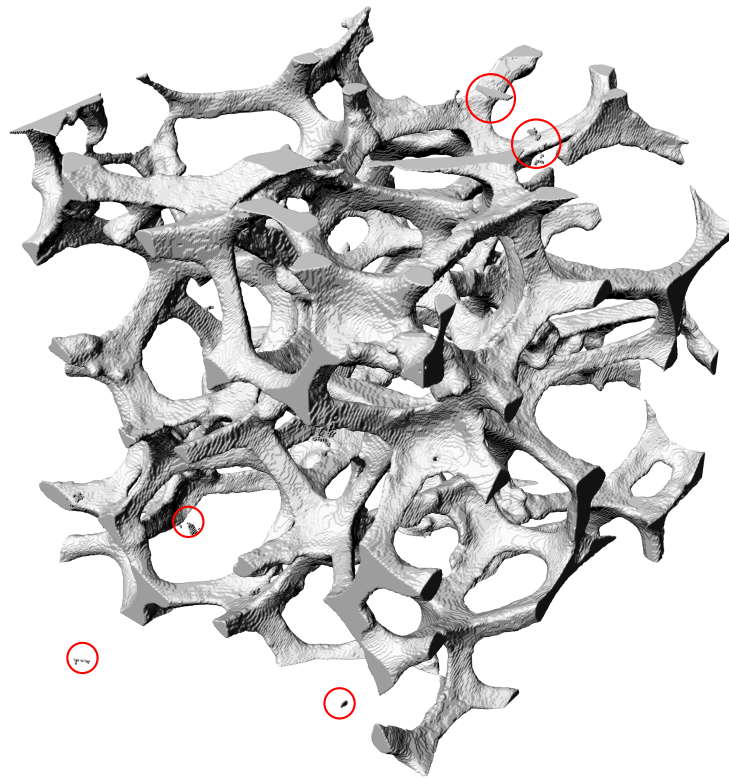


Figure 3.6: STL geometry of an aluminum foam showing disconnected regions.

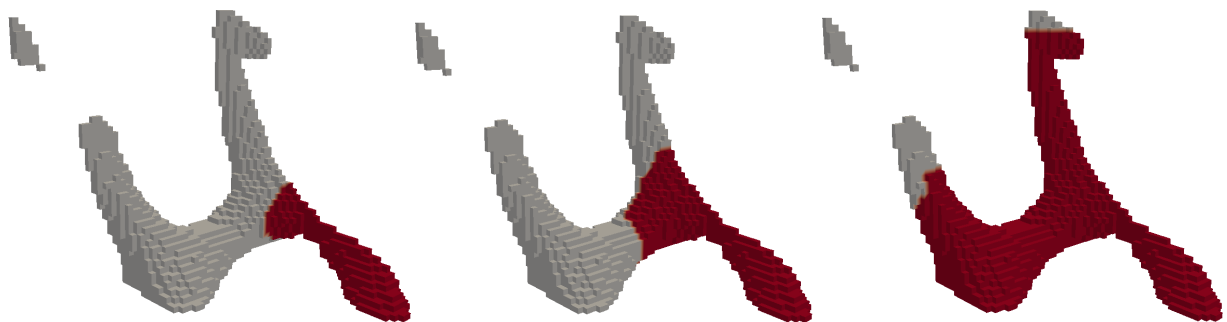


Figure 3.7: Progress of the seed-fill algorithm. The already traced part of the geometry is marked by red color.

In case the detected region is smaller than this threshold it can be classified as an isolated part and removed from the model. In a next step the seed-fill algorithm can be started with a different seed point, until a region of the desired size is detected.

Starting from this seed voxel, its neighboring voxels are selected. Different shapes of neighborhoods are possible. In this case, we consider all voxels as a neighbor, that are within a square of three voxels and connected to each other either by a vertex or a line and additionally faces in three-dimensional voxel models. In case a neighboring voxel contains some material, it is marked by a flag in the voxel vector $V[k]$ (here we use the numerical value of 2 to flag the entry) and the index k of this voxel is stored into a list $I[l]$. The list $I[l]$ stores the voxels that need to be checked for its neighbors, too. In the next step, the first value is taken from the list $I[l]$, and neighbors of the corresponding voxel are selected. Again, if one of this neighboring voxels contains some material and is not yet indicated in the voxel vector by a flag, they are marked and added to the end of the list $I[l]$. These steps are repeated until the list $I[l]$ is empty. Then all voxels in the voxel vector that belong to the connected major part of the geometry are marked and all others can be removed.

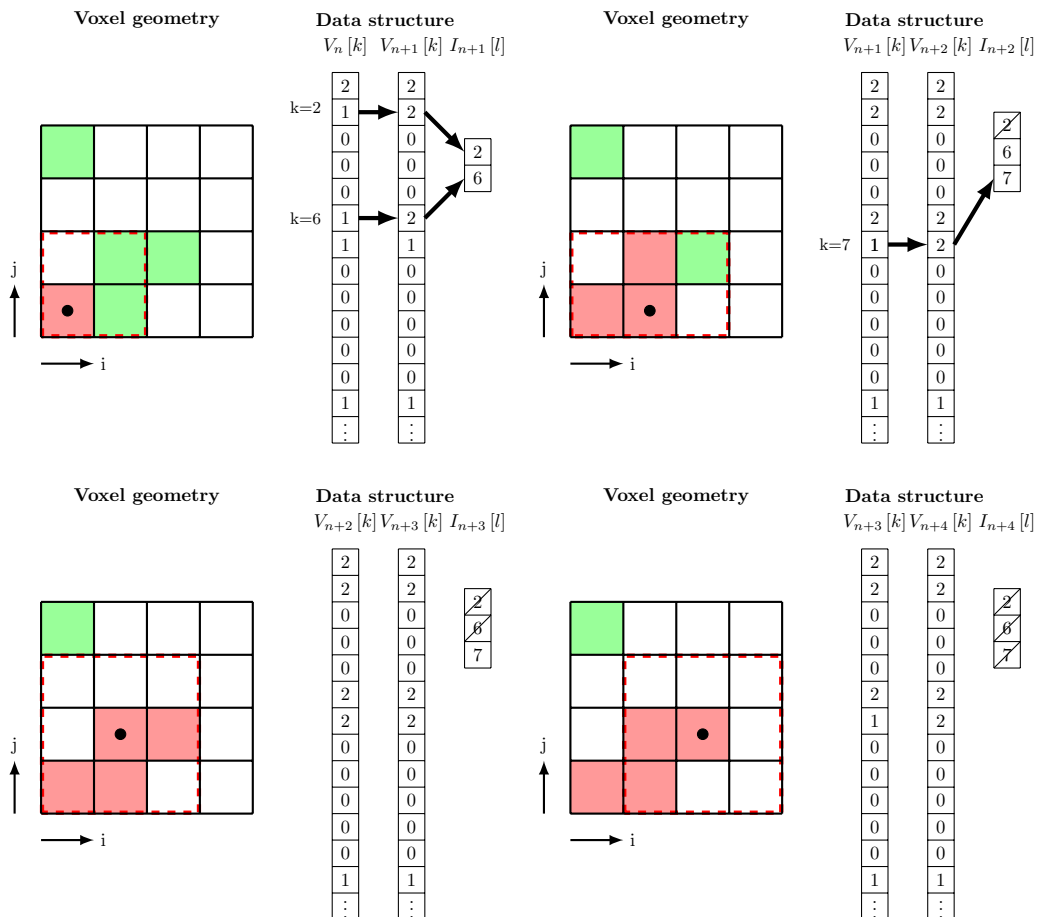


Figure 3.8: Four steps of the seed-fill algorithm.

3.3 Adaptive Gaussian quadrature schemes

The efficient quadrature of the discontinuous integrand of the stiffness matrix and load vector of a finite cell as given by Eq. (3.9) is one of the main challenges in the finite cell method. An efficient integration scheme reduces the number of integration points of the method and directly lowers the computation time since costly matrix-matrix multiplications have to be performed for every Gaussian point.

In the following we will explain adaptive Gaussian integration schemes in more detail.

Adaptive Gaussian quadrature schemes, see Fig. 3.10 or Fig. 3.13, subdivide the integration domain or standard element Ω_\square recursively along the discontinuity into smaller sub-cells sc and compute the integrand with the known integration points \mathbf{r}_i and weights ω_i on the level of the sub-cells (Eq. (3.17)). The adaptive integration schemes yield a better accuracy in terms of the number of integration points, compared to simply performing Gaussian quadrature on the original integration domain and increasing the order of the integration rule.

In geometrical linear computations the finite cells of the Cartesian grid preserve their rectangular shape. Their stiffness matrix with hierarchic shape functions of degree p includes polynomials up to the order $2p$. A Gaussian integration can exactly integrate a polynomial of order $p = 2n - 1$ with n integration points in the one-dimensional case. So a Gaussian quadrature with $n_G = (p + 1)^d$ integration points is sufficient to integrate the stiffness matrix in the d -dimensional space. Due to the fact that the integrand is normally less complex on the sub-cell level the number of Gaussian points can be reduced during each recursive refinement step [5].

Applying the proposed adaptive quadrature to every cut cell, the integration reads as follows:

$$\int_{\Omega_\square} (\cdot) \alpha(\mathbf{Q}(\boldsymbol{\xi})) \det \mathbf{J}(\boldsymbol{\xi}) d\Omega_\square = \sum_{sc=1}^{n_{sc}} \sum_{i=1}^{n_G} (\cdot) \alpha(\mathbf{Q}(\boldsymbol{\xi}(\mathbf{r}_i))) \det \mathbf{J}(\boldsymbol{\xi}(\mathbf{r}_i)) \det \mathbf{J}^{sc}(\mathbf{r}_i) \omega_{r_i}, \quad (3.17)$$

where n_G is the number of Gaussian quadrature points in each sub-cell and n_{sc} is the number of sub-cells. In this context, $\det \mathbf{J}$ and $\det \mathbf{J}^{sc}$ denote the determinant of the Jacobian related to the mapping functions between the finite cell and the standard cell \mathbf{Q} as well as the standard cell and the sub-cell $\boldsymbol{\xi}(\mathbf{r})$, respectively. In order to organize the refinement process space-partitioning tree data structures are used. The next section explains the use of quadtrees and k-d trees in the context of space subdivision by means of a two-dimensional example.

3.3.1 Quadtree space partitioning

The quadtree algorithm recursively splits the standard element of a finite cell containing a discontinuity along the (ξ, η) axes into four equal quadrants (sub-cells), see Fig. 3.10. By this a tree data structure emerges, where the standard element of the finite cell forms the root, subdivided sub-cells are represented by the branches and sub-cells that are not further subdivided are the leafs, see Fig. 3.11.

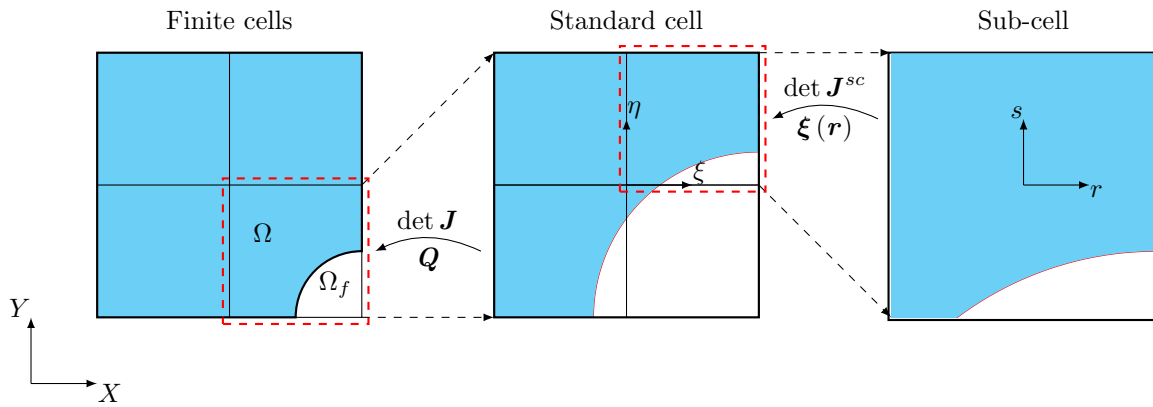


Figure 3.9: Mapping procedure used in adaptive integration schemes.

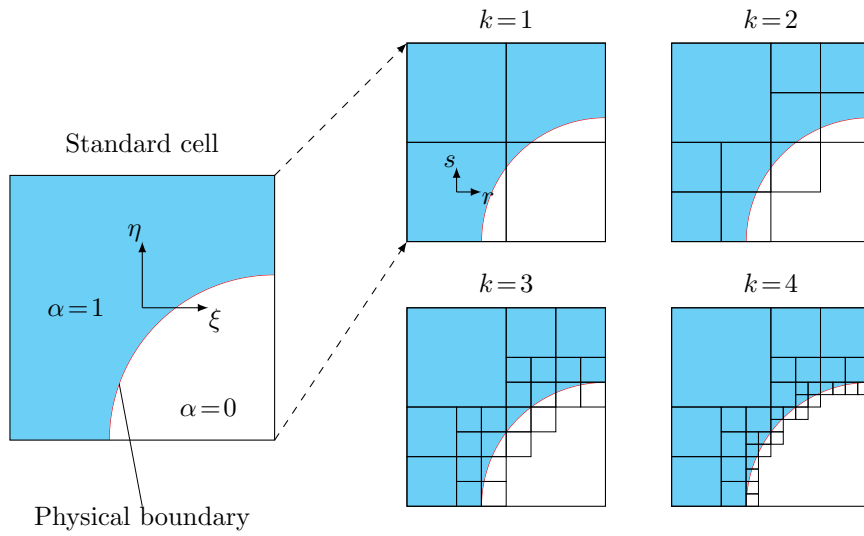


Figure 3.10: Quadtree refinement scheme. Empty sub-cells (leafs) are removed from the figure.

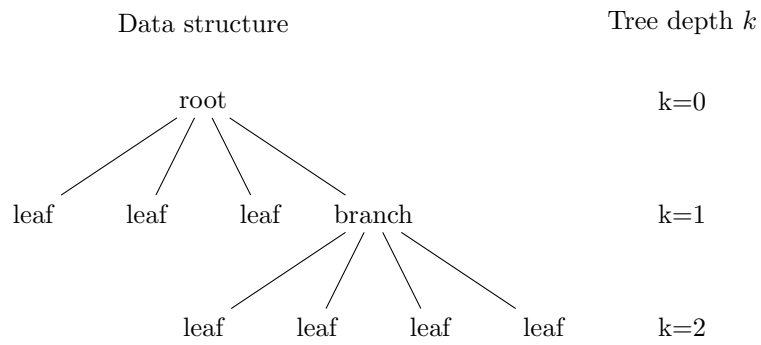


Figure 3.11: Quadtree data structure.

3.3.2 K-d tree space partitioning

A k-d tree is an axis aligned binary space tree. Within the FCM it is applied for the space decomposition of the standard cell. It recursively splits the standard cell of a finite cell containing a discontinuity either along the ξ or η axes into two sub-cells; see Fig. 3.13. The data structure of the k-d tree is similar to the quadtree but every branch can only have two children (leaves or branches), see Fig. 3.12. In particular, the efficiency of the space partitioning depends on the direction and location of the splitting axis. In order to minimize the number of cut cells and to maximize the number of non-cut cells, the algorithm needs to determine the intersection of the geometry with the sub-cells. This procedure can be costly especially when the intersection can not be determined analytically but needs to be tested by invoking a ray-tracing algorithm at different splitting positions. In this work two different approaches of the k-d tree were implemented. The first version, in the following simply referred to as k-d tree, always subdivides the parent cell in the middle. The direction of the splitting axis follows a round robin approach, meaning that the direction changes iteratively by the depth of the k-d tree. The second version allows the splitting axis to slide along the sub-cell in order to minimize the volume of the cut-cell after performing the split. The direction of the axis follows the same scheme as described before. This implementation of the k-d tree is referred to as a k-d tree with sliding midpoint.

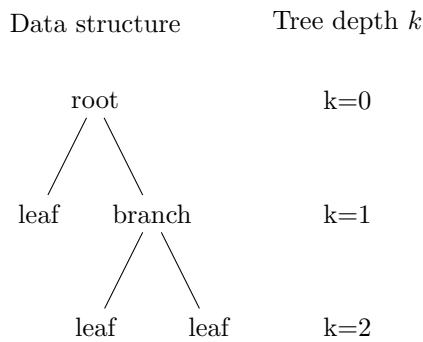


Figure 3.12: K-d tree data structure.

3.3.3 Numerical examples

In this section we compare the quadtree and the k-d tree space subdivision algorithms with and without a sliding midpoint in terms of their accuracy. To this end, we consider two different geometries – a quarter of a circle and an ellipse – as depicted in Fig. 3.14 and compute their areas by integrating the indicator function α numerically. The indicator function is a constant function, so we use one quadrature point per sub-cell and increase the accuracy of the numerical computation by increasing the depth l of the applied space tree.

$$\alpha(\xi, \eta) = \begin{cases} 1 & \text{if } \phi(\xi, \eta) \leq 0 & \forall [\xi, \eta] \in [-1, 1] \\ 0 & \text{if } \phi(\xi, \eta) > 0 & \forall [\xi, \eta] \in [-1, 1] \end{cases} \quad (3.18)$$

For each of these examples an analytical solution A_{Ana} is given and the error of the numerical

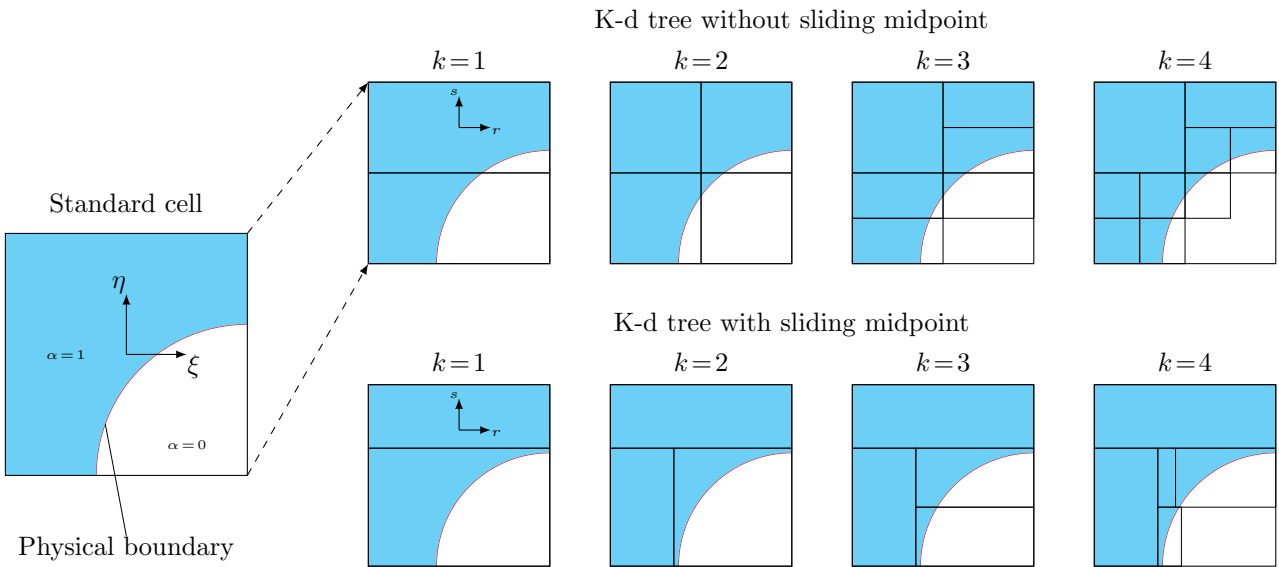


Figure 3.13: Two versions of a k-d tree refinement scheme. Empty sub-cells (leafs) are removed from the figure.

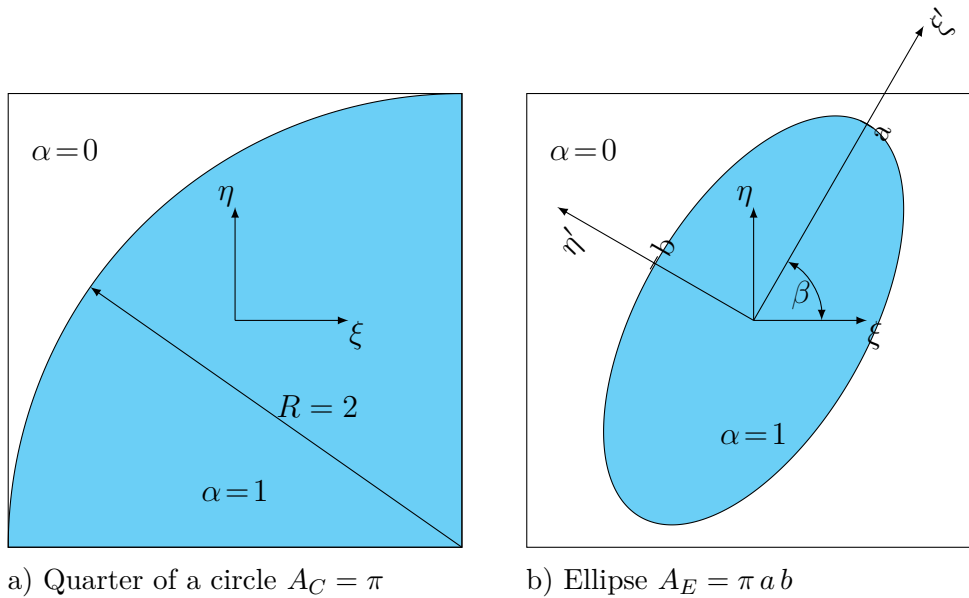


Figure 3.14: Comparison of the quadtree and the k-d tree with and without sliding midpoint.

solution A_{Num} is computed by:

$$e_A = \left| 1 - \frac{A_{\text{Num}}}{A_{\text{Ana}}} \right|. \quad (3.19)$$

The first example consists of a quarter of a circle with $R = 2$. Consequently the analytical solution for the area is $A_{\text{Ana,C}} = \pi$. The implicit function describing this geometry is:

$$\phi(\xi, \eta) = (\xi - 1)^2 + (\eta + 1)^2 - R^2. \quad (3.20)$$

The second example is an ellipse in the $[\xi', \eta']$ coordinate system where the length of the semi-major axis is $a = 1$ and semi-minor axis is $b = 0.5$. To increase the complexity of the example the ellipse is rotated by $\beta = 60^\circ$. Hence, the implicit formula describing this ellipse in the $\xi - \eta$ coordinate system is:

$$\phi(\xi, \eta) = \left(\frac{\xi \cos(\beta) + \eta \sin(\beta)}{a} \right)^2 + \left(\frac{-\xi \sin(\beta) + \eta \cos(\beta)}{b} \right)^2 - 1. \quad (3.21)$$

An analytical solution for computing the area of an ellipse is given by $A_{\text{Ana,E}} = \pi a b$.

Fig. 3.15 and Fig. 3.16 depict the error given in Eq. (3.19) of the different approaches in terms of integration points. None of the three methods is uniformly superior to the other. For the example of the circle, the k-d tree with sliding midpoint seems to give a good accuracy for 770 Gaussian points for a tree level depth $k = 17$. However, the accuracy does not increase monotonically when increasing the level of the k-d tree. For $k = 18$ it yields a worse accuracy than the quadtree and the k-d tree without sliding midpoint. For the second example the accuracy of the k-d tree with sliding midpoint levels up at a certain accuracy which is due to the subdivision with sub-cells with a high aspect ratio. It can be concluded that all subdivision schemes seem to give comparable accuracy.

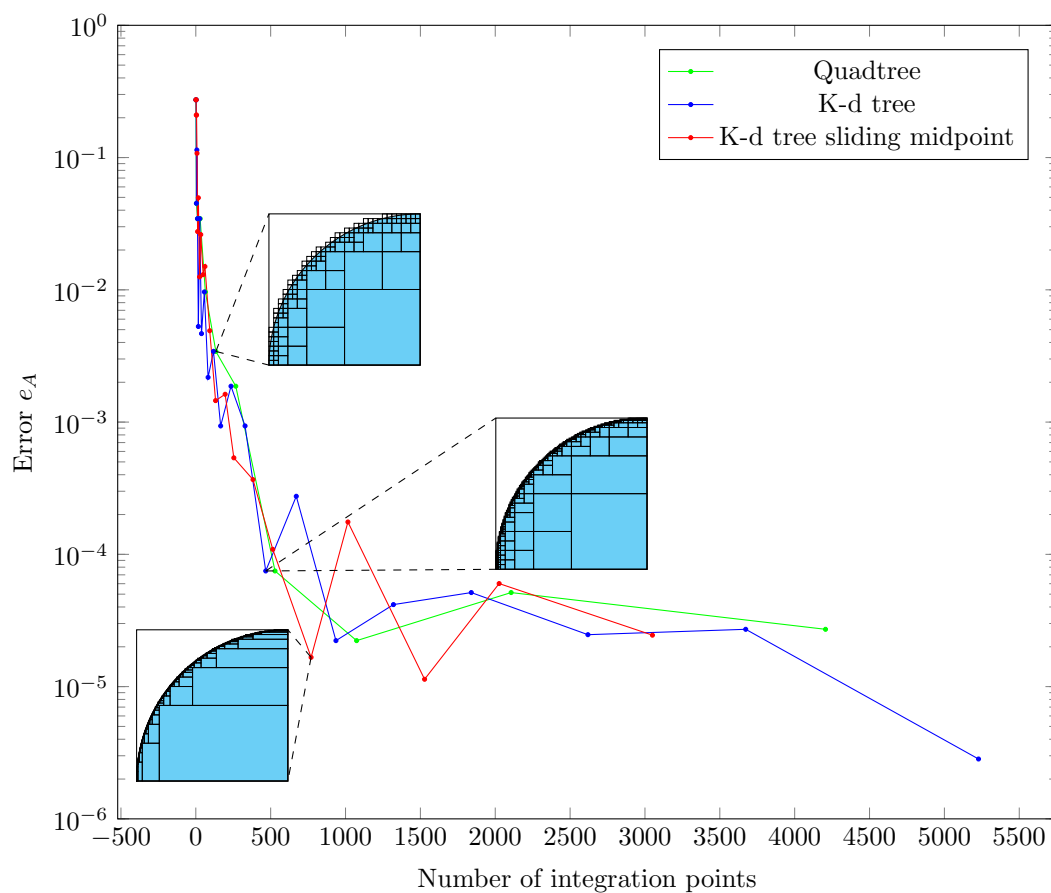


Figure 3.15: Comparison of the quadtree and the k-d tree with and without sliding midpoint space subdivision algorithms for the example of a quarter of a circle.

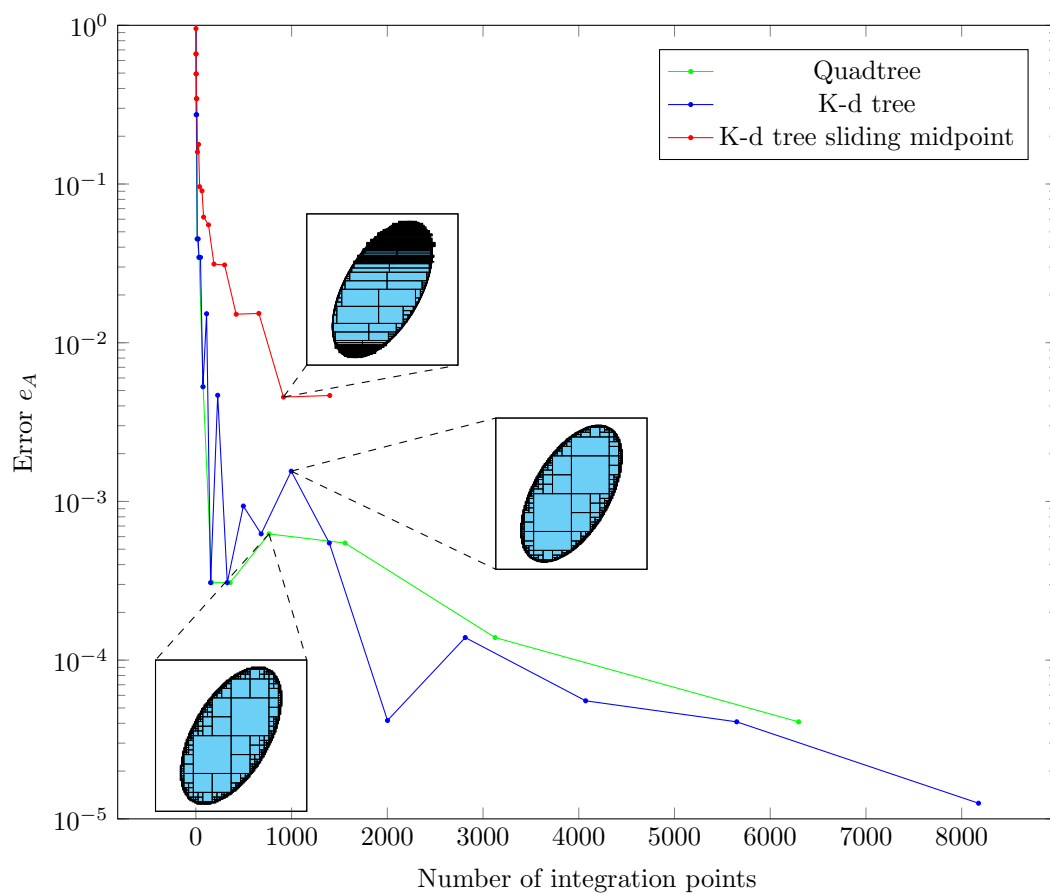


Figure 3.16: Comparison of the quadtree and the k-d tree with and without sliding midpoint space subdivision algorithms for the example of an ellipse.

3.4 Numerical stabilization methods for the FCM

The idea of the fictitious domain approach is to extend the physical domain Ω and to discretize the extended domain Ω_{ext} by finite cells. The finite cells are defined on a larger space than the physical domain. In order to be consistent with the original problem the weak form is only integrated over the physical domain, hence the solution in the fictitious part Ω_f is not constrained.

Let us illustrate the consequences of this approach by means of a simple one-dimensional bar as depicted in Fig. 3.17. The length of the bar is L but it is discretized by a larger finite cell with a length of L_c . In order to load the bar a displacement boundary condition is applied, by clamping the left end of the bar and a traction is applied to the physical part of the domain to elongate the bar. Fig. 3.18 depicts the numerical solution. While the solution follows the

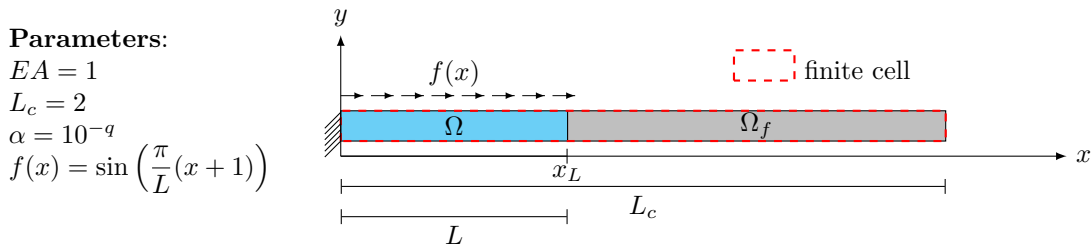


Figure 3.17: Problem setup for the one-dimensional example.

analytical solution in the physical domain, large displacements occur in the fictitious domain. For high polynomial orders p of the shape functions and a high fictitious volume fraction

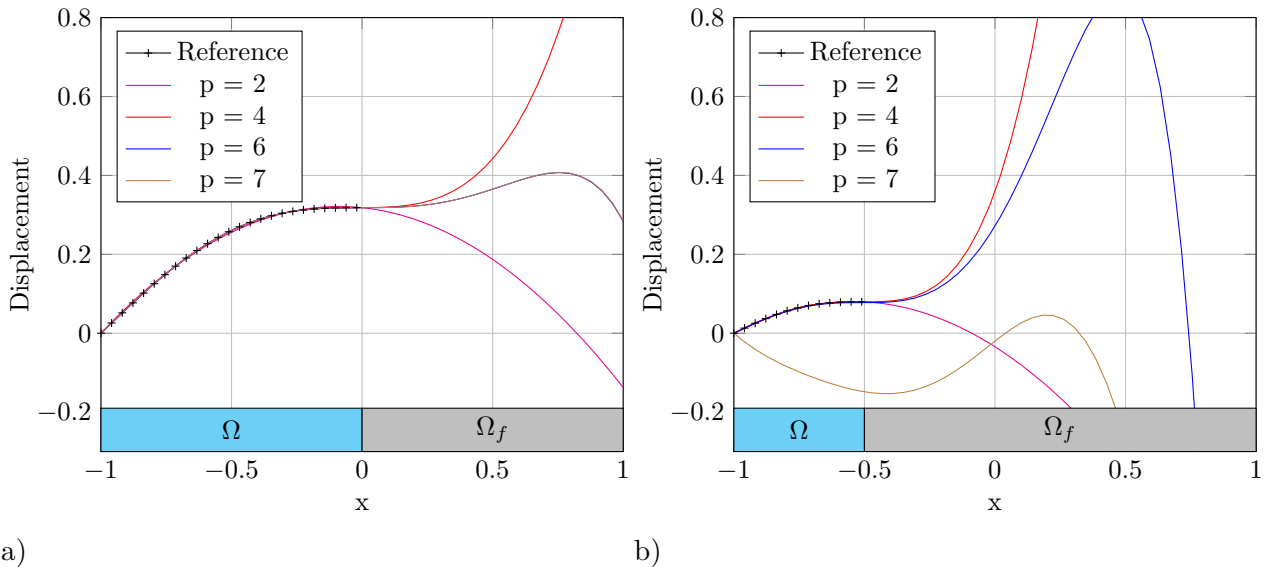


Figure 3.18: Solution behavior of the FCM demonstrated on an one-dimensional problem for different p -values and different fictitious volume fractions: a) $r_f = 0.5$ and b) $r_f = 0.75$.

$r_f = \Omega_f/\Omega_{ext}$ the stiffness matrix of the finite cell can suffer from a bad scaling that can lead to high round off errors during the solution procedure. Fig. 3.18b) depicts the solution of the problem for different polynomial orders obtained by inverting the stiffness matrix by

Gauss-Jordan elimination. For $p = 7$ round-off errors dominate the solution which leads to unphysical results. Another problem that originates from a high fictitious volume fraction is that the equation system can become nearly singular due to the linear dependency of the shape functions. This especially is a severe problem for iterative solvers. A usual measure to quantify the severity of these problems is given by the condition number, which would be quite large in such cases. In order to reduce the condition number for such problems stabilization methods were proposed by [55, 62].

The α -stabilization method, as referred to in this thesis, considers the fictitious material not as a void material, but as a second material with a low stiffness. To apply this low stiffness normally the Young's modulus of the physical domain E is penalized by the α parameter Eq. (3.3) and applied as the Young's modulus E_f in the fictitious domain.

$$E_f = \alpha E \quad (3.22)$$

In the linear case increasing α given in Eq. (3.3) decreases the condition number of the global stiffness matrix which makes solutions for high p -values and $r_f \rightarrow 1$ possible. Clearly, increasing α reduces the accuracy of the solution in the physical domain as this turns the problem into a two material problem, see [15]. Common values for α are between 10^{-12} and 10^{-4} and numerical experiments showed that an accurate solution can be achieved using these values. In nonlinear problems finding the optimal value for α is not yet fully understood. Especially for finite strain elastoplastic problems the energy contribution of the physical domain is determined by elastoplastic material parameters. Considering an elastic material in the fictitious domain would outweigh the penalty parameter and start influencing the solution in the physical domain.

3.4.1 The indicator function

In order to demonstrate the influence of the fictitious domain and the α -stabilization on the solution behavior of the FCM for different p -values and different ratios r_f , we consider the elastic rod depicted in Fig. 3.17 that is discretized by one finite cell and investigate it systematically. By changing the length of the rod $L \in [0.5, 1.0, 1.5]$ and by keeping the length of the finite cell $L_c = 2$ constant the influence of the length of the fictitious domain $L_f = L_c - L$ and the ratio r_f on the solution behavior is examined. In order to increase the accuracy of the finite cell solution we increase the polynomial degree p of the high order hierarchic basis functions.

A traction f is applied to the rod i.e. acting only on the physical part of the domain.

$$f(x) = \sin\left(\frac{\pi}{L}(x+1)\right) \quad x \in [-1, \dots, x_L] \quad (3.23)$$

For this simple example an analytical solution is given by the following function:

$$\begin{aligned} u(x) &= \left(\frac{L}{\pi}\right)^2 \sin\left(\frac{\pi}{L}(x+1)\right) - \frac{L}{\pi} \cos\left(\frac{\pi}{L}(x_L+1)\right) (x+1) \\ \sigma(x) &= \frac{L}{\pi} \cos\left(\frac{\pi}{L}(x+1)\right) - \frac{L}{\pi} \cos\left(\frac{\pi}{L}(x_L+1)\right). \end{aligned} \quad (3.24)$$

In order to compute the difference between the numerical solution and the analytical solution we measure the error as follows:

$$e_u = \frac{1}{L} \int_0^L \left(\frac{u_{\text{FCM}}(x) - u(x)}{u(x)} \right)^2 dx. \quad (3.25)$$

In a first investigation we look at the condition number κ of the problem as a function of the fictitious volume fraction r_f within one finite cell, the polynomial order p and the stabilization parameter alpha $\alpha = 10^{-q}$, see Fig. 3.19. In the reference p-FEM computation ($L = 2$) the condition number is constant during a p-refinement which is a distinctive feature of the p-FEM for one-dimensional problems. For the FCM it is observed that the condition number increases linearly in a semi-logarithmic plot when increasing the polynomial order of the shape functions. The slope of the curve depends on the fictitious volume fraction r_f . By applying the α -stabilization method, the maximum condition number is limited, irrespective of the volume fraction r_f , by 10^q , where q is the same parameter as used for the stabilization. In order to compute the error in displacements between the analytical solution and the numerical solutions we use the measure given in Eq. (3.25). Clearly, there will always be an error between the analytical and the numerical solution since the analytical solution can not be represented by polynomials. So to quantify this contribution to the absolute error and to isolate the error caused by the stabilization we compute a reference solution (p -FEM) for every polynomial order p on a cell coinciding with the physical domain $L = L_c = 2$. This reference serves as a lower bound for the error that can be theoretically reached by the finite cell method. Fig. 3.20 depicts the error defined in Eq. (3.25). The stabilization parameter decreases the rate of convergence in terms of the error e_u but also prevents the displacements from becoming unphysically large if q is sufficiently large.

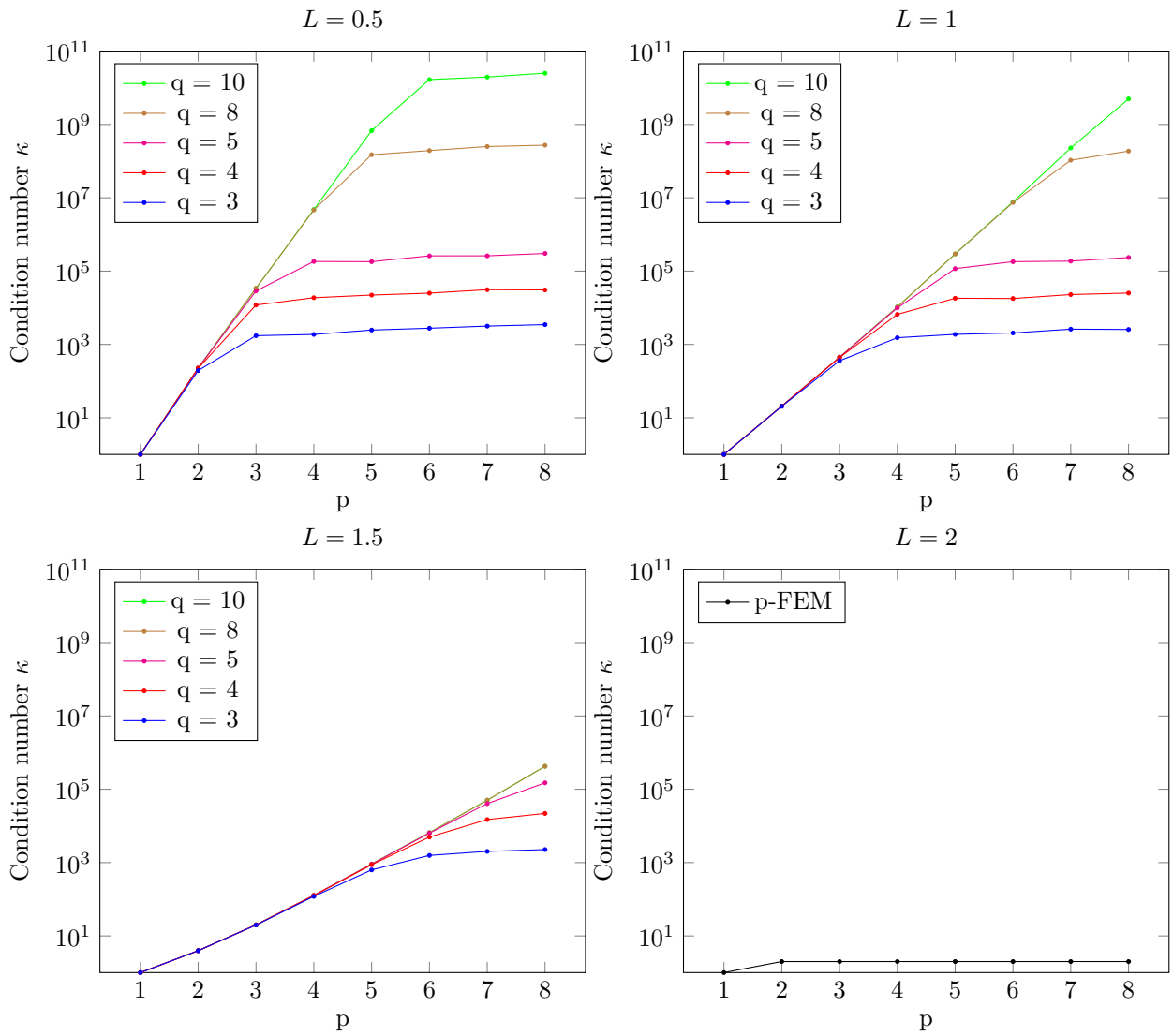
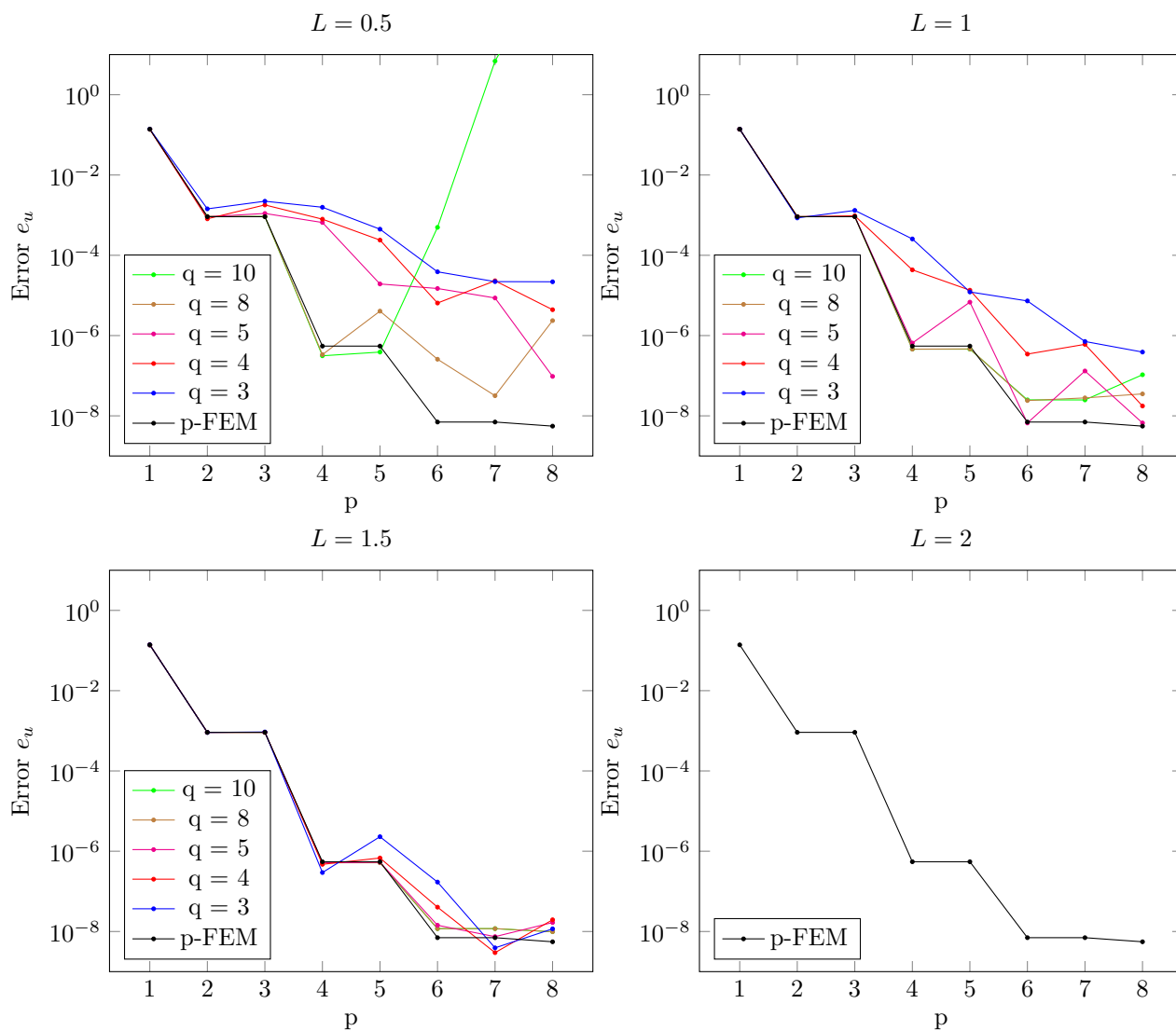


Figure 3.19: Comparison of the condition number for different volume fractions r_f .

Figure 3.20: Comparison of error in displacements for different volume fractions r_f .

Chapter 4

Numerical homogenization

Many engineering materials like cement concrete, metal foams or fiber reinforced materials possess a complicated microstructure which effects their macroscopic behavior. In order to take their heterogeneity into account we define effective material properties for such structures in a process termed *homogenization*.

Numerical homogenization methods in combination with the FCM are well suited to study microstructures. One reason for that is that their geometry can be efficiently obtained by computed tomography and a suitable discretization can be automatically derived from the CT data, see [63]. By this approach modifications of the microstructure, as in our case the application of a thin nickel coating on the struts of an aluminum foam as depicted in Fig. 4.1, can be investigated without performing experiments. Furthermore, the full multi-

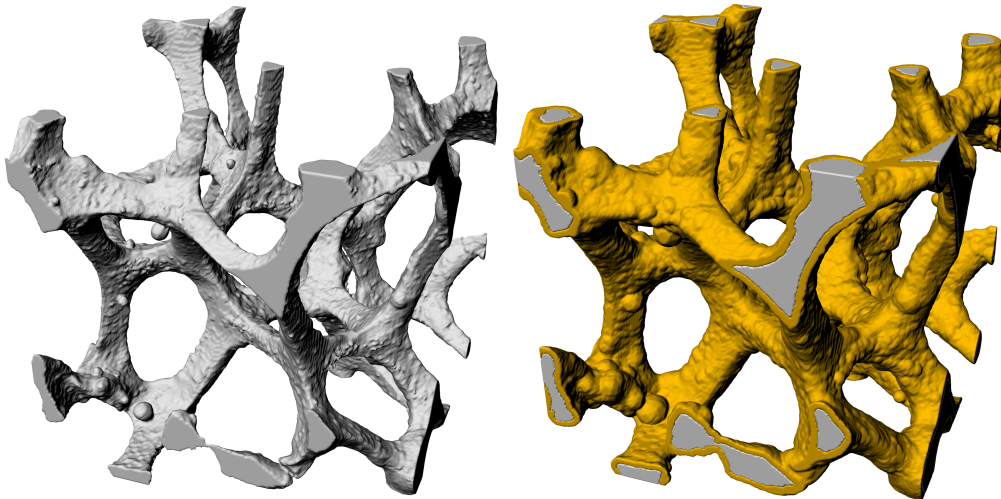


Figure 4.1: Aluminum foam and applied nickel coating.

axial properties, that are difficult to measure by experiments, can be predicted. In this chapter we first review the basic concepts of homogenization theory. For a deeper insight into theoretical aspects the reader is also referred to [51, 50]. Then a numerical homogenization method, based on the window method, see [24], is presented. Finally, we investigate the influence of a nickel coating on the homogenized effective properties of an aluminum foam.

4.1 Basic equations

In a sample of a composite material, taken far away from the boundary, where load gradients do not play a role, the stress and the strain field oscillate due to the presence of inhomogeneities around a constant mean. This means that they can be split additively into their average values $\langle \boldsymbol{\sigma} \rangle_m$, $\langle \boldsymbol{\varepsilon} \rangle_m$ and fluctuating parts $\boldsymbol{\sigma}'$, $\boldsymbol{\varepsilon}'$:

$$\boldsymbol{\sigma} = \langle \boldsymbol{\sigma} \rangle_m + \boldsymbol{\sigma}', \quad \boldsymbol{\varepsilon} = \langle \boldsymbol{\varepsilon} \rangle_m + \boldsymbol{\varepsilon}'. \quad (4.1)$$

In case of a linear elastic constitutive material behavior the *effective modulus (elasticity) tensor* \mathbf{C}^{eff} and the *effective compliance tensor* \mathbf{N}^{eff} are defined as relations between the volume averages of the stresses $\langle \boldsymbol{\sigma} \rangle_m$ and the strains $\langle \boldsymbol{\varepsilon} \rangle_m$:

$$\langle \boldsymbol{\sigma} \rangle_m = \mathbf{C}^{\text{eff}} \langle \boldsymbol{\varepsilon} \rangle_m, \quad \langle \boldsymbol{\varepsilon} \rangle_m = \mathbf{N}^{\text{eff}} \langle \boldsymbol{\sigma} \rangle_m. \quad (4.2)$$

In a geometrically nonlinear setting the same relations is given between the Piola-Kirchhoff stress tensor and its conjugated pair.

In order to obtain meaningful material parameters the volume average $\langle \cdot \rangle_m$ of the field variables, given by:

$$\langle \cdot \rangle_m = \frac{1}{V_m} \int_{V_m} (\cdot) dV_m, \quad (4.3)$$

needs to be computed over a representative sample of the microstructure, called the *representative volume element* (RVE). The existence of a RVE generally depends on the following two requirements, see [32, 12].

- *Separation of scales*

The size of a RVE must be large enough compared to the size of the coarsest heterogeneities, so that fluctuations in the stress and strain fields $\boldsymbol{\sigma}'$, $\boldsymbol{\varepsilon}'$ are small and small enough compared to the structural component, such that the applied loads on the RVE do not show a significant gradient.

- *Statistical uniformity*

The geometry of the RVE must have statistically the same features like topology, phase composition or phase contrast as any other sample taken from the structural component.

4.1.1 Average stress/ strain theorem

The *average strain*, respectively *average stress theorem* are frequently applied in the theory of homogenization. Their application allows to transform the volume integrals of the stress and strain tensor into surface integrals by applying the *divergence theorem*, also known as *Gauss theorem*. An important finding of this relation is that the average strain/stress in a given sample is completely defined in terms of the applied displacements/tractions at the boundary.

The small strain tensor can be expressed via the displacement gradient as follows:

$$\varepsilon_{ij} = \frac{1}{2} (u_{j,i} + u_{i,j}). \quad (4.4)$$

By taking the volume average we obtain, in case of a perfectly bonded material, the following surface integral:

$$\langle \varepsilon_{ij} \rangle_m = \frac{1}{V_m} \int_{V_m} \varepsilon_{ij} dV = \frac{1}{V_m} \int_{V_m} \frac{1}{2} (u_{j,i} + u_{i,j}) dV = \frac{1}{2V_m} \int_{\Gamma_m} (n_i u_j + n_j u_i) dA, \quad (4.5)$$

which reads in symbolic notation:

$$\langle \boldsymbol{\varepsilon} \rangle_m = \frac{1}{2V_m} \int_{\Gamma_m} (\mathbf{n} \otimes \mathbf{u} + \mathbf{u} \otimes \mathbf{n}) dA. \quad (4.6)$$

The averaged strains can be computed from the integral of the dyadic product of the displacements \mathbf{u} and the surface normals \mathbf{n} on the boundary. In order not to overload the notation the subscript m is omitted for the displacements and the surface normal. Particularly when prescribing displacements on the boundary of a given sample via the *macroscopic strain projection tensor* $\boldsymbol{\varepsilon}_P$

$$\mathbf{u}|_{\Gamma_m} = \boldsymbol{\varepsilon}_P \mathbf{x} \quad (4.7)$$

the average strain is directly given by $\langle \boldsymbol{\varepsilon} \rangle_m = \boldsymbol{\varepsilon}_P$.

The volume average of the stress tensor reads:

$$\langle \sigma_{ij} \rangle_m = \frac{1}{V_m} \int_{V_m} \sigma_{ij} dV. \quad (4.8)$$

In the absence of body forces, meaning $\sigma_{ij,i} = 0$, the following relation holds:

$$(\sigma_{ij} x_k)_{,i} = \sigma_{ij,i} x_k + x_{k,i} \sigma_{ij} = \delta_{ik} \sigma_{ij} = \sigma_{kj}. \quad (4.9)$$

By substituting Eq. (4.9) in Eq. (4.8) we can transform the volume integral into a surface integral through:

$$\frac{1}{V_m} \int_{V_m} \sigma_{kj} dV = \frac{1}{V_m} \int_{V_m} (\sigma_{ij} x_k)_{,i} dV = \frac{1}{V_m} \int_{\Gamma_m} n_i (\sigma_{ij} x_k) dA = \frac{1}{V_m} \int_{\Gamma_m} t_j x_k dA. \quad (4.10)$$

The same relation in symbolic notation reads:

$$\frac{1}{V_m} \int_{V_m} \boldsymbol{\sigma} dV = \frac{1}{V_m} \int_{\Gamma_m} \mathbf{t} \otimes \mathbf{x} dA. \quad (4.11)$$

Predefined tractions on the boundary of the domain can be applied via the *macroscopic stress projection tensor* $\boldsymbol{\sigma}_P$:

$$\mathbf{t}|_{\Gamma_m} = \boldsymbol{\sigma}_P \mathbf{n} \quad (4.12)$$

such that the average stress is directly given by $\langle \boldsymbol{\sigma} \rangle_m = \boldsymbol{\sigma}_P$.

4.1.2 Hill-Mandel condition

The linear displacement boundary conditions given in Eq.(4.7) or the linear traction boundary conditions given in Eq.(4.12) directly fulfill the *Hill-Mandel condition*:

$$\frac{1}{2} \langle \boldsymbol{\sigma}^T \boldsymbol{\varepsilon} \rangle_m = \frac{1}{2} \langle \boldsymbol{\sigma} \rangle_m \langle \boldsymbol{\varepsilon} \rangle_m . \quad (4.13)$$

The Hill-Mandel condition ensures the equivalence of the average of strain energy density of the macroscopic and microscopic variables and makes the microscopic and macroscopic descriptions energetically equivalent, see [51].

4.1.3 Voigt-Reuss bounds

Computing the effective material tensors by a numerical method requires to solve a boundary value problem on a finite sized sample of the material by either applying linear displacement boundary conditions via Eq. (4.7) or traction boundary conditions via Eq. (4.12). By imposing Dirichlet (displacement) boundary conditions the average strain is known and the average stress in the body can be computed in the post-processing step. Differentiating the average stress with respect to the applied average strain yields the effective elasticity tensor. The same procedure can be followed when traction boundary conditions are applied. For a representative volume element both ways are equivalent. In case a scale separation is not given, and the stress and strain field show large fluctuations on the boundary of the analyzed sample these two types of boundary conditions deliver upper (Voigt) and lower (Reuss) bounds for the real effective properties. Such properties are then called *apparent material properties* and the corresponding analyzed sample is the called *testing volume element* (TVE) [33, 79].

4.2 The window method

For highly heterogeneous materials the computation of the effective material properties of a representative volume element involves a large sample and requires a high computational effort. So the analysis of such structures is often restricted to smaller testing volume elements, where the choice of boundary conditions has a large impact on the results. A method to lower this influence is the *window method* [24, 71]. The idea of this method is to embed the TVE into a homogeneous domain (window) and apply displacement boundary conditions to the surface of the window as shown in Fig. 4.2. By this approach the influence of the boundary conditions on the results is reduced and tighter bounds for the effective properties are obtained, see [71]. The window models the infinite surrounding that a real RVE would be surrounded by, and has to have the same effective material properties as the embedded microstructure. This idea is known from analytical homogenization schemes and called *self-consistency*, see [79].

The window material has a large influence on the computed effective properties and is unknown at the beginning of the computations. Therefore it is determined from the effective material properties of the embedded microstructure in an iterative procedure, see Fig. 4.3. In the following we will explain the window method in detail.

In case of an anisotropic material the computation of all components of the elasticity tensor requires to solve six linear independent loadcases $j = 1, \dots, 6$. By every loadcase one column of the elasticity matrix can be determined. To this end, we define the macroscopic small strain

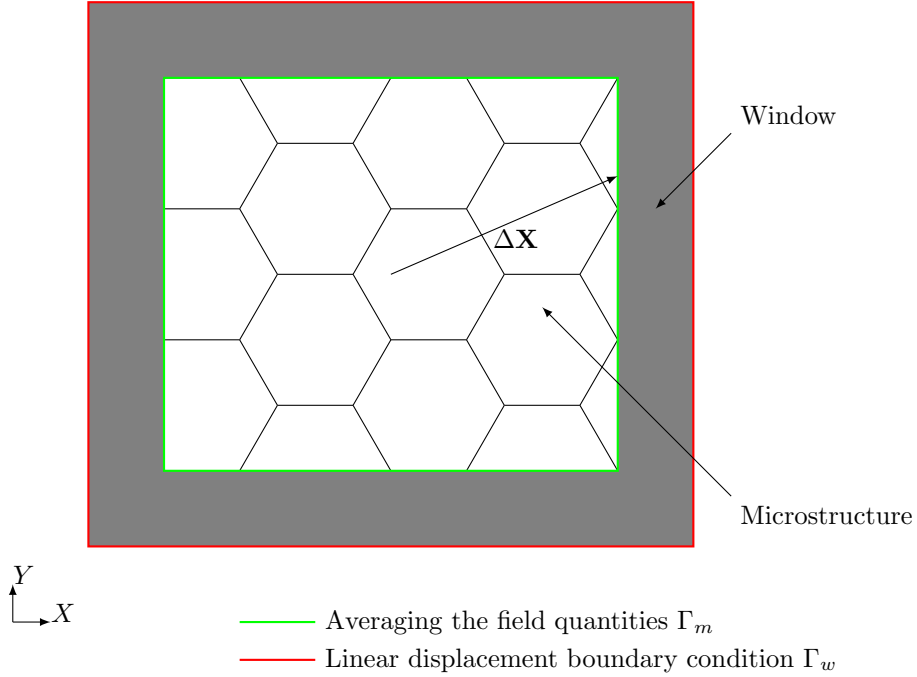


Figure 4.2: The window with embedded microstructure.

projection tensor $\boldsymbol{\varepsilon}_P$ and disturb a single component in each loadcase by a small increment. The related displacements $\Delta \bar{\mathbf{u}}$ are then imposed on the surface of the window Γ_w via the projection rule:

$$\Delta \bar{\mathbf{u}}_j = \boldsymbol{\varepsilon}_P \Delta \mathbf{X}, \quad (4.14)$$

where $\Delta \mathbf{X}$ is the branch vector that points from the center of the TVE to the location of the applied displacements. After solving the mechanical problem, the averaged stresses $\langle \boldsymbol{\sigma} \rangle_m$ and strains $\langle \boldsymbol{\varepsilon} \rangle_m$ are computed in a post-processing step. Taking advantage of the average stress and strain theorem given in Eq. (4.5) and (4.10), we only need to evaluate the surface integral over the boundary of the microstructure Γ_m . In order to average the stress field, we use the discrete form of Eq. (4.10) given by:

$$\langle \boldsymbol{\sigma} \rangle_m = \frac{1}{V_m} \sum_{i=1}^{n_{nodes}} \mathbf{r}_m^{(i)} \otimes \Delta \mathbf{X}^{(i)}. \quad (4.15)$$

Due to the *partition of unity* we can compute the average stress by summing up the dyadic product \otimes of the nodal forces $\mathbf{r}_m^{(i)}$ and the corresponding branch vector $\Delta \mathbf{X}^{(i)}$ of all nodes n_{nodes} located on the surface Γ_m of the spatial discretization of the microstructure. The computation of the average stress in Eq. (4.15) might yield an unsymmetric stress tensor which is therefore symmetrized in a subsequent step.

The averaged strains are computed using the discrete form of Eq. (4.5) given by:

$$\langle \boldsymbol{\varepsilon} \rangle_m = \frac{1}{2V_m} \sum_{i=1}^{n_{nodes}} (\mathbf{u}_m^{(i)} \otimes \mathbf{n}_m^{(i)} + \mathbf{n}_m^{(i)} \otimes \mathbf{u}_m^{(i)}) A_m^{(i)}, \quad (4.16)$$

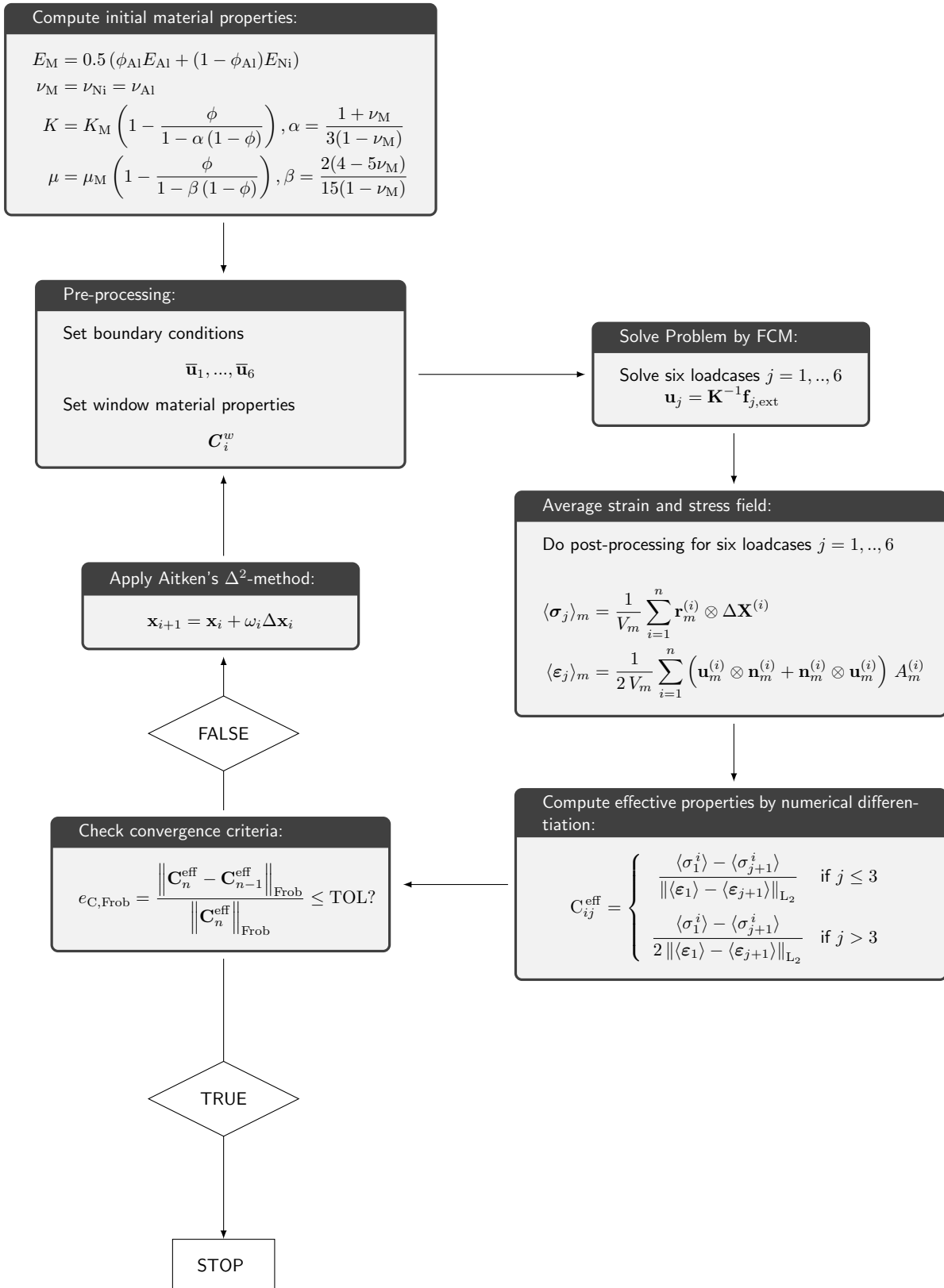


Figure 4.3: The homogenization procedure.

where $\mathbf{u}_m^{(i)}$ are the nodal displacements and $\mathbf{n}_m^{(i)}$ the surface normal vector. In Eqs. (4.15) and (4.16) V_m represents the volume of the microstructure and $A_m^{(i)}$ denotes the area associated with node (i) on the surface of the FCM mesh, see Fig. 4.4. In order to have a unique definition of the unit normal vector we consider edge nodes twice and corner nodes three times together with their associated areas and unit normal vectors. After solving a loadcase one column

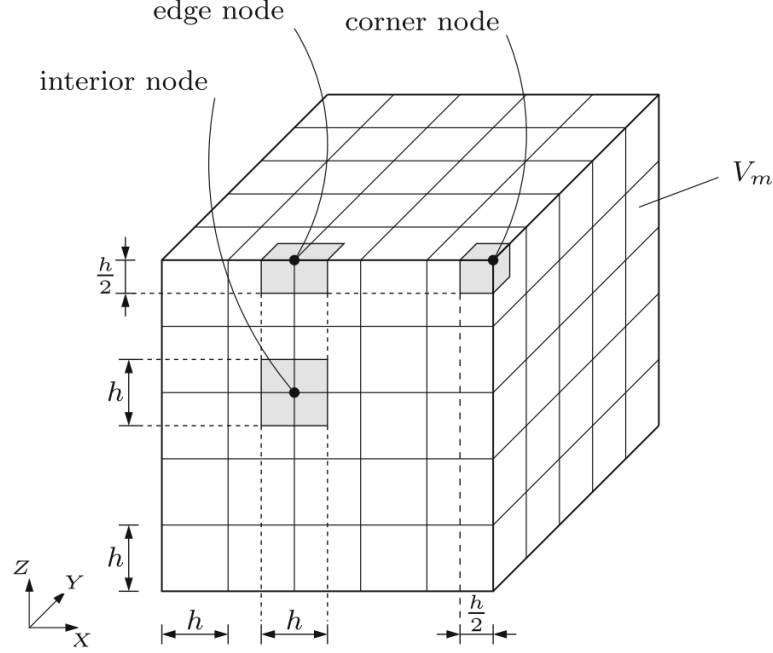


Figure 4.4: Equidistant surface mesh with cell size h . Gray-shaded areas denote $A_m^{(i)}$ [18].

of the effective elasticity matrix \mathbf{C}^{eff} is obtained by numerical differentiation of the averaged stress quantities with respect to the related applied macroscopic strains. Applying the Voigt notation for the strains and stresses this procedure reads:

$$C_{ij}^{\text{eff}} = \begin{cases} \frac{\langle \sigma_1^i \rangle - \langle \sigma_{j+1}^i \rangle}{\| \langle \boldsymbol{\varepsilon}_1 \rangle - \langle \boldsymbol{\varepsilon}_{j+1} \rangle \|_{L_2}} & \text{if } j \leq 3 \\ \frac{\langle \sigma_1^i \rangle - \langle \sigma_{j+1}^i \rangle}{2 \| \langle \boldsymbol{\varepsilon}_1 \rangle - \langle \boldsymbol{\varepsilon}_{j+1} \rangle \|_{L_2}} & \text{if } j > 3 \end{cases}, \quad (4.17)$$

where i corresponds to the stress component and $j = 1, \dots, 6$ denotes the corresponding load case. The basic load case is denoted by index 1 and can be related to a case with no loads.

In order to obtain a symmetric elasticity matrix we again symmetrize \mathbf{C}^{eff} . In order to adjust the window material in a self-consistent way, the elasticity matrix of the window \mathbf{C}^w is updated for the next iteration by the actual computed effective properties [18], see Fig. 4.3. The iterative procedure can be accelerated by the *Aitken's* Δ^2 -method which will be explained in the next subsection. The iterative procedure is considered to be converged when the difference between the effective properties of two consecutive steps falls below a prescribed tolerance $e_{C, \text{Frob}} \leq TOL$ in terms of the *Frobenius* norm:

$$e_{C, \text{Frob}} = \frac{\| \mathbf{C}_n^{\text{eff}} - \mathbf{C}_{n-1}^{\text{eff}} \|_{\text{Frob}}}{\| \mathbf{C}_n^{\text{eff}} \|_{\text{Frob}}}. \quad (4.18)$$

Readers that are interested in the convergence properties of this iterative procedure are referred to [57].

4.2.1 Acceleration of the window method

The window method updates the material properties of the window in each iteration step which results in a sequence S of effective material properties:

$$S = \{ \mathbf{C}_0^{\text{eff}}, \mathbf{C}_1^{\text{eff}}, \dots, \mathbf{C}_{n-1}^{\text{eff}}, \mathbf{C}_n^{\text{eff}} \}, \quad (4.19)$$

where n is the number of iterations needed to obtain the converged solution. In order to increase the rate of convergence of this iterative procedure we use the *Aitken's* Δ^2 -method [46, 43]. The idea of the Aitken's method is to compute modified effective material properties \mathbf{C}_{i+1} and assign them to the window material instead of directly using the effective material properties from the previous iteration \mathbf{C}_i . In the following we will briefly explain the acceleration procedure which reads as follows:

$$\mathbf{C}_{i+1}^{\text{eff}} = \mathbf{C}_i^{\text{eff}} + \omega_i \Delta \mathbf{C}_i^{\text{eff}}. \quad (4.20)$$

In Eq. (4.20) the relaxation coefficient ω_i is computed based on the results of the three previous consecutive iterations $\mathbf{C}_i^{\text{eff}}, \mathbf{C}_{i-1}^{\text{eff}}, \mathbf{C}_{i-2}^{\text{eff}}$:

$$\omega_i = - \frac{(\mathbf{C}_i^{\text{eff}} - \mathbf{C}_{i-1}^{\text{eff}}) : (\Delta \mathbf{C}_i^{\text{eff}} - \Delta \mathbf{C}_{i-1}^{\text{eff}})}{(\Delta \mathbf{C}_i^{\text{eff}} - \Delta \mathbf{C}_{i-1}^{\text{eff}}) : (\Delta \mathbf{C}_i^{\text{eff}} - \Delta \mathbf{C}_{i-1}^{\text{eff}})}. \quad (4.21)$$

There are different possibilities to compute $\Delta \mathbf{C}_i^{\text{eff}}$ and $\Delta \mathbf{C}_{i-1}^{\text{eff}}$ either based on the modified (accelerated) or unmodified (standard) values. We compute these values based on the standard values:

$$\Delta \mathbf{C}_i^{\text{eff}} = \mathbf{C}_i^{\text{eff}} - \mathbf{C}_{i-1}^{\text{eff}}, \quad \Delta \mathbf{C}_{i-1}^{\text{eff}} = \mathbf{C}_{i-1}^{\text{eff}} - \mathbf{C}_{i-2}^{\text{eff}}. \quad (4.22)$$

In order to further accelerate the iterative procedure we use an improved initial value for the effective material properties of the window instead of taking the bulk value from one of the two materials. To this end we apply different analytical homogenization schemes, also known as the *rule of mixtures*.

An improved starting value for the nickel-coated aluminum foam can be computed in two steps as follows: First, we assume that the hybrid metal foam includes no voids and use the average of *Voigt's* and *Reuss's* model [79] to compute a homogenized Young's modulus E_M by:

$$E_M = 0.5 (\phi_{\text{Al}} E_{\text{Al}} + (1 - \phi_{\text{Al}}) E_{\text{Ni}}), \quad \nu_M = \nu_{\text{Ni}} = \nu_{\text{Al}}, \quad (4.23)$$

where ϕ_{Al} and $\phi_{\text{Ni}} = (1 - \phi_{\text{Al}})$ denote the volume fractions of aluminum and nickel, respectively. The Young's modulus and Poisson's ratio of aluminum and nickel are labeled by their according indices.

The corresponding bulk K_M and shear modulus μ_M can be easily computed using the Young's modulus E_M and the Poisson ratio ν_M by:

$$K_M = \frac{E_M}{3(1 - 2\nu_M)}, \quad \mu_M = \frac{E_M}{2(1 + \nu_M)}. \quad (4.24)$$

In a second step we apply the *Mori-Tanaka* model [23] that takes into account the effect of pores on the bulk modulus K and the shear modulus μ :

$$\begin{aligned} K &= K_M \left(1 - \frac{\phi}{1 - \alpha(1 - \phi)} \right), & \alpha &= \frac{1 + \nu_M}{3(1 - \nu_M)} \\ \mu &= \mu_M \left(1 - \frac{\phi}{1 - \beta(1 - \phi)} \right), & \beta &= \frac{2(4 - 5\nu_M)}{15(1 - \nu_M)}, \end{aligned} \quad (4.25)$$

where ϕ is the volume fraction of the pores. Based on K and μ , the elasticity matrix for the window is computed accordingly as an improved starting value for the window method.

4.3 Hybrid metal foams

Aluminum metal foam can be optimized with respect to its stiffness and its energy absorption capacity by applying a thin nickel coating. In this section we analyze the influence of the coating thickness on the effective properties of aluminum foams utilizing the window method. To this end, we investigate the accuracy of the spatial discretization and the use of Aitken's method on the homogenization procedure in a preliminary study before we finally examine the coating thickness. All microstructures investigated in this section are obtained from a μ CT-scan with a resolution of $h_v = 24 \mu\text{m}$ of a 30 pores per inch (ppi) aluminum foam. The coating is applied numerically by adding additional voxels to the surface of the geometry.

4.3.1 Preliminary study

The microstructure for the preliminary study is a cubic sample with an edge length of 5.76 mm and a coating thickness of as depicted in Fig. 4.5.

4.3.1.1 Accuracy of the spatial discretization

In order to analyze the influence of the spatial discretization in terms of h - and p -refinement on the homogenized effective properties of the hybrid metal foam three different discretizations are created. Each discretization includes a different number of voxels in every cell $NVC \in \{4, 8, 16\}$. In Fig. 4.6 the discretization with $NVC = 8$ and the corresponding octree used for the numerical quadrature are depicted. The interface between the nickel coating and the aluminum foam, that induces a jump in the material properties, is not resolved by the finite cell mesh but considered by an adaptive octree integration scheme. Fig. 4.7 shows the influence of the different types of discretization on the effective properties. From this it is evident that both types of refinement, i.e. h and p , yield a similar convergence behavior for the effective material properties for $p \geq 2$. The rate of convergence of the p -refinement, which normally shows superior convergence behavior, is reduced due to the material interface of the hybrid metal foam that is not resolved explicitly by cell boundaries. Due to the material interfaces, the displacement field exhibits a kink at the material interface – which can be considered as a weak discontinuity [22]. If this discontinuity is located within the cell and is not resolved – as in this example – then the approximation may exhibit oscillations at the material interface and the convergence rate reduces accordingly [34, 35]. In addition, the voxel model is a low-order representation of the geometry, introducing singularities like re-entrant corners. This low-order

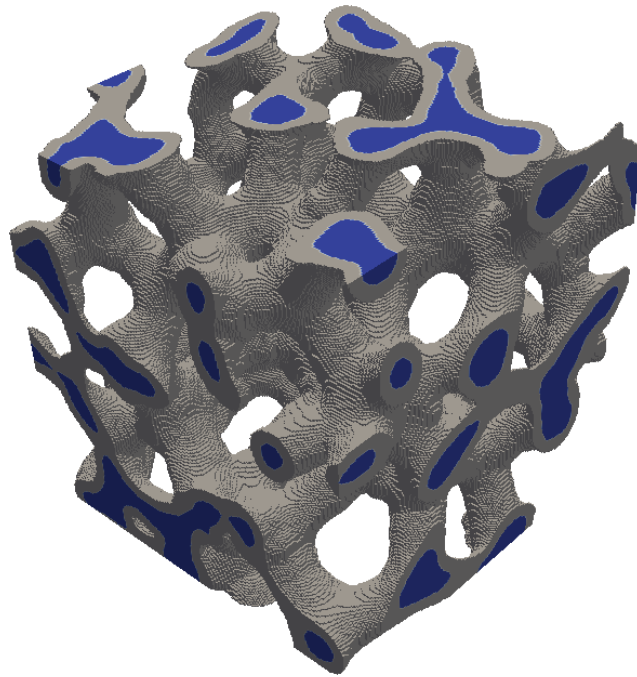
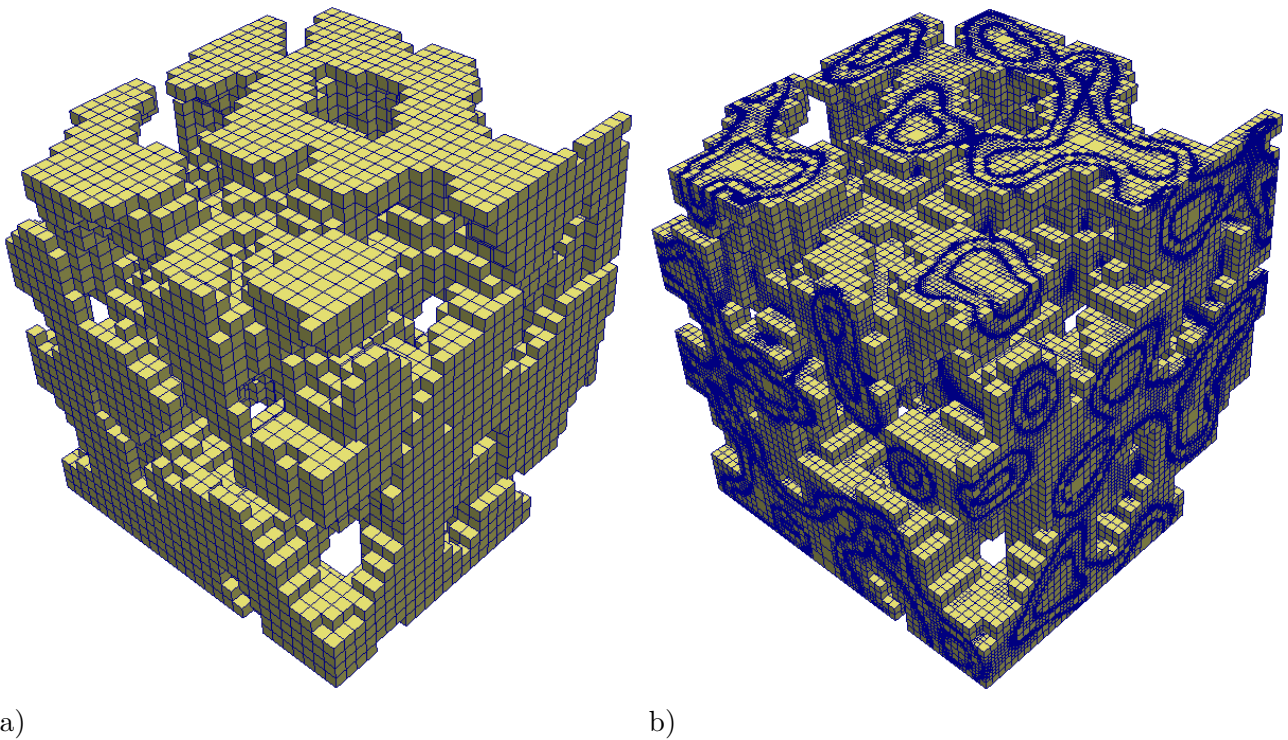


Figure 4.5: Cubic TVE ($5.76 \text{ mm} \times 5.76 \text{ mm} \times 5.76 \text{ mm}$) of a hybrid metal foam used to investigate the influence of an h - and p -refinement.



a)

b)

Figure 4.6: a) Discretization with 12,706 cells ($NVC = 8$) and b) the corresponding sub-cells generated for octree integration.

representation of the geometry can also have a considerable effect on the performance of the p -refinement. For approximately two million degrees of freedom, both refinement strategies

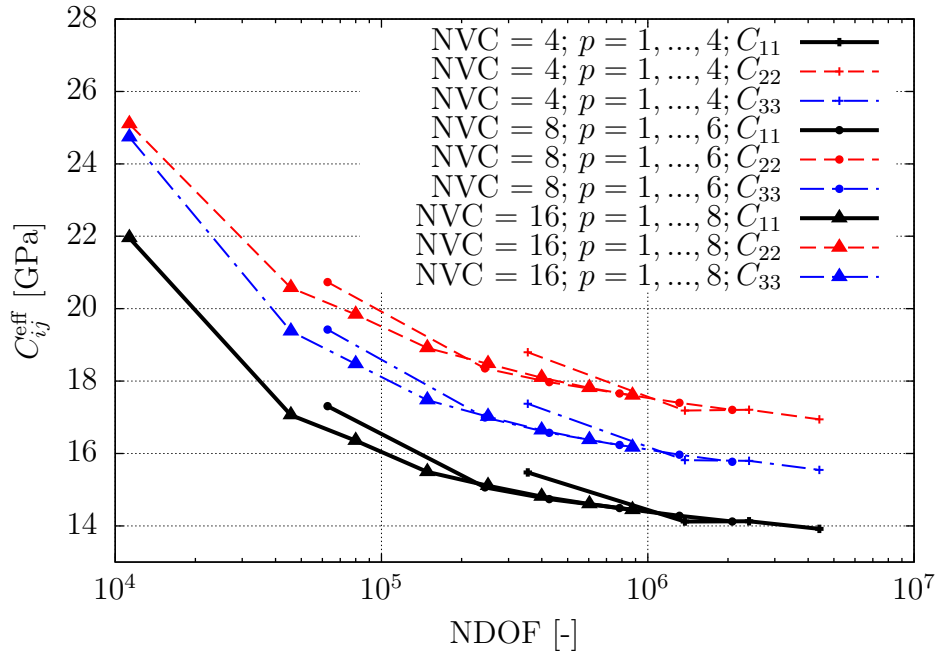


Figure 4.7: Degrees of freedom.

yield a level of accuracy that is reasonable for engineering purposes. In terms of the number of Gauss points the discretization with $p = 2$ and $NVC = 4$ seems to be the most efficient discretization, see Fig. 4.8. Based on this result, we choose a discretization with $NVC = 4$ and $p = 2$ for the following examples.

4.3.1.2 Acceleration of the window method

In this section, we study the effect of the Aitken's acceleration method on the rate of convergence of the effective properties obtained by the window method. To this end, we consider the TVE depicted in Fig. 4.5 and compute a series of effective properties. The method is considered to be converged when the difference between two consecutive results in terms of the Frobenius norm, given by Eq. (4.18), is less than $TOL = 10^{-3}$.

In a first test no acceleration technique is applied and the initial material parameters are the bulk values of nickel and aluminum, respectively. In the second computation, Aitken's method is used while the starting values are the same compared to the first example. In the third computation, we finally combine both methods; meaning that we start from an improved initial value for the effective properties obtained by the analytical homogenization scheme proposed in the Section 4.2.1 and use Aitken's method as well.

Improved initial values are obtained by assuming that the TVE contains no pores and using a combination of *Voigt's* and *Reuss's* model given by Eq. (4.23). The material parameters used in this equation are the Young's modulus of aluminum $E_{Al} = 70$ GPa and nickel $E_{Ni} = 200$ GPa and the common Poisson's ratio $\nu = 0.3$ together with the volume fraction of both materials

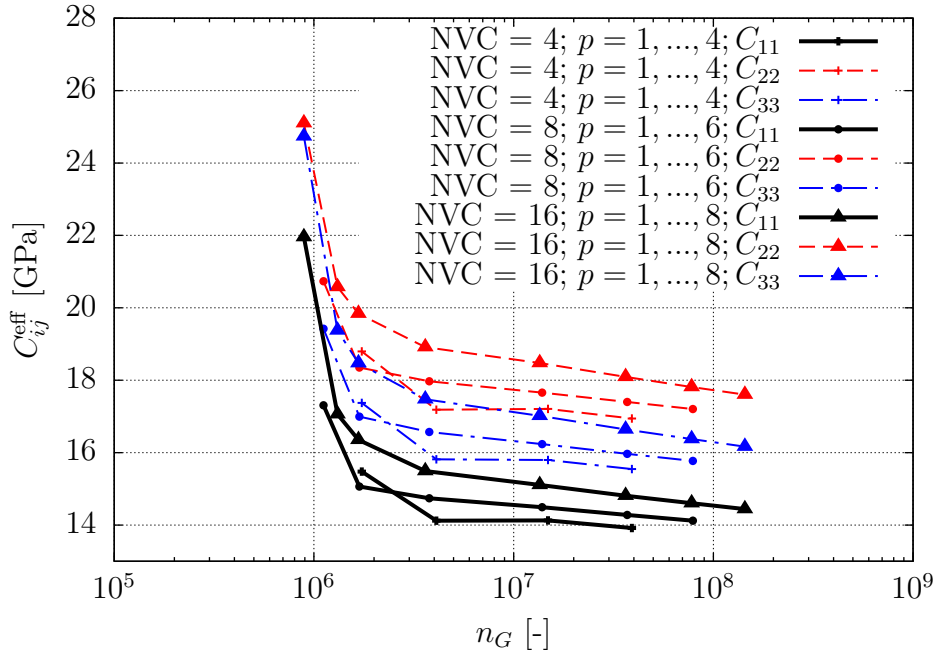


Figure 4.8: Number of Gauss points.

$\phi_{\text{Ni}} = 0.63$ and $\phi_{\text{Al}} = 0.37$. In a second step, the effect of the pores is taken into account by applying the *Mori-Tanaka* model in Eq. (4.25) with $\phi = 0.68$.

Fig. 4.9 compares the three different methods in terms of the error given by:

$$e_{ij,\text{rel}} = \left| \frac{C_{ij}^{\text{eff}} - C_{ij}^{\text{eff,Ref}}}{C_{ij}^{\text{eff,Ref}}} \right| \times 100, \quad (4.26)$$

where $C_{11}^{\text{eff,Ref}} = 13.876$ GPa corresponds to the converged value of the standard window method. Aitken's method lowers the required number of iterations by one. Employing the acceleration procedure with an improved initial value even reduces the number of iterations by three. In practical applications $e_{C,\text{Frob}} = 10^{-3}$ is a rather sharp stopping criterion, especially when we look at the convergence of the components of the elasticity matrix. Considering an error of one percent as sufficiently accurate, the window method needs approximately two iterations to converge.

4.3.2 Influence of the coating thickness

In this section we study the influence of the coating thickness on the effective properties of a 30 pores per inch (ppi) aluminum foam. The extracted TVE depicted in Fig. 4.10a) was obtained by a μCT -scan with a resolution of $h_v = 24 \mu\text{m}$. It has a cubic shape with the dimensions of $9.6 \text{ mm} \times 9.6 \text{ mm} \times 9.6 \text{ mm}$. In order to investigate the effect of a coating six different layers are numerically applied to the voxel model. Each layer has a constant thickness over the entire model and is defined in terms of voxels ($t = 2, 4, 6, 8, 10, 12$ voxels). Fig. 4.10b) shows the aluminum foam with a coating of $t = 6$ voxels. The discretization of the problem, see Fig. 4.11, is such that a finite cell includes $\text{NVC} = 4$ voxels and the order of the shape functions

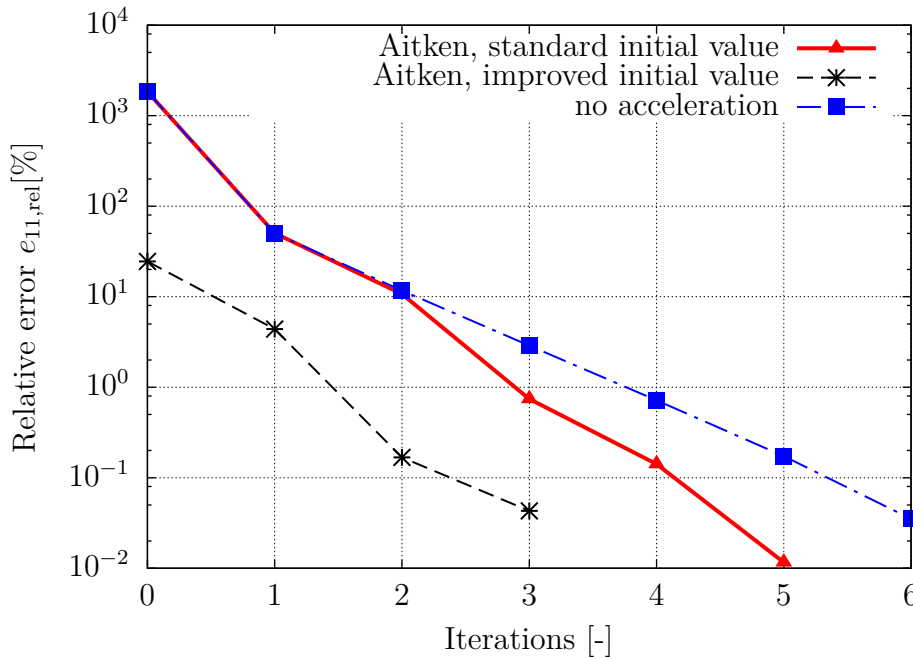


Figure 4.9: Comparison of the rates of convergence.

is $p = 2$. These discretization parameters are the same as the optimal values found based on the previous calculations in this section. Compared to an FEM voxel model in which each voxel is discretized by one finite element this discretization approach leads to a significantly lower number of cells. As an example, for $t = 10$ we discretize 23 million voxels by 496,805 cells and 6,627,596 degrees of freedom.

The influence of the displacement boundary conditions on the effective properties depends on the size of the window $t_{W_{in}}$. In a first step, we study the influence of its size on the results. To this end, the foam is coated by a thin nickel layer of $t = 2$ voxels i.e. $48 \mu\text{m}$ and the size of the window is increased from $t_{W_{in}} = 0.24 \text{ mm}$ to $t_w = 1.92 \text{ mm}$. Fig. 4.12 depicts the effective properties obtained for different sizes of the window. For $t_w \geq 0.92$, the influence of the window size on the effective properties vanishes.

The distance to the boundary is unknown in our setting. Therefore we choose $t_w = 0.48 \text{ mm}$ for the following investigations and assess the effect of the coating thickness on the effective properties. Fig. 4.13 shows the influence of the layer thickness on the effective properties \mathbf{C}^{eff} . As expected, the coating leads to an increase of stiffness – as can be clearly seen in Figure 4.13.

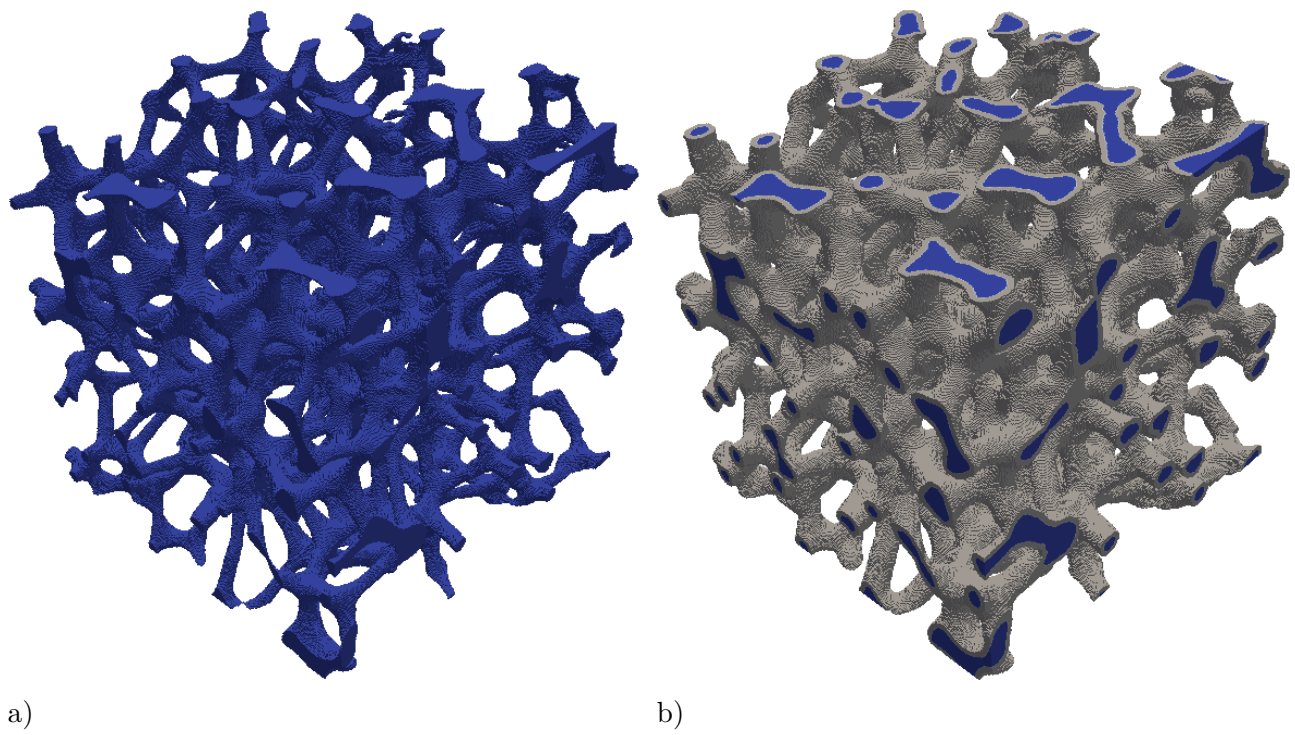


Figure 4.10: a) Aluminum foam and b) the same foam with a coating with $t = 6$ voxel.

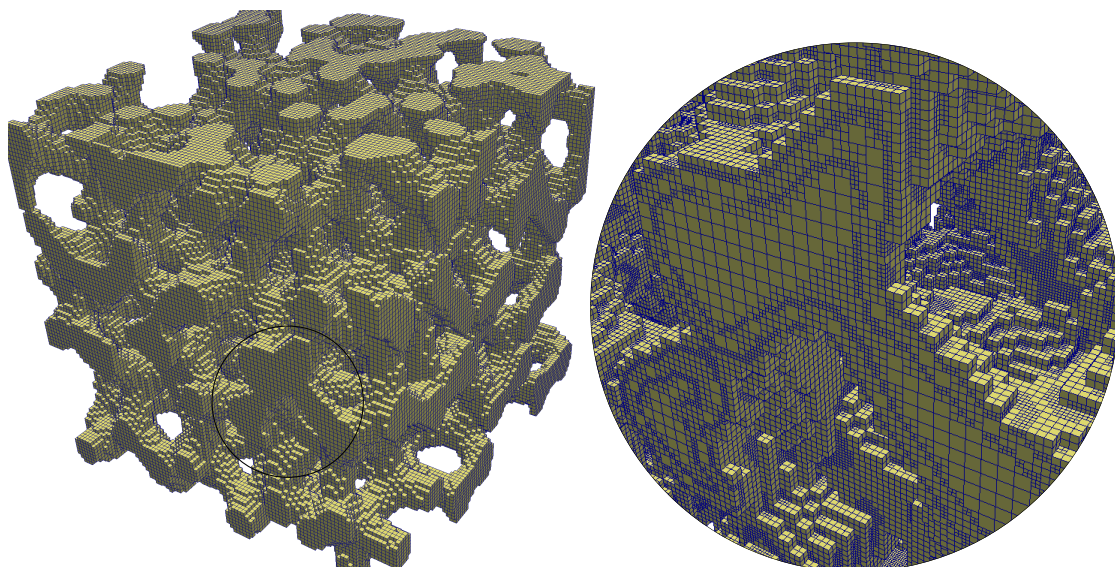


Figure 4.11: Finite cell discretization for $t = 6$ and the sub-cells generated during the octree integration.

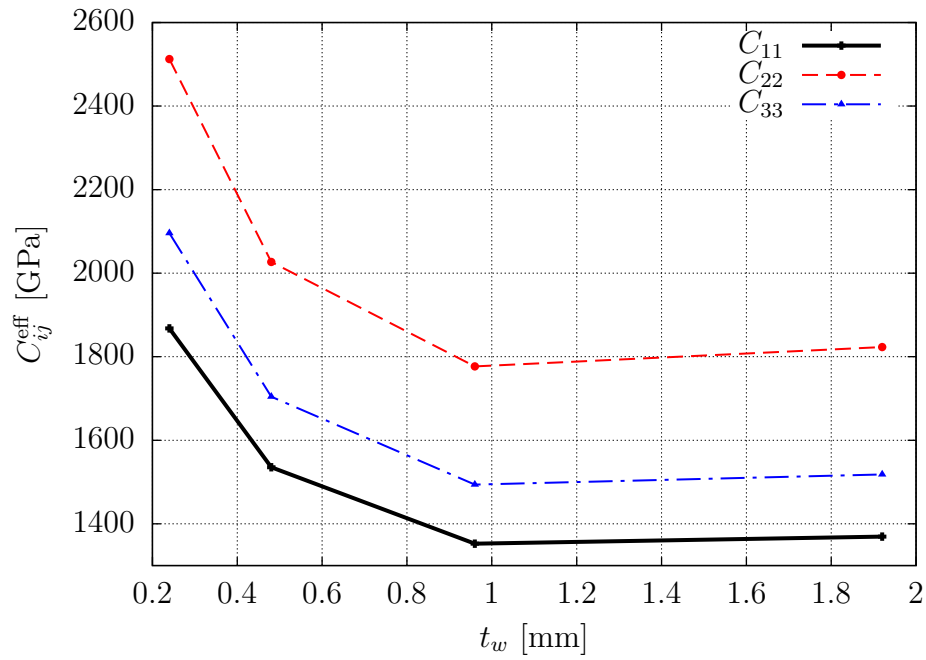
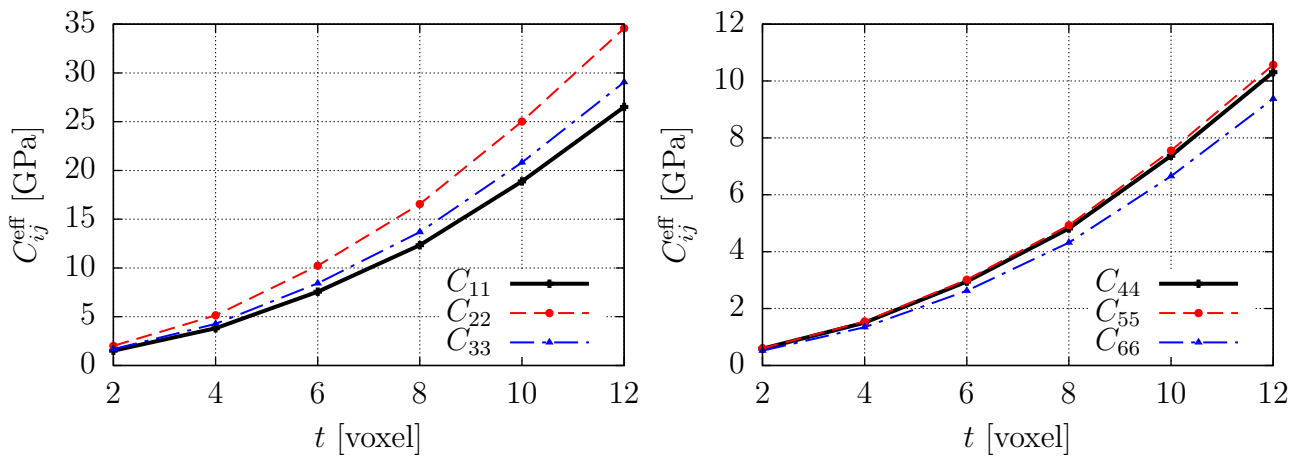


Figure 4.12: Influence of the window size on the effective properties.



a)

b)

Figure 4.13: a) and b) show the change of several components of the elasticity matrix as a result of the coating.

Chapter 5

Computational contact mechanics

The solution of contact problems is of great importance in many engineering disciplines. Some well-known examples are crash or deep drawing simulations. In the context of this work contact plays an essential role in the analysis of metal foams under compressive loading. During the densification process the struts of collapsed pores come into contact and due to this the slope of the stress-strain curve increases.

While the contact problem has been intensively studied by means of the finite element method [72, 45, 44] and various types of formulations have been developed based on the type of the contact condition, the type of the discretization and its enforcement, the solution of contact problems within the finite cell method is a recent research area.

A first approach that links the contact problem with the FCM is presented in [13]. It is based on utilizing the fictitious domain with changing material properties in order to enforce the contact conditions. In [41] a contact approach for the FCM based on an additional discretization of the contact interface is presented. This approach was recently extended by [14], with an adaptive local refinement technique based on the multi-level *hp*-method in order to remove oscillations induced by the singularity at the end of the contact interface.

In this chapter a similar approach for *frictionless*- and *sticking contact* is introduced and investigated in the following. In order to derive a contact formulation for the finite cell method we first summarize the basic kinematic relations. Subsequently we present the contact enforcement in the weak form by means of the penalty method and we also derive the linearization of these equations. The formulation is similar to the finite element formulation and interested readers are referred to the textbooks of Wriggers [72] and Konyukhov et al.[41] to obtain a deeper insight into the underlying theory.

5.1 Contact kinematics

We consider the contact problem between two bodies denoted by B^γ with $\gamma \in \{m, s\}$, that come into contact at a common interface $\Gamma_C = \varphi(\Gamma_C^m) = \varphi(\Gamma_C^s)$ as illustrated in Fig. 5.1. In order to find the potential common contact interface we need to find the minimum distance between the bodies. To this end we assume that a parametrization of the contact surfaces is given via the mapping function $\mathbf{x}^\gamma(\boldsymbol{\alpha})$, where $\boldsymbol{\alpha} = [\alpha, \beta]^T$ denotes the convective surface coordinate. To find the closest distance between the bodies we make use of the *master-slave* concept. Discrete points \mathbf{x}^s – the so-called *slave points* – are distributed over the slave surface

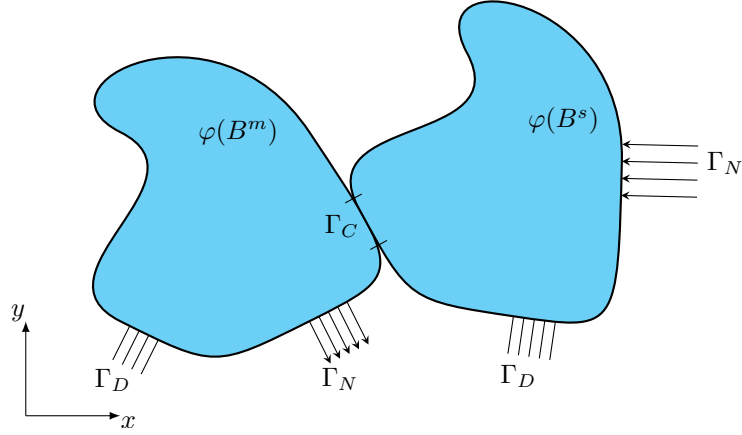


Figure 5.1: Contact of two bodies.

$\gamma = s$ and their minimum distance to the master surface $\mathbf{x}^m(\boldsymbol{\alpha})$ is computed by solving the following equation:

$$d = \min \|\mathbf{x}^s - \mathbf{x}^m(\boldsymbol{\alpha})\| = \|\mathbf{x}^s - \bar{\mathbf{x}}^m\| . \quad (5.1)$$

The solution of Eq. (5.1) – $\bar{\boldsymbol{\alpha}}$ – can be computed by solving the following equation system:

$$\begin{bmatrix} (\mathbf{x}^s - \mathbf{x}^m(\boldsymbol{\alpha})) \cdot \mathbf{x}_{,\alpha}^m \\ (\mathbf{x}^s - \mathbf{x}^m(\boldsymbol{\alpha})) \cdot \mathbf{x}_{,\beta}^m \end{bmatrix} = \mathbf{0} , \quad (5.2)$$

and is given by the orthogonal projection of the slave points onto the master surface. Here and in the following a bar over a quantity will denote its evaluation at this point.

The tangential surface vectors of the contact interface $\mathbf{x}_{,\alpha}^m, \mathbf{x}_{,\beta}^m$ are obtained by computing the derivative of the surface mapping function with respect to the convective coordinate. Together with the surface normal:

$$\mathbf{n}^m = \frac{\mathbf{x}_{,\alpha}^m \times \mathbf{x}_{,\beta}^m}{\|\mathbf{x}_{,\alpha}^m \times \mathbf{x}_{,\beta}^m\|} \quad (5.3)$$

they form a convective coordinate system that is used to describe the contact interaction locally, see Fig. 5.2. The assignment of master and slave surface is arbitrary. Normally the body with the finer discretization is chosen to be the slave surface. Of course, in the case of self-contact or large deformations master and slave surfaces can not be assigned in advance, because the contact interfaces are not initially known.

Points on the master and slave surface are not allowed to penetrate, so the non-penetration condition, given by the following local kinematical relation, must hold:

$$g_N = (\mathbf{x}^s - \bar{\mathbf{x}}^m(\boldsymbol{\alpha})) \cdot \bar{\mathbf{n}}^m \geq 0 , \quad (5.4)$$

where g_N is the normal gap between the two points and $\bar{\mathbf{n}}^m$ is the normal of the master surface evaluated at $\bar{\boldsymbol{\alpha}}$. The penalty method incorporates the constraint given by Eq. (5.4) by penalizing any penetration by the penalty parameter β and enforces the contact conditions

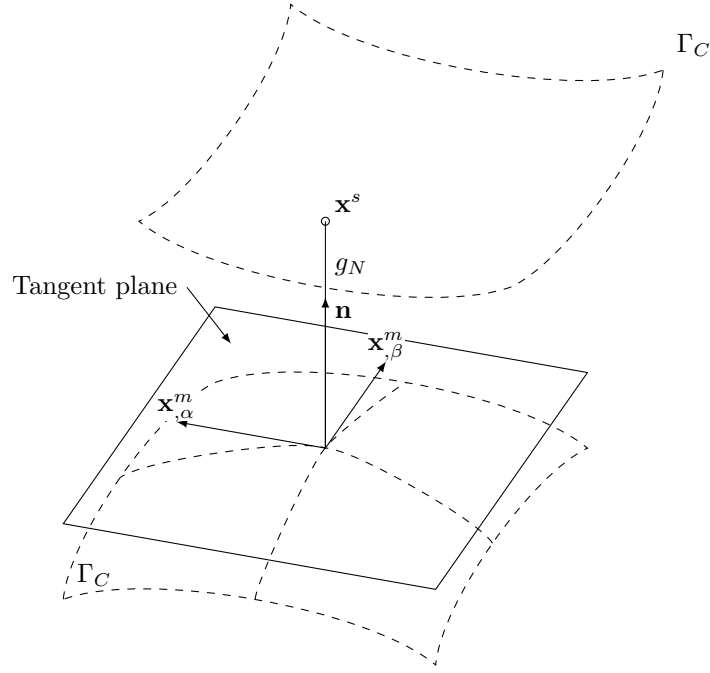


Figure 5.2: Kinematic quantities of the contact surface.

only approximately for $\beta < \infty$. For frictionless contact problems we therefore define the normal gap function:

$$g_N = \begin{cases} (\mathbf{x}^s - \bar{\mathbf{x}}^m) \cdot \bar{\mathbf{n}}^m & \text{if } (\mathbf{x}^s - \bar{\mathbf{x}}^m(\boldsymbol{\alpha})) \cdot \bar{\mathbf{n}}^m < 0 \\ 0 & \text{otherwise} \end{cases} . \quad (5.5)$$

When the contact surfaces stick together (sticking contact) at the point where they contact first $\bar{\boldsymbol{\alpha}}^0$, no relative movement of the contact interfaces is allowed. Therefore we define the total gap function \mathbf{g}_{St} which penalizes the total relative movement:

$$\mathbf{g}_{St} = \begin{cases} (\mathbf{x}^s - \mathbf{x}^m(\boldsymbol{\alpha}^0)) & \text{if } (\mathbf{x}^s - \mathbf{x}^m(\boldsymbol{\alpha}^0)) \cdot \bar{\mathbf{n}}^m < 0 \\ \mathbf{0} & \text{otherwise} \end{cases} . \quad (5.6)$$

5.1.1 Linearization and variation of the gap function

In this section we briefly repeat the linearization and the variation of the gap function for frictionless and sticking contact that are essential for the linearization of the weak form. For more detailed information the textbooks of Wriggers [72] and Konyukhov et al. [41] are recommend.

Frictionless contact

In frictionless contact conditions the normal penetration g_N of the slave points with the master surface is constrained but the tangential sliding on the master surface is allowed. Therefore the change of the contact location as well as the change of the surface coordinate system has to be taken into account when linearizing the penetration function.

The full time derivative of the normal gap function is given by:

$$\Delta g_N = \Delta \{(\mathbf{x}^s - \bar{\mathbf{x}}^m) \cdot \bar{\mathbf{n}}^m\} = (\Delta \mathbf{u}^s - \Delta \bar{\mathbf{u}}^m - \bar{\mathbf{x}}_{,\alpha}^m \Delta \alpha - \bar{\mathbf{x}}_{,\beta}^m \Delta \beta) \cdot \bar{\mathbf{n}}^m + (\mathbf{x}^s - \bar{\mathbf{x}}^m) \cdot \Delta \bar{\mathbf{n}}^m . \quad (5.7)$$

The orthogonality of $\bar{\mathbf{x}}_{,\alpha}^m \cdot \bar{\mathbf{n}}^m$, $\bar{\mathbf{x}}_{,\beta}^m \cdot \bar{\mathbf{n}}^m$ and $(\mathbf{x}^s - \bar{\mathbf{x}}^m) \cdot \Delta \bar{\mathbf{n}}^m$ allows to further simplify it resulting in the following equation:

$$\Delta g_N = [\Delta \mathbf{u}^s - \Delta \bar{\mathbf{u}}^m] \cdot \bar{\mathbf{n}}^m . \quad (5.8)$$

The variation of the gap can be directly obtained from Eq. (5.8) by exchanging $\Delta \mathbf{u}^\gamma$ with the variations $\boldsymbol{\eta}^\gamma$ and reads:

$$\delta g_N = [\boldsymbol{\eta}^s - \bar{\boldsymbol{\eta}}^m] \cdot \bar{\mathbf{n}}^m . \quad (5.9)$$

The linearization of the variation of the gap is more complicated. Under the assumption of a flat contact surface it is given by:

$$\begin{aligned} \Delta(\delta g_N) = & -\bar{a}^{\alpha\beta} \bar{\boldsymbol{\eta}}_{,\alpha}^m (\bar{\mathbf{n}}^m \otimes \bar{\mathbf{x}}_{,\beta}^m) (\Delta \mathbf{u}^s - \Delta \bar{\mathbf{u}}^m) - \bar{a}^{\alpha\beta} g_N \bar{\boldsymbol{\eta}}_{,\alpha}^m (\bar{\mathbf{n}}^m \otimes \bar{\mathbf{n}}^m) \Delta \bar{\mathbf{u}}_{,\beta}^m \\ & - \bar{a}^{\alpha\beta} \Delta \bar{\mathbf{u}}_{,\alpha}^m (\bar{\mathbf{x}}_{,\beta}^m \otimes \bar{\mathbf{n}}^m) (\boldsymbol{\eta}^s - \bar{\boldsymbol{\eta}}^m) - \bar{a}^{\alpha\beta} g_N \Delta \bar{\mathbf{u}}_{,\alpha}^m (\bar{\mathbf{n}}^m \otimes \bar{\mathbf{n}}^m) \bar{\boldsymbol{\eta}}_{,\beta}^m . \end{aligned} \quad (5.10)$$

The contravariant components of the metric tensor of the master surface $\bar{a}^{\alpha\beta}$ can be computed by first computing the covariant metric tensor $\bar{a}_{\alpha\beta}$ by the scalar product of the tangential surface vectors $\bar{a}_{\alpha\beta} = \bar{\mathbf{x}}_{,\alpha}^m \cdot \bar{\mathbf{x}}_{,\beta}^m$ and then computing its inverse.

Sticking contact

The sticking contact formulation requires the linearization of the total penetration function Eq. (5.6). The full time derivative of the total gap function is simply given by:

$$\Delta \mathbf{g}_{\text{St}} = \Delta (\mathbf{x}^s - \mathbf{x}^m(\boldsymbol{\alpha}^0)) = \Delta \mathbf{u}^s - \Delta \mathbf{u}^m(\boldsymbol{\alpha}^0) \quad (5.11)$$

due to the missing time dependency of $\boldsymbol{\alpha}^0$. The variation of the gap reads:

$$\delta \mathbf{g}_{\text{St}} = \delta(\mathbf{x}^s - \bar{\mathbf{x}}^m) = \boldsymbol{\eta}^s - \boldsymbol{\eta}^m(\boldsymbol{\alpha}^0) . \quad (5.12)$$

5.2 Weak form and enforcement of contact conditions

The extension of the weak form (Eq. (2.122)) for the contact problem, assuming that the actual contact interface is known, reads as follows:

$$\sum_{\gamma=1}^2 \left\{ \int_{\varphi(B^\gamma)} \boldsymbol{\sigma}^\gamma : \text{grad } \boldsymbol{\eta}^\gamma \, dv - \int_{\varphi(B^\gamma)} \rho \mathbf{b}^\gamma \cdot \boldsymbol{\eta}^\gamma \, dv - \int_{\varphi(\Gamma^\gamma)} \mathbf{t}^\gamma \cdot \boldsymbol{\eta}^\gamma \, da \right\} + C = 0, \quad (5.13)$$

where C denotes the additional term that enforces the contact condition in the equation system. The contact term C generally depends on the method that is used to enforce the contact condition. In order to enforce the contact conditions in the weak form we apply the penalty method which does not add any additional degrees of freedom to our global equation system and it is not affected by over-constraining problems [72]. However, large numbers for the penalty factor β can lead to an ill-conditioning of the global equation system.

The penalty formulation for the contact term C reads:

$$C = \beta \int_{\Gamma_C} \delta \mathbf{g} \cdot \mathbf{g} \, da . \quad (5.14)$$

By splitting up the contact term into a normal C_N and a tangential C_T contribution:

$$C = C_N + C_T, \quad (5.15)$$

it is possible to incorporate friction laws for the tangential term in case of sliding of the contact interfaces involving friction. The tangential contribution reads:

$$C_T = \beta \int_{\Gamma_C} \delta \mathbf{g}_T \cdot \mathbf{g}_T \, da. \quad (5.16)$$

In frictionless contact conditions no tangential forces are acting on the contact bodies, so C_T can be neglected and only the normal contribution:

$$C_N = \beta \int_{\Gamma_C} \delta g_N g_N \, da \quad (5.17)$$

has to be considered.

The sticking contact formulation does not require a split of the contact contributions, therefore we will consider Eq. (5.14) as the starting point for this formulation.

5.2.1 Linearization

In order to apply the Newton-Raphson scheme for the solution of the contact problem the linearization of the contact term is required.

Frictionless contact

In case of frictionless contact the linearization of Eq. (5.17) is obtained by applying the rule:

$$\Delta C_N = \beta \int_{\Gamma_C} (\Delta (\delta g_N) g_N + \delta g_N \Delta g_N) \, da. \quad (5.18)$$

Substituting the linearization and the variation of the gap function given in Eq. (5.8), Eq. (5.9) and Eq. (5.10) in Eq. (5.18) and omitting all terms multiplied by g_N^2 , which have only minor influence on the rate of convergence of the Newton-Raphson scheme, yields:

$$\begin{aligned} \Delta C_N = \beta \int_{\Gamma_C} & (\boldsymbol{\eta}^s - \bar{\boldsymbol{\eta}}^m) \cdot (\bar{\mathbf{n}}^m \otimes \bar{\mathbf{n}}^m) \cdot (\Delta \mathbf{u}^s - \Delta \bar{\mathbf{u}}^m) - g_N \bar{a}^{\alpha\beta} \bar{\boldsymbol{\eta}}_{,\alpha}^m \cdot (\bar{\mathbf{n}}^m \otimes \bar{\mathbf{x}}_{,\beta}^m) \cdot (\Delta \mathbf{u}^s - \Delta \bar{\mathbf{u}}^m) \\ & - g_N \bar{a}^{\alpha\beta} (\boldsymbol{\eta}^s - \bar{\boldsymbol{\eta}}^m) \cdot (\bar{\mathbf{x}}_{,\beta}^m \otimes \bar{\mathbf{n}}^m) \cdot \Delta \bar{\mathbf{u}}_{,\alpha}^m \, da. \end{aligned} \quad (5.19)$$

Sticking contact

In order to derive the linearization for the sticking contact formulation ΔC_{St} we start with Eq. (5.14). The linearization yields a simple expression:

$$\begin{aligned} \Delta C_{St} &= \beta \int_{\Gamma_C} (\Delta (\delta \mathbf{g}_{St}) \cdot \mathbf{g}_{St} + \delta \mathbf{g}_{St} \cdot \Delta \mathbf{g}_{St}) \, da = \beta \int_{\Gamma_C} \delta \mathbf{g}_{St} \cdot \Delta \mathbf{g}_{St} \, da \\ &= \beta \int_{\Gamma_C} (\boldsymbol{\eta}^s - \boldsymbol{\eta}^m(\boldsymbol{\alpha}^0)) \cdot (\Delta \mathbf{u}^s - \Delta \mathbf{u}^m(\boldsymbol{\alpha}^0)) \, da \end{aligned} \quad (5.20)$$

since $\Delta(\delta g) = \mathbf{0}$.

5.3 Discretization of contact interface

The finite cell discretization does not conform to the boundary of the geometry and therefore usually no explicit description of the geometry is directly available. However, in order to evaluate the non-penetration condition given by Eq. (5.4) an explicit representation of the boundary by surface elements and slave points is needed. To this end, we introduce a discretization of the surface Γ_h^c by triangles and appropriate quadrature points, see Fig. 5.3. Such

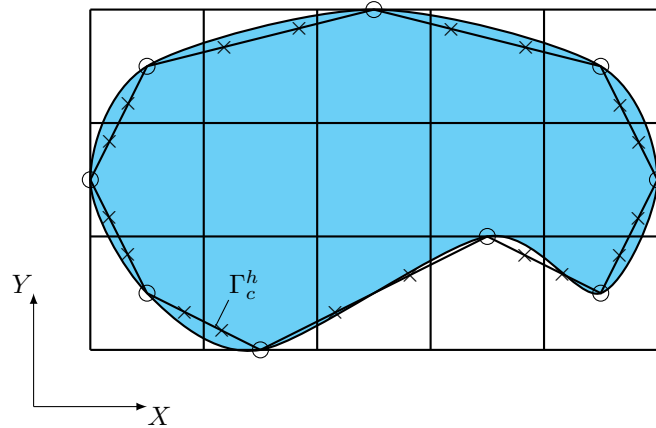


Figure 5.3: Finite cell mesh and contact surface discretization. In order to simplify the drawing the contact elements here are formed by linear segments. In three-dimensional applications the contact elements correspond to flat triangles.

a geometrical description of surfaces can be easily derived from common surface formulations used within the finite cell method like implicitly defined geometries, voxel-based data or B-rep models.

The triangle nodes \mathbf{X}^{t_I} ($I \in [1, 2, 3]$) and the slave points \mathbf{X}^s are located within a finite cell and exhibit local coordinates in terms of the finite cell coordinate system $\boldsymbol{\xi}^{t_I}$, respectively $\boldsymbol{\xi}^s$, see Fig. 5.4. The spatial positions of the triangle nodes \mathbf{x}^{t_I} and the slave points \mathbf{x}^s are modified during the simulation to track the evolving surface of the contact bodies by computing the displacements \mathbf{u}^{t_I} and \mathbf{u}^s from the displacement vector of the finite cell \mathbf{u}^C and the finite cell shape functions \mathbf{N} by:

$$\mathbf{u}^{t_I} = \mathbf{N}(\boldsymbol{\xi}^{t_I}) \mathbf{u}^C, \quad \mathbf{x}^{t_I} = \mathbf{N}(\boldsymbol{\xi}^{t_I}) \mathbf{x}^C, \text{ resp. } \mathbf{u}^s = \mathbf{N}(\boldsymbol{\xi}^s) \mathbf{u}^C, \quad \mathbf{x}^s = \mathbf{N}(\boldsymbol{\xi}^s) \mathbf{x}^C. \quad (5.21)$$

In order to discretize the displacement increment $\Delta \mathbf{u}^m$ of the master surface and the virtual displacements $\boldsymbol{\eta}^m$, we first define the nodal displacement vector $\Delta \mathbf{u}^m = [\Delta \mathbf{u}^{t_1}, \Delta \mathbf{u}^{t_2}, \Delta \mathbf{u}^{t_3}]^T$, respectively the virtual displacement vector $\mathbf{v}^m = [\mathbf{v}^{t_1}, \mathbf{v}^{t_2}, \mathbf{v}^{t_3}]^T$ of the master triangle. The displacements and virtual displacements are then related to the corresponding quantities of

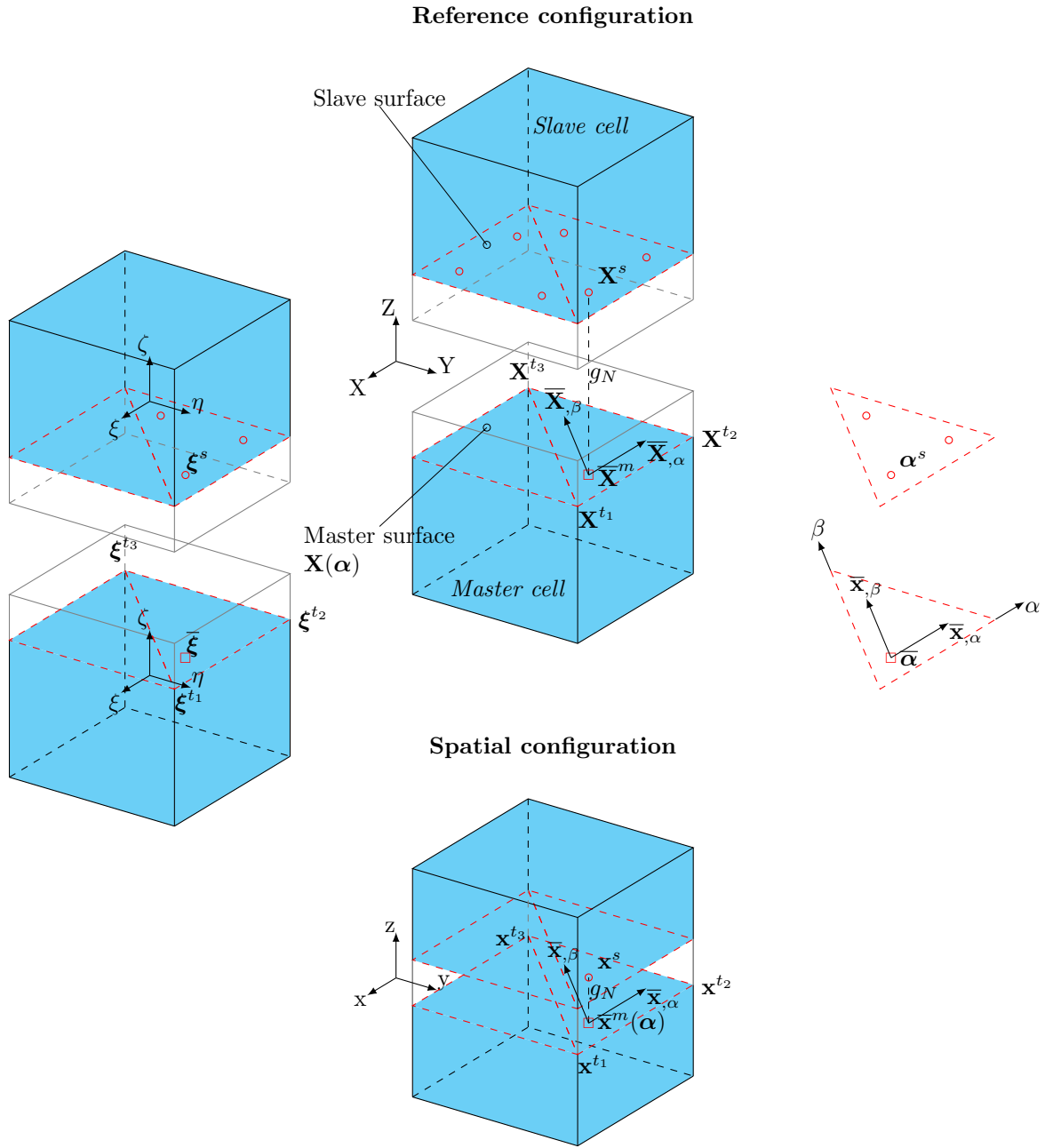


Figure 5.4: Contact surface discretization.

the finite cell $\Delta \mathbf{u}^{C(t_I)}, \mathbf{v}^{C(t_I)}$ by:

$$\begin{aligned} \Delta \mathbf{u}^m &= \begin{bmatrix} \mathbf{N}(\boldsymbol{\xi}^{t_1}) & & \\ & \mathbf{N}(\boldsymbol{\xi}^{t_2}) & \\ & & \mathbf{N}(\boldsymbol{\xi}^{t_3}) \end{bmatrix} \begin{bmatrix} \Delta \mathbf{u}^{C(t_1)} \\ \Delta \mathbf{u}^{C(t_2)} \\ \Delta \mathbf{u}^{C(t_3)} \end{bmatrix} \\ \mathbf{v}^m &= \begin{bmatrix} \mathbf{N}(\boldsymbol{\xi}^{t_1}) & & \\ & \mathbf{N}(\boldsymbol{\xi}^{t_2}) & \\ & & \mathbf{N}(\boldsymbol{\xi}^{t_3}) \end{bmatrix} \begin{bmatrix} \mathbf{v}^{C(t_1)} \\ \mathbf{v}^{C(t_2)} \\ \mathbf{v}^{C(t_3)} \end{bmatrix}, \end{aligned} \quad (5.22)$$

It is important to mention that every node of the master triangle can be associated with a different cell which is indicated by the superscript $C(t_I)$. The size of these matrices is therefore $[9 \times (\text{ndof}_{C_1} + \text{ndof}_{C_2} + \text{ndof}_{C_3})]$, where ndof_{C_i} are the degrees of freedom of the finite cells. The displacement increment $\Delta \mathbf{u}^s$ and the virtual displacements of the slave points are directly given by the displacement, resp. virtual displacements of its associated finite cell:

$$\Delta \mathbf{u}^s = \mathbf{N}(\boldsymbol{\xi}^s) \Delta \mathbf{u}^C, \quad \mathbf{v}^s = \mathbf{N}(\boldsymbol{\xi}^s) \mathbf{v}^C. \quad (5.23)$$

In Eq. (5.19) the discretization of the increment of the gap ($\Delta \mathbf{u}^s - \Delta \mathbf{u}^m$) and its variation ($\boldsymbol{\eta}^s - \boldsymbol{\eta}^m$) requires to define the projection matrix \mathbf{P} :

$$\mathbf{P} = \begin{bmatrix} \mathbf{N}(\boldsymbol{\xi}^s) & & & \\ & \mathbf{N}(\boldsymbol{\xi}^{t_1}) & & \\ & & \mathbf{N}(\boldsymbol{\xi}^{t_2}) & \\ & & & \mathbf{N}(\boldsymbol{\xi}^{t_3}) \end{bmatrix}, \quad (5.24)$$

which relates the displacements of the finite cell to the displacements of a slave point and its associated master triangle by:

$$\begin{bmatrix} \Delta \mathbf{u}^s \\ \Delta \mathbf{u}^{t_1} \\ \Delta \mathbf{u}^{t_2} \\ \Delta \mathbf{u}^{t_3} \end{bmatrix} = \mathbf{P} \begin{bmatrix} \Delta \mathbf{u}^{C(s)} \\ \Delta \mathbf{u}^{C(t_1)} \\ \Delta \mathbf{u}^{C(t_2)} \\ \Delta \mathbf{u}^{C(t_3)} \end{bmatrix}, \quad \begin{bmatrix} \mathbf{v}^s \\ \mathbf{v}^{t_1} \\ \mathbf{v}^{t_2} \\ \mathbf{v}^{t_3} \end{bmatrix} = \mathbf{P} \begin{bmatrix} \mathbf{v}^{C(s)} \\ \mathbf{v}^{C(t_1)} \\ \mathbf{v}^{C(t_2)} \\ \mathbf{v}^{C(t_3)} \end{bmatrix}. \quad (5.25)$$

We interpolate the displacements and the test functions linearly between the nodes of each triangle, so the discrete displacement and the virtual displacements within one triangle are given by:

$$\mathbf{u}^m = N_I(\alpha, \beta) \mathbf{u}^{t_I}, \quad \mathbf{v}^m = N_I(\alpha, \beta) \mathbf{v}^{t_I}, \quad (5.26)$$

where $N_I(\alpha, \beta)$ are the corresponding linear shape functions:

$$N_1(\alpha, \beta) = 1 - \alpha - \beta, \quad N_2(\alpha, \beta) = \alpha, \quad N_3(\alpha, \beta) = \beta. \quad (5.27)$$

With the interpolation of the master surface at hand we can express the gap increment ($\Delta \mathbf{u}^s - \Delta \mathbf{u}^m$) and ($\boldsymbol{\eta}^s - \boldsymbol{\eta}^m$) by:

$$\Delta \mathbf{u}^s - \Delta \mathbf{u}^m = \mathbf{A} \begin{bmatrix} \Delta \mathbf{u}^s \\ \Delta \mathbf{u}^{t_1} \\ \Delta \mathbf{u}^{t_2} \\ \Delta \mathbf{u}^{t_3} \end{bmatrix}, \quad (\boldsymbol{\eta}^s - \boldsymbol{\eta}^m) = \mathbf{A} \begin{bmatrix} \mathbf{v}^s \\ \mathbf{v}^{t_1} \\ \mathbf{v}^{t_2} \\ \mathbf{v}^{t_3} \end{bmatrix}, \quad (5.28)$$

where the interpolation matrix \mathbf{A} reads:

$$\mathbf{A} = \begin{bmatrix} 1 & 0 & 0 & \alpha + \beta - 1 & 0 & 0 & -\alpha & 0 & 0 & -\beta & 0 & 0 \\ 0 & 1 & 0 & 0 & \alpha + \beta - 1 & 0 & 0 & -\alpha & 0 & 0 & -\beta & 0 \\ 0 & 0 & 1 & 0 & 0 & \alpha + \beta - 1 & 0 & 0 & -\alpha & 0 & 0 & -\beta \end{bmatrix}. \quad (5.29)$$

By computing the derivatives of the interpolation matrix \mathbf{A} with respect to the convective surface coordinates, we obtain $\mathbf{A}_{,\alpha}$ and $\mathbf{A}_{,\beta}$:

$$\begin{aligned} \mathbf{A}_{,\alpha} &= \begin{bmatrix} 0 & 0 & 0 & 1 & 0 & 0 & -1 & 0 & 0 & 0 & 0 & 0 \\ 0 & 0 & 0 & 0 & 1 & 0 & 0 & -1 & 0 & 0 & 0 & 0 \\ 0 & 0 & 0 & 0 & 0 & 1 & 0 & 0 & -1 & 0 & 0 & 0 \end{bmatrix} \\ \mathbf{A}_{,\beta} &= \begin{bmatrix} 0 & 0 & 0 & 1 & 0 & 0 & 0 & 0 & 0 & -1 & 0 & 0 \\ 0 & 0 & 0 & 0 & 1 & 0 & 0 & 0 & 0 & 0 & -1 & 0 \\ 0 & 0 & 0 & 0 & 0 & 1 & 0 & 0 & 0 & 0 & 0 & -1 \end{bmatrix} \end{aligned} \quad (5.30)$$

and can express the derivatives $\boldsymbol{\eta}_{,\alpha}$, $\boldsymbol{\eta}_{,\beta}$, $\Delta \mathbf{u}_{,\alpha}^m$ and $\Delta \mathbf{u}_{,\beta}^m$ via:

$$\boldsymbol{\eta}_{,\alpha} = \mathbf{A}_{,\alpha} \begin{bmatrix} \mathbf{v}^s \\ \mathbf{v}^m \end{bmatrix}, \quad \boldsymbol{\eta}_{,\beta} = \mathbf{A}_{,\beta} \begin{bmatrix} \mathbf{v}^s \\ \mathbf{v}^m \end{bmatrix}, \quad \Delta \mathbf{u}_{,\alpha}^m = \mathbf{A}_{,\alpha} \begin{bmatrix} \Delta \mathbf{u}^s \\ \Delta \mathbf{u}^m \end{bmatrix}, \quad \Delta \mathbf{u}_{,\beta}^m = \mathbf{A}_{,\beta} \begin{bmatrix} \Delta \mathbf{u}^s \\ \Delta \mathbf{u}^m \end{bmatrix} \quad (5.31)$$

5.3.1 The contact stiffness matrix and right-hand side

In this section we complete the discretization of the contact contributions for sticking and frictionless contact by stating the contact stiffness matrices \mathbf{k}_c , \mathbf{k}_c^{St} and the right-hand side load vectors \mathbf{f}_c , \mathbf{f}_c^{St} .

Frictionless contact

The discretization of the weak form of the frictionless contact formulation reads after substituting Eq. (5.25) and Eq. (5.28) into Eq. (5.17):

$$C_N = \sum_{c=1}^{n_t} \mathbf{v}^T \mathbf{f}_c, \quad (5.32)$$

where n_t is the number of active triangles on the slave surface, which means that they have at least one slave point that fulfills the contact conditions. The right-hand side is denoted by \mathbf{f}_c and reads:

$$\mathbf{f}_c = \beta \int_{\Gamma_C} \mathbf{P}^T \mathbf{A}^T \bar{\mathbf{n}} g_N da. \quad (5.33)$$

After substituting the discrete expressions from Eq. (5.24), Eq. (5.28) and Eq. (5.31) into Eq. (5.19) we obtain the following expression for the discretization of the linearization of the weak form:

$$\Delta C_N = \sum_{c=1}^{n_t} \mathbf{v}^T \mathbf{k}_c \begin{bmatrix} \Delta \mathbf{u}^{C(s)} \\ \Delta \mathbf{u}^{C(t_1)} \\ \Delta \mathbf{u}^{C(t_2)} \\ \Delta \mathbf{u}^{C(t_3)} \end{bmatrix}, \quad (5.34)$$

where \mathbf{k}_c denotes the contact contribution for the stiffness matrix:

$$\begin{aligned} \mathbf{k}_c = & \beta \int_{\Gamma_C} \mathbf{P}^T \mathbf{A}^T (\bar{\mathbf{n}}^m \otimes \bar{\mathbf{n}}^m) \mathbf{A} \mathbf{P} - g_N \bar{a}^{\alpha\beta} \mathbf{P}^T \mathbf{A}_{,\alpha}^T (\bar{\mathbf{n}}^m \otimes \bar{\mathbf{x}}_{,\beta}^m) \mathbf{A} \mathbf{P} \\ & - g_N \bar{a}^{\alpha\beta} \mathbf{P}^T \mathbf{A}^T (\bar{\mathbf{x}}_{,\beta}^m \otimes \bar{\mathbf{n}}^m) \mathbf{A}_{,\alpha} \mathbf{P} \, da. \end{aligned} \quad (5.35)$$

Sticking contact

The discretization of the contact contribution for sticking contact given in Eq. (5.14) and Eq. (5.20) yields a much simpler expressions. The surface elements appear only during the contact detection but vanish in the equation system, that constrains the movement of discrete points located in different cells. The increment $\Delta \mathbf{g}_{\text{St}}$ and the variation $\delta \mathbf{g}_{\text{St}}$ of the total gap between the slave point \mathbf{x}^s , that sticks to the master surface at \mathbf{x}^m ($\boldsymbol{\alpha}^0$), can be expressed via:

$$\Delta \mathbf{g}_{\text{St}} = \begin{bmatrix} \mathbf{N}(\boldsymbol{\xi}^s) & -\mathbf{N}(\boldsymbol{\xi}^0) \end{bmatrix} \begin{bmatrix} \Delta \mathbf{u}^{C(s)} \\ \Delta \mathbf{u}^{C(0)} \end{bmatrix}, \quad \delta \mathbf{g}_{\text{St}} = \begin{bmatrix} \mathbf{N}(\boldsymbol{\xi}^s) & -\mathbf{N}(\boldsymbol{\xi}^0) \end{bmatrix} \begin{bmatrix} \mathbf{v}^{C(s)} \\ \mathbf{v}^{C(0)} \end{bmatrix}, \quad (5.36)$$

after mapping the triangle surface coordinate $\boldsymbol{\alpha}^0$ to its local finite cell coordinate system $\boldsymbol{\xi}^0$. The discretization of the weak form of the sticking contact formulation given in Eq. (5.13) then reads:

$$C_{\text{St}} = \sum_{c=1}^{n_t} \mathbf{v}^T \mathbf{f}_c^{\text{St}}, \quad (5.37)$$

where n_t is the number of active triangles on the slave surface and \mathbf{f}_c^{St} represents the right-hand side:

$$\mathbf{f}_c^{\text{St}} = \beta \int_{\Gamma_C} \begin{bmatrix} \mathbf{N}(\boldsymbol{\xi}^s) \\ -\mathbf{N}(\boldsymbol{\xi}^0) \end{bmatrix} \mathbf{g} \, da. \quad (5.38)$$

The discretization of the linearization of the weak form of the sticking contact formulation reads:

$$\Delta C_{\text{St}} = \sum_{c=1}^{n_t} \mathbf{v}^T \mathbf{k}_c^{\text{St}} \Delta \mathbf{u}, \quad (5.39)$$

where \mathbf{k}_c^{St} is the stiffness matrix related to the contact contribution:

$$\mathbf{k}_c^{\text{St}} = \beta \int_{\Gamma_C} \begin{bmatrix} \mathbf{N}(\boldsymbol{\xi}^s) \\ -\mathbf{N}(\boldsymbol{\xi}^0) \end{bmatrix} \begin{bmatrix} \mathbf{N}(\boldsymbol{\xi}^s) & -\mathbf{N}(\boldsymbol{\xi}^0) \end{bmatrix} \, da. \quad (5.40)$$

Collocation

The integration over the contact slave surface in Eq. (5.38) and Eq. (5.40) is not necessary for the exact enforcement of the contact conditions. Instead the integral can be replaced by a sum over all active contact slave points n_s . In numerical mathematics such a method is known

as a collocation method [41]. Hence we can rewrite the formula for the stiffness matrix (5.35) and the residual (5.35) for frictionless contact as:

$$\begin{aligned} \mathbf{k}_c &= \beta \sum_{n=1}^{n_s} \mathbf{P}^T \mathbf{A}^T (\bar{\mathbf{n}}^m \otimes \bar{\mathbf{n}}^m) \mathbf{A} \mathbf{P} - g_N \bar{a}^{\alpha\beta} \mathbf{P}^T \mathbf{A}_{,\alpha}^T (\bar{\mathbf{n}}^m \otimes \bar{\mathbf{x}}_{,\beta}^m) \mathbf{A} \mathbf{P} - \\ &\quad - g_N \bar{a}^{\alpha\beta} \mathbf{P}^T \mathbf{A}^T (\bar{\mathbf{x}}_{,\beta}^m \otimes \bar{\mathbf{n}}^m) \mathbf{A}_{,\alpha} \mathbf{P} \, da, \\ \mathbf{f}_c &= \beta \sum_{n=1}^{n_s} \mathbf{P}^T \mathbf{A}^T \mathbf{n} g_N da, \end{aligned} \quad (5.41)$$

and for sticking contact as:

$$\begin{aligned} \mathbf{k}_c^{\text{St}} &= \beta \sum_{n=1}^{n_s} \begin{bmatrix} \mathbf{N}(\boldsymbol{\xi}^s) \\ -\mathbf{N}(\boldsymbol{\xi}^0) \end{bmatrix} \begin{bmatrix} \mathbf{N}(\boldsymbol{\xi}^s) & -\mathbf{N}(\boldsymbol{\xi}^0) \end{bmatrix}, \\ \mathbf{f}_c^{\text{St}} &= \beta \sum_{n=1}^{n_s} \begin{bmatrix} \mathbf{N}(\boldsymbol{\xi}^s) \\ -\mathbf{N}(\boldsymbol{\xi}^0) \end{bmatrix} \mathbf{g}_{\text{St}}. \end{aligned} \quad (5.42)$$

5.4 The mapping procedure

Due to the additionally introduced contact surface discretization, several mappings are required before the contact conditions can be enforced within the global equation system of the finite cell method. In order to explain the mapping procedure, we consider the two-dimensional problem depicted in Fig. 5.5.

The body is clamped on one side and loaded by a force on its top and on its bottom. Due to the loading self-contact occurs. The problem is discretized by a set of finite cells, which do not conform with the surface of the geometry, and contact elements formed by linear segments – linear triangles for a 3D problem – are placed on the boundary of the body. On each of these elements a set of quadrature points is distributed, which are the slave points.

For each node of the contact element, the slave points and the master points, we have to distinguish between four different coordinate representations. That are their local coordinates in terms of the contact surface discretization by triangles $\boldsymbol{\alpha} = [\alpha, \beta]^T$, their global spatial coordinates in the deformed and undeformed configuration, $\mathbf{x} = [x, y, z]^T$, resp. $\mathbf{X} = [X, Y, Z]^T$, and their local coordinates in terms of the finite cell they are located in $\boldsymbol{\xi} = [\xi, \eta, \zeta]^T$. During the simulation three different types of mappings between these different representations are involved.

The slave surface

On each triangle a set of slave points is defined to evaluate the non-penetration condition at these discrete positions. To this end we use a symmetric set of Gauss-Legendre quadrature points that is defined on the standard triangle. As there are two sets of quadrature points, known as Gauss-Legendre quadrature points, we evaluate the one where no points are located on the boundary of the triangle because this would lead to multiple quadrature points at the same positions for neighboring triangles and in turn to an inefficient contact detection procedure. Fig. 5.6 shows the set of quadrature points for $n_o = 2$. The coordinates of the

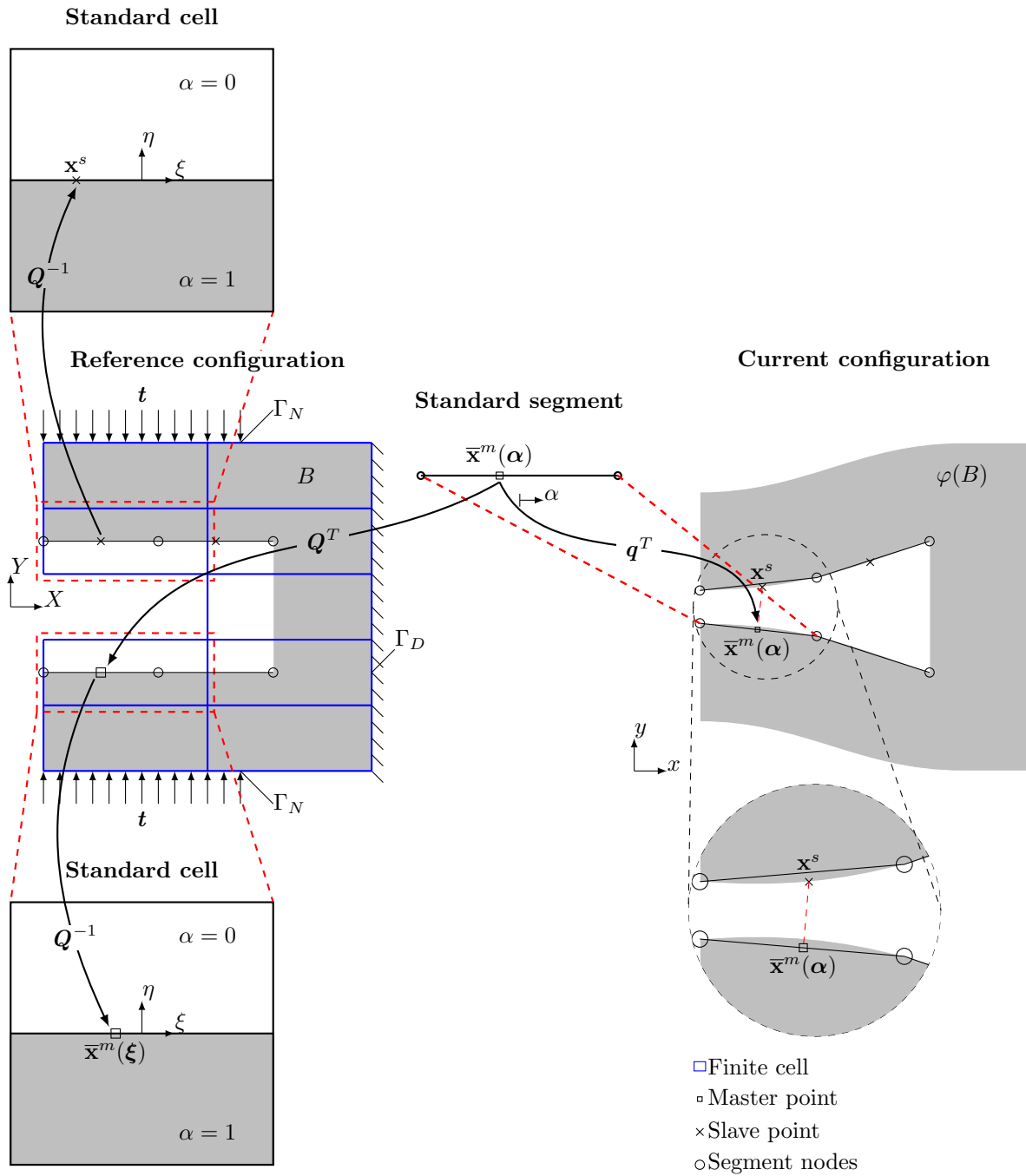


Figure 5.5: Schematic view of the contact approach showing the involved mappings.

slave points in the undeformed setting can be computed, by first mapping its local coordinates $[\alpha^s, \beta^s]^T$ to the global coordinate system by:

$$\mathbf{X}^s = \mathbf{Q}^t(\alpha^s, \beta^s) = \sum_{I=1}^3 N_I(\alpha^s, \beta^s) \mathbf{X}^{tI} \quad (5.43)$$

using Lagrange shape functions $N_i(\alpha, \beta)$:

$$N_1(\alpha, \beta) = 1 - \alpha - \beta, N_2(\alpha, \beta) = \alpha, N_3(\alpha, \beta) = \beta \quad (5.44)$$

and then performing an inverse mapping to the finite cell coordinate system:

$$[X^s, Y^s, Z^s]^T \xrightarrow{\mathbf{Q}^{-1}} [\xi^s, \eta^s, \zeta^s]^T. \quad (5.45)$$

By this their displacements can be computed from the finite cell displacement field and consequently their spatial coordinates can be updated. As already mentioned due to the approximation of a possibly curved contact surface by straight sided elements an error might be introduced and the integration points are not exactly placed on the real boundary of the geometry.

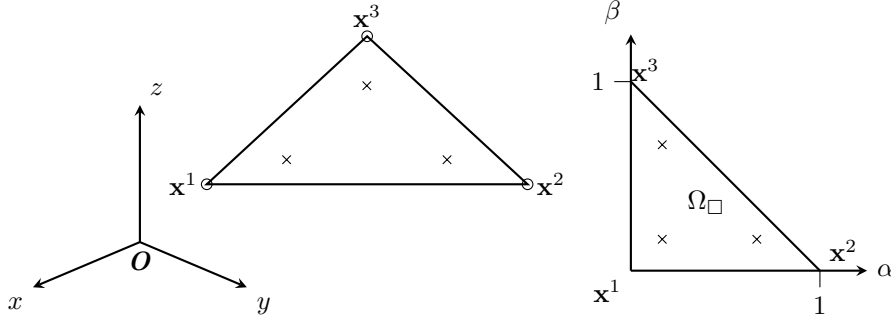


Figure 5.6: Triangle with Gauss-Legendre quadrature points. The quadrature points for higher orders of the quadrature are listed in Tab. A.1 and can be found for example in [16].

The master surface

The coordinates of the contact element nodes in the undeformed setting are initially given. After searching for the finite cell they are included in, we perform an inverse mapping to the finite cell coordinate system using the mapping function \mathbf{Q}^{-1} .

$$[X, Y, Z]^T \xrightarrow{\mathbf{Q}^{-1}} [\xi, \eta, \zeta] \quad (5.46)$$

Knowing the local coordinates $\boldsymbol{\xi}^{tI} = [\xi, \eta, \zeta]^T$ of the nodes in terms of the finite cell coordinate system allows to track the deforming surface by computing the displacements at the nodes and updating their spatial positions. The mapping for one triangle between its standard coordinate system and its description in the spatial global coordinate system is given by:

$$\mathbf{q}^t = \mathbf{x}(\boldsymbol{\alpha}) = \sum_{I=1}^3 N_I(\alpha, \beta) \mathbf{x}^{tI}, \quad \text{with} \quad \mathbf{x}^{tI} = \mathbf{X}^{tI} + \mathbf{u}^{tI}, \quad (5.47)$$

where \mathbf{x}^{t_i} are the spatial coordinates of the nodes which are computed from the initial nodal positions \mathbf{X}^{t_i} and the actual displacements at the nodes \mathbf{u}^{t_i} .

During the contact search the slave nodes are projected onto the master surface. In case of contact the local coordinates of these projection points in terms of the surface parametrization $\bar{\alpha}$ are computed by solving the minimum distance problem. By assuming that the displacement field within a surface segment can be interpolated linearly from the spatial positions of the nodes, the coordinates in the undeformed configuration can be computed and mapped to the local finite cell coordinates. Of course this assumption introduces another error, see Fig. 5.5.

$$[\bar{\alpha}, \bar{\beta}] \xrightarrow{\mathbf{Q}^t} [\bar{X}, \bar{Y}, \bar{Z}]^T \xrightarrow{\mathbf{Q}^{-1}} [\bar{\xi}, \bar{\eta}, \bar{\zeta}]^T \quad (5.48)$$

Importantly, the surface discretization approximates the initial geometry exactly only if the surface is planar. In case the geometry is not described by a straight line an approximation error is introduced. In the FCM the displacement of the surface is usually described by the high order shape functions of order p . For this reason a straight line in the initial configuration can deform into a curved line and due to this the error of the spatial mapping of the triangle \mathbf{q}^t can increase during the computations, see Fig. 5.5. In order to diminish this error high order surface elements are required. However, we introduce low order Lagrange triangles with linear shape functions to recover the surface and try to lower the error by a surface mesh refinement.

5.4.1 Global contact search

During the iterative solution procedure a search algorithm is required to detect the contact zones that are not known *a priori* after each load-step. Furthermore, when self-contact is included in the problem, it becomes a labor-intensive task to check each slave node for contact against each triangle. Normally advanced search algorithms that are based on partitioning the space by k-d (binary) search trees, are required in these cases. However, within the finite cell method a more advanced method than a rudimentary quadratic search detection algorithm is naturally given. When discretizing the contact surface each contact element and its slave points need to be assigned to a finite cell. This assignment can be used to speed up the contact search, by first using the bounding box of the finite cell for a coarse contact search and then considering the associated triangles. Such a procedure was proposed as one of the first implementations within the finite element method for large deformation contact problems by Benson et al. [10] and was called the bucket search.

After this first rough contact search, the exact contact zone has to be determined. In case of linear triangular elements we can rewrite Eq. (5.2) as:

$$\mathbf{x}_{,\alpha}^m \alpha + \mathbf{x}_{,\beta}^m \beta + \mathbf{n}^m g_N = \mathbf{x}^s - \mathbf{x}^{1,m} \quad (5.49)$$

and directly compute the minimum distance g_N between a slave point \mathbf{x}^s to its orthogonal projection point $\bar{\mathbf{x}}^m(\boldsymbol{\alpha})$ on the master triangle as depicted in Fig. 5.7. For the local coordinates the conditions $\alpha, \beta \in [0, \dots, 1]$ and $\alpha + \beta \leq 1$ need to hold for a point within the triangle.

5.5 Hertzian contact

In 1882 Heinrich Hertz investigated how the optical properties of multiple stacked lenses might change with the force holding them together [27]. During his research he found an analytical

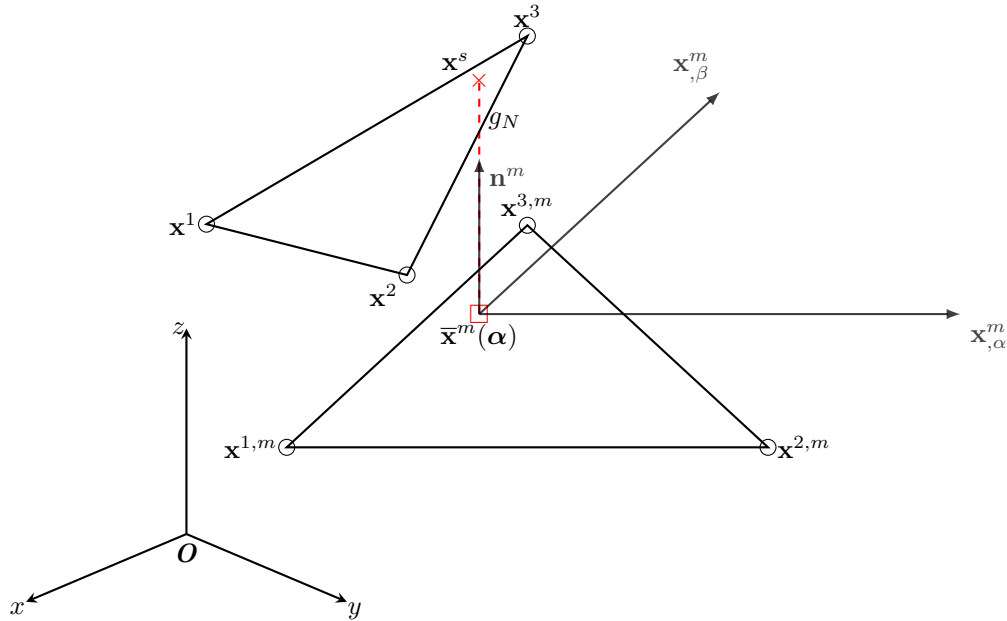


Figure 5.7: Projection of slave point onto the master surface.

solution for the contact of two elastic infinite cylinders from which also the special cases of the contact between a cylinder and a rigid plate can be derived. Here, we briefly introduce the most important formulas and summarize the underlying assumptions of the analytical solution introduced by Hertz:

Each body can be regarded as an elastic, homogeneous and isotropic half-space loaded over a small elliptical region of its smooth surface. The surfaces are assumed to be frictionless, the contact interface is assumed to be small compared to the surfaces' radii and body's dimensions. Under these conditions the contact pressure distribution can be directly computed from the force F that presses the cylinders onto each other by applying the following formula:

$$p(s) = \frac{2F}{\pi L b^2} \sqrt{b^2 - s^2}. \quad (5.50)$$

Here L denotes the length of the cylinders and s the arc length along the surface of the cylinder as shown in Fig. 5.8. The width of the contact zone b can be computed by:

$$b = \sqrt{\frac{4F R^*}{\pi L E^*}}, \quad (5.51)$$

where R^* is the common radius given by the following formula:

$$\frac{1}{R^*} = \frac{1}{R_1} + \frac{1}{R_2}, \quad (5.52)$$

and E^* is common Young's modulus that can be computed by:

$$\frac{1}{E^*} = \frac{1 - \nu_1^2}{E_1} + \frac{1 - \nu_2^2}{E_2}. \quad (5.53)$$

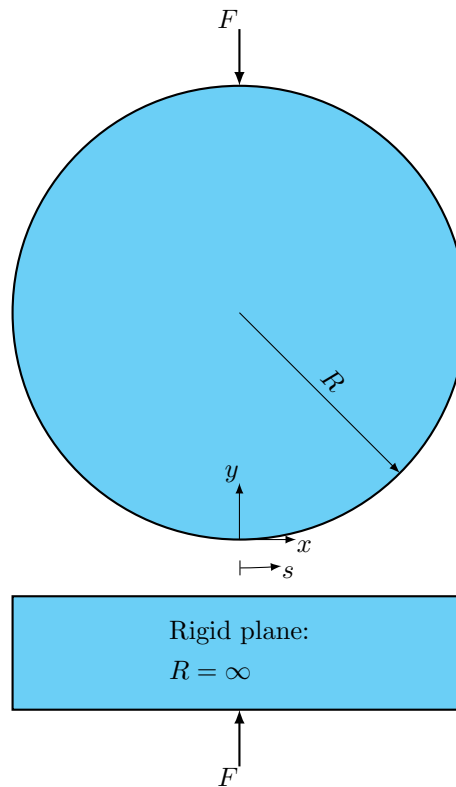


Figure 5.8: Contact of a cylinder with a rigid body.

5.6 Numerical examples

In this section we investigate the presented formulations for sticking and frictionless contact and apply them to compute the self-contact of a metal foam pore. To study the accuracy of the methods we compare the numerical solutions to different analytical benchmark examples. Since the analytical solutions assume only small deformations, we also assume small deformations in the numerical computations. Of course the presented contact formulations are not only suitable for small deformations but could also be applied to large deformations.

5.6.1 Patch test

Before looking at the contact of complex geometries, we consider the sticking contact between two finite cells as depicted in Fig. 5.9 and investigate how many slave points on the contact interface are necessary to enforce the contact conditions. The contact conditions are enforced at the discrete positions of the slave points, therefore it is expected that a certain number of points is needed in order to enforce the contact condition over the whole contact interface.

The example comprises two cubic finite cells with $\Delta x = \Delta y = \Delta z = 10$ mm that are partly filled with material $l = 7.5$ mm. An additional discretization by two triangular elements forms the contact interface. Quadrature points for triangles are distributed over the triangles in order to detect the contact. Symmetry boundary conditions are chosen such that a homogeneous stress state evolves from pressing the top surface of the upper cell downwards against the contact zone of the other cell. The displacement boundary conditions are applied increment wise. In the first load-step the initial gap g_0 is closed. In the following steps the displacement

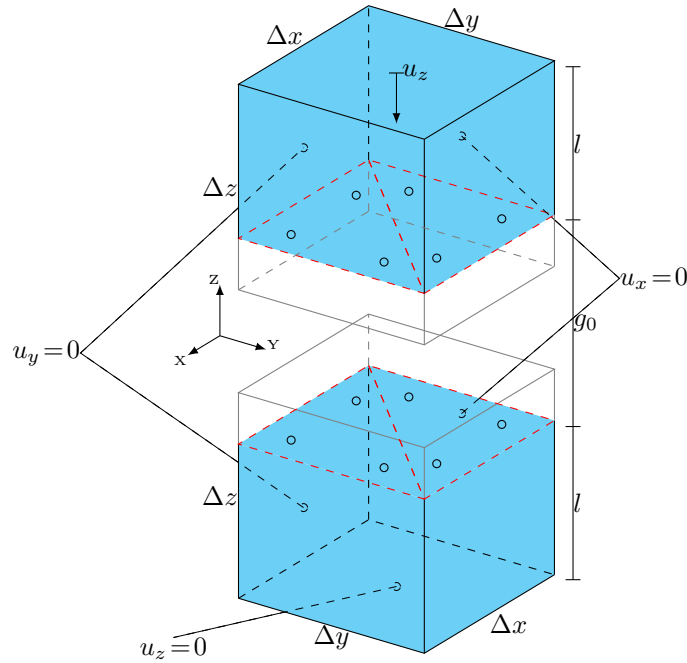


Figure 5.9: Problem setup for the patch test.

is applied in increments of $\Delta u_z = 0.05$ mm. The material is assumed to be linear elastic with Young's modulus $E = 200$ GPa and a Poisson ratio $\nu = 0.3$. The model resembles a one-dimensional bar with a homogeneous constant stress distribution when contact occurs. Therefore an analytical solution for the problem can easily be obtained by:

$$\sigma_{zz,\text{ref}} = -E \frac{(u_z - g_0)}{2l} \quad \text{if } u_z \geq g_0. \quad (5.54)$$

In the second load-step the analytical solution is $\sigma_{zz,\text{ref}} = 666.\bar{6}$ MPa with $u_z - g_0 = 0.05$ mm. To measure the difference between the analytical and numerical solution we define the following error:

$$e_\sigma = \frac{1}{10} \sum_{i=1}^{10} \left| \frac{\sigma_{zz} - \sigma_{zz,\text{ref}}}{\sigma_{zz,\text{ref}}} \right|, \quad (5.55)$$

and compute it at 10 equidistant positions on a diagonal line defined on the contact interface from $[X, Y, Z]^T = [0, 0, 7.5]^T$ to $[X, Y, Z]^T = [10, 10, 7.5]^T$. The line does not coincide with the slave points, where the contact condition is automatically fulfilled and therefore gives an impression how accurate the contact conditions are fulfilled over the entire contact interface. Fig. 5.10 shows the error defined in Eq. (5.55) in dependency of the number of slave points n_s . It is evident that when changing the polynomial order of the ansatz p more slave points are necessary to enforce the contact conditions not only point-wise at the slave points, but for the whole contact interface. In Fig. (5.11) the normal stresses σ_{zz} and the slave points are plotted on the deformed master surface. For the combination of $p = 2$ and $n_s = 8$ as well as for $p = 3$ and $n_s = 13$ enough slave points are defined. The contact surface is therefore straight and normal stress has a constant value of $\sigma_{zz,\text{ref}} = 666.\bar{6}$ MPa. When $p = 3$ and only $n_s = 8$

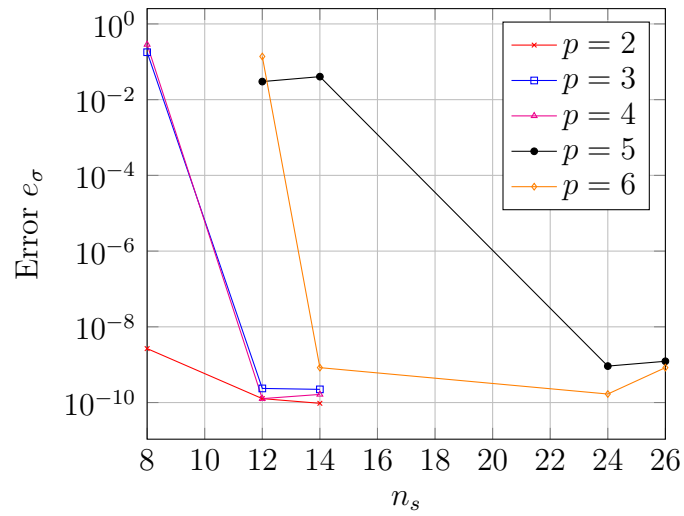
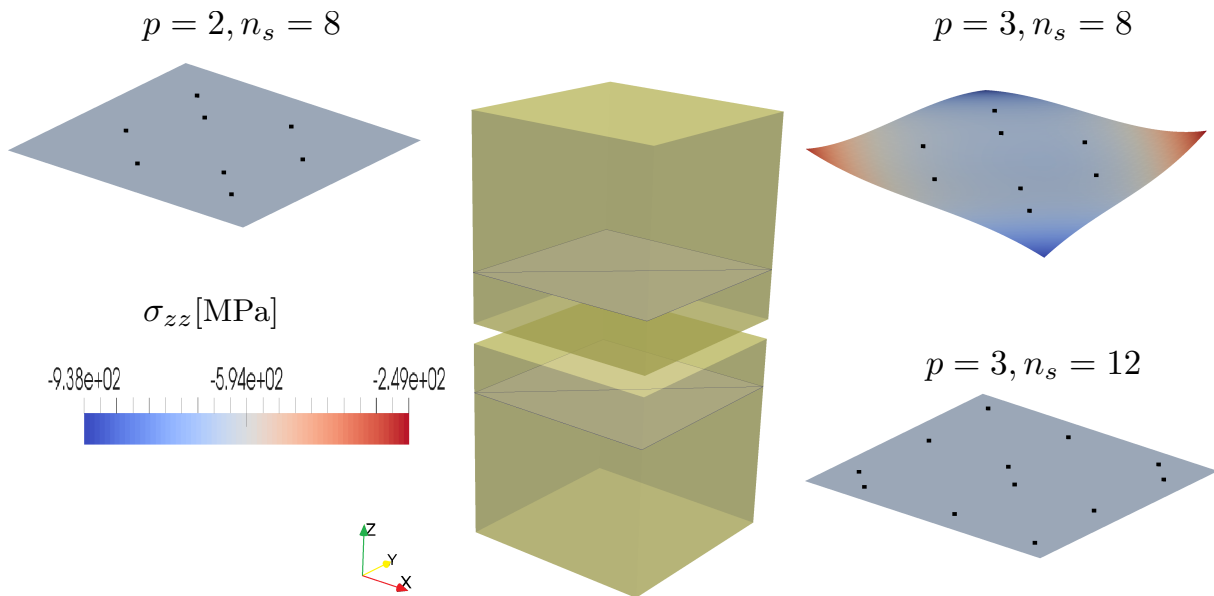


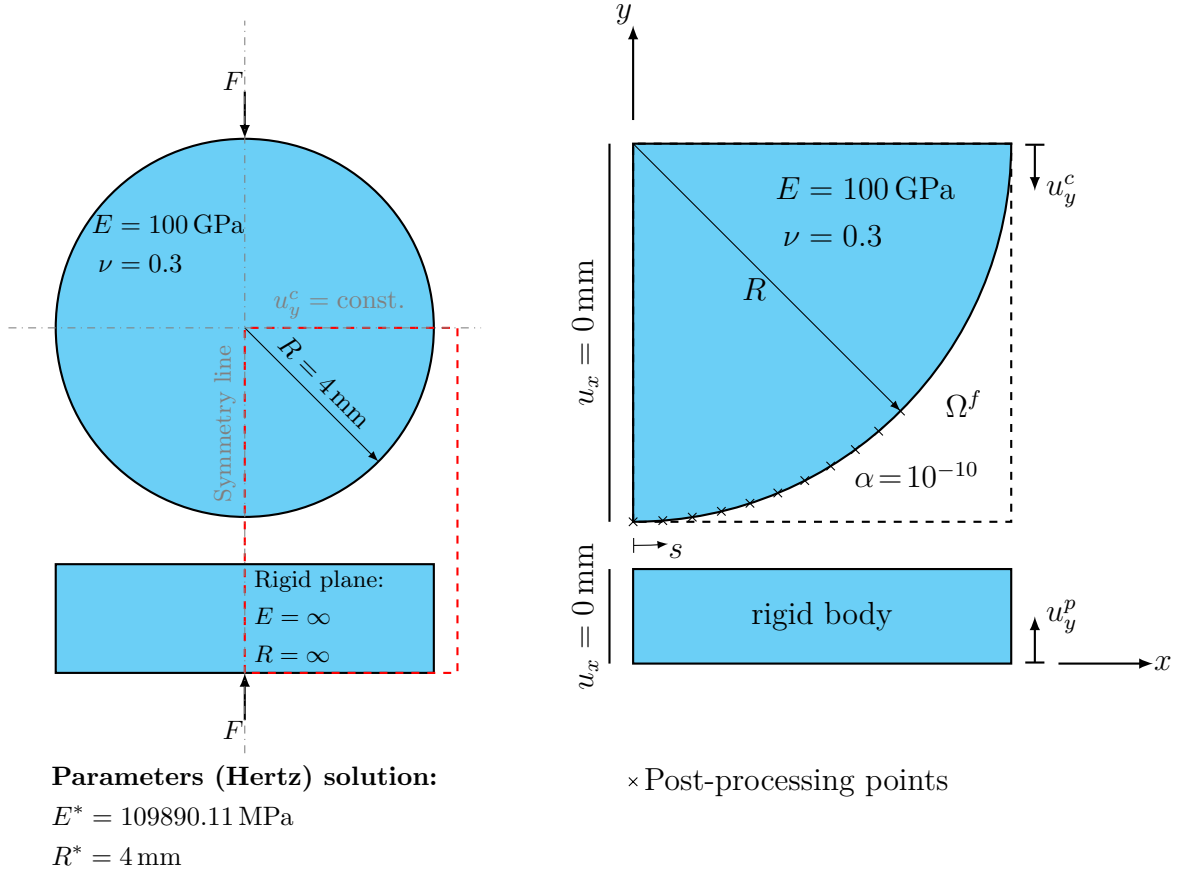
Figure 5.10: Results of the patch test.

slave points are distributed, the contact is only enforced at the slave point but the contact interfaces can still intersect. The stress values are therefore not constant and the contact interface deforms. Although there might be more efficient distributions of slave points, the results presented in Fig. 5.10 can be seen as a rule of thumb for the minimum required number of slave points.

Figure 5.11: Normal stresses σ_{zz} plotted at the contact interface and slave points.

5.6.2 Sticking contact between a cylinder and a rigid plate

In this section we investigate the unilateral contact problem between a cylinder and a rigid plane as shown in Fig. 5.12a). The numerical solution is then compared to the analytical solution derived by Hertz. Please note that the Hertzian solution is for frictionless contact.



a)

b)

Figure 5.12: Contact of a cylinder with a rigid plate. a) shows a two-dimensional slice of the whole geometry and b) the numerical model after introducing all simplifications.

Therefore we do not expect to meet the analytical solution in case of the sticking contact formulation exactly but still to have a good reference for the accuracy of the solution.

The contact between two infinite bodies, in our case an elastic cylinder and a rigid plate, can be reduced to a two-dimensional plane strain problem by setting the length of the cylinder and the plate as $L = 1 \text{ mm}$ and constraining the motion in z -direction at both ends ($u_z = 0 \text{ mm}$). In addition, due to the symmetry of the model only one half of the original geometry has to be considered when prescribing symmetry boundary condition ($u_x = 0 \text{ mm}$) on the symmetry line. As already investigated by [21] the displacements on a horizontal line in the middle of the cylinder, see Fig. 5.12a), are nearly constant $u_y^c = \text{const.}$ This additional assumption reduces the model size to one fourth of the original size as shown in Fig. 5.12b). In order to move both bodies towards each other the prescribed displacements at the bottom of the plate $u_y^p = \lambda_i \cdot 0.005 \text{ mm}$ as well as on the top surface of the cylinder $u_y^c = \lambda_i \cdot 0.005 \text{ mm}$ are increased step by step using the load factor $\lambda_i \in \{100, 1, \dots, 1\}$. The force F needed to

press the bodies onto each other is then computed in a post-processing step by integrating the stresses σ_{yy} over the top surface of the cylinder. In the first load-step both bodies are moved such that the initial gap $g_0 = 1$ is closed. In all further steps the indentation is increased constantly by 0.01 mm. In order to compare the numerical and the analytical solution we use the analytically computed stress profile and compare it to the contact stress of the numerical model. To this end 180 post-processing points are distributed over the cylinder surface from $s = [0, \frac{\pi}{180}, \dots, \pi]$, giving a fine post-processing grid to extract the high frequency oscillations that can occur in the contact zone, see Fig. 5.12b). Different parameters of the numerical method and their influence on the results have to be considered. Let us briefly summarize these parameters and discuss their expected influence on the results.

- **The influence of a h - and p -refinement**

In order to investigate the influence of the finite cell discretization on the results we consider three different Cartesian grids, where the cell size is $h_c = 1$ mm, 0.4 mm and 0.1 mm, see Fig. 5.13. Since the plate is rigid it is sufficient to discretize it by one finite cell. In addition for each cell discretizing the cylinder we increase the polynomial order from $p = 4$ to $p = 6$.

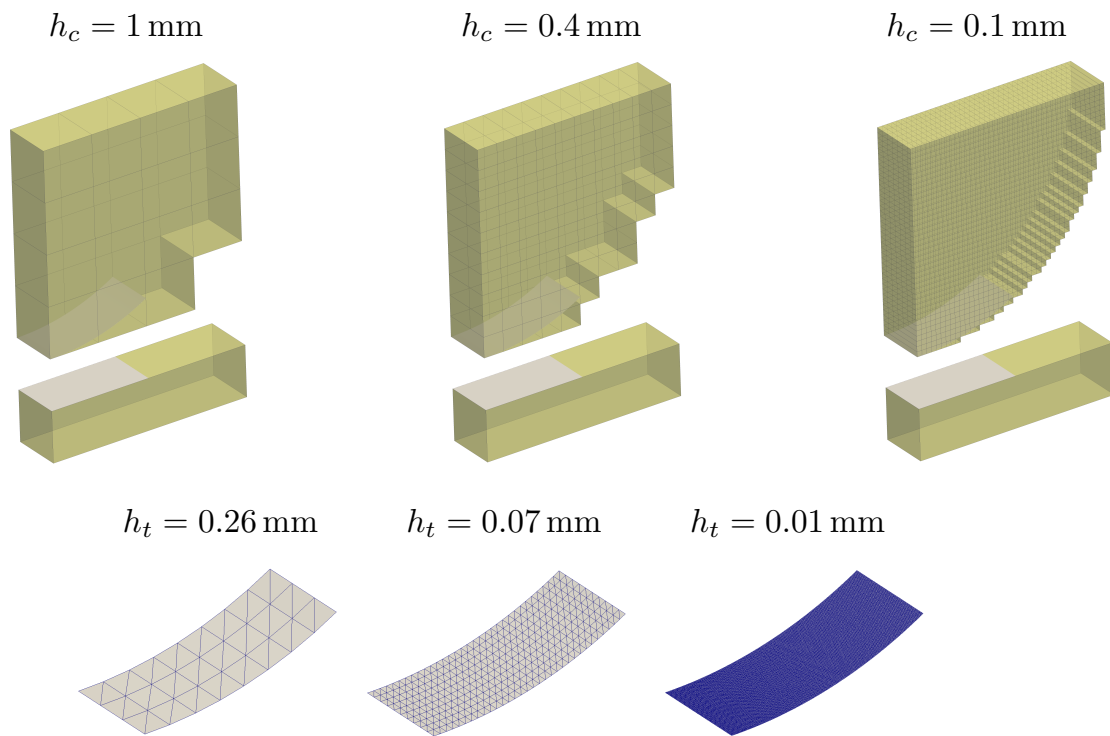


Figure 5.13: Finite cell mesh showing the location of the contact surface and the contact surface discretizations by triangles. Empty finite cells are removed from the discretization leading to the staircase shape of the discretization.

- **The size of the contact triangles h_t and the number of slave points n_s**

The number of triangles distributed over the contact interface has a direct influence on the geometrical approximation error e_g , see Fig. 5.14. In order to study this effect

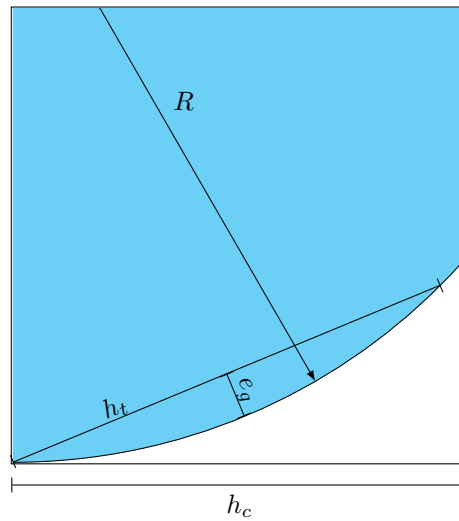


Figure 5.14: Measure of the geometrical discretization error given by the point on the triangle that has the maximum deviation from the cylindrical surface.

the contact surface of the cylinder is discretized by three different regular grids where the triangle edge length changes $h_t \in [0.26 \text{ mm}, 0.07 \text{ mm}, 0.01 \text{ mm}]$, see Fig. 5.13. The maximum geometrical approximation error is then computed as $e_g = 2.113 \cdot 10^{-3} \text{ mm}$ for $h_t = 0.26 \text{ mm}$, $1.531 \cdot 10^{-4} \text{ mm}$ for $h_t = 0.07 \text{ mm}$ and $3.125 \cdot 10^{-6} \text{ mm}$ for $h_t = 0.01 \text{ mm}$, respectively. The contact interface of the rigid plate is planar and is therefore discretized by two triangles only.

The numerical model enforces the contact conditions at discrete positions, therefore the number of slave points distributed over the contact triangles n_s has a direct influence on the accuracy of the numerical approximation. We study this effect by increasing the order of the integration rule n_o used to collocate the contact conditions. For the numerical integration we use Gauss-Legendre integration points for triangles, see Tab. A.1. In order to map the order of the integration rule n_o and the size of the contact elements h_t to the number of slave points distributed in one cell we refer to Tab. 5.1 which represents the maximum number of slave points in one cell. It is noteworthy that only at a subset of these the contact conditions will be enforced in one cell.

- **The penalty factor β**

In order to enforce the contact conditions we use the penalty method. On the one hand a high penalty factor reduces the penetration of the bodies which leads to a more stringent fulfillment of the non-penetration condition and in turn to more accurate results. On the other hand it can also lead to ill-conditioning of the stiffness matrix which can cause inaccurate results and convergence problems.

- **Influence of the indentation depth d**

When increasing the indentation depth $d \in [0.1 \text{ mm}, 0.2 \text{ mm}, \dots, 0.9 \text{ mm}]$ it is expected that the solution improves because the contact zone increases and hence the load is distributed over a larger area. In particular we expect that when the end of the contact zone coincides with a cell interface the induced oscillations are clearly reduced.

		$h_c = 0.1 \text{ mm}$		$h_c = 0.4 \text{ mm}$		$h_c = 1 \text{ mm}$	
		n_o	n_s	n_o	n_s	n_o	n_s
$h_t = 0.01 \text{ mm}$	1	2200	1	8500	1	21700	
	2	6600	2	27500	2	65100	
	3	8900	3	34300	3	86900	
	4	13400	4	51600	4	130400	
	5	15600	5	60100	5	152100	
$h_t = 0.07 \text{ mm}$	1	40	1	130	1	330	
	2	110	2	410	2	990	
	3	160	3	510	3	1320	
	4	220	4	800	4	1980	
	5	240	5	920	5	2310	
$h_t = 0.26 \text{ mm}$	1	6	1	12	1	24	
	2	9	2	30	2	72	
	3	12	3	42	3	96	
	4	21	4	60	4	153	
	5	32	5	69	5	177	

Table 5.1: Maximum number of slave points per cell.

5.6.2.1 Contact mesh refinement

In a first study we investigate the influence of a contact mesh refinement on the results. In particular we consider the interplay between the contact surface and the finite cell discretization. To this end we perform an h -refinement of the finite cell discretization together with a refinement of the triangles h_t used to discretize the contact zone. Increasing the number of slave points n_s distributed over each triangle has a similar effect on the results than increasing the number of triangles itself, but leads to a larger geometrical error since they are not exactly located on the boundary of the geometry, see Fig. 5.14. Therefore we investigate this influence at the same time. Tab. 5.1 gives the number of slave points that are distributed over one finite cell depending on the integration order, the size of the contact elements and the size of the finite cells. The polynomial order of the shape functions of the finite cells is chosen as $p = 4$. The contact conditions are enforced using a penalty value of $\beta = 10^7$ and an α -value of 10^{-10} is used to penalize the fictitious domain. Fig. 5.15 shows the results of this study by comparing the normal contact stress to the analytical solution for $d = 0.09 \text{ mm}$. The numerical contact stress was extracted at the positions as shown in Fig. 5.12b) and normalized by the maximum analytical contact stress using Eq. (5.50) and the width of the contact interface obtained from the analytical solution given by Eq. (5.51). Before we discuss the individual results in detail, let us first summarize the most important findings.

- The enforcement of contact conditions introduces a singularity which leads to oscillations of higher amplitude outside the contact zone. These oscillations are a well-known and documented problem, see [20].
- In the example with the discretizations of $h_t = 0.26 \text{ mm}$ and $h_c = 0.1 \text{ mm}$ with $n_o \in$

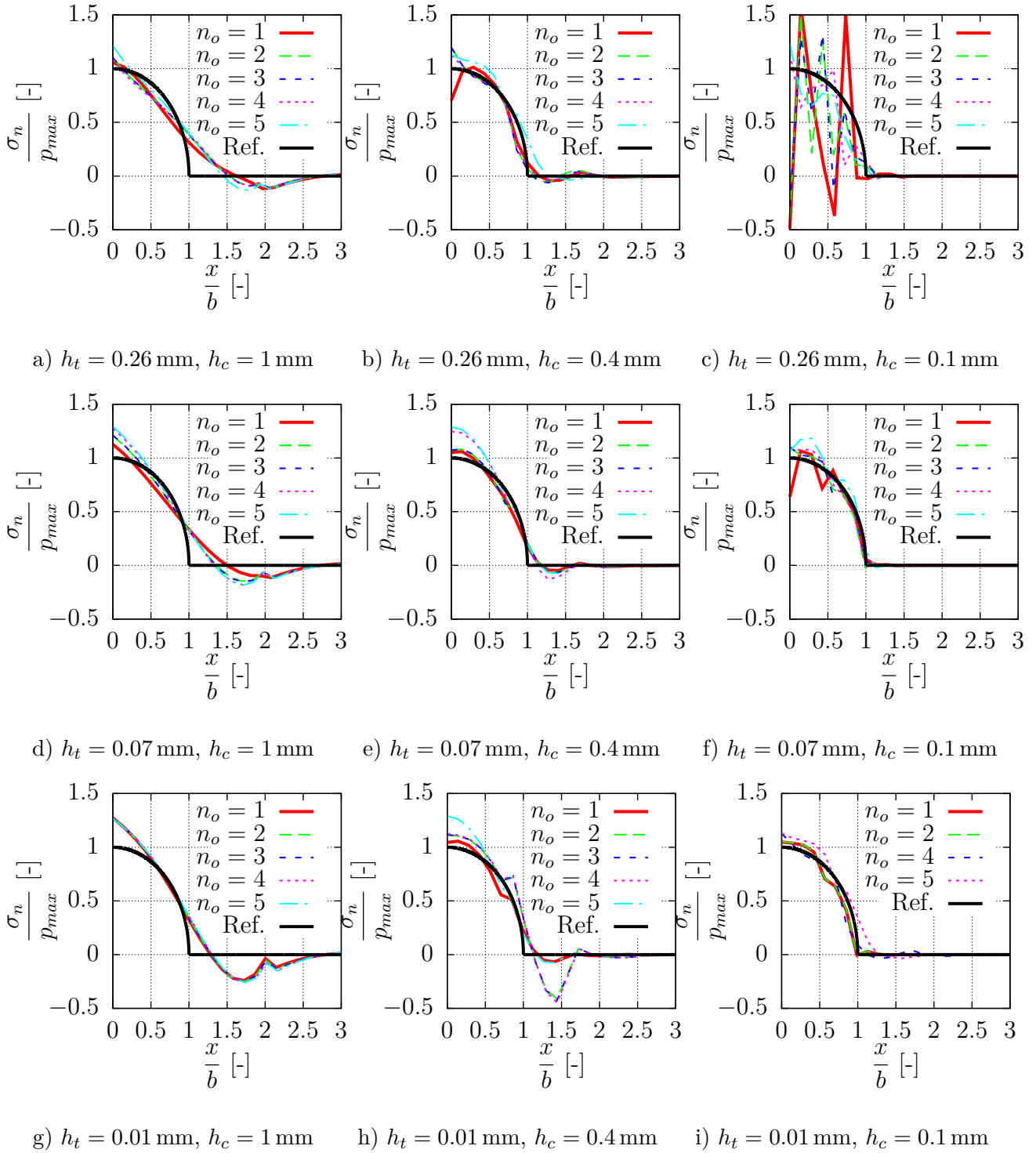


Figure 5.15: Comparison of contact stresses for different contact surface discretizations.

[1, 2, 3] to few slave points are distributed on the contact interface in order to enforce the contact conditions which leads to large deviations from the analytically computed stress profile. This result corresponds to the results shown in Fig. 5.10 where for a polynomial order of $p = 4$ at least $n_s = 12$ slave points were needed to enforce the contact conditions.

5.6.2.2 h - and p -refinement

In the following we use the surface discretization with $h_t = 0.01$ mm and one slave point $n_s = 1$ to investigate the influence of a p - and h -refinement on the contact stresses for an indentation depth of $d = 0.09$. The penalty factor used in this example is the same as in the previous example $\beta = 10^7$. Fig. 5.16 shows exemplarily the contact stress distribution on the cylinder. In Fig. 5.17 the detailed contact stress distribution of the numerical computations is compared

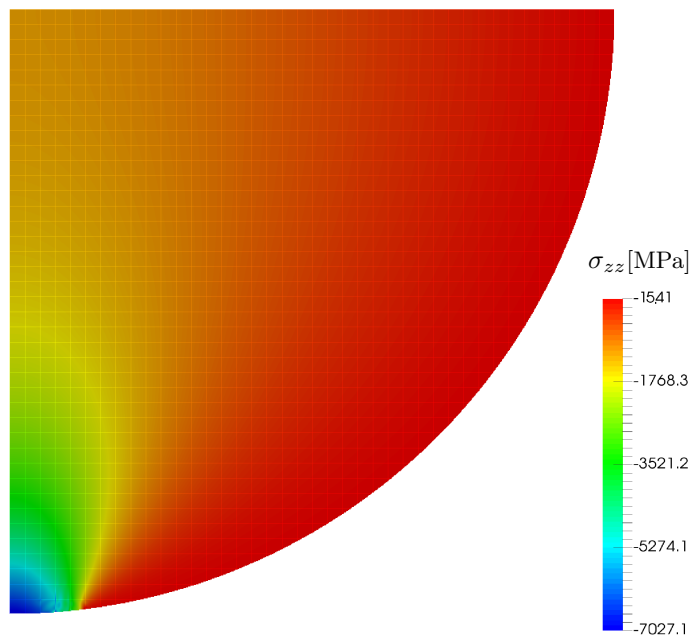
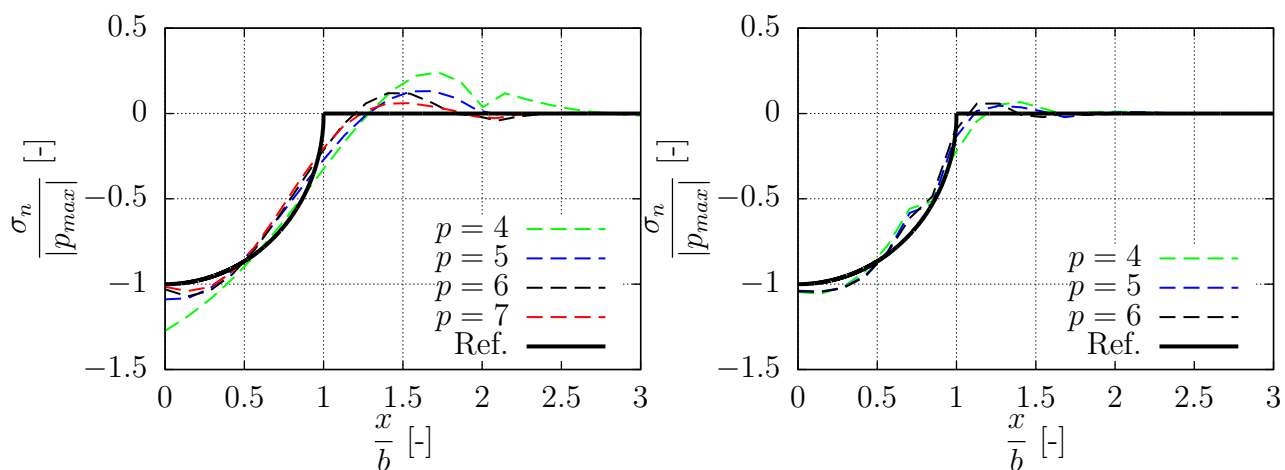
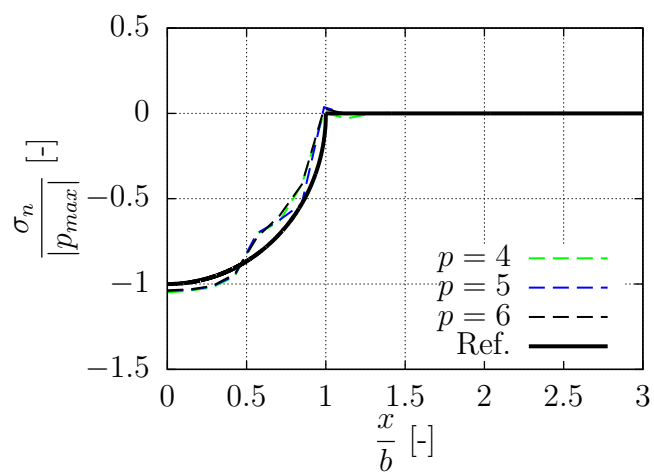


Figure 5.16: Contact stress distribution σ_{zz} for $h_t = 0.01$ mm and $p = 6$.

to the analytical solution of the problem. The numerical solution approximates the analytical solution more closely when using a higher polynomial degree. An h -refinement reduces the zone where the stresses oscillate which also leads to a better approximation of the contact stresses. The findings from this study can be summarized as follows:

- An h -refinement reduces the zone of stress oscillations which are generally damped out within one to two finite cells.
- A p -refinement also reduces the zone of stress oscillations but is less effective than an h -refinement.

a) $h_c = 1$ mmb) $h_c = 0.4$ mmc) $h_c = 0.1$ mmFigure 5.17: Comparison of contact stresses profiles for an h - and p -refinement.

5.6.2.3 Influence of the penalty factor

In another study we investigate the influence of the penalty factor on the results. A high penalty value leads to less penetration of the contact bodies and the non-penetration condition is fulfilled more accurately. On the other hand a high penalty value leads to ill-conditioning of the global equation system. In Fig. 5.18 the results of this investigation are presented. A penalty value of $\beta = 10^7$ seems to give the same solution for $p \in [4, 5, 6]$. Higher values

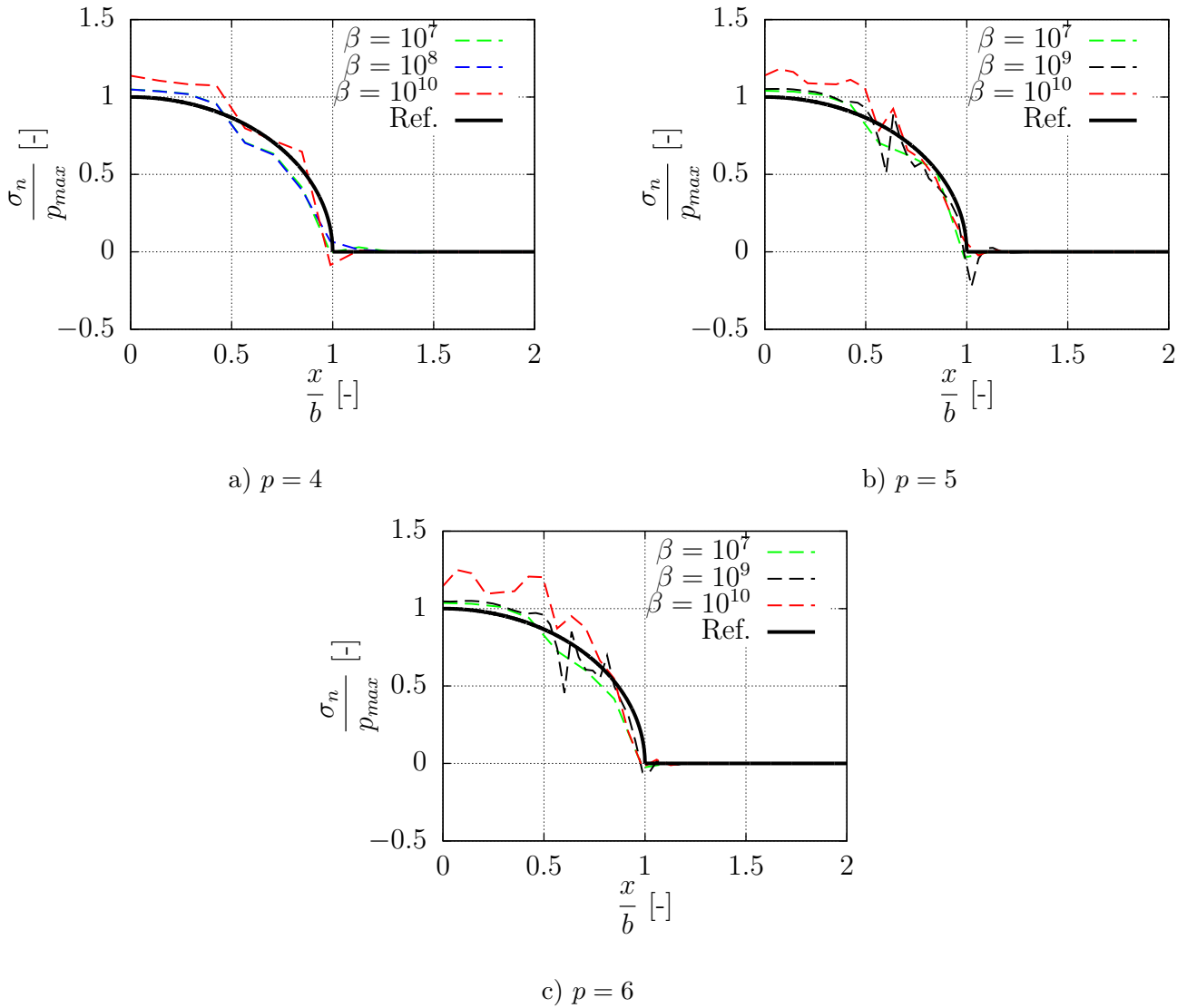


Figure 5.18: Comparison of contact stresses for different penalty parameters.

lead to stress oscillations at the contact interface, which can be especially seen for $p \in [5, 6]$. For penalty values of $\beta = 10^{10}$ the stresses diverge from the analytical solution. Interestingly $p \in [5, 6]$ seem to be more affected than $p = 4$ which still shows an acceptably accurate stress profile for $\beta = 10^{10}$. For $\beta = 10^{11}$ or $\beta = 10^{12}$ the stress distribution strongly deviates from the analytical solution as shown in Fig. 5.19.

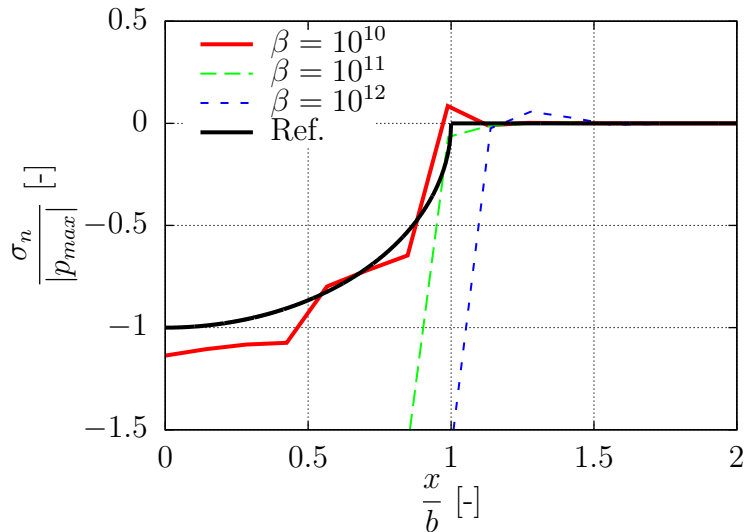


Figure 5.19: Comparison of contact stresses profiles for $p = 4$ with $\beta \geq 10^{10}$.

5.6.2.4 Influence of indentation depth

In the next study we investigate the contact stress for different indentation depths $d \in [0.2, 0.3, \dots, 0.9]$. The size of the finite cells in this example is $h_c = 0.1$ mm and the size of the contact elements is $h_t = 0.01$ mm.

The results of this investigation are presented in Fig. 5.20 and Fig. 5.21 for a polynomial degree of $p = 4$ and $p = 6$ respectively. In Fig. 5.20a) and Fig. 5.21a) we compare the contact stress profiles. In order to compare the numerical to the analytical results and to compare different load-steps we scaled the x - and y -axis to the analytically computed contact width using Eq. (5.51) and the analytically computed maximum contact stress using Eq. (5.50) respectively. The first load-step $d = 0.02$ mm overestimates the contact stresses and the oscillations outside the contact zone are large. For larger indentation values the oscillations reduce and the contact stress profile seems to converge to stress values slightly higher than the analytical solution.

Fig. 5.20b) and Fig. 5.21b) depict the gap function evaluated at the post-processing points. As a trend we see that the contact zone is overestimated for small indentations. Especially for the first load-step $d = 0.02$ mm the contact width is overestimated, for $d > 0.03$ mm it converges to the analytical solution. The location of the end of the contact zone with respect to cell interfaces seems to have only minor effects on the amount of oscillations outside the contact zone for the investigated discretizations. Otherwise for some indentation depth, where the end of the contact zone coincides with a cell interface, the oscillations should be clearly reduced. Interestingly, there is a general trend which shows that for higher indentation depths the oscillations are dampened out. This might be due to the fact that a larger contact zone leads to less stress concentration at the contact interface and consequently a less pronounced singularity. The findings from this study can be summarized as follows:

- The contact stress has the same profile as the analytical solution but with a slightly higher peak stress.
- The contact surface width is overestimated for small indentation depths.

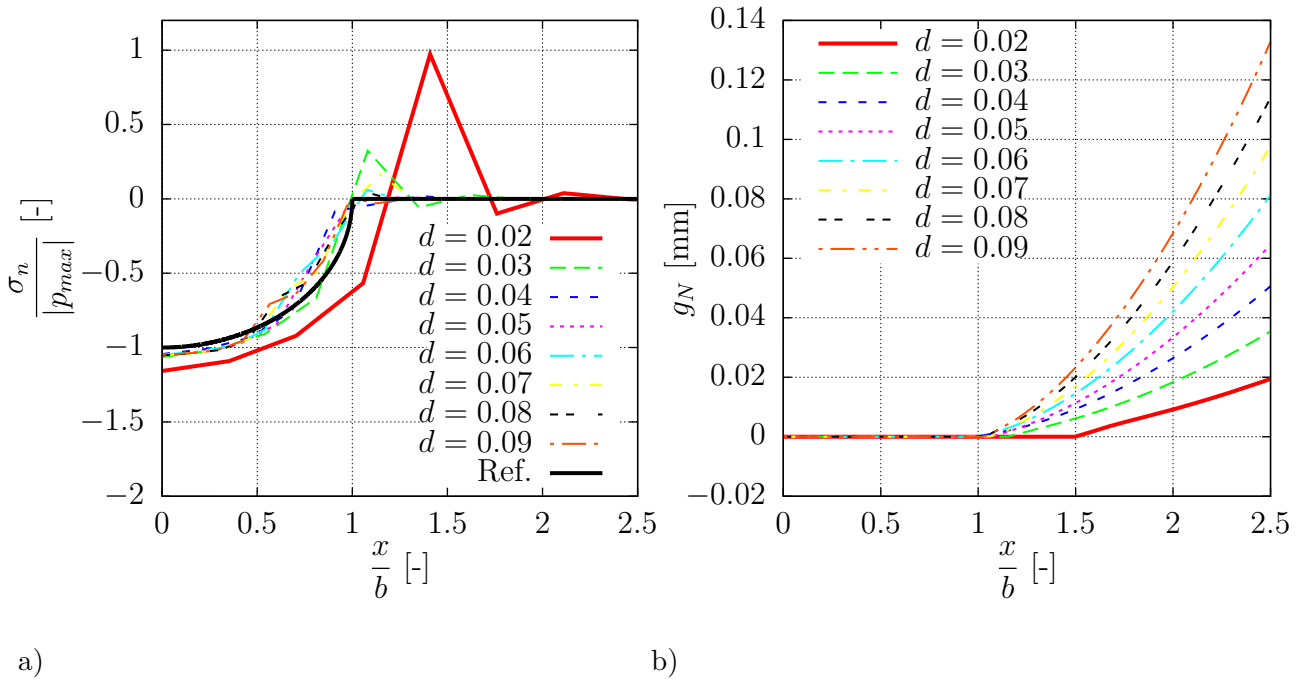


Figure 5.20: Influence of indentation depth $p = 4$ on a) contact stress and b) gap vs. normalized contact width.

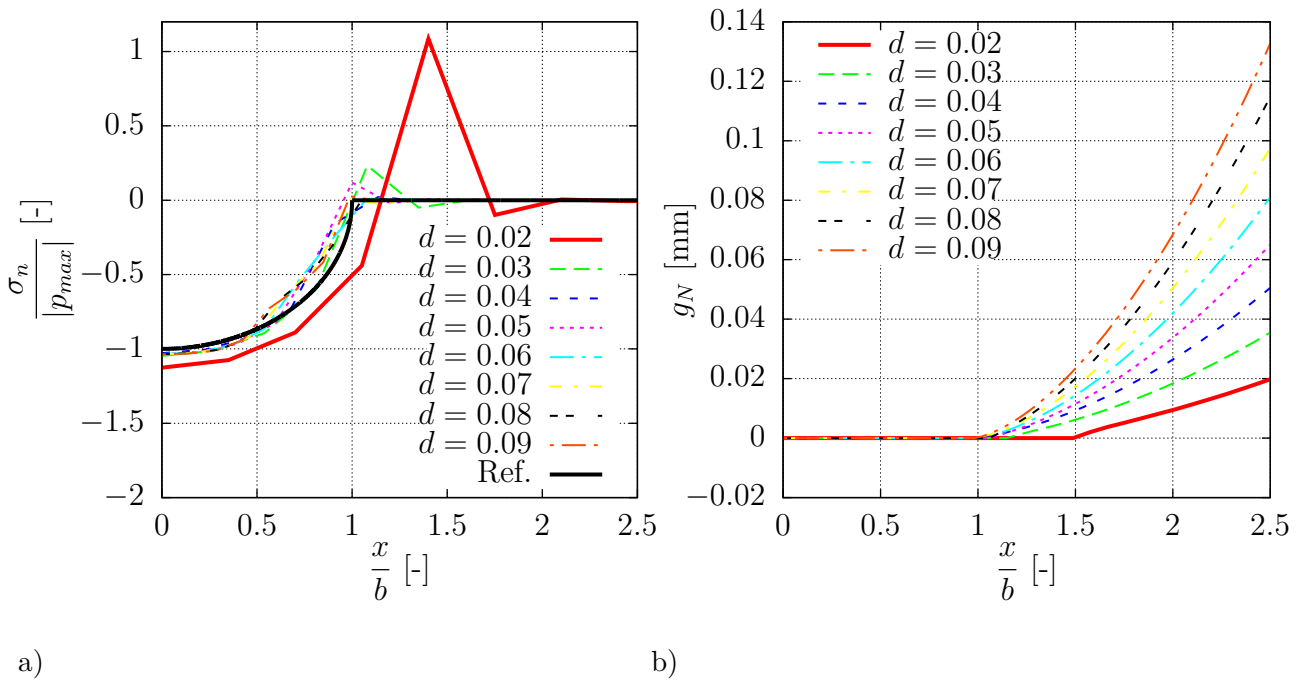


Figure 5.21: Influence of indentation depth for $p = 6$ on a) contact stress and b) gap vs. normalized contact width.

- For a higher indentation the contact stress oscillations are reduced.

5.6.2.5 Influence of the fictitious domain

The fictitious domain in the finite cell method is penalized by the indicator function $\alpha = 10^{-q}$ which serves to stabilize the computations. A higher value for the indicator function leads to more stable computations but also affects the solution. Hence it is important to examine its influence. In Fig. 5.22 the difference in the stress profile for two different values of the indicator function are presented. The chosen values $\alpha = 10^{-5}$ and $\alpha = 10^{-10}$ represent the range of what is usually applied for stabilization. Since there is no obvious difference between

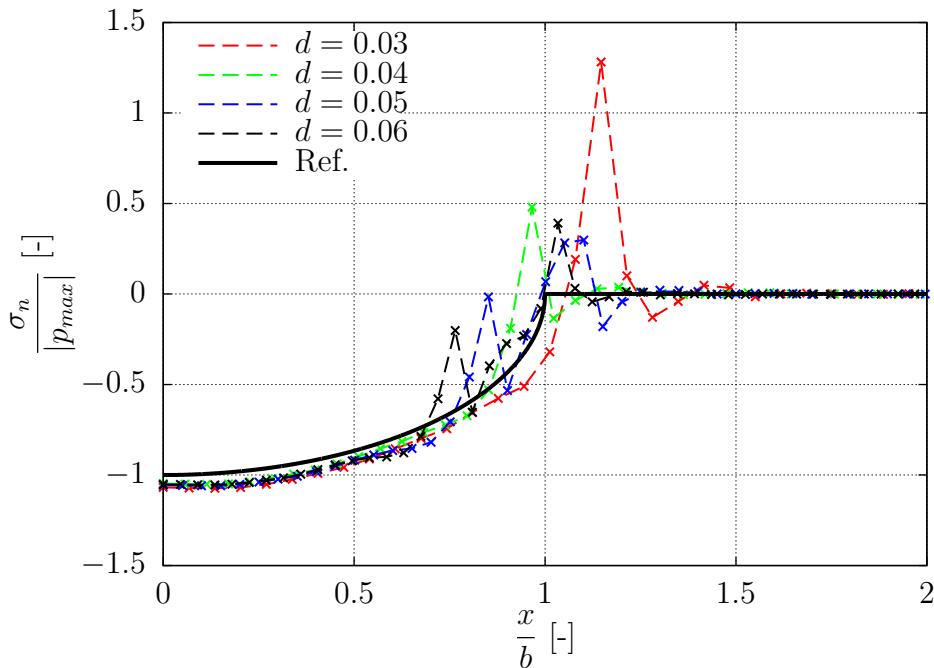


Figure 5.22: Influence of the fictitious domain on contact stress. The dashed lines show the contact stress for $\alpha = 10^{-5}$ and the cross markings show the profile for $\alpha = 10^{-10}$.

the solutions we conclude that a penalization of the fictitious domain by $\alpha = 10^{-5}$ still gives accurate results.

5.6.2.6 Influence of the numerical quadrature scheme

The finite cell method requires a special quadrature to integrate cut cells. In section 3.3 the adaptive Gaussian quadrature based on an octree refinement scheme was explained. A new method for the integration of cut cells which provides less quadrature points is the *moment-fitting method*. Details explaining the method are given in [36, 31]. By means of a small example we compare both methods in terms of the contact stress. Comparing the stress profile in Fig. 5.23 there is no significant influence of the quadrature scheme on the results of the FCM computation. Hence it is preferable to use the moment-fitting method in order to reduce the computational costs.

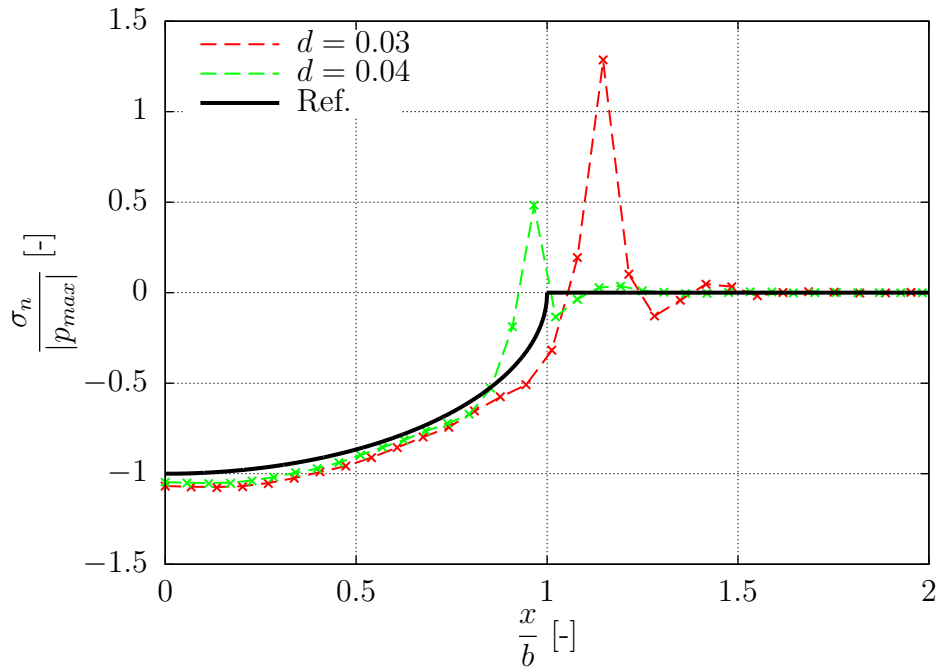


Figure 5.23: Influence of the quadrature scheme on the contact stress profile. The dashed line shows the contact stress profile using the moment fitting method and the cross points show the profile for the adaptive integration.

5.6.2.7 Investigation of contact conditions

In the previous examples the contact algorithm was such that whenever a penetration was detected the contact conditions were enforced, giving the contacting body no option to separate after a first initial contact even if the contact stresses become tensile stresses. By a slight variation of the contact algorithm the stresses at the slave points are evaluated after each Newton-Raphson iteration and whenever tensile normal stresses occur in the contact zone, the contact conditions are released. This option is investigated in the following. Similar to the previous examples we choose the finite cell discretization with $h_c = 0.1$ mm and a polynomial order of $p = 6$ for the shape functions. The contact surface discretization is set to $h_t = 0.01$ mm. The penalty parameter for the contact is $\beta = 10^9$ and the indicator function is $\alpha = 10^{-10}$.

Fig. 5.24 depicts the results of this study. Compared to the example where the contact surface can not separate, see Fig. 5.21, the width of the contact zone is now close to the analytical solution for $d = 0.02$ mm and the contact stress profile in Fig. 5.24a) has the same shape as the analytical.

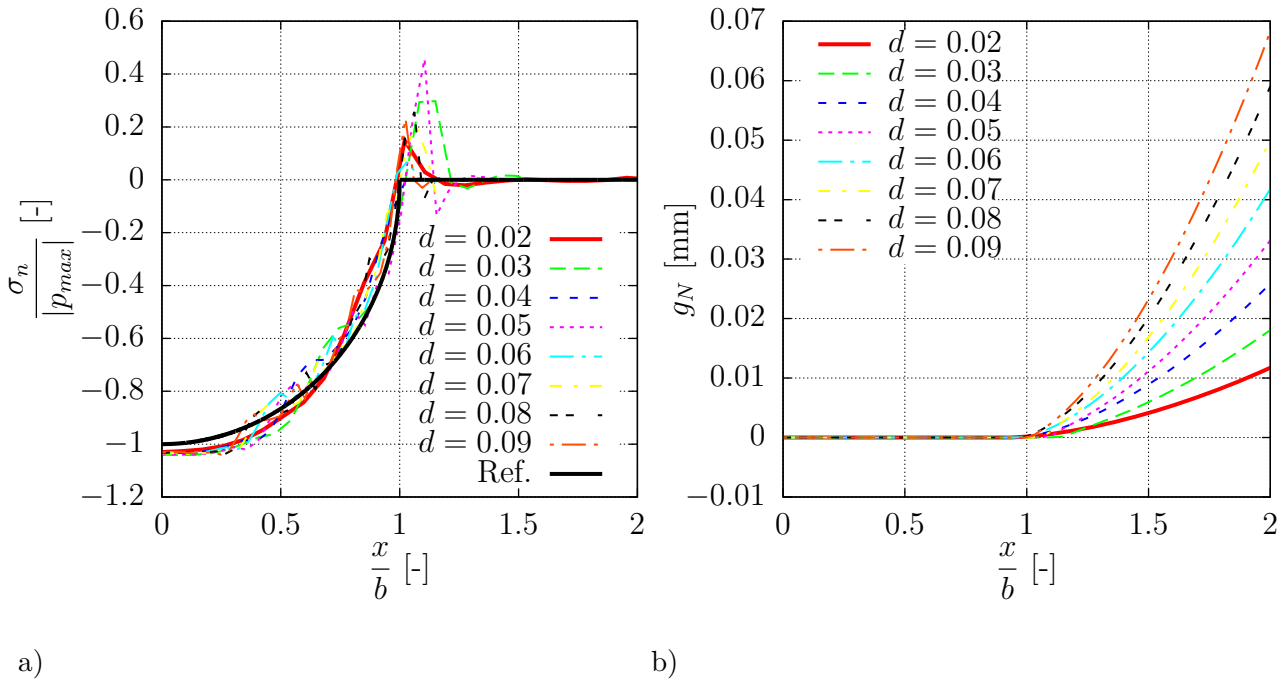


Figure 5.24: a) Normalized contact stress profile and b) gap vs. normalized contact width.

5.6.3 Frictionless contact

5.6.3.1 Cylinder and a rigid plate

In this section we investigate the frictionless contact formulation for the same problem already presented in section 5.6.2. To shorten the investigations we assume that the optimal parameters found in the previous investigations also hold for the frictionless contact example. These are especially the penalty factor of $\beta = 10^7$ and an integration (collocation) order of $n_o = 1$ for the contact elements. Further we use the contact surface discretization with an element size of $h_t = 0.01$ mm and finite cells with a size of $h_c = 0.1$ mm. The results of the simulation for different polynomial orders $p \in [4, 5, 6]$ are presented in Fig. 5.25. A comparison of the results obtained with the sticking contact formulations, as shown in Fig. 5.21a) and Fig. 5.24a), with the results of the frictionless contact formulation, as depicted in Fig. 5.25c) for $p = 6$, shows that the stress oscillations at the end of the contact interface are visibly reduced and also the profiles match much better.

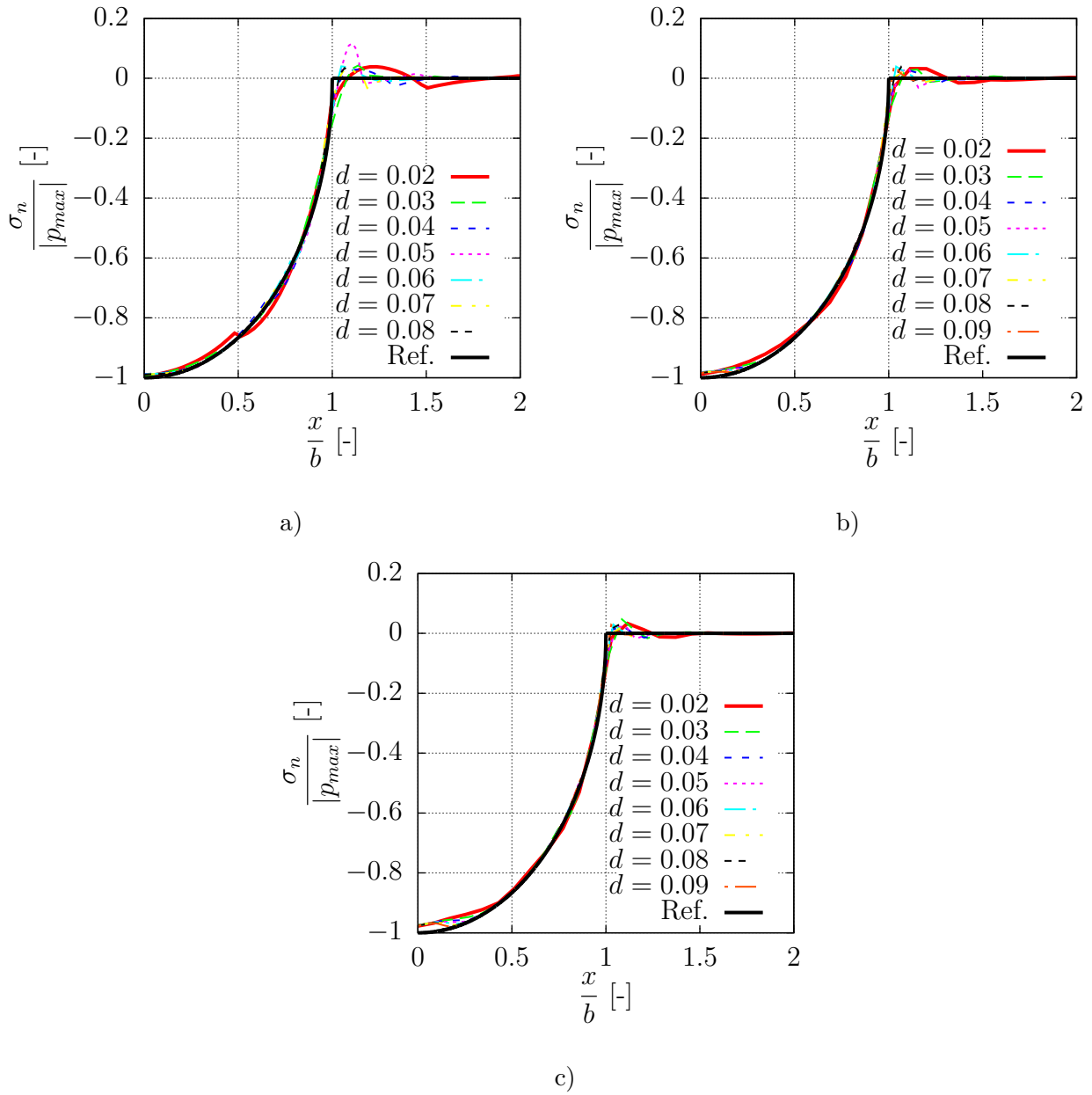


Figure 5.25: Distribution of the normal contact stress for a) $p = 4$, b) $p = 5$ and c) $p = 6$.

5.6.3.2 Cylinder and a rigid plate with sliding

In the following we use the frictionless contact formulation for a problem where large sliding between the contact interfaces of a deformable cylinder and a rigid plate occurs, see Fig. 5.26. At time $t = 0$ the cylinder is located at the left end of the plate, without being in contact with the plate. The initial interference between the contact zones is $d = 0.1$ mm. The cylinder is then moved in tangential direction of the top surface of the rigid plane.

The discretization of the problem consists of finite cells with a size of $h_c = 0.4$ mm and

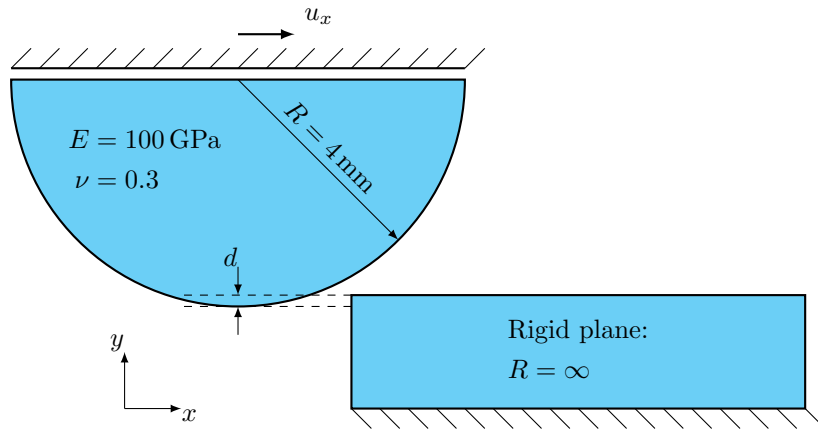


Figure 5.26: Geometrical setting for the sliding cylinder.

the polynomial order of the shape functions is $p = 4$. The contact elements have a size of $h_t = 0.07$ mm and $n_o = 2$ slave (Gaussian) points are located on each triangle of the contact interfaces, see Fig. 5.27. In every load-step where the cylinder is totally located on

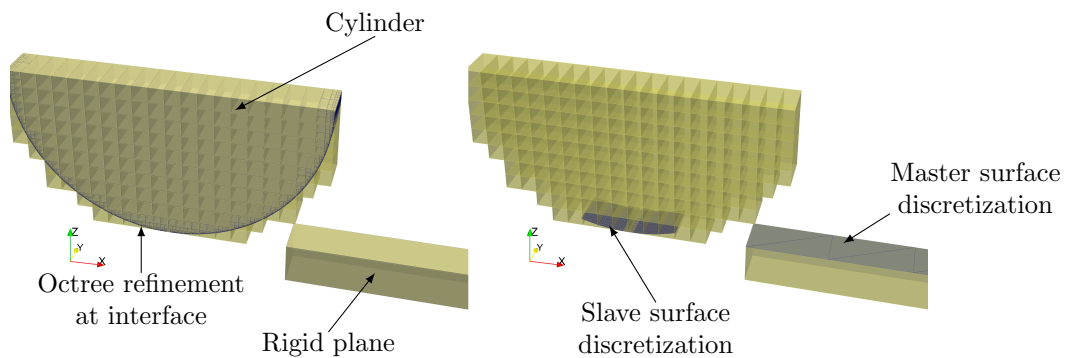


Figure 5.27: Discretization of the problem.

the rigid plane an analytical solution can be derived from the Hertz analytical solution using Eq. (5.50). A comparison of the numerical and analytical stress profiles for two different load-steps is shown in Fig. 5.28. Due to the too large finite cells the singular point at the end of the contact zone is not resolved accurately. Fig. 5.29 depicts a color plot of the stresses σ_{zz} at two different load-steps.

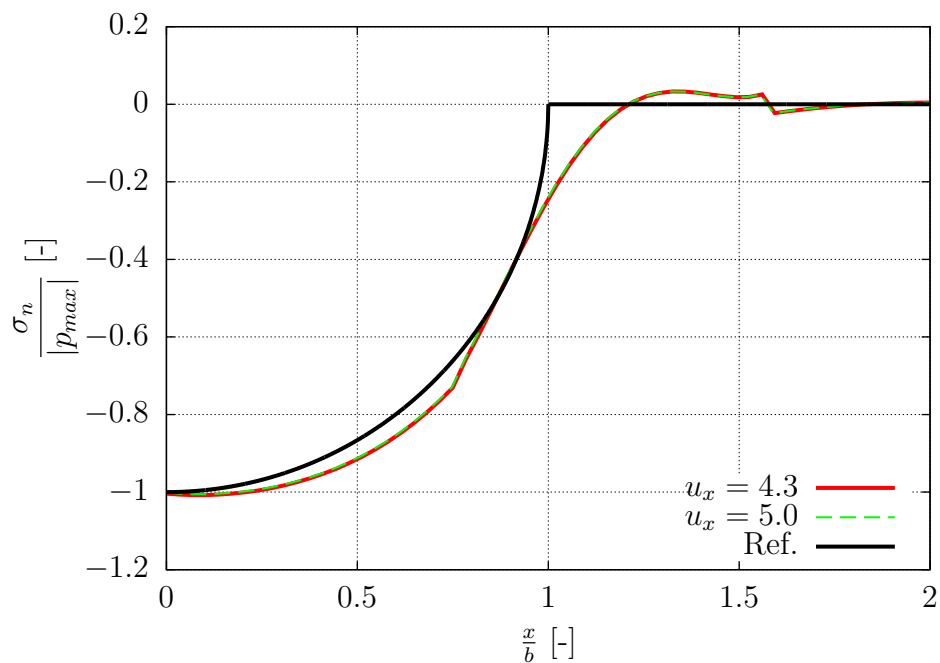
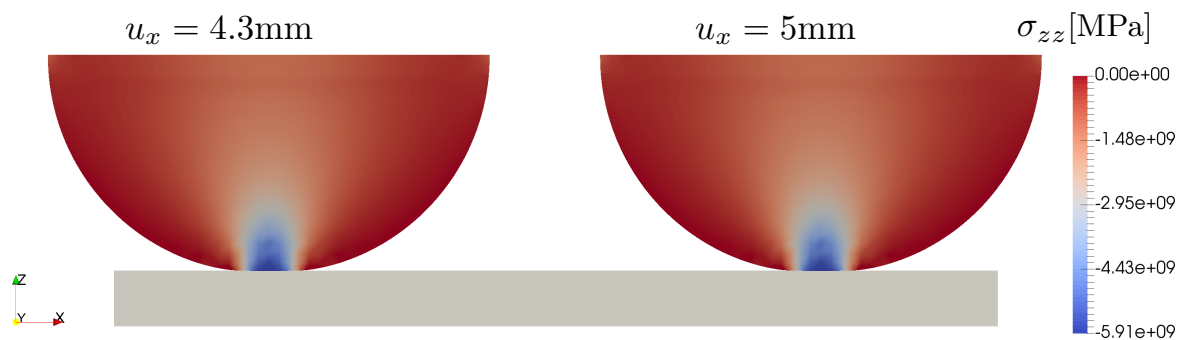


Figure 5.28: Contact stress distribution for two different load-steps.

Figure 5.29: Contact stress distribution at $u_x = 4.3$ mm and $u_x = 5$ mm.

5.6.3.3 Two deformable cylinders

In this section we present an example showing the contact between two deformable cylinders of the same size, see Fig. 5.30. In analogy to the unilateral sticking contact between a cylinder and a rigid plane presented in section 5.6.2, we used the symmetry of the model to reduce the model size to one half of the original geometry and prescribed symmetry boundary condition ($u_x = 0$ mm) on the symmetry line. As already investigated by [21] the displacements on a horizontal line in the middle of the cylinders, see Fig. 5.30, are nearly constant $u_y^1 = \text{const.}$, $u_y^2 = \text{const.}$. This additional assumption reduces the model size to one fourth of the original size as shown in Fig. 5.30. In order to move both bodies towards each other, we prescribed displacements at the top and bottom face of the cylinders $\Delta u_y^1 = -0.005$ mm, $\Delta u_y^2 = 0.005$ mm. The force F needed to press the bodies onto each other is then computed in a post-processing step by integrating the stresses σ_{yy} over the top surface of the cylinders and used to generate the analytical solution using Eq. (5.50). For the discretization of the problem we used 662 finite cells with a cell size of $h_c = 0.5$ mm and contact elements with a size of $h_t = 0.07$ mm. The polynomial order of the shape functions is $p = 3$. The elastic material parameters used for

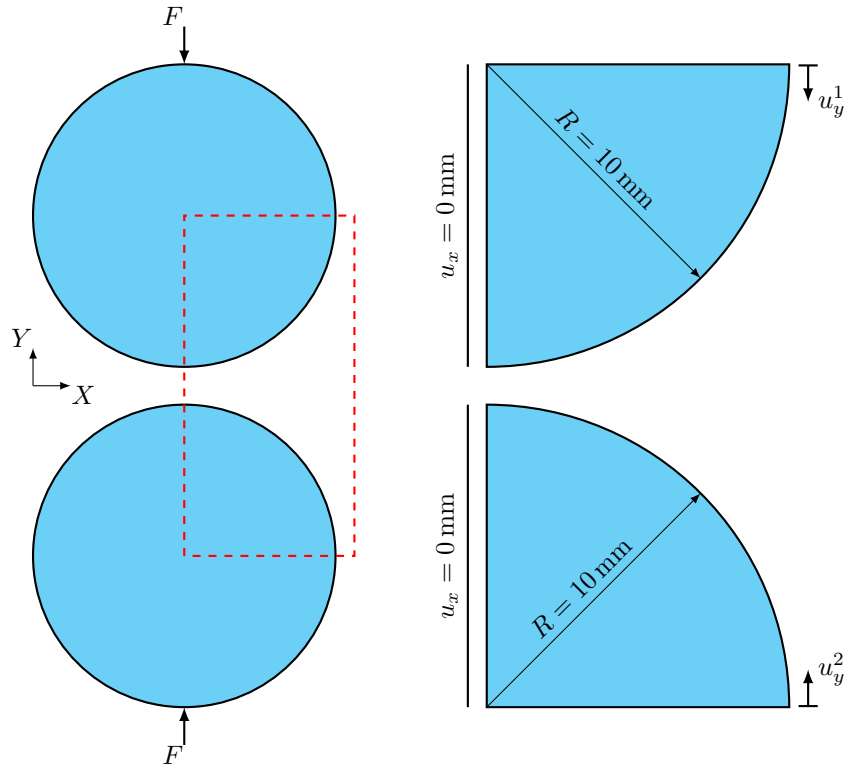


Figure 5.30: Contact between two deformable cylinders of the same size. For the numerical computations the model size was reduced.

the simulation are given in Tab. 5.2. In Fig. 5.31a) the contact stress profile for different indentations $d = \Delta u_y^2 - \Delta u_y^1$ are presented and compared to the analytical solution by Hertz. Fig. 5.31b) compares the contact stress on the master and the slave surface that only show small differences.

Parameter	Value		
Material	Hooke		
Young's modulus	E	100000	MPa
Poisson ratio	ν	0.3	
Order of ansatz	p	3	
Cell size	h_c	0.5	mm
Contact element size	h_t	0.07	mm
Loading (top)	Δu_y^1	-0.005	mm
Loading (bottom)	Δu_y^2	0.005	mm

Table 5.2: Material parameters applied in the simulation.

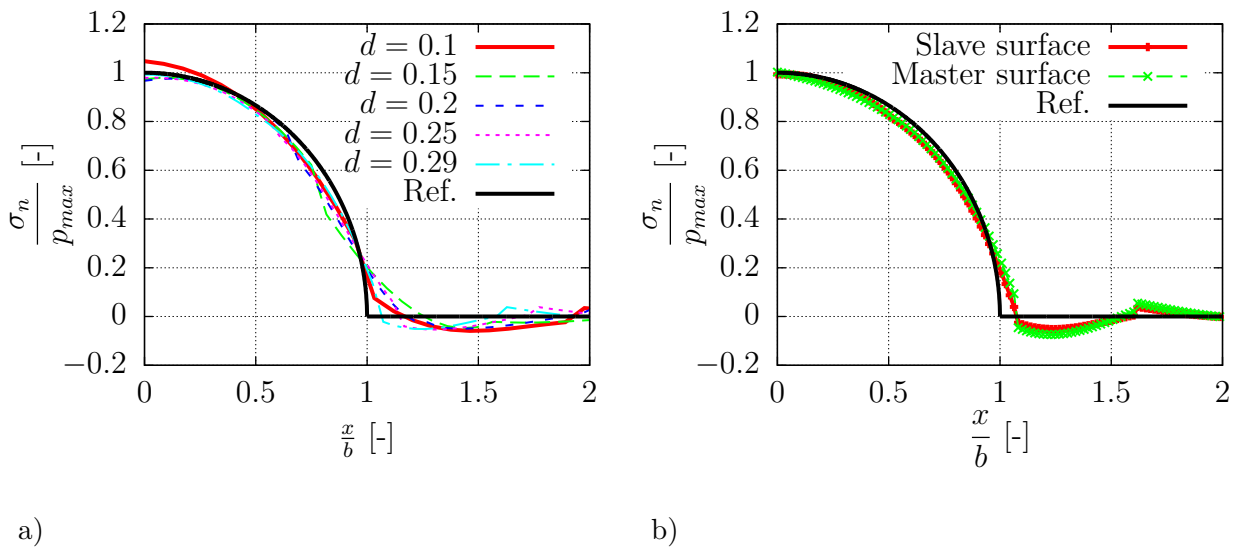


Figure 5.31: Contact stress distribution contact of two deformable cylinders. a) Normal stress for different indentation depths and b) comparison of normal stress on master and slave surface for $d = 0.29$ mm.

5.6.4 Self-contact of a metal foam

In the next example we consider the self-contact of a metal foam pore. From the pore a geometrical model describing its surface by triangles (STL) is available, see Fig. 5.32a). In order to test the contact approach for voxel models, a voxel model with a resolution of $31.64 \mu\text{m}$ is created, see Fig. 5.32b). Furthermore a discretization of the contact surface, see Fig. 5.33a),

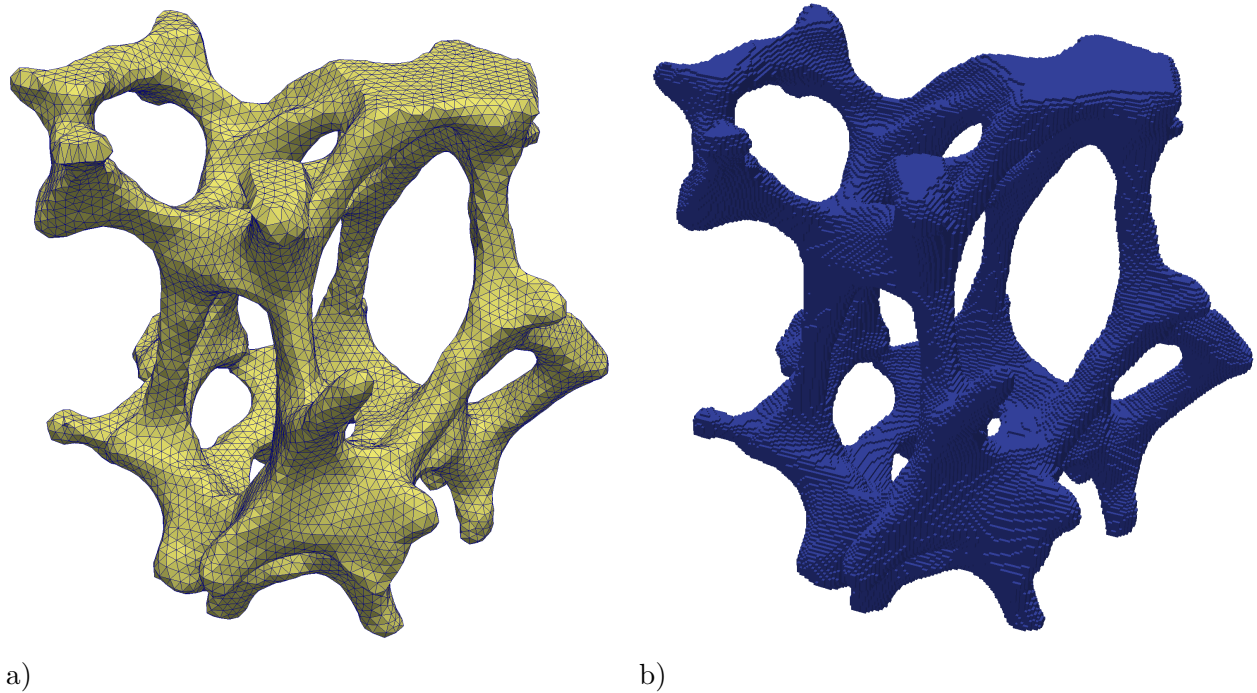


Figure 5.32: a) STL geometry and b) related voxel model of the pore.

is created from the STL geometry by moving its nodes such that they are located within the voxel model. In order to compress the pore displacement boundary conditions are applied to its upper and lower end suppressing all degrees of freedom. The load is applied by pressing the top surface of the pore downwards with increments of $\Delta u_y = -0.002 \text{ mm}$. Further parameters used for the simulation are given in Tab. 5.3. It needs to be mentioned that the geometrical nonlinearity is not taken into account in this simulation. While this assumption is not realistic it is necessary to obtain a stable simulation until self-contact can be observed. Fig. 5.34 shows the deformations of the pore for different load-steps. The first self-contact occurs at a displacement of 2.4 mm. Due to this the slope of the load-displacement curve increases slightly, see Fig. 5.35. From a displacement of about 3.5 mm on more and more points come into contact such that the slope increases even further. Fig. 5.34c) shows the pore when it is totally compressed. Self-contact can be observed at many locations indicated by a dot.

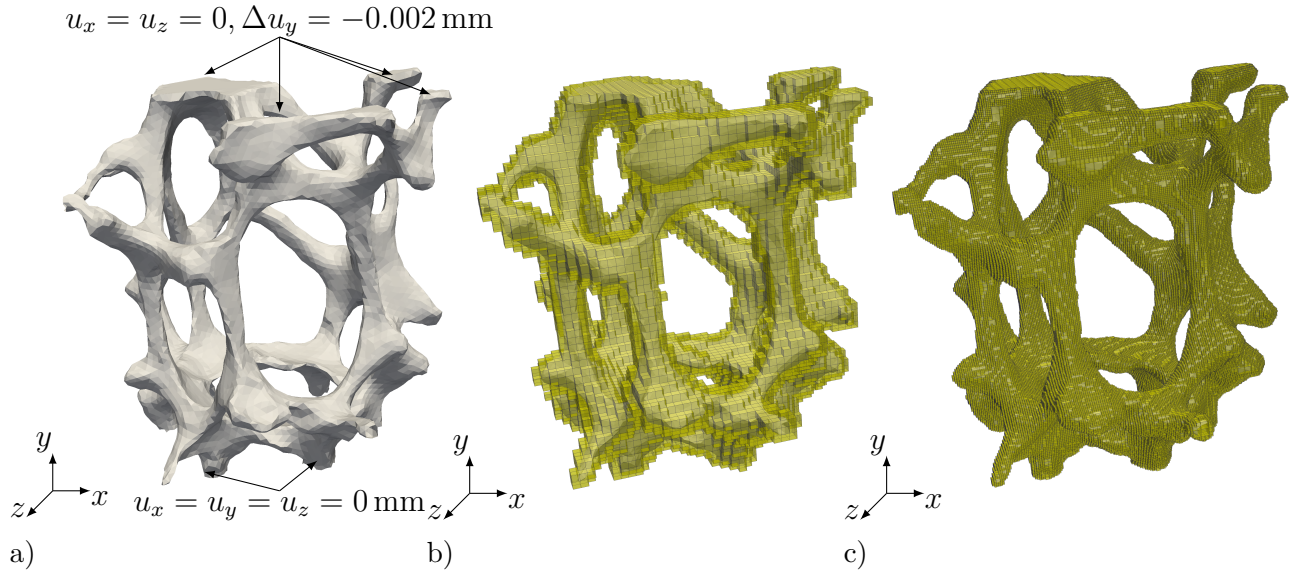


Figure 5.33: a) Contact surface discretization b) discretization of the geometry by 15228 cells and c) sub-cells used during adaptive integration.

Parameter		Value	
Material	Prandtl-Reuss		
Young's modulus	E	3838.95	MPa
Poisson's ratio:	ν	0.33	
Initial yield stress	σ_0	52.27	MPa
Hardening modulus	h	291.41	
Number of cells		15228	
Voxel/Cell		4^3	
Polynomial degree	p	3	
Loading (top)	$u_x = u_y = u_z$	0.0	mm
Loading (bottom)	$u_x = u_z$	0.0	mm
	Δu_y	-0.002	mm

Table 5.3: Parameter applied in the simulation.

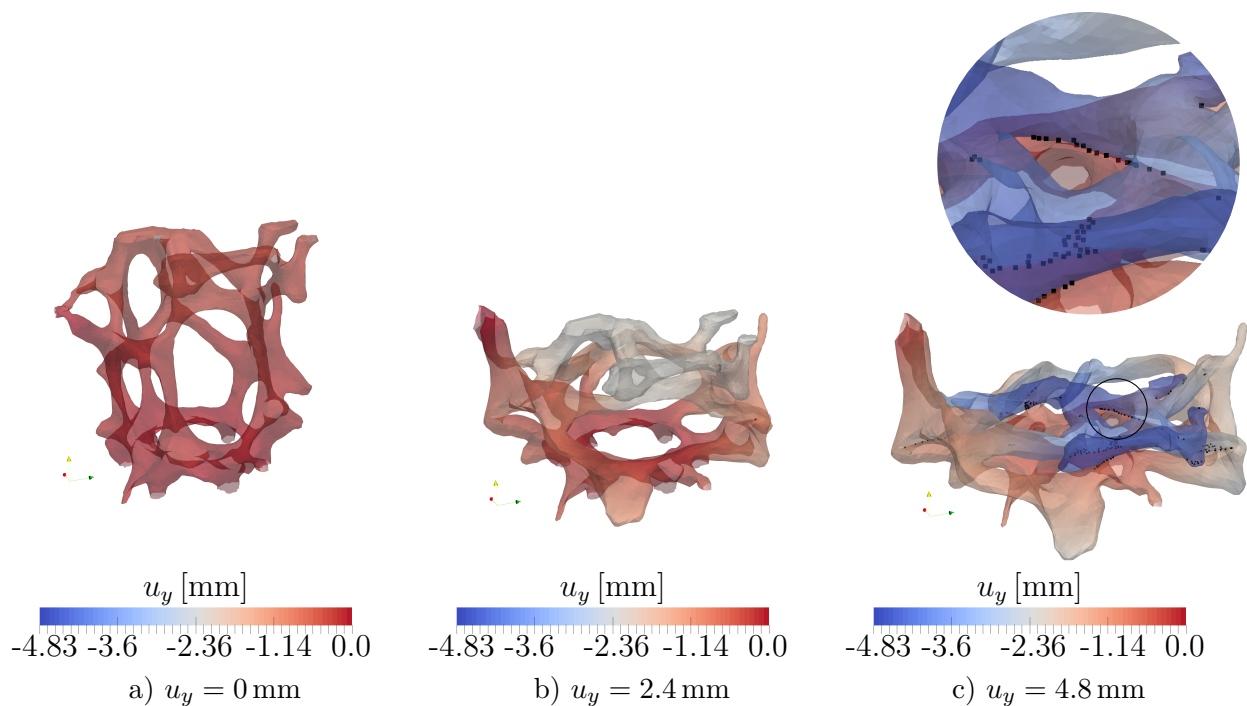


Figure 5.34: Deformation process of a pore with self-contact.

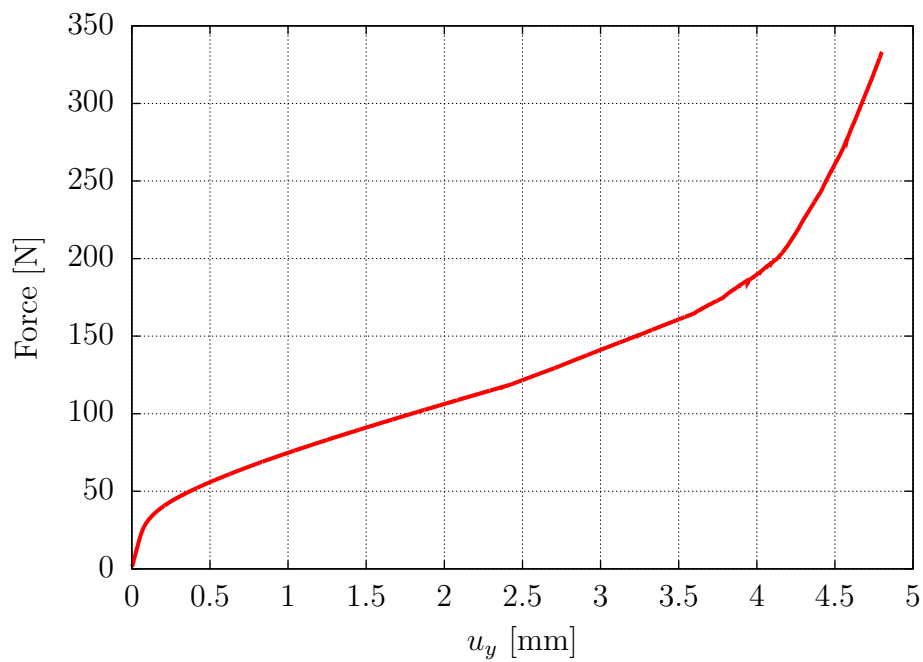


Figure 5.35: Load displacement curve for pore with self-contact.

Chapter 6

Aluminum foams

In this chapter we investigate the mechanical properties of aluminum foams on different scales numerically by means of the finite cell method and compare the results to experiments. Aluminum foams are highly heterogeneous materials. Their structure can be divided into several hierarchical levels, the *macro scale*, the *meso scale* and the *micro scale*, see Fig. 6.1. The

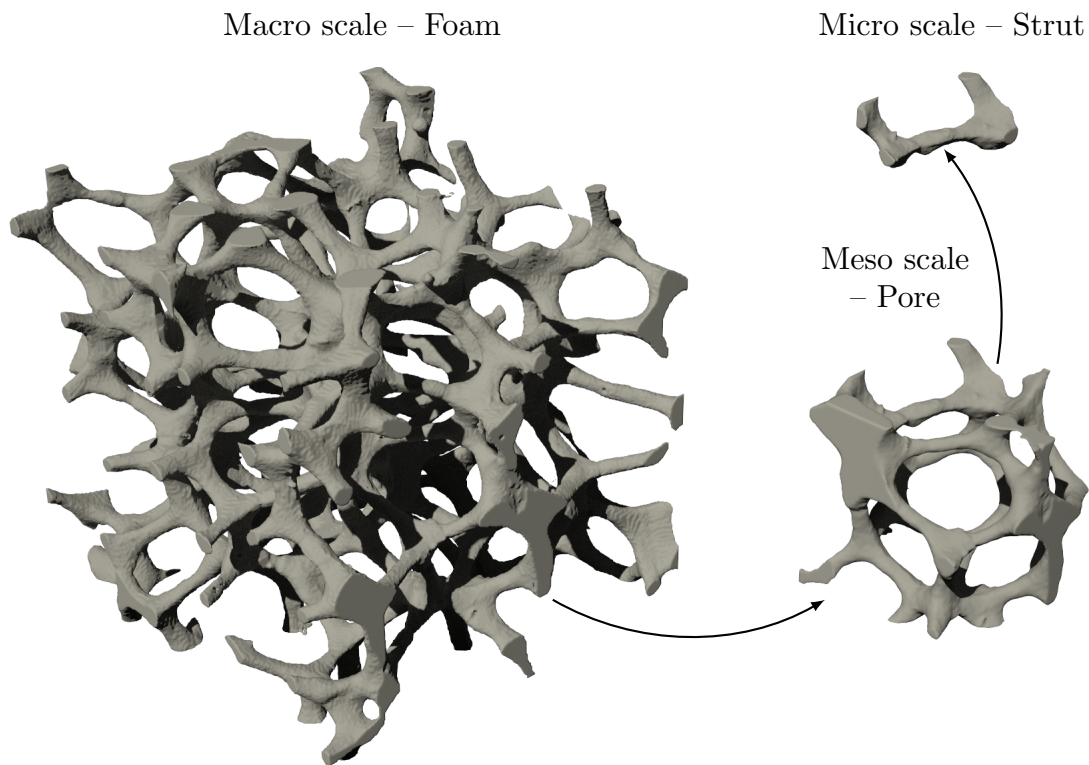


Figure 6.1: Scales of a metal foam.

definition of the different length scales of the foam is somehow arbitrary and depends on the purpose of the investigation. We will make use of the following definitions for the different scales:

- **Macro scale**

The macro scale comprises a representative sample of the foam, including at least 4 pores

in each direction and can be treated as a homogeneous media with effective material properties.

- **Meso Scale**

The meso scale includes a single pore.

- **Micro Scale**

The micro scale is formed by the struts of a pore and the knots that connect the struts.

6.1 The foam struts

Aluminum foams not only have a heterogeneous geometry with stochastic variations from pore to pore but the aluminum alloy also has a heterogeneous grain structure. Hence the material parameters of the aluminum are different compared to the bulk material.

Micro tensile test

In order to obtain meaningful material parameters for the aluminum foam, single struts were subjected to microscopic tensile tests by [38]. The average value for the Young's modulus obtained from these experiments is given in Tab. 6.1. In order to determine the yielding

Parameter	Value		
Young's modulus	E	54.71 ± 9.58	GPa
Poisson's ratio:	ν	0.33	
Initial yield stress	σ_0	100.694	MPa
Saturation stress	σ_∞	412.484	MPa
Linear hardening	h	-584.166	MPa
Hardening exponent	ω	4.34	

Table 6.1: Material parameters for aluminum obtained from micro tensile tests [38].

curve, we extracted the plastic part of one of the stress-strain curve and performed a least squares fit of the following function:

$$\sigma(\alpha) = \sigma_0 + h\alpha + (\sigma_\infty - \sigma_0)(1 - e^{-\omega\alpha}) \quad (6.1)$$

to the experimental data. Here σ_0 denotes the *initial yield stress*, h the *hardening modulus*, σ_∞ the *saturation stress*, ω the *hardening exponent*. The parameters obtained from the least squares fit are also given in Tab. 6.1.

Micro compression test

Besides the micro tensile experiments the struts were also tested under compressive loading [39]. The average value for the Young's modulus obtained from these tests is given in Tab. 6.2. Again we performed a least squares fit to the experimental yielding curve as described for the micro tensile tests and obtained the parameters for the yielding curve given in Tab. 6.2.

Parameter		Value	
Young's modulus	E	19.18 ± 7.67	GPa
Poisson's ratio:	ν	0.33	
Initial yield stress	σ_0	160.00	MPa
Saturation stress	σ_∞	236.23	MPa
Linear hardening	h	67.57	MPa
Hardening exponent	ω	102.78	

Table 6.2: Material parameters for aluminum obtained from micro compression tests [39]

6.2 Single pore experiments

In this section we investigate the deformation behavior of metal foams by means of single pores numerically and compare the results to experiments. To this end, different pores were extracted from a 20ppi aluminum foam ($\text{AlSi}_7\text{Mg}_{0.3}$). Before the pores were tested mechanically they were digitized by taking images from different perspectives [37]. From these pictures a 3D surface model was reconstructed using the commercial software *3DSOM*[®] [2]. Fig. 6.2 shows the triangulated surface models of the pores. In order to measure the load-displacement curve of the pores experimentally they were attached to plates by molding their ends into Wood's alloy and mounted into a micro compression device, see Fig. 6.5. The obtained load-deflection curves, see Fig. 6.3, and the digital models of the pores were then used to find the microscopic material parameters of the aluminum alloy. To this end a finite element model consisting of 10-noded tetrahedral elements was generated [25]. In a first parameter fit the material was assumed to be described by Hooke's law and a Prandtl-Reuss flow rule with linear isotropic hardening in the plastic regime, see section 2.3.2. The material parameters, the Young's modulus E , the initial yield stress σ_y and the isotropic hardening modulus h , were then changed systematically until the best fit to the experimental load-deflection curves was obtained. The final material parameters for all pores determined by this procedure are given in Tab. 6.3a) and are the starting point for our investigations. In a second parameter fit the material model presented in section 2.3.3 was used for the inverse finite element computations. The obtained material parameters for all pores obtained are given in Tab. 6.3b). For more details regarding the method, see [25, 11].

Pore	E [MPa]	σ_y [MPa]	h [MPa]	Pore	E [MPa]	σ_y [MPa]	h [MPa]
1	4111.90	46.91	124.51	1	4222.93	46.18	270.19
2	3831.95	52.27	291.41	2	3495.28	71.32	299.87
3	3767.77	30.85	231.58	3	3563.13	34.15	299.98
4	4151.59	52.29	299.99	4	3940.86	61.94	299.98
5	3977.37	49.44	125.58	5	3688.69	58.56	160.68
\emptyset	3968.12	46.35	214.61	\emptyset	3737.81	54.72	266.06

a)
b)

Table 6.3: Identified material parameters for five pores a) using a small strain and b) using a large strain elasto-plastic material model.

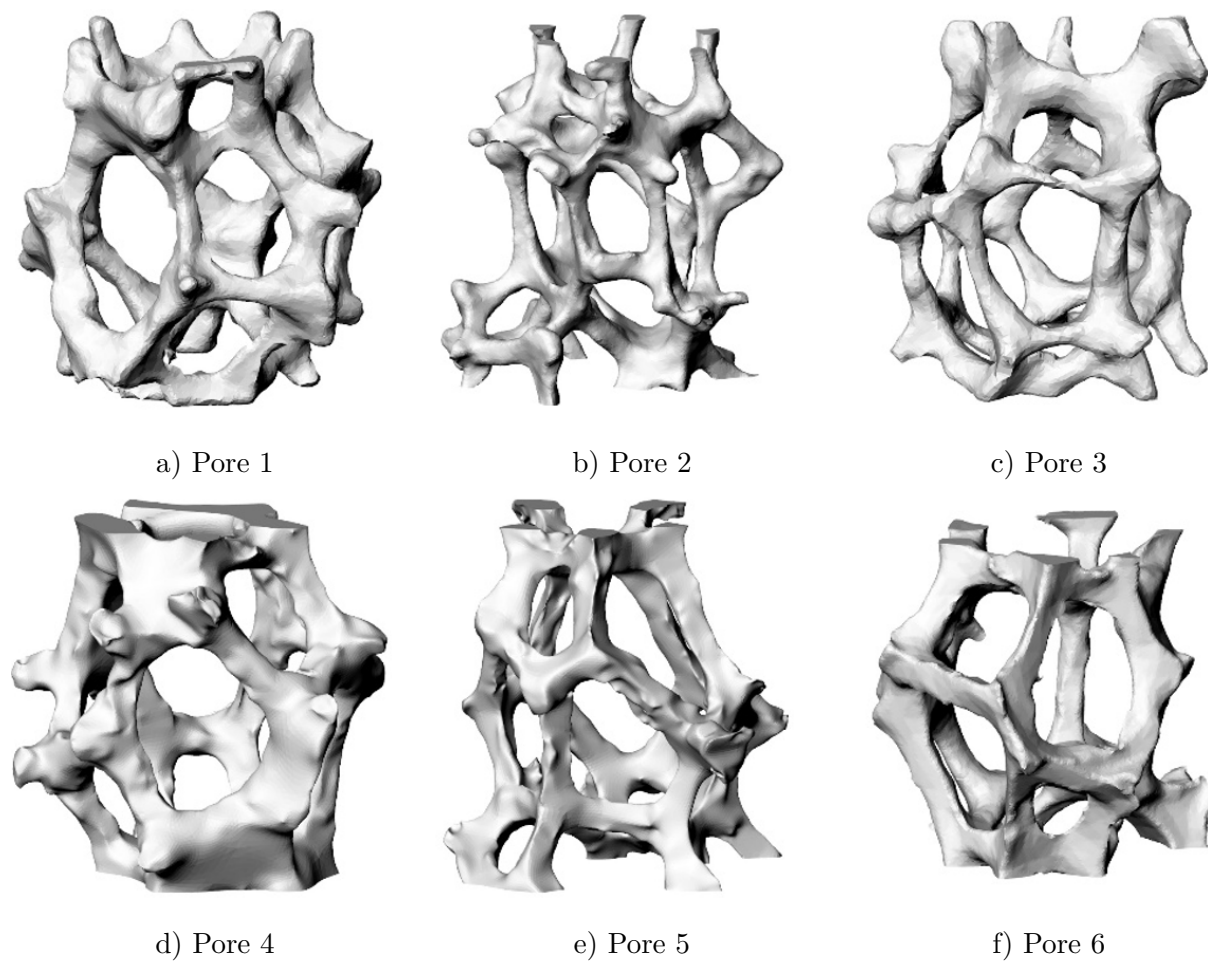


Figure 6.2: Surface models of the pores under investigation [25].

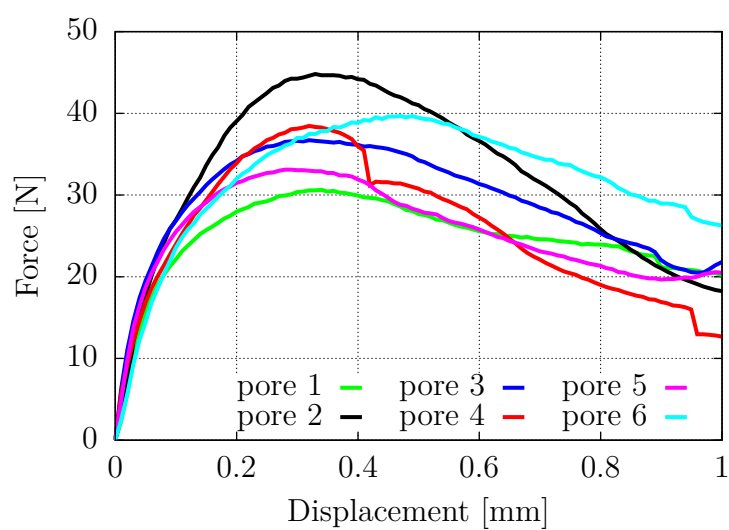


Figure 6.3: Experimentally obtained load-displacement curves for the micro compression test of five individual pores [25].

6.2.1 Mesh size

Before we analyze the pores in detail, we first investigate the influence of the finite cell discretization on the results in the small strain as well as in the large strain regime. The material model used in the small strain regime is described in section 2.3.2 and does not include geometrical nonlinear effects but the material nonlinearity induced by plastic deformations. In the large strain regime the model presented in section 2.3.3 is used which accounts for the geometrical as well as for the material nonlinearity. In the small strain regime we use the material parameters given in Tab. 6.4a) and in the large strain regime we use the material parameters given in Tab. 6.4b). Exemplary for all pores we choose pore2 as depicted in

Parameter	Value			Parameter	Value		
Young's modulus	E	3831.95	MPa	Young's modulus	E	3495.28	MPa
Poisson's ratio:	ν	0.33		Poisson's ratio	ν	0.33	
Initial yield stress	σ_0	52.27	MPa	Initial yield stress	σ_0	71.32	MPa
Linear hardening	h	291.41	MPa	Linear hardening	h	299.87	MPa

a) b)

Table 6.4: Material parameters of pore2 used for mesh study: a) in small strain regime and b) in large strain regime.

Fig. 6.4a) and generate two different discretizations. The coarser mesh contains 4678 cells and a full cell includes 8^3 voxels. The finer mesh contains 15228 cells with 4^3 voxels in a full cell. Fig. 6.4b) and Fig. 6.4c) show the automatically generated meshes. For both discretizations,

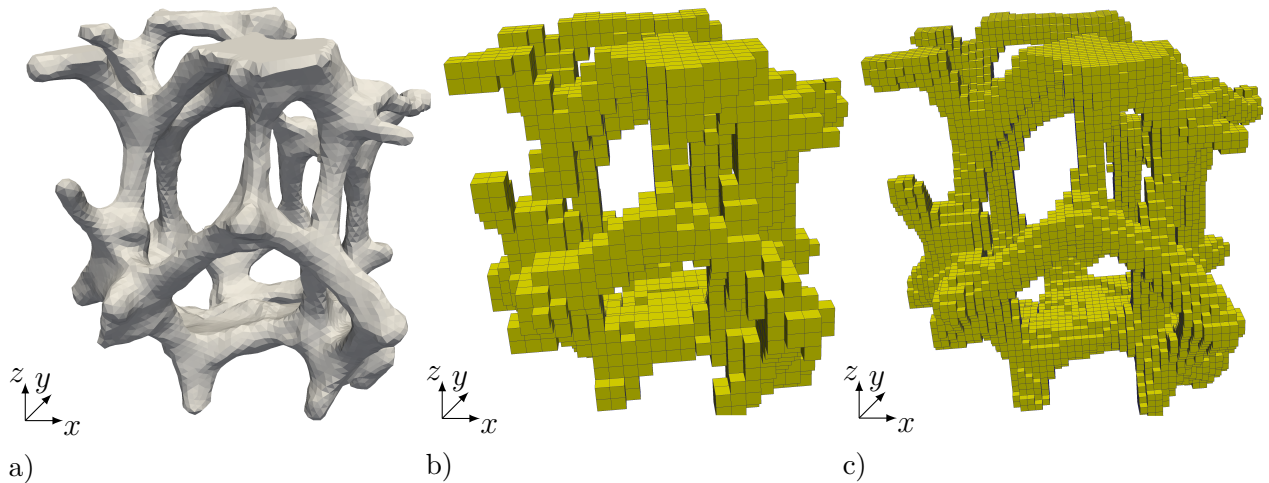


Figure 6.4: a) Pore 2 of size $6.327 \text{ mm} \times 6.424 \text{ mm} \times 6.688 \text{ mm}$ b) discretization with 4678 cells c) discretization with 15228 cells [25].

we choose shape functions of order $p = 3$ and the fictitious domain is penalized by $\alpha = 10^{-5}$. The boundary conditions are the same as in the experimental setup. In the experiment, the top and the bottom of the pore are poured in Wood's metal so that the struts can not move or rotate. In the finite cell model the displacements $u_x = u_y = 0 \text{ mm}$ are therefore constrained

in horizontal direction at these locations, see Fig. 6.5. To subject the pore to compressive loads the bottom surface $u_z = 0$ mm is fixed, and displacements are applied in increments of $\Delta u_z = -0.002$ mm on the upper surface.

In order to compare the results we use the load-deflections curves obtained from different

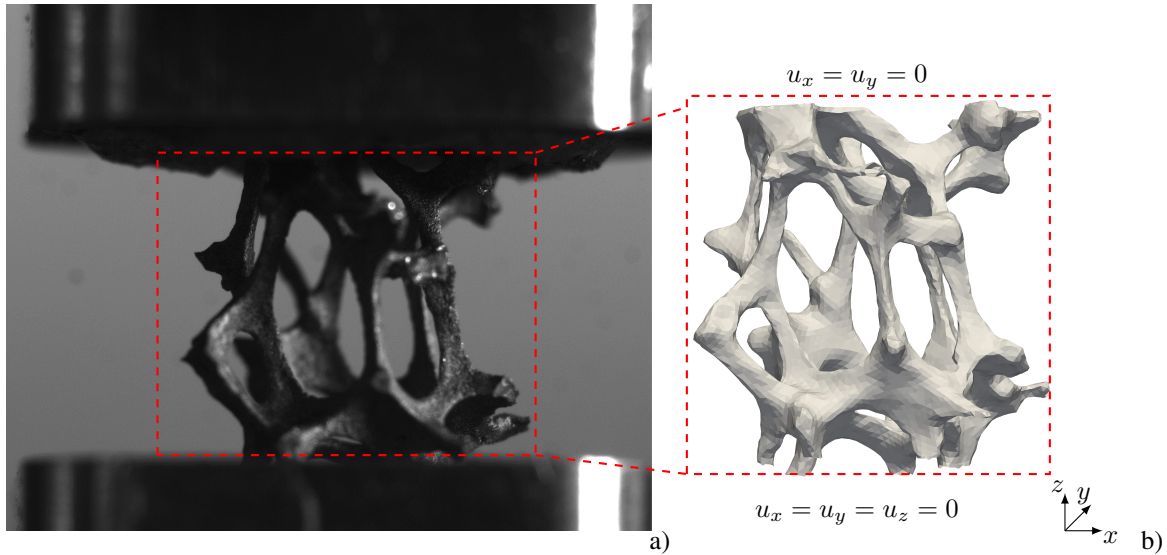


Figure 6.5: a) Experimental setup and b) geometric model used for the simulations [25].

simulations. As the simulations are controlled by displacements we compute the equivalent force to compress the pore in a post-processing step. Fig. 6.6 shows the results from this mesh study for both material models. Obviously there is nearly no difference in terms of the load-deflection curve between the two different discretizations. Hence, we use the coarser mesh in the following computations for the pores which increases the computational efficiency of the simulations.

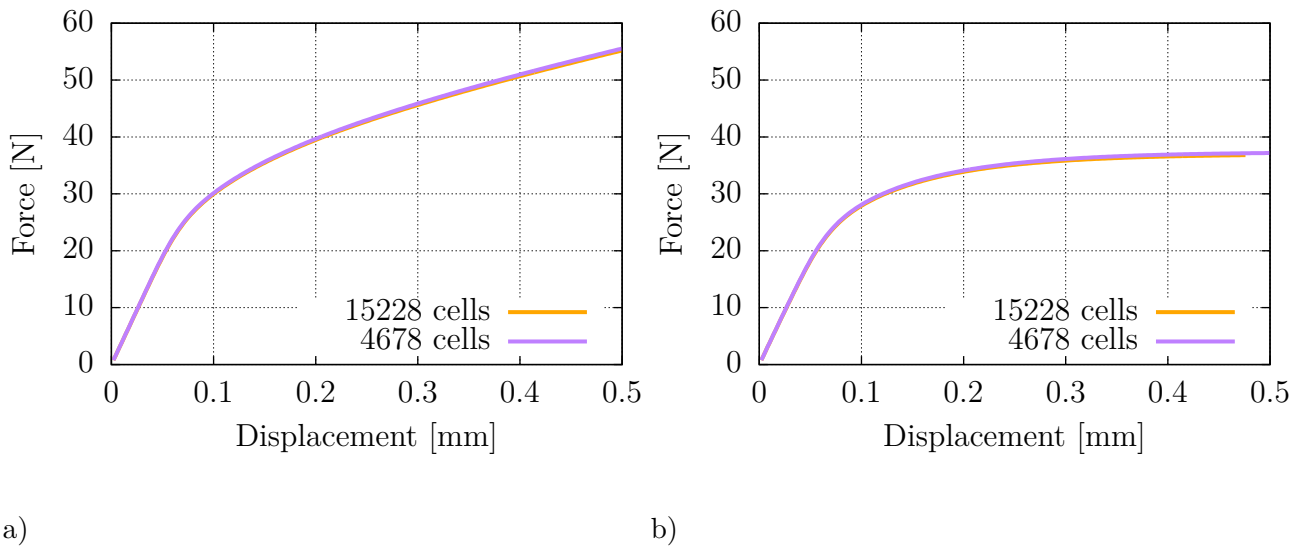


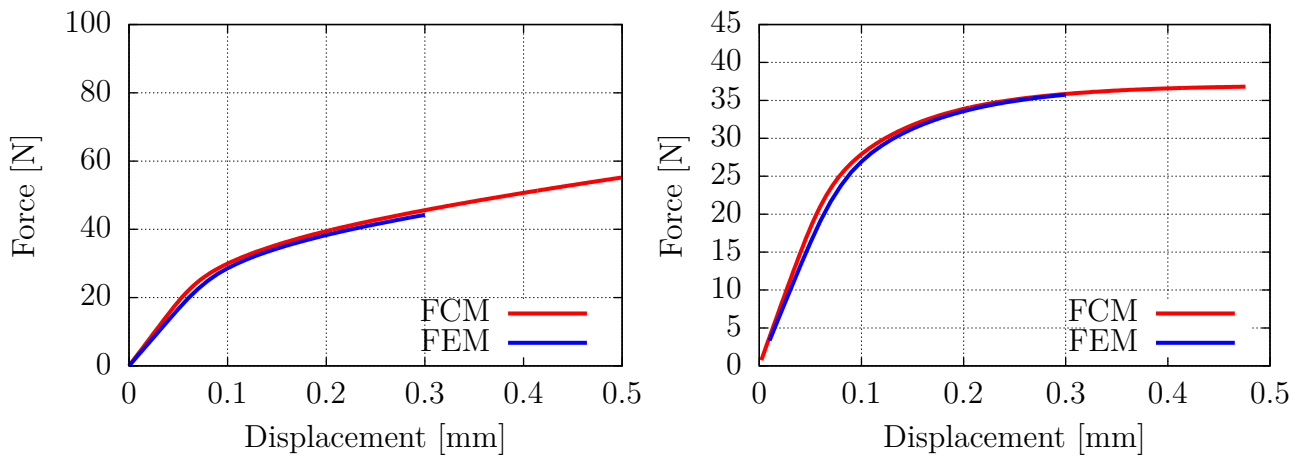
Figure 6.6: Results of the mesh study of pore 2 a) for the small strain and b) large strain material model.

6.2.2 Comparison of finite element and finite cell computations

As another verification for the accuracy of the finite cell computations we compare our results to the finite element computations of pore 2 that were performed to obtain the material parameters given in Tab. 6.3a) and Tab. 6.3b). The comparison is done for moderate and large deformations. The results of this study are depicted in Fig. 6.7a) and Fig. 6.7b). By comparing the load-deflection curves it is evident that both methods give comparable results and small deviations which are due to the different discretizations can be neglected.

6.2.3 Comparison of small and large strain simulations with experiments

In this section we investigate the influence of large deformations in the numerical model. To this end we use the material model specific material parameters for the small strain material model as given in Tab. 6.4a) and the large strain material parameters as given in Tab. 6.4b). The small strain material model does not take into account the geometrical nonlinearity of the structure, but it is difficult to quantify the amount of deformation where this effect becomes significant. In Fig. 6.8 we therefore compare both computations and the experiment as well. At the beginning of the loading both numerical simulations and the experiment are in good agreement. This is not surprising since the material parameters were fitted to meet the experimental curve in the small strain regime and the large strain model converges to the small strain model for small strains. When the displacement exceeds 0.3 mm which corresponds to a compressive deformation of about 4.48%, the small strain computation starts deviating from the experimental curve and the numerical simulation including large deformations. Therefore we conclude that starting from approximately 5% deformations it is necessary to consider large deformations in the model due to the onset of buckling of the foam struts. When further increasing the deformation and now comparing the experimental and the large strain curve



a)

b)

Figure 6.7: Comparison of the load displacement curve of pore 2 obtained by finite element and finite cell computations a) for the small strain and b) large strain material model.

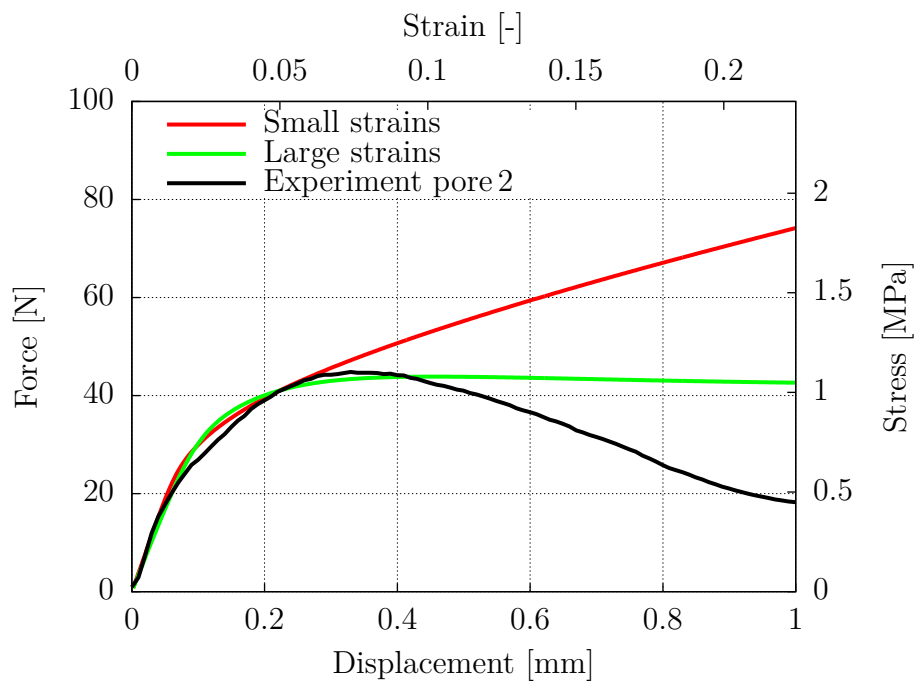


Figure 6.8: Comparison of the small strain and large strain material model.

they seem to coincide up to a displacement of 0.4 mm. From this point onwards other physical effects, for example the initiation of cracks as shown in Fig. 6.9, play a more dominant role and cause the strong softening of the structure. However, as seen from the simulations the pronounced softening in the experimental force-displacement curves after the plastic collapse can not be captured.

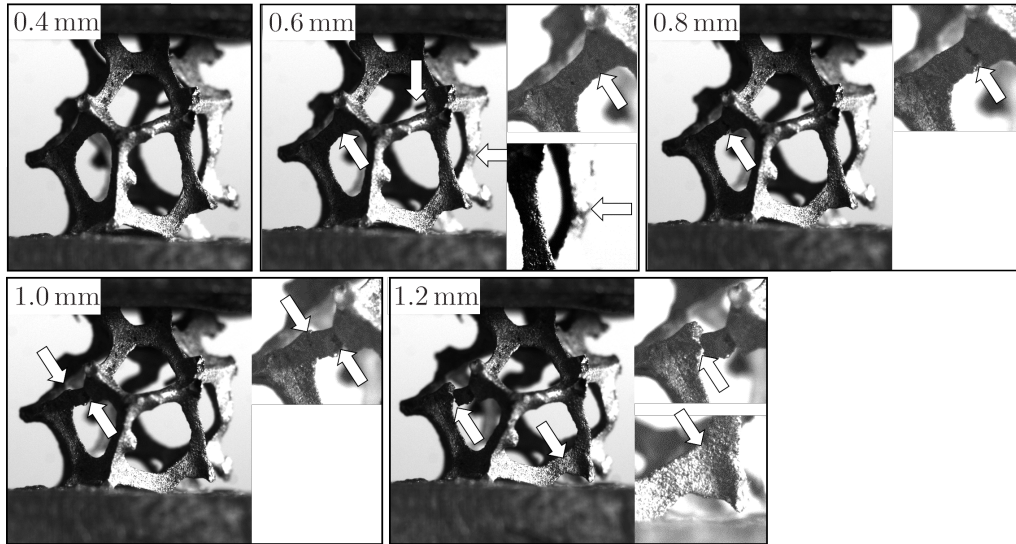


Figure 6.9: Damage evolution in pore 6. White arrows indicate the formation of cracks [25].

6.2.4 Comparison of a pore with averaged properties to experiments

In this section we aim to quantify how representative the material parameters are that were obtained from large and small strain inverse finite element computations. The investigated pores are depicted in Fig. 6.2. Pore 1 – 5 were used to compute average values for the material parameters which are given in Tab. 6.3a) and Tab. 6.3b). Now, we apply the averaged material properties to pore 6 that was not considered so far. Fig. 6.10 shows the range of the experimentally obtained load-displacement curves of the six investigated pores. The blue curve represents a finite cell computation assuming only small strains using averaged material properties given in Tab. 6.3a) and the orange curve represents a finite cell computation assuming large strains with the material properties given in Tab. 6.3b). The red curve represents the experiment performed on pore 6. By comparing the curves we can conclude that the averaged material parameter obtained from inverse finite element computations can describe the material behavior of pores. Small and large strain computations are nearly equivalent up to a displacement of about 0.2 mm. Beyond this point the geometrical nonlinearity plays a more dominant rule. This effect can only be covered with the large strain material model. This material model gives good results up to a displacement of about 0.5 mm. After this point the deviations to the experiment increase. The missing softening behavior after exceeding a total displacement of 0.5 mm as shown in Fig. 6.10 is mainly affected from excluding the effect of cracks in the simulations.

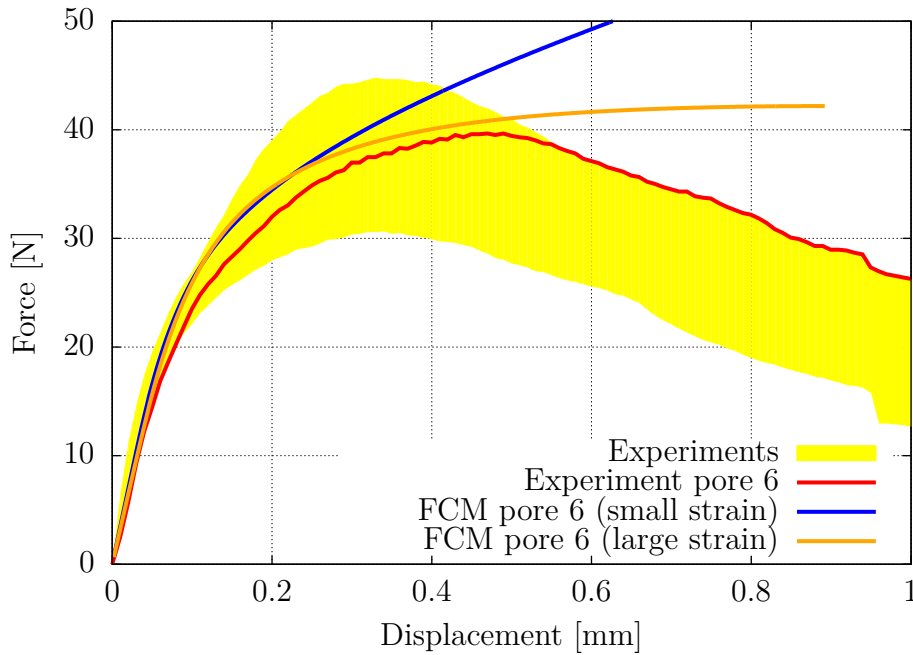


Figure 6.10: Comparison of experimental and numerical results for pore 6 using effective pore level material parameters [25].

6.3 20 ppi aluminium foam

6.3.1 The geometrical representative volume element

In this section we investigate the mechanical behavior of larger samples taken from a 20ppi open-cell aluminum foam ($\text{AlSi}_7\text{Mg}_{0.3}$) produced by Celltec Materials (Dresden, Germany). To this end our first goal is to find a geometrical representative volume element in order to investigate the macroscopic behavior of such metal foams. In a first step, we only consider the geometry of the foam. and analyze them regarding their relative density $V_{\text{vox}}/V_{\text{bb}}$. Here V_{bb} represents the volume of an imaginary bounding box surrounding the sample and V_{vox} denotes the volume of all voxels containing some material. The mid points of all cubic samples coincide with the whole sample, see Fig. 6.11 for the selection of samples. Tab. 6.5 shows the results of this analysis. Before the samples are analyzed mechanically floating structures need to be removed. These floating structures either represent artifacts in the CT-image or are generated due to cutting out the sub-samples from the whole scan. Column 3 – 5 represent the number of voxels in the sub-sample n_{vox} , the volume of these voxels V_{vox} and the volumetric density $V_{\text{vox}}/V_{\text{bb}}$ before and Column 6 – 8 contain the same properties of the sample after removing all artifacts. The specimens have an average density of 7.473%. Interestingly, when enlarging the edge length of the sub-sample from 600 voxels to the whole sample the relative volume drops significantly. This effect can be explained due to cutting out the specimens mechanically from a larger sample or the non axis aligned placement of the cubic specimen in the CT scanner. In the following we will therefore exclude this specimen from our investigations.

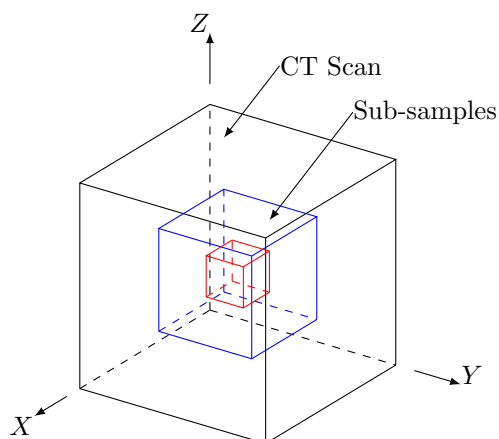


Figure 6.11: Location of the sub-samples relative to the whole CT-scan.

Δ	V_{bb} mm^3	Before pre-processing			After pre-processing		
		n_{Vox}	V_{Vox} mm^3	V_{Vox}/V_{bb} %	n_{Vox}	V_{Vox} mm^3	V_{Vox}/V_{bb} %
100	13.772	77698	1.071	7.777	77698	1.071	7.777
200	110.247	603819	8.32	7.547	602642	8.304	7.532
300	372.005	1875500	25.843	6.947	1874829	25.833	6.944
400	881.974	4948376	68.184	7.731	4934670	67.995	7.709
500	1722.39	9717023	133.892	7.774	9703622	133.707	7.763
600	2976.042	17238685	237.534	7.982	17212490	237.173	7.969
683	4199.392	20188916	278.186	6.624	20170903	277.937	6.619

Table 6.5: Geometrical information 20ppi foam.

6.3.2 The mechanical representative volume element

In a next step, we analyze the mechanical properties of different samples by comparing their load-displacement curves under compression. The computations are controlled by applying a prescribed displacement d on one of the side faces of the foam. In order to compare different sample sizes later on, the results are normalized by the length of the sample in loading direction and the area of the surface where the load is applied. Assuming that the cubic foam samples fit into a bounding box enables us to define labels for each face, see Fig. 6.12. The boundary condition then applies for the struts that touch these imaginary faces. Let us now define two

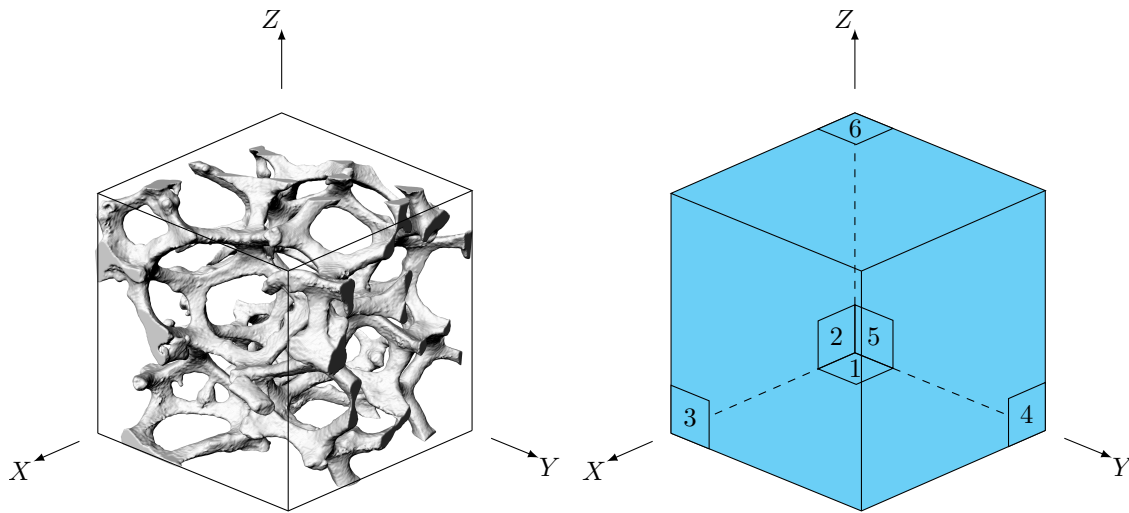


Figure 6.12: Definition of the boundary faces by labels.

sets of loads as given in Tab. 6.6. The first set of loads is referred to as symmetry boundary conditions. They can be defined for each spatial direction $F_{x,\text{Sym}}, F_{y,\text{Sym}}, F_{z,\text{Sym}}$ and would lead to a homogeneous stress distribution in a fictitious homogeneous sample. The second set of load cases $F_{x,\text{Enc}}, F_{y,\text{Enc}}, F_{z,\text{Enc}}$ is named encastre boundary conditions and resembles more the situation in the experiment. For the investigation of the representative volume element we use

	$F_{x,\text{Sym}}$			$F_{y,\text{Sym}}$			$F_{z,\text{Sym}}$			$F_{x,\text{Enc}}$			$F_{y,\text{Enc}}$			$F_{z,\text{Enc}}$		
	u_x	u_y	u_z															
1			0			0			0							0	0	0
2		0			0			0					0	0	0			
3	-d									-d	0	0						
4					-d								0	-d	0			
5	0			0				0	0	0								
6											-d					0	0	-d

Table 6.6: Definition of different sets of boundary conditions.

the material properties given in Tab. 6.7. In order to stabilize the solution behavior we prevent the material in the fictitious domain to yield. To this end the yield stress $\sigma_0 = 160 \cdot 10^6$ MPa is set to a high value. Additionally the contribution from the fictitious domain is penalized by

Parameter		Value	
Young's modulus	E	14035.31	MPa
Poisson's ratio:	ν	0.33	
Initial yield stress	σ_0	160.00	MPa
Saturation stress	σ_∞	236.23	MPa
Linear hardening	h	67.57	MPa
Hardening exponent	ω	102.78	

Table 6.7: Material parameters used to find a RVE.

$\alpha = 10^{-5}$. In section 4.3.1.1 and 6.2.1 we already investigated the influence of the discretization on the results. From both studies we can conclude that a discretization where a cell includes 8^3 voxels and the order of the shape functions is $p = 3$ results in an approximation with a reasonable accuracy. Therefore we relinquish on a detailed mesh study here and take over these parameters for the following examples.

6.3.2.1 Comparison of sample size

In this section we investigate the influence of the sample size on the macroscopic stress strain curve. To this end, we choose four different samples with an edge length of 7.672 mm, 9.59 mm, 14.384 mm, 15.343 mm, respectively 320, 400, 600, 640 voxels and subject them to symmetry boundary conditions $F_{z,Sym}$. The samples were all extracted at the same position within a larger sample. The material parameters used for this computation are given in Tab. 6.7, respectively Tab. 6.2 and were obtained from micro compression tests on single struts, see section 6.1.

Fig. 6.13 presents the stress-strain curves obtained from the simulations. In order to compare different sample sizes with each other the results are normalized. The reaction force needed to compress the pores is computed at the location where the displacement boundary conditions are applied and divided by the area which results in a normalized force (stress). The normalized compression (strain) is computed by dividing the applied displacements by the length of the sample in loading direction. All sample sizes except the largest one show a similar stress-strain curve for this type of loading. The largest sample shows a reduced stiffness which confirms the observation of the geometrical analysis and can be explained by the lower density. Interestingly the smallest sample with only two pores in loading direction, see Fig. 6.15, has a similar load-displacement curve than the larger samples. Since the different samples were extracted at the same positions their geometry should be similar. A difference in the load-displacement curves should therefore be predominantly affected by size effects in conjunction with the applied boundary conditions. The smallest sample is therefore suited as an RVE in case statistical variations in the geometry play a less pronounced role. Therefore we will investigate this sample size in more detail in the next section.

6.3.2.2 Investigation of different voxel samples

Another test for the representativeness of a sample is to extract it at different locations from different foam plates. To this end, we extract three different samples with an edge length

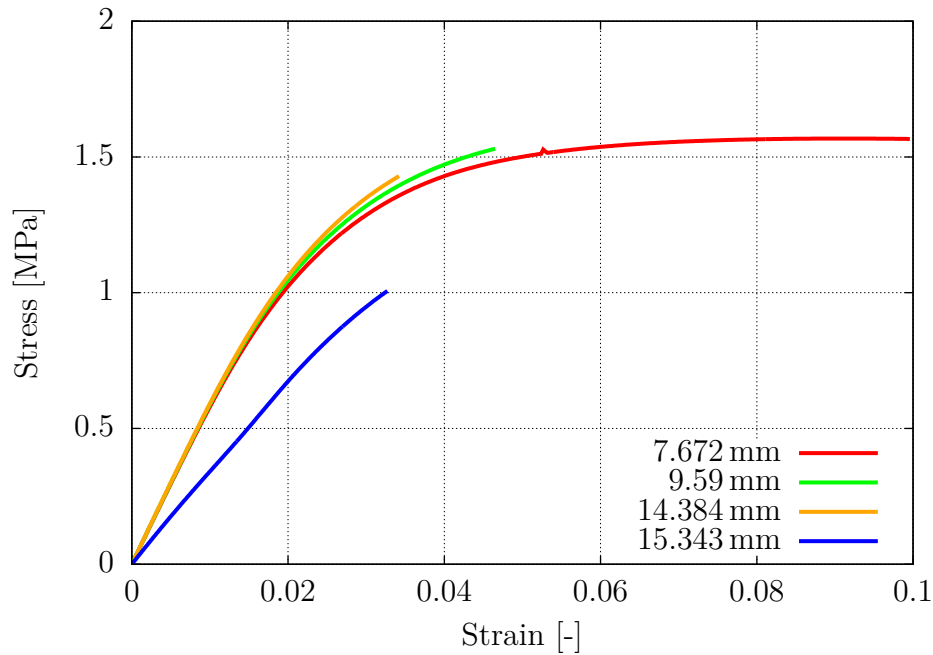


Figure 6.13: Comparison of different samples of the same size.

of 320 voxels and subject them to a compressive load using symmetry boundary conditions as defined in Tab. 6.6. The results of this investigation are presented in Fig. 6.15. In order

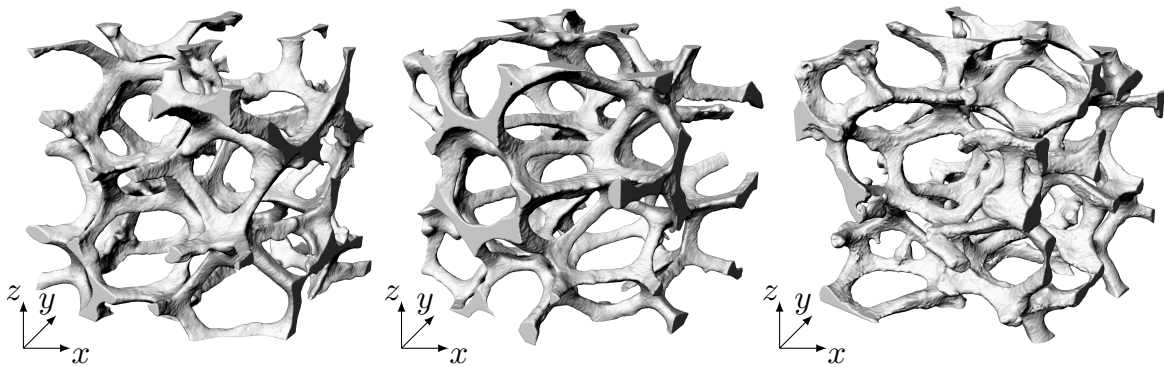


Figure 6.14: Different samples taken from 20ppi aluminum foam.

to compare the curves it is important to know that the foam has an anisotropic behavior which is due to the elongated shape of the pores. The elongation direction of the pores is indicated by the index l and the perpendicular directions are indicated by the index r . The curves should only be compared keeping this local direction in mind. The large scattering of the different curves indicate that a sample with an edge length of 7.672 mm (320 voxels) is not representative. For the second sample the elongation direction of the pores is not even evident from the stress strain curve which is also due to the sample size being too small. Fig. 6.14 shows that the samples include only two pores in each direction. As a rule of thumb at least four pores [63] are necessary for a representative volume element.

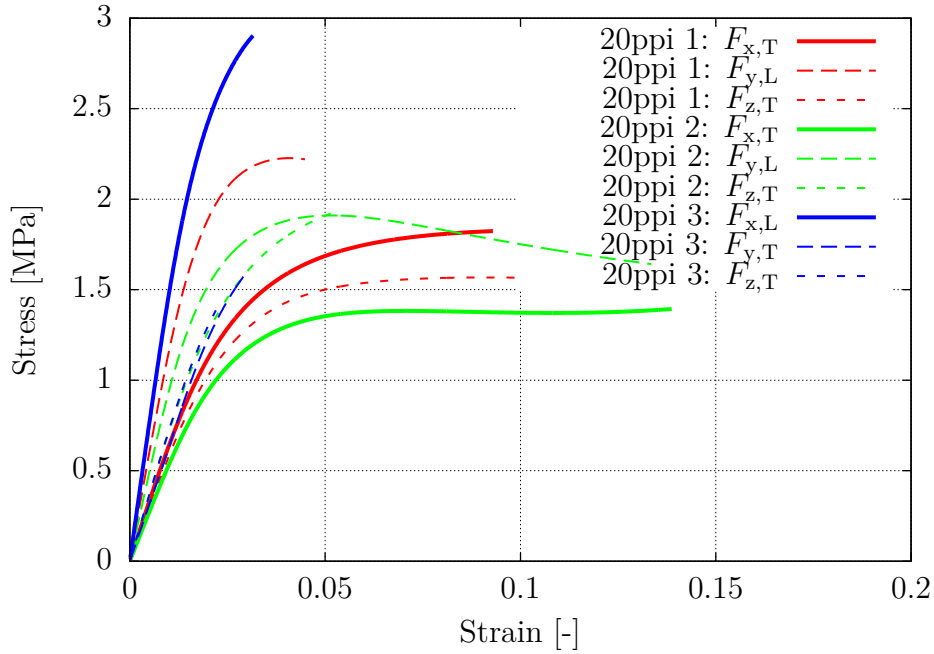


Figure 6.15: Comparison of the stress strain curve of different cubic samples with an edge length 7.672 mm (320 voxels) that were extracted at different locations from the foam.

6.3.3 Comparison of simulations and experiments

In this section we finally compare the numerical simulation of uni axial compression tests. The experimentally tested specimens had a cubic shape with an edge length of 20 mm. Due to the limited size of the used CT-Scanner the maximum size of the voxel models is restricted to approximately 16 mm. Furthermore, due to some irregularities at the boundaries of the scanned samples, the maximum possible sample size of the voxel models is further reduced to about 14.38 mm (600 voxels). Therefore we perform the numerical computations on two different $600 \times 600 \times 600$ voxel samples and compare the results to experiments.

Different material parameters for the aluminum alloy were obtained depending on what method was used. Therefore we apply two different sets of material properties. The parameters determined by micro compression tests on single struts as described in section 6.1 and the averaged material properties obtained by inverse computations on single pores under large deformations as described in section 6.2. Due to the manufacturing process metal foams exhibit a structural anisotropy with elongated pores in one direction and a rotationally symmetric shape in the transversal direction, see Fig. 6.16. In the elongation direction the pores provide a higher stiffness since the struts are loaded in axial direction while they are bent when they are stressed in the orthogonal direction. In order to compare the results between the experiment and the simulation we apply the load in the direction of the elongation of the pores. The boundary conditions are chosen to be the same as in the experiments, clamping the top and bottom surface as described in Tab. 6.6.

Fig.6.17 shows the results from this study. In the experiment several samples were tested leading to a distribution range of the load displacement curve which is compared to a computation of two different samples with changing material properties. When the material properties

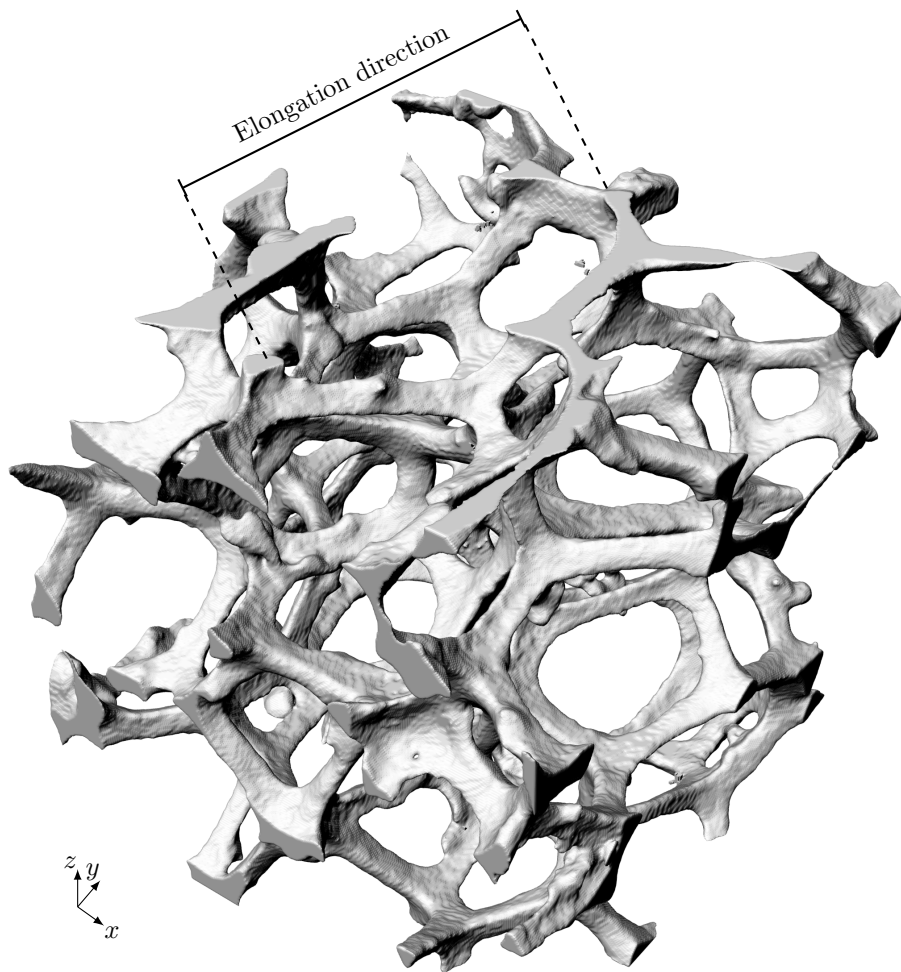


Figure 6.16: Cubic sample with an edge length of 9.5896 mm (400 voxels) taken from 20ppi aluminum foam showing the elongation direction of the pores.

obtained by micro compression tests on single struts are used, the stiffness of the pore is over estimated, see Fig. 6.17 for sample 1. Therefore in a next step the material parameters obtained by inverse computations and compression tests on single pores are taken and applied to sample 1 and sample 2. Obviously using these properties, the numerical computations are much closer to the experiments and can be explained as follows. When a pore is subjected to a compressive load, its struts start to bend, leading locally to tensile and compressive stress states, furthermore cracks start to evolve. When performing inverse computations on single pores to obtain the corresponding material parameters all these phenomena are described by the material parameters. In comparison to this, in micro compression no cracks can occur and they are not taken into account by the material properties.

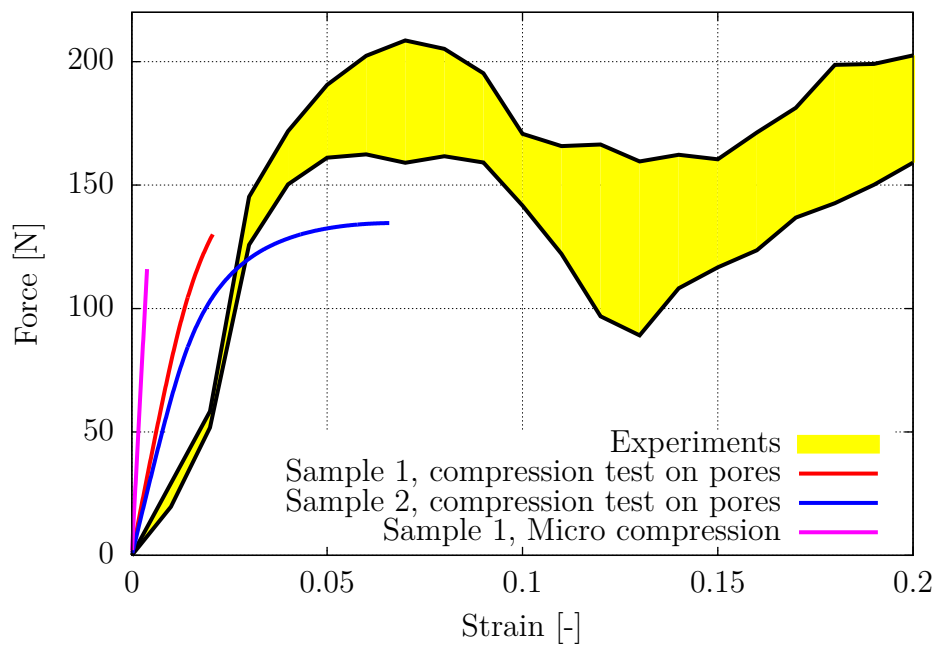


Figure 6.17: Comparison of different material parameters used to recompute the experimentally obtained force-strain curve.

Chapter 7

Summary and Outlook

The finite cell method is a powerful simulation method for the investigation of cellular materials. It has shown to offer a fast and automatic discretization method for image-based geometries like voxel models stemming from CT Data. The aim of this thesis was to extend the finite cell method to nonlinear problems like *plastic material behavior*, *large deformations* and *contact problems* which was motivated by the challenge to investigate the mechanical behavior of metal foams which strongly depends on these phenomena.

The first part of the work concerned the development of automatic discretization algorithms for CT image-based voxel models. The focus here was less on creating the mesh which is a simple Cartesian grid but on removing artifacts from voxel models. Besides that algorithms to modify the voxel data were developed as well. This allowed to add a coating layer to the voxel models and examine the increase in stiffness using a numerical homogenization scheme based on the window method.

In order to enable the computation of large deformations combined with elastoplastic material behavior the finite cell method was extended by a suitable material model. The model was compared to some benchmark examples [69],[70],[68] and applied to different structural levels of aluminum foams ranging from single pores to larger representative samples. The main difficulty for the simulation of the deformation of metal foams was to find the material parameters of the aluminum which strongly differ from the bulk material properties. Without knowing these only relative statements on metal foams can be made, when comparing the same structure before and after applying a change to the numerical model. Material parameters were obtained from tensile and compression experiments on single struts by [39]. Both sets of parameters were fundamentally different. By inverse computations on single pores [25] more realistic material parameters could be obtained which could also be applied to larger foam samples.

In order to investigate the influence of self-contact on the deformation behavior of metal foams, the FCM was extended by a contact algorithm for sticking and frictionless contact. Both approaches were investigated in detail by varying different parameters and comparing their results to the analytical solution provided by Hertz. Later on the sticking contact model was applied for the computation of the self-contact of a single pore.

Let us now give an outlook to possible future research topics regarding the finite cell method.

- **Computational costs of the numerical quadrature**

The finite cell method offers a simple and automatic discretization technique which allows the user to generate a discretization of complicated geometries like cellular structures without many manual adjustments. The time saved during mesh generation is shifted to the integration of the finite cell stiffness matrix. For broken cells usually a lot of integration points are required to compute the underlying discontinuous integrand, especially when using an adaptive quadrature scheme based on spatial subdivision of the integration domain using an octree. Recently, a new integration scheme based on the moment-fitting method has been proposed [48]. It has already been applied in the context of the FCM addressing linear problems [36, 31] and provides less integration points. For nonlinear problems this method seems to add extra difficulties which needs to be investigated in future research.

- **Stability**

The shape functions of broken cells are defined over the whole domain, but are only integrated in the physical domain. This leads to linear dependencies of the shape functions and adds difficulties when solving the global equation system, even when robust direct solvers are employed. The severity of this problem especially depends on the volume fraction of the finite cells, the polynomial order of the shape functions as well as the underlying type of problem, meaning linear or nonlinear problems. A simple method to reduce such problems is to penalize the fictitious domain by the indicator function $\alpha = 10^{-q}$ with $q \in [5, \dots, 12]$. Under moderate deformation this method works well but questions arise when considering elastoplastic materials and large deformations. In elastoplastic problems the material changes its stiffness when yielding occurs. This of course also happens in the fictitious domain, where deformations and strains are high. Due to this the contribution of the fictitious domain to the stiffness matrix changes and computations can become unstable. The same problem arises when considering large deformations due to the use of nonlinear strain measures. In addition, the indicator functions can be applied in many different ways in numerical codes, for instance either before or after computing the constitutive equations. It is not yet understood how the stabilization should be carried out for nonlinear problems. Recently a new stabilization method based on an algebraic preconditioner, the *Symmetric Incomplete Permuted Inverse Cholesky* (SIPIC) preconditioner [55] has been developed. Such a method is interesting to apply in the future but needs to be investigated regarding its effectivity and numerical costs.

- **Contact problems**

In this thesis a contact approach based on an additional discretization of the contact surface was presented. In the future this formulation should be extended to incorporate contact problems involving friction. Besides that further methods to reduce the stress oscillations at the end of the contact zone should be investigated.

Appendix A

Gauss-Legendre quadrature for triangles

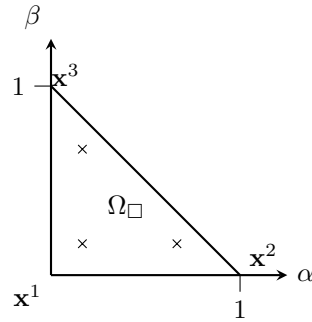


Figure A.1: Standard triangle with Gauss-Legendre quadrature points

n_o	n_g	α	β	w
1	1	0.333333333333333	0.333333333333333	1.000000000000000
2	3	0.166666666666667	0.166666666666667	0.333333333333333
		0.166666666666667	0.666666666666667	0.333333333333333
		0.666666666666667	0.166666666666667	0.333333333333333
3	4	0.333333333333333	0.333333333333333	-0.562500000000000
		0.200000000000000	0.200000000000000	0.520833333333333
		0.200000000000000	0.600000000000000	0.520833333333333
		0.600000000000000	0.200000000000000	0.520833333333333
4	6	0.44594849091597	0.44594849091597	0.22338158967801
		0.44594849091597	0.10810301816807	0.22338158967801
		0.10810301816807	0.44594849091597	0.22338158967801
		0.09157621350977	0.09157621350977	0.10995174365532
		0.09157621350977	0.81684757298046	0.10995174365532
		0.81684757298046	0.09157621350977	0.10995174365532

Go to next page

n_o	n_g	α	β	w
5	7	0.333333333333333	0.333333333333333	0.225000000000000
		0.47014206410511	0.47014206410511	0.13239415278851
		0.47014206410511	0.05971587178977	0.13239415278851
		0.05971587178977	0.47014206410511	0.13239415278851
		0.10128650732346	0.10128650732346	0.12593918054483
		0.10128650732346	0.79742698535309	0.12593918054483
		0.79742698535309	0.10128650732346	0.12593918054483
6	12	0.24928674517091	0.24928674517091	0.11678627572638
		0.24928674517091	0.50142650965818	0.11678627572638
		0.50142650965818	0.24928674517091	0.11678627572638
		0.06308901449150	0.06308901449150	0.05084490637021
		0.06308901449150	0.87382197101700	0.05084490637021
		0.87382197101700	0.06308901449150	0.05084490637021
		0.31035245103378	0.63650249912140	0.08285107561837
		0.63650249912140	0.05314504984482	0.08285107561837
		0.05314504984482	0.31035245103378	0.08285107561837
		0.63650249912140	0.31035245103378	0.08285107561837
		0.31035245103378	0.05314504984482	0.08285107561837
		0.05314504984482	0.63650249912140	0.08285107561837
7	13	0.333333333333333	0.333333333333333	-0.14957004446768
		0.26034596607904	0.26034596607904	0.17561525743321
		0.26034596607904	0.47930806784192	0.17561525743321
		0.47930806784192	0.26034596607904	0.17561525743321
		0.06513010290222	0.06513010290222	0.05334723560884
		0.06513010290222	0.86973979419557	0.05334723560884
		0.86973979419557	0.06513010290222	0.05334723560884
		0.31286549600487	0.63844418856981	0.07711376089026
		0.63844418856981	0.04869031542532	0.07711376089026
		0.04869031542532	0.31286549600487	0.07711376089026
		0.63844418856981	0.31286549600487	0.07711376089026
		0.31286549600487	0.04869031542532	0.07711376089026
		0.04869031542532	0.63844418856981	0.07711376089026

Go to next page

n_o	n_g	α	β	w
8	16	0.333333333333333	0.333333333333333	0.14431560767779
		0.45929258829272	0.45929258829272	0.09509163426728
		0.45929258829272	0.08141482341455	0.09509163426728
		0.08141482341455	0.45929258829272	0.09509163426728
		0.17056930775176	0.17056930775176	0.10321737053472
		0.17056930775176	0.65886138449648	0.10321737053472
		0.65886138449648	0.17056930775176	0.10321737053472
		0.05054722831703	0.05054722831703	0.03245849762320
		0.05054722831703	0.89890554336594	0.03245849762320
		0.89890554336594	0.05054722831703	0.03245849762320
		0.26311282963464	0.72849239295540	0.02723031417443
		0.72849239295540	0.00839477740996	0.02723031417443
		0.00839477740996	0.26311282963464	0.02723031417443
		0.72849239295540	0.26311282963464	0.02723031417443
		0.26311282963464	0.00839477740996	0.02723031417443
		0.00839477740996	0.72849239295540	0.02723031417443

Table A.1: Symmetric Gauss-Legendre quadrature points for triangles taken from [16]

Appendix B

Flow chart of finite J_2 plasticity implementation

The presented material model is implemented in the high order finite element code *AdhoC*. Instead of presenting the source code, we only give a flow chart of the mathematical relations that are one by one implemented in **AdhoC**.

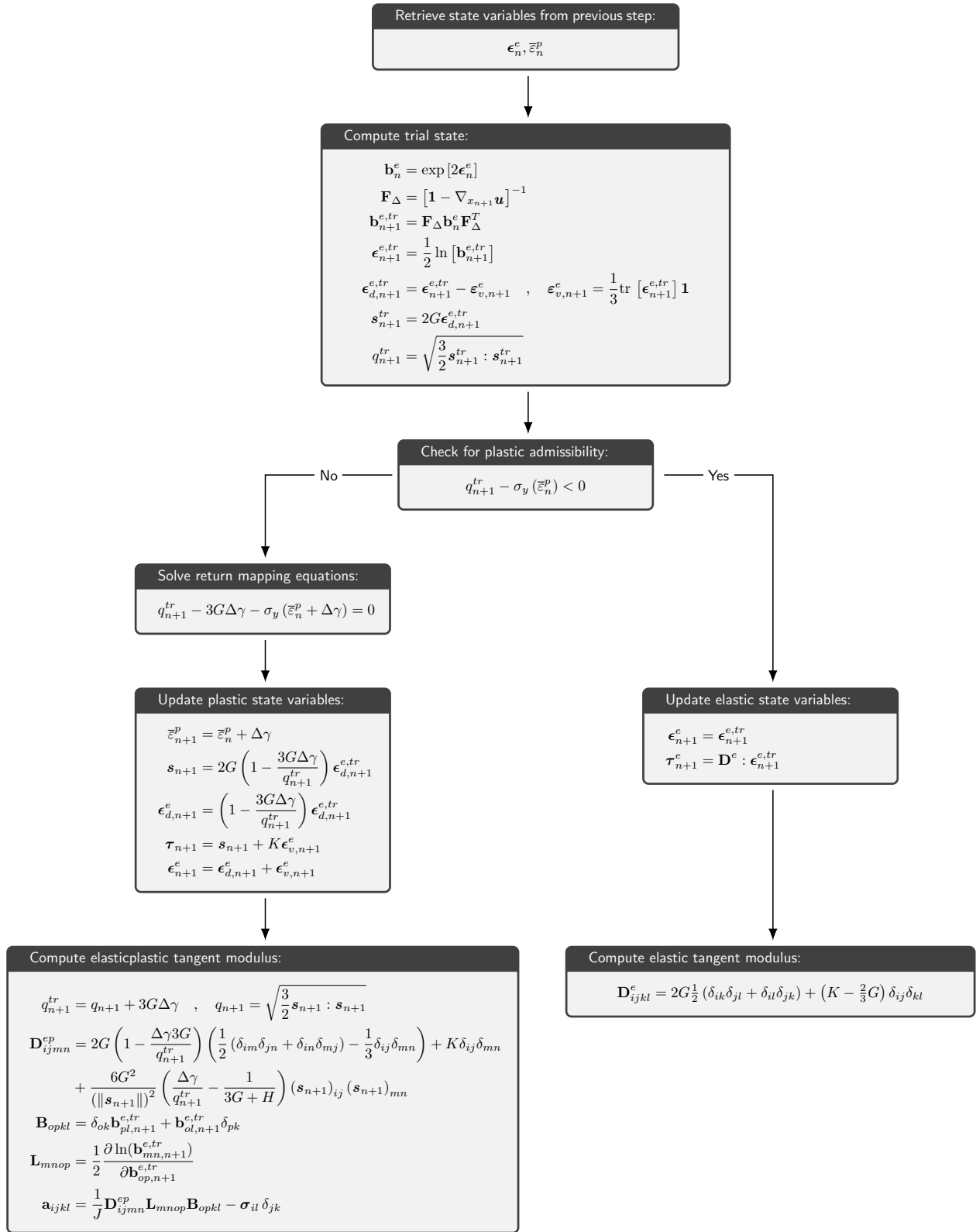


Figure B.1: Implemented equations of the material model

Bibliography

- [1] Encyclopædia Britannica. URL: <https://www.britannica.com/science/bone-anatomy> (visited on 03/18/2018).
- [2] Creative Dimension Solutions Limited. URL: <http://www.3dsom.com/contact-us/> (visited on 09/18/2017).
- [3] A. Abedian, J. Parvizian, A. Düster, H. Khademyzadeh, and E. Rank. The Finite Cell Method for Elasto-Plastic Problems. *Proceedings of the Tenth International Conference on Computational Structures Technology*. Civil-Comp Press, 2010.
- [4] A. Abedian, J. Parvizian, A. Düster, and E. Rank. Finite cell method compared to h -version finite element method for elasto-plastic problems. *Applied Mathematics and Mechanics* 35.10, pp. 1239–1248, 2014.
- [5] A. Abedian, J. Parvizian, A. Düster, and E. Rank. The finite cell method for the J_2 flow theory of plasticity. *Finite Elements in Analysis and Design* 69, pp. 37–47, 2013.
- [6] M. K. Agoston. *Computer Graphics and Geometric Modeling : Implementation and Algorithms*. London: Springer-Verlag London Limited, 2005.
- [7] I. Babuška, B. A. Szabo, and I. N. Katz. The p -Version of the Finite Element Method. *SIAM Journal on Numerical Analysis* 18, pp. 515–545, 1981.
- [8] J. Baumeister and J. Weise. Metal Foams. *Structural Materials and Processes in Transportation*. Wiley-VCH Verlag GmbH & Co. KGaA, 2013, pp. 415–444.
- [9] T. Belytschko, W. Liu, and B. Moran. *Nonlinear finite elements for continua and structures*. John Wiley & Sons, 2000.
- [10] D. J. Benson and J. O. Hallquist. A single surface contact algorithm for the post-buckling analysis of shell structures. *Computer Methods in Applied Mechanics and Engineering* 78, pp. 141–163, 1990.
- [11] T. Bleistein, A. Jung, and S. Diebels. Parameter identification for open cell aluminium foams using inverse calculation. *Archive of Applied Mechanics*, 2018. Submitted.
- [12] H. J. Boehm. *A short introduction to basic aspects of continuum micromechanics*. Tech. rep. Institute of Lightweight Design and Structural Biomechanics (ILSB) Vienna University of Technology, 2012.
- [13] T. Bog, N. Zander, S. Kollmannsberger, and E. Rank. Normal contact with high order finite elements and a fictitious contact material. *Computers & Mathematics with Applications* 70, pp. 1370–1390, 2015.

- [14] T. Bog, N. Zander, S. Kollmannsberger, and E. Rank. Weak imposition of frictionless contact constraints on automatically recovered high-order, embedded interfaces using the finite cell method. *Computational Mechanics*, 2017.
- [15] M. Dauge, A. Düster, and E. Rank. Theoretical and Numerical Investigation of the Finite Cell Method. *Journal of Scientific Computing* 65.3, pp. 1039–1064, 2015.
- [16] D. A. Dunavant. High degree efficient symmetrical Gaussian quadrature rules for the triangle. *International Journal for Numerical Methods in Engineering* 21.6, pp. 1129–1148, 1985.
- [17] A. Düster, J. Parvizian, Z. Yang, and E. Rank. The finite cell method for three-dimensional problems of solid mechanics. *Computer Methods in Applied Mechanics and Engineering* 197, pp. 3768–3782, 2008.
- [18] A. Düster, H.-G. Sehlhorst, and E. Rank. Numerical homogenization of heterogeneous and cellular materials utilizing the finite cell method. *Computational Mechanics* 50, pp. 413–431, 2012.
- [19] A. L. Eterovic and K.-J. Bathe. A hyperelastic-based large strain elasto-plastic constitutive formulation with combined isotropic-kinematic hardening using the logarithmic stress and strain measures. *International Journal for Numerical Methods in Engineering* 30.6, pp. 1099–1114, 1990.
- [20] D. Franke, A. Düster, V. Nübel, and E. Rank. A comparison of the h-, p-, hp-, and rp-version of the FEM for the solution of the 2D Hertzian contact problem. *Computational Mechanics* 45, pp. 513–522, 2010.
- [21] D. Franke, E. Rank, and A. Düster. Computational contact mechanics based on the rp-version of the finite element method. *International Journal of Computational Methods* 8, pp. 493–512, 2011.
- [22] T.-P. Fries and T. Belytschko. The extended/generalized finite element method: An overview of the method and its applications. *International Journal for Numerical Methods in Engineering* 84.3, pp. 253–304, 2010.
- [23] D. Gross and T. Seelig. Mikromechanik und Homogenisierung. *Bruchmechanik*. Ed. by D. Gross. Springer Berlin Heidelberg, 2011, pp. 241–314.
- [24] M. Hain and P. Wriggers. Numerical homogenization of hardened cement paste. *Computational Mechanics* 42, pp. 197–212, 2008.
- [25] S. Heinze, T. Bleistein, A. Düster, S. Diebels, and A. Jung. Experimental and numerical investigation of single pores for identification of effective metal foams properties. *Zeitschrift für Angewandte Mathematik und Mechanik* 98.5, pp. 682–695, 2017.
- [26] S. Heinze, M. Joulaian, and A. Düster. Numerical Homogenization of Hybrid Metal Foams Using the Finite Cell Method. *Computers & Mathematics with Applications* 70.7, pp. 1501–1517, 2015.
- [27] H. Hertz. Über die Berührung fester elastischer Körper. *Journal für die reine und angewandte Mathematik* 92, pp. 156–171, 1881.
- [28] T. Hipke. Funktionsintegrierter Leichtbau im Maschinenbau und in der Fahrzeugtechnik : Vortrag gehalten beim 9. VEMAS-Anwenderworkshop "Leichtbau - Werkstoffe, Verfahren und Anwendungen", 18. April 2013, Chemnitz. 2013.

- [29] T. Hipke and C. Lies. Gestaltung und Fertigungstechnologie großformatiger ebener und gekrümmter Metallschaum-Sandwichsysteme für den Schiffbau : Teilvorhaben: MESCHLAS: Fügen großformatiger Metallschaumsandwichs in der Schiffskonstruktion mittels Laser-Schweißen. 2012.
- [30] J. Hohlfeld, R. Ketzscher, C. Drebenstedt, and C. Lies. Entwicklung einer Triebkopf-abine aus Aluminiumschaum-Verbund für Hochgeschwindigkeitszüge. 7. *Landshuter Leichtbau-Colloquium 2015*. 2015, pp. 162–170.
- [31] S. Hubrich, M. Joulaian, P. Di Stolfo, A. Schröder, and A. Düster. Efficient numerical integration of arbitrarily broken cells using the moment fitting approach. *Proceedings in Applied Mathematics and Mechanics* 16, pp. 201–202, 2016.
- [32] C. Huet. Application of variational concepts to size effects in elastic heterogeneous bodies. *Journal of the Mechanics and Physics of Solids* 38.6, pp. 813–841, 1990.
- [33] C. Huet. Order relationships for boundary conditions effect in heterogeneous bodies smaller than the representative volume. *Journal of the Mechanics and Physics of Solids* 42.12, pp. 1995–2011, 1994.
- [34] M. Joulaian and A. Düster. Local enrichment of the finite cell method for problems with material interfaces. *Computational Mechanics* 52, pp. 741–762, 2013.
- [35] M. Joulaian and A. Düster. The hp-d version of the finite cell method with local enrichment for multiscale problems. *Proceedings in Applied Mathematics and Mechanics*. Vol. 13. 2013, pp. 259–260.
- [36] M. Joulaian, S. Hubrich, and A. Düster. Numerical integration of discontinuities on arbitrary domains based on moment fitting. *Computational Mechanics* 57, pp. 979–999, 2016.
- [37] A. Jung, M. Reis, T. Bleistein, and T. Scheffer. A new method for 3D-reconstruction for a mechanical characterisation of real single foam pores by photogrammetry. *Experimental Mechanics*, 2017. Submitted.
- [38] A. Jung, M. Wocker, Z. Chen, and H. Seibert. Microtensile testing of open-cell metal foams – Experimental setup, micromechanical properties. *Materials & Design* 88, pp. 1021–1030, 2015.
- [39] A. Jung. Cellular Materials: Structure-Property Relationships and Mechanical Modelling. Habil. Universität des Saarlandes, 2016.
- [40] R. Ketzscher, C. Lies, C. Drebenstedt, and T. Hipke. Revolutionärer Schienenfahrzeugbau. *Industrie-Anzeiger* 136.21, pp. 42–45, 2014.
- [41] A. Konyukhov, C. Lorenz, and K. Schweizerhof. Various contact approaches for the finite cell method. *Computational Mechanics* 56.2, pp. 331–351, 2015.
- [42] J. Korelc and S. Stupkiewicz. Closed-form matrix exponential and its application in finite-strain plasticity. *International Journal for Numerical Methods in Engineering* 98.13, pp. 960–987, 2014.
- [43] U. Küttler and W. Wall. Fixed-point fluid-structure interaction solvers with dynamic relaxation. *Computational Mechanics* 1.43, pp. 61–72, 2008.

- [44] T. A. Laursen. *Computational Contact and Impact Mechanics. Fundamentals of Modeling Interfacial Phenomena in Nonlinear Finite Element Analysis*. 1st ed. Springer, 2003.
- [45] L. Lorenzis, P. Wriggers, and C. Weißenfels. Computational Contact Mechanics with the Finite Element Method. *Encyclopedia of Computational Mechanics Second Edition*. American Cancer Society, 2017, pp. 1–45.
- [46] A. MacLeod. Acceleration of vector sequences by multi-dimensional Δ^2 methods. *Communications in Applied Numerical Methods* 1, pp. 3–20, 1986.
- [47] F. Matassi, A. Botti, L. Sirleo, C. Carulli, and M. Innocenti. Porous metal for orthopedics implants. *Clinical Cases in Mineral and Bone Metabolism* 10, pp. 111–115, 2013.
- [48] B. Müller, F. Kummer, and M. Oberlack. Highly accurate surface and volume integration on implicit domains by means of moment-fitting. *International Journal for Numerical Methods in Engineering* 96, pp. 512–528, 2013.
- [49] J. Muth, M. Poggie, G. Kulesha, and R. Michael Meneghini. Novel Highly Porous Metal Technology in Artificial Hip and Knee Replacement: Processing Methodologies and Clinical Applications. *JOM* 65.2, pp. 318–325, 2013.
- [50] S. Nemat-Nasser and M. Hori. *Micromechanics*. North Holland, Amsterdam, 1993.
- [51] S. Nemat-Nasser and M. Hori. *Micromechanics: Overall Properties of Heterogeneous Materials*. 2nd ed. North-Holland, 1999.
- [52] M. Ortiz, R. A. Radovitzky, and E. A. Repetto. The computation of the exponential and logarithmic mappings and their first and second linearizations. *International Journal for Numerical Methods in Engineering* 52.12, pp. 1431–1441, 2001.
- [53] C. G. Paganias, G. A. Tsakotos, S. D. Koutsostathis, and G. A. Macheras. Osseous integration in porous tantalum implants. *Indian Journal of Orthopaedics* 46, pp. 505–513, 2012.
- [54] J. Parvizian, A. Düster, and E. Rank. Finite cell method – h- and p-extension for embedded domain problems in solid mechanics. *Computational Mechanics* 41, pp. 121–133, 2007.
- [55] F. de Prenter, C. V. Verhoosel, G. J. van Zwieten, and E. H. van Brummelen. Condition number analysis and preconditioning of the finite cell method. *ArXiv e-prints*, 2016.
- [56] M. Robinson, J. Carruthers, C. O’Neill, S. Ingleton, and M. Grasso. Transport of DE-LIGHT: The Design and Prototyping of a Lightweight Crashworthy Rail Vehicle Driver’s Cab. *Procedia - Social and Behavioral Sciences* 48, pp. 672–681, 2012.
- [57] V. Salit and D. Gross. On the convergence of the iterative self-consistent embedded cell model. *Computational Materials Science* 81, pp. 199–204, 2014.
- [58] V. K. Saul’ev. A method for automatization of the solution of boundary value problems on high performance computers. *Dokl. Akad. Nauk SSSR 144 (1962), 497-500 (in Russian)*. *English translation in Soviet Math. Dokl.* 3, pp. 763–766, 1963.
- [59] V. K. Saul’ev. On solution of some boundary value problems on high performance computers by fictitious domain method. Russian. *Siberian Mathematical Journal* 4, pp. 912–925, 1963.

- [60] D. Schillinger, A. Düster, and E. Rank. The *hp-d*-adaptive finite cell method for geometrically nonlinear problems of solid mechanics. *International Journal for Numerical Methods in Engineering* 89, pp. 1171–1202, 2012.
- [61] D. Schillinger, M. Ruess, A. Düster, and E. Rank. The Finite Cell Method for large deformation analysis. *Proceedings in Applied Mathematics and Mechanics* 11, pp. 271–272, 2011.
- [62] D. Schillinger, M. Ruess, N. Zander, Y. Bazilevs, A. Düster, and E. Rank. Small and large deformation analysis with the p- and B-spline versions of the finite cell method. *Computational Mechanics* 50, pp. 445–478, 2012.
- [63] H.-G. Sehlhorst. Numerical homogenization strategies for cellular materials with applications in structural mechanics. PhD thesis. Fachgebiet für Numerische Strukturanalyse mit Anwendungen in der Schiffstechnik, TU Hamburg-Harburg, 2011.
- [64] J. C. Simo and T. J. R. Hughes. *Computational Inelasticity*. Springer-Verlag, 1998.
- [65] J. Simo, R. Taylor, and K. Pister. Variational and projection methods for the volume constraint in finite deformation elasto-plasticity. *Computer Methods in Applied Mechanics and Engineering* 51, pp. 177–208, 1985.
- [66] E. A. de Souza Neto, D. Perić, and D. R. J. Owen. *Computational Methods for Plasticity, Theory and Applications*. John Wiley & Sons, 2008.
- [67] B. Szabó and I. Babuška. *Finite element analysis*. John Wiley & Sons, 1991.
- [68] A. Taghipour, J. Parvizian, S. Heinze, and A. Düster. p-version finite elements and finite cells for finite strain elastoplastic problems. *Proceedings in Applied Mathematics and Mechanics* 16, pp. 243–244, 2016.
- [69] A. Taghipour, J. Parvizian, S. Heinze, and A. Düster. The finite cell method for nearly incompressible finite strain plasticity problems with complex geometries. *Computers & Mathematics with Applications* 75, pp. 3298–3316, 2018.
- [70] A. Taghipour, J. Parvizian, S. Heinze, E. Rank, and A. Düster. Computation of nearly incompressible finite strain plasticity problems using a high-order finite element method. *Journal of mechanical engineering science*, 2017. under Revision.
- [71] I. Temizer, T. Wu, and P. Wriggers. On the optimality of the window method in computational homogenization. *International Journal of Engineering Sciences* 64.0, pp. 66–73, 2013.
- [72] P. Wriggers. *Computational Contact Mechanics*. 2nd ed. Springer, 2006.
- [73] P. Wriggers. *Nonlinear Finite-Element-Methods*. Springer-Verlag, 2009.
- [74] P. Wriggers, J. Schröder, and A. Schwarz. A finite element method for contact using a third medium. *Computational Mechanics* 52.4, pp. 837–847, 2013.
- [75] H. Xiao and L. Chen. Hencky’s elasticity model and linear stress-strain relations in isotropic finite hyperelasticity. English. *Acta Mechanica* 157.1-4, pp. 51–60, 2002.
- [76] Z. Yang, A. Düster, M. Ruess, and E. Rank. The Finite Cell Method for Interactive Orthopaedic Simulation. *BIO Materialien* 10 (1/2), p. 66, 2009.

-
- [77] Z. Yang, A. Düster, M. Ruess, and E. Rank. The Finite Cell Method for Orthopaedic Simulation. *BIO Materialien* 9 (1/2), p. 74, 2008.
- [78] Z. Yang, S. Kollmannsberger, A. Düster, M. Ruess, E. Garcia, R. Burgkart, and E. Rank. Non-standard bone simulation: interactive numerical analysis by computational steering. *Computing and Visualization in Science* 14, pp. 207–216, 2012.
- [79] T. Zhodi and P. Wriggers. *An Introduction to Computational Micromechanics*. Vol. 20. Lecture Notes in Applied and Computational Mechanics. Springer, 2005.

Lebenslauf

Name	Heinze
Vorname	Stephan
Staatsangehörigkeit	deutsch
Geburtsdatum	05.01.1987
Geburtsort	Eckernförde, Deutschland
08.1993 - 07.1997	Richard-Vosgerau-Schule (Grundschule), Eckernförde
08.1997 - 07.2006	Jungmannschule (Gymnasium), Eckernförde
08.2006 - 09.2006	Grundpraktikum Lindenau-Werft, Kiel
10.2006 - 11.2012	Schiffbaustudium an der Technischen Universität Hamburg Abschluss: Diplom
12.2012 - 03.2017	Wissenschaftlicher Mitarbeiter an der Technischen Universität Hamburg
09.2017 - 09.2018	Wissenschaftlicher Mitarbeiter an der Technischen Universität Hamburg
12.2012 - heute	Promotion